Durham E-Theses

Hillslope memory and spatial and temporal distributions of earthquake-induced landslides

PARKER, ROBERT,NEVILLE

How to cite:

PARKER, ROBERT,NEVILLE (2013) *Hillslope memory and spatial and temporal distributions of earthquake-induced landslides*, Durham theses, Durham University. Available at Durham E-Theses Online: http://etheses.dur.ac.uk/7761/

Use policy

The full-text may be used and/or reproduced, and given to third parties in any format or medium, without prior permission or charge, for personal research or study, educational, or not-for-profit purposes provided that:

- a full bibliographic reference is made to the original source
- a link is made to the metadata record in Durham E-Theses
- the full-text is not changed in any way

The full-text must not be sold in any format or medium without the formal permission of the copyright holders.

Please consult the full Durham E-Theses policy for further details.

Academic Support Office, Durham University, University Office, Old Elvet, Durham DH1 3HP
e-mail: e-theses.admin@dur.ac.uk Tel: +44 0191 334 6107
http://etheses.dur.ac.uk

Hillslope memory and spatial and temporal distributions of earthquake-induced landslides

Robert Parker

Institute of Hazard, Risk and Resilience

Department of Geography

Durham University

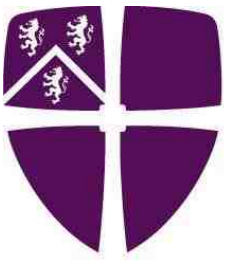

Thesis submitted for the degree of Doctor of Philosophy

2013

Abstract

Large earthquakes commonly trigger widespread and destructive landsliding. However, current approaches to modeling regional-scale landslide activity do not account for the temporal evolution of progressive failure in brittle hillslope materials. Progressive failure allows hillslopes to possess a memory of previous earthquakes, which has the potential to influence landslide activity in future earthquakes. The original contribution of this thesis is to address the influence of hillslope memory on spatial and temporal patterns of earthquake-triggered landslide activity, through a combination of landslide inventory analysis and numerical modeling.

An understanding of spatial distributions of earthquake-triggered landslides is first established, through analysis of inventories of landslides triggered by five large (M_w > 6.7) earthquakes. The results show how current landscape conditions at the time of earthquakes influence hillslope failure probability. By identifying factors exhibiting a common influence on landslides triggered by all five earthquakes, general spatial models of landslide probability are developed, which are transferrable between different earthquakes and regions. Analysis of model performance for landslide distributions triggered by two sequential earthquakes is then used to establish where this spatial approach breaks down. Errors in the landslide distribution predicted for the second earthquake suggest that the legacy of damage to hillslope materials accrued from the first earthquake is an important control on landslide occurrence.

Given the infrequent recurrence of large earthquakes and limited temporal coverage of landslide data, a new modelling approach is developed to understand how hillslope memory influences long-term patterns of earthquake-triggered landslide activity. The model integrates the site-scale evolution of hillslope progressive failure into modeling regional-scale earthquake-triggered landslide activity, in response to sequences of earthquakes. The model results suggest that the sensitivity of landscapes to landslide-triggering increases following large earthquakes, due to damage accumulated in hillslopes that do not reach the point of failure, and decays as these hillslopes fail in response to subsequent, lower-magnitude events. Prolonged elevated levels of rainfall-triggered landslide activity observed following large earthquakes appear to reflect this result. Using the model outputs, a methodology is proposed for predicting

temporal variability in landslide activity using records of seismic data. The model results also suggest that, when hillslopes undergo progressive failure, relationships between seismic forcing and landslides are influenced by the magnitude-frequency distribution of earthquakes. As a result, current approaches that use these relationships to predict levels of long-term landslide hazard and erosion rates, but do not account for regional differences in earthquake distributions, may suffer from systematic under- or over-prediction. These significant implications for predicting the geomorphological and human impact of landslides highlight the need for detailed multi-temporal datasets recording the evolution of landslide activity following major earthquakes, in order to quantitatively investigate the influence of hillslope memory in real landscape settings.

Declaration

I confirm that no part of the material presented in this thesis has previously been submitted for a degree in this or any other university. In all cases the work of others, where relevant, has been fully acknowledged.

The copyright of this thesis rests with the author. No quotation from it should be published without the author's prior written consent and information derived from it should be acknowledged.

Robert Parker

Durham University

Acknowledgements

"…one who knew how to get around him men who were cleverer than himself"

- Andrew Carnegie

So thank you…

To Nick Rosser, for your mentoring, encouragement, sarcasm, open door, brilliance and everything else since a chance conversation back in 2007 that set me on this course. To Dave Petley, for teaching me so much, being full of encouragement and healthy skepticism, and being the source of numerous fantastic opportunities. To Alex Densmore, for sharing your clear vision, guidance, and for seeing the hook and helping to get my first paper published. To Rashmin Gunasekera, Matt Foote, Rowan Douglas and everyone at Willis Re. past and present, for introducing me to the fascinating world of cat-modeling and providing the inspiration and the funding for this project. Thank you to my two examiners Bob Hilton and Oliver Korup for sharing their insight and enthusiasm, and for an invigorating and passionate scientific discussion during the viva. Also to Bob, for helping me find the focus in the early stages and for friendly conversations along the way.

To everyone in the Durham University Geography Department that let me drop in to ask a 'quick' question. To Dave Milledge, for being an astonishingly understated mathematician. To Matt Brain and Mike Lim for helping me get to grips with soil and rock mechanics, and Angel Ng for showing me how site investigations are done 'Hong Kong style'. Nick Cox for your incredible patience in teaching the art of statistics for geomorphologists. To all the people who helped from afar, and provided data, code, advice and encouragement: Peter Stafford, Randy Jibson, Dave Keefer, Lucille Tatard, JR Grasso, and many more. To office mates past and present, for sharing the journey and putting up with my fidgety approach to office work. Particularly to Dave Damby, for having an incredible scientific mind, a zest for playing and exploring, and being an absolutely great friend. I hope we get to Alaska one day. To Andy, Sarah and Josh, for spending New Year 2012 enthusiastically discussing theoretical models.

To all the students of the 2010 LARAM School, and particularly Cody Jones for a crash course in Mohr-Coulomb. To Phil Garnett and John Bissell, for helping me get to grips

with numerical models. To the kiwi contingent: Graham Hancox, Chris Massey, Mauri McSaveney, Angelique and all the team a GNS Science, for booking helicopters, providing data, and being unbelievably helpful at a time when things were so busy for you. To Bill Murphy, for your friendly advice over beer, enthusiasm and eagerness to explain things out in the field, and for letting me hang out of the side of the helicopter. To all the Geography labs and support staff, particularly Greg, Helen, Mark, Dave, Steve and Terry, for making the computer work again and again, and accepting my drop-in approach to seeking IT support.

To Van Mildert College and Durham University, for 7½ great years of not letting my degree get in the way of my education. To the many friends who have come and gone in Durham over the years, and helped make life exciting, enjoyable and bearable when things got tough. To Haz, for being a great friend and coming along for the ride. To Dave, Alice, Alison, Katie… for getting me out of the office and into a kayak/onto the climbing wall once in a while. To Beth, for the best coffee mug in the world, jam roly-poly and all the little things.

And finally, to Mum, Dad and Tim, for support, understanding, strength and perspective, now and consistently since 1986.

Table of Contents

Abstract ..... **i**

Declaration ..... **iii**

Acknowledgements ..... **iv**

Table of Contents ..... **vi**

List of Figures ..... **x**

List of Tables ..... **xv**

Glossary of terms ..... **xvi**

Glossary of abbreviations ..... **xxiii**

Chapter 1 - Introduction to the study **1**

1.1 Rationale 1

1.2 Aims and Objectives 5

1.3 Organisation of the thesis 5

Chapter 2 - Conceptual background **9**

2.1 Hillslope material properties and site-scale hillslope stability 9

2.1.1 Stress, strain and strength 9

2.1.2 Hillslope material strength 10

2.1.3 Rock mass strength and scale 13

2.1.4 Hillslope stability 13

2.1.5 Stress-strain behaviour of soil and rock 15

2.2 Seismic slope stability modelling 18

2.2.1 Pseudostatic analysis 18

2.2.2 High resolution geomechanical analysis 19

2.2.3 Permanent displacement analysis: Newmark sliding block model 20

2.2.4 Simplified Newmark analysis 22

2.2.5 Interpretation of modelled displacements 25

2.2.6 The representativeness and accuracy of Newmark 26

2.2.7 Summary 29

2.3 Regional-scale earthquake-triggered landslide activity 29

2.3.1 Regional-scale landslide data 29

2.3.2 Landslide magnitude-frequency distributions 30

2.3.3 The spatial distribution of earthquake-triggered landslides 32

2.3.4 The temporal distribution of landslides associated with earthquakes 41

2.4 Summary 44

Chapter 3 - Study areas and datasets **46**

3.1 1929 Buller and 1968 Inangahua earthquakes, New Zealand 47
3.1.1 Geological setting 47
3.1.2 Topographic data 49
3.1.3 Climate 49
3.1.4 The 1929 Buller earthquake 50
3.1.5 The 1968 Inangahua earthquake 54
3.1.6 Event comparison 58
3.1.7 Landslide mapping 63
3.1.8 Separation of landslide source areas 69
3.2 Comparative earthquake-triggered landslide datasets 70
3.2.1 1994 Northridge earthquake 71
3.2.2 1999 Chi-Chi earthquake 72
3.2.3 2008 Wenchuan earthquake 72
3.3 Landslide dataset comparison 77
3.3.1 Landslide inventory completeness 77
3.3.2 Timing of landslide data acquisition 80
3.4 Summary 81
Chapter 4 - Spatial models of earthquake-triggered landslide probability 83
4.1 Methodology: Hillslope failure probability modelling 83
4.1.1 Introduction to logistic regression 84
4.1.2 Landslide probability 86
4.1.3 Matrix grid sampling of variables for analysis 86
4.2 Landslide probability models for the 1929 Buller and 1968 Inangahua earthquakes .. 87
4.2.1 Response variables 88
4.2.2 Predictor variables 90
4.2.2.1 Normalised distance from stream-channel to ridge crest 95
4.2.2.2 Hillslope orientation with respect to the seismic source 98
4.2.2.3 Local hillslope gradient 101
4.2.2.4 Local relief 102
4.2.2.5 Regional geology 105
4.2.2.6 Orientation of dominant structures 105
4.2.2.7 Distance from mapped faults 108
4.2.2.8 Solar insolation 109
4.2.2.9 Precipitation 111
4.2.3 Variables summary 114

4.2.4 Model fitting 114
4.2.5 Buller and Inangahua earthquake-triggered landslide probability models 115
4.2.6 Coefficient variability 123
4.2.7 Predicted and observed probability comparison 126
4.2.8 Model fit breakdown 130
4.2.9 Discussion of model components and implications 132
4.3 General earthquake-triggered landslide probability models 135
4.3.1 Earthquake magnitude, seismic source distance and hillslope gradient model 136
4.3.2 Earthquake magnitude, PGA and hillslope gradient model 138
4.4 Discussion and Summary 146
Chapter 5 - Hillslope failure and regional-scale landslide activity 148
5.1 Hillslope failure via seismically-induced strain 148
5.1.1 The failure cycle 148
5.1.2 Failure cycles in populations of potential landslide masses 149
5.1.3 Model assumptions and limitations 152
5.2 Interpretation of earthquake-triggered landslide distributions 155
5.2.1 Spatial patterns of landslide density 155
5.2.2 The influence of hillslope memory on landslide activity 157
5.2.3 Formulation and testing of a landscape memory hypothesis 158
5.3 A mechanism of temporal changes in landslide propensity 163
5.4 Summary 164
Chapter 6 - Numerical modelling of regional-scale landslide activity 166
6.1 Model architecture 166
6.1.1 Hillslope component: potential landslide mass population 167
6.1.2 PLM magnitude-frequency distribution 170
6.1.3 PLM geometry 171
6.1.4 Seismic component: Earthquake magnitude and PGA time series 174
6.1.5 Model set-up, parameters and outputs 179
6.2 Calibration of model parameters 182
6.2.1 Calibration of αPLM 184
6.2.2 Calibration of τfp and k 185
6.2.3 Summary 187
6.3 Model behaviour and experiments 187
6.3.1 Landslide propensity changes in response to and between large earthquakes 188

6.3.2 Controls on the temporal response of landslide propensity to large earthquakes 197

6.3.3 Long-term behaviour 206

6.4 Summary 213

Chapter 7 - Discussion 215

7.1 What is the impact of large earthquakes on subsequent landslide activity? 216

7.1.1 Spatial variability in the landslide propensity response to large earthquakes 217

7.1.2 Observed temporal changes in landslide propensity 220

7.2 How can long-term patterns of variability in landslide propensity be linked to seismic history? 227

7.2.1 Long-term patterns of landslide propensity variability 227

7.2.2 Seismic history and uncertainty in global earthquake-triggered landslide relationships 235

7.3 How does the way in which landslides evolve affect the importance of earthquake-triggered landslides in long-term erosion rates and levels of landslide hazard? 241

7.3.1 The influence of earthquake magnitude-frequency distributions on earthquake-triggered landslide relationships 241

7.3.2 Seismicity and the long-term impact of rainfall-triggered landslides 249

7.4 Developments required for further quantitative investigation 253

Chapter 8 - Conclusions 256

8.1 Objective 1 256

8.2 Objective 2 257

8.3 Objective 3 258

8.4 Objective 4 258

8.5 Original contribution to knowledge 261

8.6 Recommendations for future research 262

Appendix A - Additional earthquake-triggered landslide event information 264

i. 1968 Inangahua earthquake 264

ii. 1994 Northridge earthquake 265

iii. 1999 Chi-Chi earthquake 266

iv. 2008 Wenchuan earthquake 269

Appendix B - Paper presented at the 2012 International Symposium on Earthquake-induced landslides 271

References 280

List of Figures

Figure 2-1 Illustration of infinite slope model for a cohesionless slope in dry conditions 15
Figure 2-2 Idealised stress-strain curves for brittle (A) and ductile (B) material (after Petley and Allison, 1997: 749). 16
Figure 2-3 Illustration of the Newmark sliding block model 21
Figure 2-4 Illustration of the Newmark integration method of Wilson and Keefer (1983) 22
Figure 2-5 Plot of Newmark displacements as a function of critical acceleration ratio 25
Figure 2-6 Plot showing the accuracy of predicted Newmark displacement, compared with displacements observed in physical and coupled analysis models, relative to the Tuning ratio 27
Figure 2-7 Illustration of characteristic landslide magnitude-frequency distribution ratio 31
Figure 2-8 Plots showing observed relationships between earthquake magnitude and different metrics of landslide activity 34
Figure 2-9 Relationships between landslide area density and PGA, constrained using inventories of landslides triggered by the 1994 Northridge earthquake (USA) and the 1999 Chi-Chi (Taiwan), (after Meunier et al., 2007) 35
Figure 2-10 Patterns of P- and S-wave topographic amplification ratio modelled for a simplified topography composed of two adjacent triangular ridges (after Meunier et al., 2008: 228) 37
Figure 2-11 Relationship between landslide-point density, landslide-area density and hillslope gradient for the 2008 Wenchuan earthquake (after Dai et al., 2011: 892) 38
Figure 2-12 Conceptual model of factors controlling the density of earthquake-triggered landslides 40
Figure 2-13 Time-series of landslide activity prior to and following the 1999 Chi-Chi earthquake (after Hovius et al., 2011: 351) 42
Figure 2-14 Time series of landslide activity and rainfall prior to and following the 2005 Kashmir earthquake (after Saba et al., 2010: 24) 43
Figure 3-1 Map of tectonostratigraphic units of the north-west Nelson Region 48
Figure 3-2 Map of the 1929 Buller earthquake epicentre , focal mechanism (Dowrick, 1994, Anderson et al., 1994), fault and locations of major aftershocks (GeoNET, 2011) .. 52
Figure 3-3 Map of locations of large landslides triggered by the 1929 Buller earthquake and MMI isoseismals inferred from building damage and landslide observations (Hancox et al., 2002: 65) 54
Figure 3-4 Map of the 1968 Inangahua earthquake epicentre , focal mechanism, fault model and aftershocks (data from Anderson et al., 1994) 57
Figure 3-5 Isoseismal map for the 1968 Inangahua earthquake (Downes, 1995: 68) 58
Figure 3-6 Map of MMI difference for the 1929 Buller and 1968 Inangahua earthquakes 60
Figure 3-7 Map showing distributed mean annual precipitation for the study area 62
Figure 3-8 Plot showing the annual distribution of rainfall for the study area 63
Figure 3-9 Oblique aerial images of landslides triggered by the 1929 Buller earthquake 66
Figure 3-10 Map of landslides (full landslide areas including source, runout and deposit) triggered by the 1929 Buller earthquake 67
Figure 3-11 Map of landslides (full landslide areas including source, runout and deposit) triggered by the 1968 Inangahua earthquake 68

Figure 3-12 Illustration of landslide source area extraction technique 70
Figure 3-13 Landslide inventory map for the 1994 Northridge earthquake 74
Figure 3-14 Landslide inventory map for the 1999 Chi-Chi earthquake 75
Figure 3-15 Landslide inventory map for the 2008 Wenchuan earthquake 76
Figure 3-16 Landslide frequency density as a function of landslide area for the Buller earthquauke, Inangahua earthquake, Northridge earthquake, Chi-Chi earthquake and Wenchuan earthquake landslide inventories 80
Figure 4-1 Landslide binary grids for the 1929 Buller earthquake (A) and 1968 Inangahua earthquake (B) 89
Figure 4-2 Maps of fault line distance (A) and fault plane distance (B) for the 1929 earthquake 92
Figure 4-3 Maps of fault line distance (A) and fault plane distance (B) for the 1968 earthquake 93
Figure 4-4 Maps of hanging wall binary variables for the 1929 (A) and 1968 (B) earthquakes . 94
Figure 4-5 Plot of local hillslope gradient against upslope area for the study region 96
Figure 4-6 Map of normal distance from stream to ridge crest variable 98
Figure 4-7 Maps of hillslope orientation with respect to the 1929 (A) and 1968 (B) seismic sources (fault lines). Inset maps show the location within the 1929 and 1968 landslide mapping overlap area. 100
Figure 4-8 Map of local hillslope gradient variable 102
Figure 4-9 Maps of relief variables 104
Figure 4-10 Maps of structural domains within geological units (A) and dip slope binary variable (B) 107
Figure 4-11 Map of distance from mapped faults in the New Zealand active fault database . 109
Figure 4-12 Map of annual solar radiation variable 110
Figure 4-13 Maps of gridded precipitation variables for the 1929 Buller earthquake 112
Figure 4-14 Maps of gridded precipitation variables for the 1968 Inangahua earthquake 113
Figure 4-15 Plots of observed and predicted hillslope failure probabilities for the 1929 (PLSA1929) and 1968 (PLSA1968) earthquakes relative to the distance from the earthquake coseismic fault planes (FPD) 119
Figure 4-16 Plots of observed and predicted hillslope failure probabilities for the 1929 (PLSA1929) and 1968 (PLSA1968) earthquakes relative to the relative to the normalised distance from stream channels to ridge crests (NDS) 119
Figure 4-17 Plots of observed and predicted hillslope failure probabilities for the 1929 (PLSA1929) and 1968 (PLSA1968) earthquakes relative to the variable FPD*NDS 120
Figure 4-18 Plots of observed and predicted PLSA1929 and PLSA1968, relative to SL 122
Figure 4-19 Plots of observed and predicted PLSA1929 and PLSA1968, relative to DS 122
Figure 4-20 Plots of observed and predicted PLSA1929 and PLSA1968, relative to ES 123
Figure 4-21 Plots of observed and predicted PLSA1929 and PLSA1968, relative to SR 123
Figure 4-22 Comparison plots of predictor coefficients for the 1929 and 1968 probability models 125
Figure 4-24 Map projected predicted probabilities (A) and observed landslide source locations (B) for the 1929 earthquake. 128
Figure 4-25 Map projected predicted probabilities (A) and observed landslide source locations (B) for the 1968 earthquake. 129

Figure 4-26 Plots showing the relative contribution of predictor variables to the fit of the 1929 and 1968 hillslope failure probability models 131
Figure 4-27 Map projected probability values for the 1929 Buller earthquake 141
Figure 4-28 Map projected probability values for the 1968 Inangahua earthquake 142
Figure 4-29 Map projected probability values for the 1994 Northridge earthquake 143
Figure 4-30 Map projected probability values for the 1999 Chi-Chi earthquake 144
Figure 4-31 Map projected probability values for the 2008 Wenchuan earthquake 145
Figure 5-1 Illustration of the failure cycle occurring in a single section of hillslope 149
Figure 5-2 Illustration of a hypothetical landscape with hillslopes composed of a population of potential landslide masses 150
Figure 5-3 Illustration of potential landslide mass (PLM) characteristics that determine the response to seismic accelerations 152
Figure 5-4 Landslide density ($\mathrm{PLS(A)}$) plotted by hillslope gradient (5^{o} bins) for areas within 5 km of the seismic source, for the Buller, Inangahua, Chi-Chi, Wenchuan and Northridge earthquakes. 158
Figure 5-5 Plotted comparison of observed and predicted hillslope failure probability for the 1968 Inangahua earthquake distributed by predicted probability for the 1929 earthquake 160
Figure 5-6 Map of delineated sectors of the 1929 landslide probability space in Figure 5-5, overlain by mapped landslides from the 1968 earthquake 161
Figure 5-7 Hypothetical stability (FS) histograms for a landscape in more sensitive and less sensitive states 164
Figure 6-1 Model parameters $\tau\mathrm{fp}$, $\tau\mathrm{fr}$ and k, illustrated on an idealised stress-strain curve. . 168
Figure 6-2 Flow diagram of the full failure cycle simulation sequence 170
Figure 6-3 Scatter plot of relationship between full landslide area (AL) and landslide source area (ALS), and regression output statistics 173
Figure 6-4 Scatter plot of relationship between landslide source area (ALS) and landslide source length (l), and regression output statistics 174
Figure 6-5 Earthquake magnitude probability density function, derived using $\mathrm{mmin} = 4$, $\mathrm{mmax} = 8$, $\mathrm{b} = 1$ 177
Figure 6-6 PGA-distance curves predicted using Equation 6-13. 179
Figure 6-7 Schematic diagram of model experimental set-up 180
Figure 6-8 Model FS-Area space 182
Figure 6-9 Time series showing the stabilisation of variables used in the model calibration process 184
Figure 6-10 Relationship between scaling the exponents $\alpha\mathrm{FLM}$ (distribution of failed landslide mass areas) and $\alpha\mathrm{PLM}$ (distribution of potential landslide masse areas) 185
Figure 6-11 Relationship between model parameter $\tau\mathrm{fp}$ (peak strength) and the minimum magnitude of earthquake required for the PGA to exceed ac in PLMs at peak strength. 186
Figure 6-12 Calibrated relationship between model parameters $\tau\mathrm{fp}$ and k, showing fitted values given by Equation 6-14 187
Figure 6-13 Time series showing initial model stabilisation where $\mathrm{PGALm} > \mathrm{ac}(\tau\mathrm{fp})$ 190
Figure 6-14 Time series showing the model response to a high magnitude earthquake, where $\mathrm{PGALm} > \mathrm{ac}(\tau\mathrm{fp})$ 192

Figure 6-15 Model time series and FS-A plots, when subjected to a sequence of constant magnitude earthquakes, where $\mathrm{PGALm} < \mathrm{ac}(\tau\mathrm{fp})$ 194
Figure 6-16 Model time series and FS-A plots, when subjected to a high magnitude earthquake, where $\mathrm{PGALm} < \mathrm{ac}(\tau\mathrm{fp})$ 196
Figure 6-17 Model time series showing the mean response to a HM earthquake averaged from 30 repeated simulations 198
Figure 6-18 Illustration of attributes used to characteristise the amplitude and period of the $\mathrm{PPLs}A$ impulse response, for quantitative analysis 200
Figure 6-19 Model output showing the landslide propensity ($\mathrm{PPLs}A$) response to a single large earthquake, and the effect of changing the large earthquake's magntiude (MWHM) 203
Figure 6-20 Model output showing the landslide propensity ($\mathrm{PPLs}A$) response to a single large earthquake, and the effect of changing the magnitude of subsequent small earthquakes (MWLM) 204
Figure 6-21 Model output showing the landslide propensity ($\mathrm{PPLs}A$) response to a single large earthquake, and the effect of changing the PLM peak strength ($\tau\mathrm{fp}$) 205
Figure 6-22 Long term landslide propensity ($\mathrm{PPLs}A(\mathrm{Mw} = 7.9)$) time-series in response to a series of GR distributed earthquakes, when $\tau\mathrm{fp} = 1.1$ (A) and $\tau\mathrm{fp} = 1.5$ (B), and $\mathrm{b} = 1$ 208
Figure 6-23 Plots showing the change in landslide propensity ($\mathrm{PPLs}A(\mathrm{Mw} = 7.9)$) produced by inidivudal earthquakes in the time series given in Figure 6-22 209
Figure 6-24 Long term $\mathrm{PPLs}A(\mathrm{Mw} = 7.9)$ time-series in response to GR distributed earthquakes when *b* = 1 (A) and *b* = 1.5 (B), and $\tau\mathrm{fp} = 1.1$ 210
Figure 6-25 Long-term distributions of landslide propensity (A), $\mathrm{PPLs}A(\mathrm{Mw} = 7.9)$, for different values of $\tau\mathrm{fp}$ 212
Figure 6-26 Long-term distributions of landslide propensity, $\mathrm{PPLs}A(\mathrm{Mw} = 7.9)$, for different values of b 213
Figure 7-1 Schematic diagram of showing characteristics of spatial variability in temporal changes in landslide propensity following large earthquakes 219
Figure 7-2 Landslide propensity changes produced by different magnitude model earthquakes, expressed as a ratio of landslide propensity prior to each earthquake 221
Figure 7-3 Density distributions of landslides triggered by the 1999 Chi-Chi earthquake and subsequent typhoon triggered landslides, with respect to the seismogenic fault (after Hovius et al., 2011: 352) 222
Figure 7-4 Relationship between the number of earthquakes required to reduce landslide propensity to background mean levels and material peak strength 226
Figure 7-5 Time-series of cumulative seismic moment released following the 1999 Chi-Chi and 2005 Kashmir earthquakes 226
Figure 7-6 Plot of Mt threshold 229
Figure 7-7 Schematic diagram showing how the seismic strength ratio (SSR) is calculated 231
Figure 7-8 Plot showing the relationship between seismic strength ratio (*SSR*) and landslide propensity ($\mathrm{PPLSA}(\mathrm{Mw} = 7.9)$), described using a logistic function 233
Figure 7-9 Time series comparison of numerical mode landslide propensity ($\mathrm{PPLs}A$) and landslide propensity predicted as a function of seismic strength ratio (SSR) 234

Figure 7-10 Relationships between observed and predicted numbers of landslides, using Equation 7-3 238
Figure 7-11 Residual in predictions of number of landslides using Equation 7-3, plotted against the magnitude of the largest (A) and most recent (B) earthquakes..... 240
Figure 7-12 Relationship between Gutenberg-Richter b-value and long-term landslide activity 242
Figure 7-13 Relationships between earthquake magnitude and mean landslide density $\mathrm{PLS}(\mathrm{A})$, as defined by the time-independent model from Equation 4-10, and by the time-dependent model for different Gutenberg-Richter b-values..... 243
Figure 7-14 Relationships between landslide density and horizontal and vertical components of PGA (after Meunier et al., 2007)..... 244
Figure 7-15 Mean area of landslides triggered by the largest aftershock (defined as the mainshock Mw-1.2), according to Båth's law (Båth, 1965), as a percentage of the mean area of landslides triggered by mainshocks, for different b-values..... 246
Figure 7-16 Map showing global variability in Gutenberg-Richter b-values, across 27 zones (after Bayrak et al., 2002)..... 248
Figure 7-17 Map showing spatial variability in Gutenberg-Richter b-value across the Himalaya and adjacent regions, derived from recorded seismicity (after Wiemer and Wyss, 2002) 249
Figure 7-18 Hypothetical FS-Area plots to illustrate interactions between earthquake and rainfall-triggered landslide activity..... 252

List of Tables

Table 2-1 Regression equations for predicting Newmark displacement 24
Table 3-1 Source and details of imagery used for landslide mapping for the 1929 and 1968 earthquakes 64
Table 3-2 Summary details of earthquake-triggered landslide datasets 79
Table 4-1 Variables used to logistic regression analysis for the 1929 Buller and 1968 Inangahua earthquakes 114
Table 4-2 Logistic regression statistics for the 1929 Buller earthquake model 116
Table 4-3 Logistic regression statistics for the 1968 Inangahua earthquake model 117
Table 4-4 Variables used in logistic regression analysis for all earthquake events 135
Table 4-5 Landslide inventory mapping coverage areas and sample sizes used in analysis 136
Table 4-6 Logistic regression statistics for earthquake magnitude, seismic source distance and hillslope gradient model 137
Table 4-7 Logistic regression statistics for Earthquake magnitude, PGA and hillslope gradient model 139
Table 4-8 Logistic regression statistics for Earthquake magnitude, PGA and hillslope gradient model, with PGA interaction term 140
Table 6-1 Numerical model parameters 181
Table 7-1 Comparison of mean annual precipitation and seismic moment release following the Chi-Chi and Kashmir earthquakes 223
Table 7-2 Reported numbers of landslides for recent earthquakes, and characteristics of pre-earthquake seismicity 236
Table 7-3 Outputs statistics for regression relationship between the number of landslides triggered and earthquake magnitude and depth 237

Glossary of terms

Landslide modelling and analysis variables

Variable	Description	Units
$\boldsymbol{F}$	Force	N or kg m s^{-2}
$\boldsymbol{A}$	Area	m^2
$\boldsymbol{\sigma}$	Normal stress	Pa or kg m^{-1} s^{-2}
$\boldsymbol{\sigma'}$	Effective normal stress	Pa or kg m^{-1} s^{-2}
$\boldsymbol{\tau}$	Shear stress	Pa or kg m^{-1} s^{-2}. Note that in Chapter 6 numerical modeling this is defined as a static coefficient of friction.
$\boldsymbol{\tau_f}$	Shear strength	Pa or kg m^{-1} s^{-2}. Note that in Chapter 6 numerical modeling this is defined as a static coefficient of friction.
$\boldsymbol{\tau_{fp}}$	Peak shear strength	Pa or kg m^{-1} s^{-2}. Note that in Chapter 6 numerical modeling this is defined as a static coefficient of friction.
$\boldsymbol{\tau_{fr}}$	Residual shear strength	Pa or kg m^{-1} s^{-2}. Note that in Chapter 6 numerical modeling this is defined as a static coefficient of friction.
$\boldsymbol{\varepsilon}$	Shear strain	None (m/m)
$\boldsymbol{\dot{\varepsilon}}$	Shear strain rate	s^{-1}

$\boldsymbol{k}$	Rate of shear strength decay with shear strain ($\frac{\Delta\tau_f}{\Delta\varepsilon}$)	Pa or kg m^{-1} s^{-2}
$\boldsymbol{\phi}$	Friction angle	Radians
$\boldsymbol{\phi'}$	Effective friction angle	Radians
$\boldsymbol{c}$	Cohesion	Pa or kg m^{-1} s^{-2}
$\boldsymbol{c'}$	Effective cohesion	Pa or kg m^{-1} s^{-2}
$\boldsymbol{u}$	Pore-water pressure	Pa or kg m^{-1} s^{-2}
$\boldsymbol{\beta}$	Hillslope gradient	Degrees (converted to radians in calculations)
$\boldsymbol{g}$	Gravitational acceleration	9.8 m s^{-2}
$\boldsymbol{\rho_s}$	Soil density	kg m^{-3}
$\boldsymbol{z}$	Vertical depth to the shear plane	m
$\boldsymbol{z_w}$	Height of water table above the failure plane	m
$\boldsymbol{\rho_w}$	Water density	kg m^{-3}
$\boldsymbol{FS}$	Factor of safety $FS = \frac{\tau_f}{\tau}$	Dimensionless ratio
$\boldsymbol{e}$	Exponential constant	
$\boldsymbol{q}$	Material void ratio	
$\boldsymbol{C}$	Material composition	
$\boldsymbol{H}$	Material stress history	
$\boldsymbol{T}$	Temperature	K
$\boldsymbol{S}$	Material structure	
$\boldsymbol{l}$	Landslide mass downslope length	m
$\boldsymbol{a_c}$	Newmark critical acceleration	g (1 g = 9.81 m s^{-2})

$\boldsymbol{a_c(\tau_{fp})}$	Critical acceleration when material is at peak strength	g (1 g = 9.81 m s^{-2})
$\boldsymbol{D_N}$	Newmark displacement	cm
$\boldsymbol{A_L}$	Full landslide area (including source, run-out and deposit)	m^2
$\boldsymbol{A_{LS}}$	Area of landslide source zone (excluding zones on run-out and deposit)	m^2
$\boldsymbol{A_{min}}$	Magnitude-frequency distribution lower bound landslide area A_L	m^2
$\boldsymbol{A_{max}}$	Magnitude-frequency distribution upper bound landslide area A_L	m^2
$\boldsymbol{\alpha}$ and $\boldsymbol{\vartheta}$	Power-law scaling exponents, where $\alpha = \vartheta + 1$	
$\boldsymbol{\alpha_{PLM}}$	Power-law scaling exponent for distribution of potential landslide masses	
$\boldsymbol{\alpha_{FLM}}$	Power-law scaling exponent for distribution of failed landslide masses	
$\boldsymbol{N_L}$	Number of landslides triggered by an earthquake	
$\boldsymbol{P_{ls}(A)}$	Landslide source area (hillslope failure) probability, $P_{ls}(A) = \frac{\sum A_{LS}}{\sum A_t}$	
$\boldsymbol{\widehat{P}_{LS}(A)}$	Landslide source area (hillslope failure) probability predicted by logistic regression model	

Variables for landslide probability spatial analysis calculated at 30 m pixel resolution		
LS	Landslide source binary variable	
FLD	Distance from coseismic fault line	km
FPD	Distance from coseismic fault plane	km
HW	Hanging-wall binary variable	
NDS	Normalised distance from stream channel to ridge crest	
IA	Local hillslope orientation with respect to coseismic source (incidence angle of seismic waves)	Degrees
SL	Local hillslope gradient derived from a 30 m resolution DEM	Degrees
ER	Drainage basin elevation range derived from a 30 m resolution DEM	m
ES	Drainage basin elevation standard deviation (m) derived from a 30 m resolution DEM-	m
GT	Geology indicator variable	
DS	Dip-slope binary variable	
SR	Solar Radiation	WH/m^2
FDA	Distance from all mapped faults	km
$PD3$	Spatially distributed mean precipitation for the month of a given earthquake plus the previous 2 months	mm
$PD6$	Spatially distributed mean precipitation for the month of a given earthquake plus the previous 5 months	mm

Earthquake modelling and analysis variables		
$\boldsymbol{a}$	Earthquake ground acceleration	g (1g = 9.81 m s^{-2})
$\boldsymbol{I_a}$	Arias intensity	m s^{-1}
$\boldsymbol{PGA}$	Peak ground acceleration	g (1 g = 9.81 m s^{-2})
$\boldsymbol{M}$and $\boldsymbol{m}$	Earthquake magnitude (generic)	
$\boldsymbol{M_W}$	Earthquake moment magnitude	
$\boldsymbol{M_s}$	Earthquake surface wave magnitude	
$\boldsymbol{M_L}$	Earthquake local magnitude	
$\boldsymbol{M_o}$	Seismic moment	N m
$\boldsymbol{D}$	Earthquake focal depth	m
$\boldsymbol{b}$	Gutenberg-Richter b-value	
$\boldsymbol{\delta}$	Gutenberg-Richter scaling exponent, $\delta = \ln(10)\, b$	
$\boldsymbol{m_{min}}$	Gutenberg-Richter distribution lower-bound earthquake magnitude	
$\boldsymbol{m_{max}}$	Gutenberg-Richter distribution upper-bound earthquake magnitude	
$\boldsymbol{R}$	Distance from seismic source	km
$\boldsymbol{M_w(HM)}$and $\boldsymbol{M_w(LM)}$	Magnitude of HM (high magnitude) earthquakes and LM (low magnitude) earthquakes respectively, where the relative size of earthquakes is of relevance to the system behaviour	
$\boldsymbol{PGA(HM)}$ and $\boldsymbol{PGA(LM)}$	PGA produced by HM (high magnitude) earthquakes and LM (low magnitude) earthquakes respectively, where the relative size of earthquakes is of relevance to the system behaviour	g (1 g = 9.81 m s^{-2})
$\boldsymbol{t}$	Time in model iterations, where each	

	iteration represents the occurrence of a single mainshock earthquake	
$\boldsymbol{M_t}$	Threshold magnitude separating model earthquakes where $PGA \geq a_c(\tau_{fp})$ and $PGA < a_c(\tau_{fp})$, used in the calculation of SSR	
$\boldsymbol{M_{op}}$	A given total of previously released seismic moment, used in the calculation of SSR	N m or m^2 kg s^{-2}
$\boldsymbol{SSR}$	Seismic strength ratio: the ratio recently released seismic moment contributed from earthquakes where $PGA \geq a_c(\tau_{fp})$ and $PGA < a_c(\tau_{fp})$. Provides an index for estimating current landslide propensity from past seismic history	$(SSR = \frac{log(M_{op})}{log(M_{op})} \begin{matrix} M_w > M_t \\ M_w < M_t \end{matrix})$

Numerical model analysis variables

$\boldsymbol{PP_{LSA}(M_w = 7.9)}$	Potential landslide source area probability: $P_{ls}(A)$ that would result if an earthquake of a given magnitude (7.9 in this example) occurs
Pmax	PP_{LsA} at $t = t(HM) + 1$. Describes the peak landslide propensity immediately following the HM earthquake
Pmin	minimum PP_{LsA} reached in the minima following Pmax
Pmean	long-term mean PP_{LsA} calculated across 10,000 iterations prior to the HM earthquake
Pminit	iteration at which Pmin is reached

Pmeanit1	iteration at which PP_{LsA} reaches Pmean following Pmax and is the initial model-time period taken for PP_{LsA} to decay from its peak back to mean conditions
Pmeanit2	model-time period taken for PP_{LsA} to reach Pmean following Pmin
$\boldsymbol{M_{max}}$	Magnitude of the largest recorded earthquake prior to a given landslide-triggering earthquake
$\boldsymbol{M_{last}}$	Magnitude of the last recorded earthquake prior to a given landslide-triggering earthquake

Regression parameters

$\boldsymbol{R^2}$	Regression fit statistic ($\boldsymbol{R^2}$ or pseudo-R^2 where indicated)
$\boldsymbol{c_{...}}$	Where c is followed by a subscript it denotes a regression coefficient (e.g.: c_{PGA})

Glossary of abbreviations

Abbreviation	Description
MF	Magnitude-frequency
MMI	Modified Mercalli Intensity
DEM	Digital elevation model
PLM	Potential landslide mass
FLM	Failed landslide mass
GR	Gutenberg-Richter
USGS	United States Geological Survey
GNS	New Zealand Institute of Geological and Nuclear Sciences
MSA	Multiple series average, which refers to the average $PP_{LSA}(M_w = 7.9)$ time series output from 30 numerical model runs
ETL	Earthquake-triggered landslide

Chapter 1 - Introduction to the study

This thesis explores relationships between distributions of earthquake-triggered landslides (ETL) and the potential influence of landscape memory of past earthquakes. The combination of widespread hillslope failure produced by earthquakes, and the potential of seismic waves to irreversibly damage and weaken hillslope materials, even in hillslopes that do not undergo failure, means that the condition of hillslopes does not remain static through time. As a result, the current sensitivity of landscapes to earthquake-triggered landsliding, or landslide propensity (the number, area or volume of landslides that a given earthquake will trigger), will be dependent upon the legacy of previous earthquakes. This relationship remains poorly understood, primarily due to the limited temporal record of regional-scale landslide activity across the return periods of large earthquakes. This investigation offers an alternative approach, which integrates hillslope material failure mechanics into ETL modelling, in order to relate regional-scale landslide activity to the site-scale evolution of hillslope progressive failure via brittle deformation processes.

1.1 Rationale

High magnitude earthquakes in steep mountainous regions commonly trigger large numbers of landslides across extensive areas (Keefer, 2002, Bommer and Rodriguez, 2002, Rodríguez et al., 1999). For example, the 2008 Wenchuan earthquake caused over 56,000 landslides distributed across an area of over 40,000 km^2 (Dai et al., 2011). Such events drive orogen-scale geomorphic changes (Keefer, 1994, Korup et al., 2010, Malamud et al., 2004b, Hovius et al., 2011, Parker et al., 2011) and pose a major hazard to life and infrastructure across wide areas (Cui et al., 2011, Keefer, 2002, Dahal et al., 2012). An understanding of the nature and behaviour of orogen-scale, seismically-driven geomorphological processes has important implications for understanding landscape evolution and gauging risks posed to communities living in active mountain regions.

Current approaches to analysing regional-scale ETL activity involve primarily spatial interpretation of the links between landslide occurrence and static landscape conditions, including the properties of hillslope materials (Parise and Jibson, 2000, Clarke and Burbank, 2011), structure (Guzzetti et al., 1996), morphology (Montgomery,

2001, Montgomery and Brandon, 2002), and the characteristics of triggering mechanisms (Meunier et al., 2007, Meunier et al., 2008, Malamud et al., 2004b). This work has provided insights into factors controlling spatial distributions of ETLs, which can be modelled as a function of variables that provide proxies for the stability of hillslopes and the spatial distribution of ground accelerations (e.g.: Lee et al., 2008a, Meunier et al., 2007, Pal et al., 2008, Garcia-Rodriguez et al., 2008, Miles and Keefer, 2009, Jibson, 2007, Godt et al., 2009, Jibson, 2011). However, two characteristics of these approaches limit the extent to which ETL distributions are understood, which in turn limits the spatial and temporal transferability of current models.

Firstly, the majority of published ETL spatial models have been produced for the purposes of hazard assessment, through analysis of landslides specific to a single earthquake or region (Yilmaz and Keskin, 2009, Lee et al., 2008a, Kamp et al., 2008, Garcia-Rodriguez et al., 2008, Lee and Evangelista, 2006, Ayalew and Yamagishi, 2005, Lin and Tung, 2004). Although these models have a number of similarities, modelling approaches and input variables differ extensively, and the fit of models has previously been given more emphasis over understanding physical links between predictor variables and ETL processes. As a result, there is a lack of a generalised, albeit simplified model, which describes ETL distributions in a manner transferable between different earthquakes and regions. This complex, non-unified conception of ETL distributions has prevented general characteristics of the system behaviour from being studied in more detail.

Secondly, and following on from this, the underlying basis of the landslide process in these models does not account for the temporal evolution of failure in hillslope materials, specifically progressive failure. The probability that a hillslope fails is considered as dependent on the current earthquake and other landscape characteristics that are assumed to be temporally static, and independent of all preceding events. However, movement patterns in failing landslide masses (Loew et al., 2012, Petley et al., 2002, Crosta and Agliardi, 2003) and the results of laboratory tests (Petley et al., 2005b, Petley et al., 2005a) have shown that brittle hillslope materials undergo strain-dependent weakening prior to failure (Leroueil et al., 2012). ETL failure in brittle materials therefore develops through time, such that hillslopes have a memory of past earthquakes that drive the strain-weakening process. That

memory is recorded through a cyclic process of incremental reduction in material strength and the subsequent failure and removal of weakened material. Whether or not a hillslope fails in response to an earthquake is a function of both the current event and by definition the history of damage accumulated in that hillslope from past events. It follows that landslide activity in response to a given earthquake is therefore dependent on the legacy of damage previously accumulated in hillslopes across the landscape. The same earthquake could conceivably trigger different numbers and distributions of landslides depending on when it occurs, and those hillslopes that do not undergo failure may experience weakening that primes them for failure in future events.

Regional-scale empirical evidence tentatively indicates the influence of hillslope memory on landslide activity, although the mechanics and long-term nature of this behaviour remain unclear. Limited temporal data suggests a 7-fold increase in rainfall-triggered landslide activity in the wake of the 1999 Chi-Chi earthquake (e.g.: Hovius et al., 2011, Lin et al., 2006, Lin et al., 2004, Lin et al., 2008a) and preliminary results suggest similar behaviour associated with the 2008 Wenchuan (Whadcoat, 2011, Tang et al., 2011) and 2005 Kashmir earthquakes (Saba et al., 2010). Although this behaviour has been associated with the damage and disturbance to hillslope materials produced by large earthquakes (Hovius et al., 2011; Lin et al., 2008), the temporal mechanics of the process have not been explored. Additionally, predictive models of regional-scale landslide activity exhibit large uncertainties. Spatial models (described above) suffer from uncertainty in their ability to predict the discrete locations of landslides (Lee et al., 2008a, van Westen et al., 2006), while global relationships reveal up to an order of magnitude variance in the number and volume of landslides for earthquakes of comparable size and depth (Keefer, 2002, Keefer, 1984, Bommer and Rodriguez, 2002, Rodríguez et al., 1999, Malamud et al., 2004b, Keefer, 1994). Although these uncertainties are generally attributed to unconstrained variability in climate, earthquake characteristics, landscape morphology and hillslope material properties, local to regional differences in the legacy of past events provides another potential contributing factor. The discrete locations of landslides will be determined by those hillslopes sufficiently weakened and primed for failure prior to the triggering earthquake, and earthquakes will trigger more landslides in regions where more

hillslopes are primed for failure, and vice-versa. However, the absence of ETL data for sequences of earthquakes has resulted in a limited quantitative understanding of how past events influence present ETL activity. This applies both to short-term changes in landslide activity in the wake of large earthquakes, as well as the impact of hillslope memory on long-term patterns of landslide activity. Consequently, many models used to undertake quantitative assessment of landslide hazard and erosion rates assume that the impact of earthquakes is not correlated across time (e.g.: Guzzetti et al., 2006, Guzzetti et al., 2003, Guzzetti et al., 2005, Malamud et al., 2004b, Keefer, 1994). If hillslope memory affects landslide activity then this assumption is false and the validity of these models must be scrutinised (Witt et al., 2010, Korup et al., 2012, Tatard et al., 2010).

Despite the lack of multi-temporal landslide data, there currently exists an extensive range of geotechnical models with which to simulate progressive hillslope failure (Stead et al., 2012, Kramer, 1996, Leroueil et al., 2012, Eberhardt et al., 2004). As these techniques have been developed for site-scale landslide investigations, advances in geotechnical models have generally focused on providing a physically realistic representation of site-scale failure processes and movement mechanisms (e.g.: Wasowski et al., 2011, Stead et al., 2006, Moore et al., 2011). A lack of research has considered the application of these models to investigate regional-scale landslide activity. The innovative nature of this study is to develop a new approach to modelling regional-scale ETL activity, as the product of progressive failure processes. This provides the basis for investigating landslide activity from a temporal perspective not attainable from current landslide data, and developing an understanding of the potential influence of hillslope memory on spatial and temporal patterns of earthquake-triggered landslides.

1.2 Aims and Objectives

The principle aim of this study is to establish the effect of hillslope material memory on regional-scale landslide activity in areas affected by earthquakes. This is achieved by addressing the following objectives:

1. To produce a generalised earthquake-triggered landslide spatial model that is transferrable between different earthquakes and regions, by using statistical models to investigate the influence of current earthquake and static landscape conditions on the probability of hillslope failure;

2. To test for the influence of hillslope memory and establish the errors involved in a spatial approach to modelling earthquake-triggered landslides, by undertaking a detailed analysis of spatial distributions of landslides triggered by multiple earthquakes in the same region;

3. To develop a new conceptual and numerical model that integrates the site-scale evolution of hillslope progressive failure via brittle deformation processes into modelling regional-scale earthquake-triggered landslide activity;

4. To investigate the implications of the model results for landslide hazard, predictability and sediment generation through the following research questions:

i. What is the impact of large earthquakes on subsequent landslide activity?

ii. How can long-term patterns of variability in landslide propensity be linked to seismic history?

iii. How does the way in which landslides evolve affect the importance of earthquake-triggered landslides in long-term erosion rates and levels of landslide hazard?

1.3 Organisation of the thesis

The structure of this thesis reflects an attempt to progressively build an understanding of the influence of hillslope memory on regional-scale landslide activity.

Chapter 2 provides a review of current research into hillslope processes at different scales relevant to this investigation. This starts by examining hillslope material properties and how these influence the stability of individual landslide masses. A review of seismic slope stability models is provided, with detailed consideration given to the Newmark sliding block method, which is used throughout this investigation. Finally, regional-scale landslide activity is addressed by reviewing studies into the aggregate characteristics and spatio-temporal distributions of ETLs.

Chapter 3 presents the inventories of ETLs used in analysis. The data consist of five landslide inventories and accompanying thematic data, selected to provide insight into spatial patterns of landslide activity associated with earthquakes across different regions. Included are two new datasets for large earthquakes occurring in close proximity, which triggered landslides across an overlapping region. These events provide the foundations to examine the consistency of spatial patterns of hillslope failure and to test for the influence of hillslope memory from one earthquake to the next. Three additional datasets from previous investigations are also introduced, and a comparison of all five datasets is undertaken in order to determine considerations for analysis.

Chapter 4 presents a spatial analysis of earthquake-triggered landslide distributions, in order to address Objective 1 and provide the basis for addressing Objective 2 in Chapter 5. This is achieved using logistic regression models to constrain the spatial probability of hillslope failure probability, as a function of variables that provide proxies for the stability of hillslopes and the spatial distribution of ground accelerations. These variables represent the present, static landscape conditions when earthquakes occur, but not the legacy inherited from past earthquakes. A detailed spatial analysis is carried out for the 1929 and 1968 New Zealand earthquakes, identifying patterns of hillslope failure consistent for the two events and the strength of different variables in influencing failure probability. A combined analysis of all five landslide distributions is undertaken to develop a general model of earthquake-induced hillslope failure probability, which is transferrable between different earthquakes and regions.

Chapter 5 presents a conceptual model that integrates the site-scale evolution of hillslope progressive failure via brittle deformation processes into modelling regional-scale earthquake-triggered landslide activity, thereby addressing Objective 3. The model is necessarily simplified, but represents the key mechanisms of first-time earthquake-triggered hillslope failure in brittle hillslope materials. The model is used to infer the role of hillslope memory in spatial patterns of landslide activity, and uses further analysis of data from the 1929 and 1968 earthquakes to test this hypothesis (Objective 2). From the model, a mechanism of potential temporal variability in landslide propensity is identified, providing the justification for numerical modelling undertaken in Chapter 6.

Chapter 6 examines how hillslope memory might influence the legacy of large earthquakes and long-term temporal variability in landslide activity, through numerical modelling. The model system is based on the principles outlined in Chapter 5 and calibrated using landslide distribution characteristics observed in Chapter 4. The model simulates the development of hillslope failure in populations of landslide masses in response to multiple earthquakes. The results show the potential effects of hillslope material memory on regional-scale landslide activity across timescales of the return period of individual earthquakes and long-term behaviour in response to earthquake distributions. The results provide the basis for addressing Objective 4 and the research questions, which are discussed in Chapter 7.

Chapter 7 provides a synthesis of outputs from numerical modelling in Chapter 6, with the understanding of ETL spatial distributions developed in Chapters 4 and 5, in order to address the three research questions. (*i*) The impact of large earthquakes on landslide activity is examined through comparison of temporal patterns of landslide activity predicted by the numerical model with observed changes in landslide activity following large earthquakes. (*ii*) A means of predicting temporal variability in landslide activity from past seismic data is proposed and tested through a reanalysis of numbers of landslides triggered by different earthquakes. (*iii*) The influence on hillslope memory on the long-term impact of landslides is investigated through comparison of outputs from the time-dependent model developed in Chapter 6, which integrates hillslope memory, and the time-independent model developed in Chapter 4, which does not. Finally, future research requirements are identified, for testing and further

quantitative investigation of the influence of hillslope failure processes on regional-scale landslide activity.

Chapter 8 provides the conclusions of the investigation, with respect to the study objectives and research questions. The original contribution to knowledge is outlined and recommendations for future research are summarised.

Chapter 2 - Conceptual background

In order to investigate the influence of hillslope memory on landslide activity, it is necessary to consider current understanding of landslide processes at different spatial scales. These can be broadly separated into the process-scale of brittle deformation and progressive failure, the site-scale of individual landslide masses and the regional-scale encompassing multiple landslide masses. The strength and stress-strain behaviour of hillslope materials is determined by deformation and fracture processes that essentially occur at the molecular scale. However, the properties of hillslope materials that result from this process are studied and generalised through laboratory tests on material samples at scales of ~0.10 m. The site-scale stability of hillslopes, and their response to seismic accelerations, is then inferred by further generalising this behaviour across the scale of individual landslide masses. As the scale of landslide masses ranges over several orders of magnitude, the most relevant conceptual scale may be tens to thousands of metres in length. The third level is the regional-scale, which refers to that encompassing multiple landslides across a region. This is the scale at which large numbers of discrete landslide events can be studied using aggregate statistics, and generally considers areas upwards of the scale of individual drainage basins. The behaviour of landslides at this scale is the product of the combination of hillslope material properties and site-scale stability mechanics in large numbers of potential landslide masses in hillslopes. The following sections review the current understanding of landslide processes relevant to this investigation at these different scales.

2.1 Hillslope material properties and site-scale hillslope stability

2.1.1 Stress, strain and strength

Understanding hillslope material properties requires a clear definition of the concepts of stress, strain and material strength. Stress (σ or τ, kg$\cdot$ m$^{-1}\cdot$ s^{-2}) is the average force (F, kg$\cdot$ m$\cdot$ s^{-2}) acting on a unit area (A, m^2) in any chosen direction, generating tension, shear or compression):

Equation 2-1

$$\sigma = \frac{F}{A}$$

Stresses acting on a plane may be resolved into three perpendicular components, with one component acting normal to the surface (normal stress, σ, kg· m^{-1}· s^{-2}) and the other two acting parallel to the surface (shear stresses, τ, kg· m^{-1}· s^{-2}). Normal stresses tend to change the volume of the material and are resisted by the bulk modulus. Shear stresses tend to deform the material without changing its volume, and are resisted by the shear modulus.

Strain (ε, dimensionless) is deformation, as measured as a ratio of the change in dimensions of the stressed body (du) to its original dimensions (dx):

Equation 2-2

$$\varepsilon = \frac{du}{dx}$$

Strain may occur as an increase or decrease in dimensions and may involve changes in length (linear strain), volume (volumetric strain) or distortion (shear strain). Where the strain in one direction is much less than the strain in the other orthogonal directions the smallest strain can be ignored and the body is said to experience plane strain. This is important for slope stability models since plane strain is a key assumption for limit equilibrium methods (Section 2.1.3).

The term strength is used in three senses in the earth sciences (Selby, 2005): 1) the ability of material to resist deformation by compressive, tensile or shear stresses, 2) the ability of a rock or soil to resist abrasion, and 3) to indicate the resistance of loose or unconsolidated mineral grains to being transported by a fluid. Here and throughout this thesis strength is used in the first of these senses.

2.1.2 Hillslope material strength

In evaluating the resistance of hillslope material to landsliding, the shear strength of the material is of primary relevance, rather than its resistance to failure under tension or compression. The shear strength of a material depends upon many factors. Selby (2005:51) hypothesised that a complete equation to characterise shear strength may take the form:

Equation 2-3

$$\tau_f = f(q, \phi, C, \sigma', c', H, T, \varepsilon, \dot{\varepsilon}, S)$$

Where:

τ_f is the shearing resistance

q is the void ratio

ϕ is the frictional property of the material

C is the composition

σ' is the effective normal stress holding materials in contact

c' is the effective cohesion of the material

H is the stress history

T is the temperature

ε is the strain

$\dot{\varepsilon}$ is the strain rate

S is the structure of the material

Many of these components are not independent and cannot be evaluated quantitatively. However, in general hillslope material strength can be simplified to two components, cohesion and friction, which can be evaluated and measured in controlled conditions (Selby, 2005, Simons et al., 2001). Cohesion results from a variety of inter-particle bonding processes including chemical bonds, Van der Waals forces, electrostatic forces and magnetic forces. Apparent cohesion occurs as a result of capillary stresses and interlocking of particles on a microscopic level due to surface roughness. Cohesion is generally expressed in units of stress (Selby, 2005).

Friction results from resistance of particles to sliding past each other, grain crushing and volume change, and is the basic control on the strength of soil and rocks (Selby, 2005, Simons et al., 2001). Frictional strength or resistance is directly proportional to the normal stress holding grain surfaces in contact and is influenced by the number of point contacts in the volume of material, the arrangement, size, shape and resistance

to crushing of grains, as well as by voids and dilatancy (Selby, 2005). Frictional strength is commonly expressed in terms of a friction angle (ϕ, radians):

Equation 2-4

$$\tan\phi = \frac{\tau}{\sigma}$$

Where τ is the shear stress acting along the plane, and σ is stress acting normal to the plane of contact. ϕ is the angle of inclination of the resultant stress on the sliding interface, measured from the slope normal. The total resistance of a material to shear or shear strength at failure (τ_f) can be expressed using the Coulomb equation. For perfectly dry soil or rock the equation is:

Equation 2-5

$$\tau_f = c + \sigma \cdot \tan\phi$$

where c is the cohesion of the material (kg· m^{-1}· s^{-2}).

Both cohesion and friction are altered by the presence of water in soil or porous and permeable rock. When water is present, surface tension produces apparent cohesion between particles, resulting in negative pore pressures. However, surface tension forces are lost in fully saturated material and a proportion of the normal stress is transferred from the hillslope material to the water. Although the confined water can withstand compressive stress, it cannot withstand shear stress. Therefore, as pore pressures rise the material shear strength is reduced (Skempton, 1960, Terzaghi, 1936). For saturated materials the Coulomb equation is thus written as:

Equation 2-6

$$\tau_f = c' + (\sigma - u) \cdot \tan\phi'$$

where c' is the effective cohesion (as reduced by loss of surface tension), u is the pore-water pressure (kg· m^{-1}· s^{-2}) derived from the unit weight of water and the height of the free water column in the soil, and $\phi'$is the friction angle with respect to effective stresses (Selby, 2005).

2.1.3 Rock mass strength and scale

While the Coulomb model is based on the strength of intact materials studied in small material samples, in reality the strength of intact rock holds little significance for determining the strength of rock masses (Hoek, 2000). This is due to the presence of discontinuities such as bedding planes, joints, shear zones and faults. At shallow depths, where stresses are low, failure of the intact rock material is minimal and the behaviour of the rock mass is controlled by resistance to sliding on these discontinuities (Hoek, 2000). With increasing spatial scale the strength of rock masses decreases as discontinuities become more frequent, creating greater potential for strain localisation along weak zones and interactions between discontinuities (Chemenda et al., 2005, Schmidt and Montgomery, 1995, Hoek, 2000). However, by generalising bulk rock mass strength on the basis of properties of the intact rock and observed characteristics that reduce these properties, Coulomb cohesion and friction parameters can be applied to rock masses at scale (e.g.: Hoek et al., 2002, Hoek and Brown, 1997, Londe, 1988, Ucar, 1986, Hoek, 1983, Hoek et al., 1995). Therefore, the Coulomb model can be used to analyse the site-scale stability of hillslopes.

2.1.4 Hillslope stability

The stability of hillslopes can be expressed in terms of a factor of safety, FS, where:

Equation 2-7

$$FS = \frac{sum\ of\ resisting\ forces}{sum\ of\ driving\ forces}$$

Where the forces resisting sliding and instability are exactly equal to the forces driving sliding instability FS = 1, meaning the slope is just stable; where FS < 1 the slope is in a condition for failure; where FS > 1 the slope is stable (Selby, 2005). To model the stability of a potential landslide, the infinite slope procedure is commonly used (Taylor, 1948, Skempton and De Lory, 1957). Here the potential landslide mass is modelled as a 2-dimensional rigid block of uniform thickness, which rests on a planar slope of constant gradient and of infinite length (Figure 2-1). Two key assumptions are imposed by the model:

1. Sliding occurs along a plane parallel to the ground surface

2. The slope extends infinitely in all directions so that the stresses are the same on the two planes perpendicular to the slope. As these forces are collinear, equal in magnitude and opposite in direction, they exactly balance each other and can therefore be ignored.

FS of a rectangular block can be calculated for hydrostatic conditions as (Selby, 2005):

Equation 2-8

$$FS = \frac{c + (\cos^2 \beta \, (\rho_s g(z - z_w) + (\rho_s g - \rho_w g) z_w)) \tan \phi}{\rho_s g z \cos \beta \sin \beta}$$

Where β is the slope gradient (radians), ρ_s is the soil density (kg/m^3), g is the gravitational acceleration (9.8 m s^{-2}), z is the vertical depth to the shear plane (m), ρ_w is water density (kg/m^3) and z_w is the height of the water table above the failure plane (m). For cohesionless slopes FS is independent of the depth of the failure plane, such that:

Equation 2-9

$$FS = \frac{(\cos^2 \beta - u) \tan \phi}{\cos \beta \sin \beta}$$

Where u is the pore-water pressure. In this case FS is the same for small and large depths (Milledge, 2008). Disregarding the influence of pore water pressure, this can be simplified further, such that:

Equation 2-10

$$FS = \frac{\tan \phi}{\tan \beta}$$

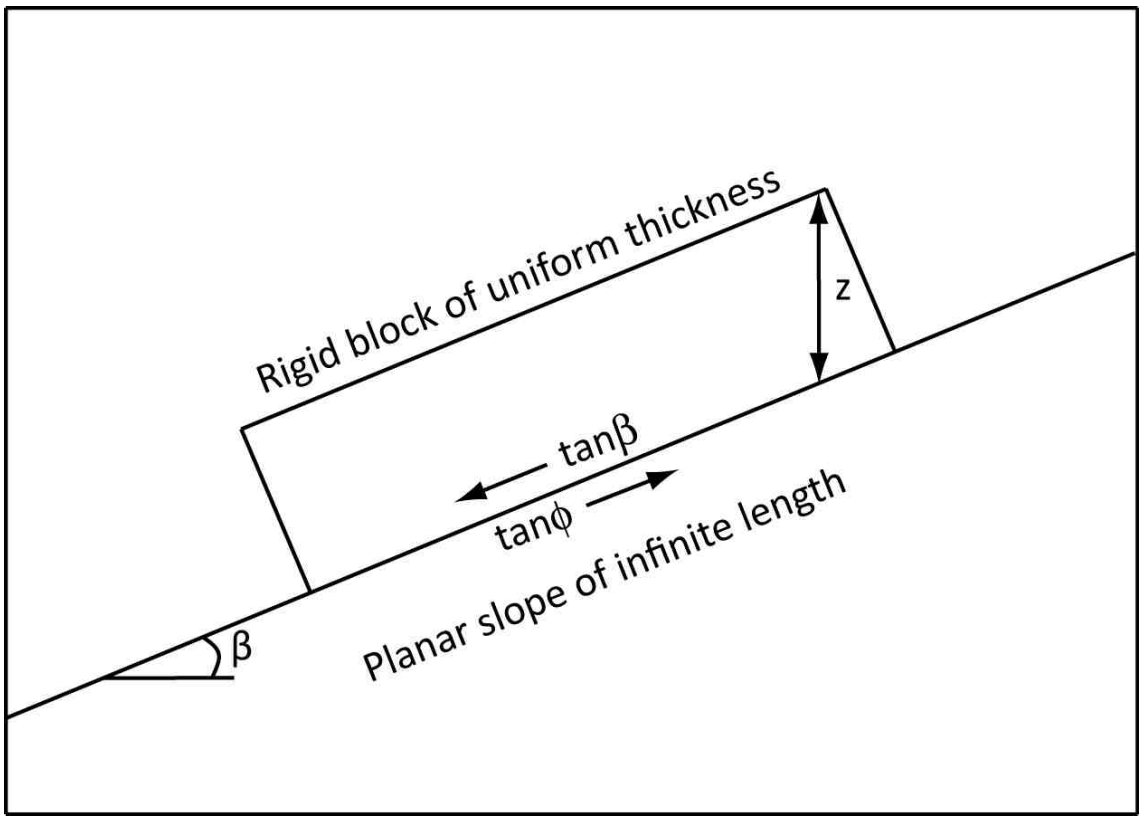

Figure 2-1 Illustration of infinite slope model for a cohesionless slope in dry conditions, where β is the slope angle, ϕ is the friction angle, and FS is independent of the depth of the failure plane.

2.1.5 Stress-strain behaviour of soil and rock

The stress-strain behaviour of soil and rock can be broadly divided into two stages. When stress levels are relatively low, crystalline solids respond to imposed loads elastically (i.e.: strain is proportional to load and the original dimensions are recoverable, Selby (2005)). During this stage bonds resulting from grain-grain adhesion (Johnson, 1985) between particles are being loaded but not breaking, so no permanent changes to the structure of the material take place. When the stress levels exceed the threshold capacity of the solid to deform elastically it undergoes irrecoverable deformation. The mechanism of this permanent deformation is generally distinguished as one of two types, relating to the stress-strain behaviour of the material (Engelder, 1993).

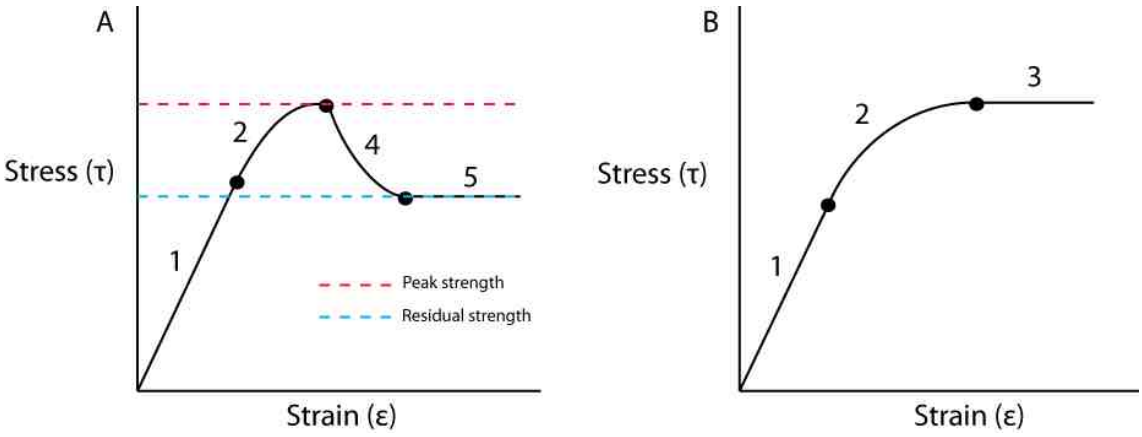

Figure 2-2 Idealised stress-strain curves for brittle (A) and ductile (B) material (after Petley and Allison, 1997: 749).

Brittle deformation for an idealised laboratory sample is illustrated in Figure 2-2 A. After the initial elastic phase (1) the weakest and most intensely stressed bonds begin to break. At this stage the material undergoes a combination of elastic and plastic deformation, characterised by a decrease in the gradient of the stress-strain curve as the material approaches its peak strength (2). This is the maximum value of shear stress attained during failure, and is the product of the peak values of cohesion and friction. As deformation continues, bonds continue to break and strain becomes localised, forming a shear zone of weakened material. Here the shear stress falls to the residual value (4) that then remains constant, even for large shear displacements (5). This is the residual strength and is the product of residual values of cohesion (which is generally considered to be zero) and friction. This behaviour is commonly referred to as “strain-softening”.

Ductile deformation is illustrated in Figure 2-2B. Again the initial elastic phase (1) is followed by a phase of elastic-plastic deformation resulting from inter-particle bond breakage, similar to that displayed by brittle materials (2). However, strain is not able to localise to form a single shear plane. While the material becomes gradually restructured as inter-particle bonds are broken, it cannot weaken and so experiences purely plastic deformation at constant stress (3). In theory the deformation will continue in this manner to infinite strain, although in reality a gradual decrease in strength may still occur as the result of particle reorientation (Petley and Allison, 1997).

Brittle deformation generally occurs in bonded or cemented materials at relatively low, near-surface confining pressures. Most engineering soils display brittle behaviour at confining pressures in the range 1–250 kPa, mudrocks may also display brittle behaviour at confining pressures in the range 0–2MPa, while harder geological materials display brittle behaviour up to greater confining pressures (Petley and Allison, 1997). Ductile deformation generally occurs in materials with little or no inter-particle bonding (Fan et al., 1994) and at higher confining pressures and temperatures experienced at greater depth (Ng, 2007, Hudson and Harrison, 1997). For near surface materials, ductile deformation may occur in non-cohesive soils (Selby, 2005), very poor quality, soft rock masses (Hoek, 2000) and where brittle deformations have already reduced rock mass strength to residual values. This indicates that, at low confining pressures representative of shallow slope failures, rocks will generally display strain-softening behaviour for first-time failures. This will also be the case for deeper landslides occurring in harder bedrock materials, where sudden failures result from the formation of basal shear surfaces through brittle deformation (Petley and Allison, 1997). This suggests that the majority of first-time failures are likely to occur via brittle deformation in rock.

The mechanism and temporal development of landslide failure via brittle deformation can be understood in terms of the progressive failure model (Bjerrum, 1967). Based on observations of pre-failure landslide movement patterns (Petley et al., 2002, Kilburn and Petley, 2002) and the results of stress path triaxial tests, (Petley et al., 2005a, b) proposed a conceptual model for the development of progressive first-time failure in hillslopes formed from brittle, cohesive materials. The authors proposed that when a temporary reduction in factor of safety (FS) occurs due to elevated pore pressures, local stresses may exceed material strength in parts of a potential landslide mass, even though the global FS is still greater than unity. This allows strain-softening to take place in these segments, causing them to transition from peak to residual strength. The stress is then redistributed to other unsheared portions of the potential landslide, which subsequently undergo the same transition. This transfer process eventually reaches the point at which shear stress exceeds shear strength across the whole of the shear zone, such that failure becomes inevitable regardless of pore pressure state, as long as the shear stress is greater than the residual strength of the material. After this

point the potential landslide mass experiences a catastrophic acceleration in the rate of deformation as the final sections of the shear zone fail, resulting in the total failure of the section of hillslope. While this model was developed for instability associated with hydrologically-triggered landslides, dynamic stresses from the passage of seismic waves may also serve to produce the temporary instabilities required for progressive failure (Petley et al., 2005b, Loew et al., 2012, Moore et al., 2012).

2.2 Seismic slope stability modelling

The passage of seismic waves causes temporary changes in the distribution of stresses acting on hillslope materials (Newmark, 1965). Effects of earthquakes on the stresses relevant to slope stability include cyclic changes in shear and normal stresses as well as elevated pore water pressures associated with collapse of the soil structure and liquefaction (Kramer, 1996). The change in stresses required to produce instability is closely related to the static stability of hillslopes (Section 2.1.4). As a result, many commonly used methods of assessing the stability or performance of slopes during earthquakes rely on static stability analysis (Kramer, 1996, Newmark, 1965, Jibson, 1993). Methods developed to date can be grouped into three general categories:

1. Pseudostatic analysis
2. High-resolution geomechanical analysis
3. Permanent displacement analysis

These techniques differ primarily in the accuracy with which the earthquake ground motion and the dynamic response of the slope are represented, ranging from the simple to the highly complex.

2.2.1 Pseudo-static analysis

The simplest approach to evaluating the performance of a slope under seismic shaking is pseudo-static analysis. Here, the earthquake acceleration acting on the landslide mass is applied as a permanent static body force acting in the downslope direction in limit-equilibrium analysis (Terzaghi, 1950). The earthquake-acceleration required to reduce FS to 1 is called the critical acceleration, exceedence of which is defined as failure. The technique is straightforward to apply, requiring only the peak ground

acceleration, PGA (g), plus the information required for static factor of safety analysis (Section 2.1.3). In general, only the horizontal component of the earthquake shaking is modelled because the effects of vertical forces are assumed to average out to near zero (Jibson, 2011). In fact vertical components of ground motion can be of considerable importance to the stability of hillslopes (Elgamal and He, 2004), although this assumption is useful for simplifying analysis.

Pseudo-static analysis has several disadvantages. Characterising the earthquake shaking as a permanent, unidirectional body force assumes that the full force of the PGA acts only in the direction promoting instability, and is therefore extremely conservative. To correct for this the technique relies heavily on selection of a pseudo-static coefficient. However, there exists no robust, widely-accepted, rational basis for coefficient selection, with engineering judgement along with the standard practice of different groups generally invoked in the selection process (Jibson, 2011, Kramer, 1996, Ozcep et al., 2012, Bozbey and Gundogdu, 2011, Chen et al., 2004). The technique also tells the user nothing about what happens after equilibrium is exceeded. The analysis determines whether the slope is either stable or unstable, however the consequences of instability cannot be judged. To assume failure of a slope as soon as equilibrium is reached would be to assume perfectly elastic behaviour of the hillslope material, with immediate failure upon exceedence of the elastic limit. As hillslope materials exhibit elasto-plastic and strain-softening behaviour (Section 2.1.5), this indicates that exceedence of yield acceleration does not result directly in failure, but rather in deformation from which weakening and failure may later result. While pseudo-static analysis is easy to use, its simplicity stems from a crude characterisation of the physical process, which results in both difficulties in its implementation and in assessing the likelihood of failure.

2.2.2 High resolution geomechanical analysis

At the other end of the spectrum there is a huge range of recently developed modelling techniques that provide a more physically realistic representation of failure processes. These techniques include finite element, finite difference, distinct element, discrete element and finite fracture network codes, as well as recently developed particle flow and lattice spring approaches (e.g.: Stead et al., 2012, Kramer, 1996,

Leroueil et al., 2012, Stead et al., 2006, Rockfield, 2011, Eberhardt et al., 2004, Tang, 1997). Using these methods, complex failure mechanisms can be modelled, incorporating both structural and rock mass controls on material strength, brittle fracture processes within the rock mass, and even associate changes in hillslope hydrology (Havaej et al., 2012, Stead et al., 2012). These techniques can, theoretically, provide the most accurate representation of landslide geometry, and failure processes. However, this accuracy depends heavily on high-resolution, high-quality input data, much of which has been attained using site-scale remote sensing techniques (Stead et al., 2012). In the context of this investigation, this level of detailed modelling is not required, nor is it practical for modelling failure processes in large number of landslides at regional-scales (Jibson, 2011).

2.2.3 Permanent displacement analysis: Newmark sliding block model

The Newmark (1965) sliding block model, provides a means of evaluating the dynamic performance of hillslopes in a way that provides more useful information than pseudo-static analysis, but is less complex and more practical than high resolution geomechanical analysis in the context of this study. The technique was originally developed for evaluating potential deformations in dams and embankments, and can be used to predict approximate displacements of both flat and sloping ground, produced when the shear strength of rocks and soils is exceeded by earthquake-induced stresses (Ambraseys and Menu, 1988). In the last 30 years the technique has undergone significant development in its application to landslides in both natural and man-made slopes (e.g.: Ambraseys and Srbulov, 1994, Wilson and Keefer, 1983, Jibson, 1993, Jibson et al., 2000, Jibson, 2007). As this study uses the Newmark model as the basis for a general conceptual model and numerical simulations, a detailed review is provided.

A potential sliding mass is modeled as a rigid-plastic block, sitting on a flat or inclined plane (Figure 2-3). As in pseudostatic analysis, the technique considers only the horizontal component of ground accelerations. The block has a known critical acceleration, a_c (g), which is the threshold acceleration required to overcome shearing resistance and initiate sliding. When the critical acceleration is exceeded, the combination of static and dynamic shear stress exceeds the shear strength of the

material. At this point FS < 1 and so displacement takes place. The output of the analysis is the cumulative, permanent displacement of the block as it is subject to an earthquake acceleration time history, termed the Newmark displacement, D_N (cm).

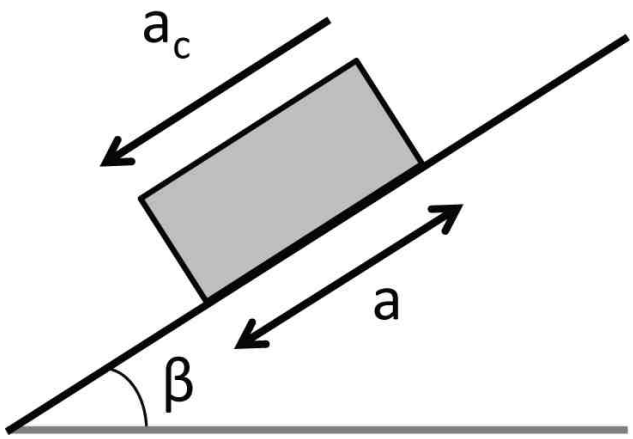

Figure 2-3 Illustration of the Newmark sliding block model, after (Jibson, 2011: 45), where a is the earthquake ground acceleration at the base of the block, a_c is the critical acceleration of the block., and β is the angle of inclination of the sliding surface.

Conducting Newmark analysis involves first determining the critical acceleration of the potential landslide block, which is a function of FS and the landslide geometry (Newmark, 1965):

Equation 2-11

$$a_c = (FS - 1)g \sin\beta$$

Where a_c is the critical acceleration in terms of g (1 g = 9.81 m s^{-2}). β is the angle from the horizontal in which the centre of gravity of the slide mass moves when displacement occurs, which is the slope angle for an infinite slope (Newmark, 1965). Once the critical acceleration is determined, Newmark displacement is calculated by double integrating the sections of the strong motion record which lie above the critical acceleration (e.g.: Newmark, 1965, Makdisi and Seed, 1978, Chang et al., 1984, Ambraseys and Menu, 1988, Wilson and Keefer, 1983), as illustrated in Figure 2-4. Accelerations exceeding a_c are integrated over time to derive the time series of velocity between the block and the ground. The full relative velocity time series is then again integrated to give the cumulative, relative displacement of the landslide block. Although displacement may occur in both the downslope and upslope directions, a_c in

the upslope direction is generally much greater than a_c in the downslope direction, and in the majority of cases PGA does not exceed upslope a_c. Upslope a_c can therefore be assumed to be infinitely large without introducing errors into the analysis (Newmark, 1965, Franklin and Chang, 1977, Chang et al., 1984, Ambraseys and Menu, 1988, Lin and Whitman, 1986).

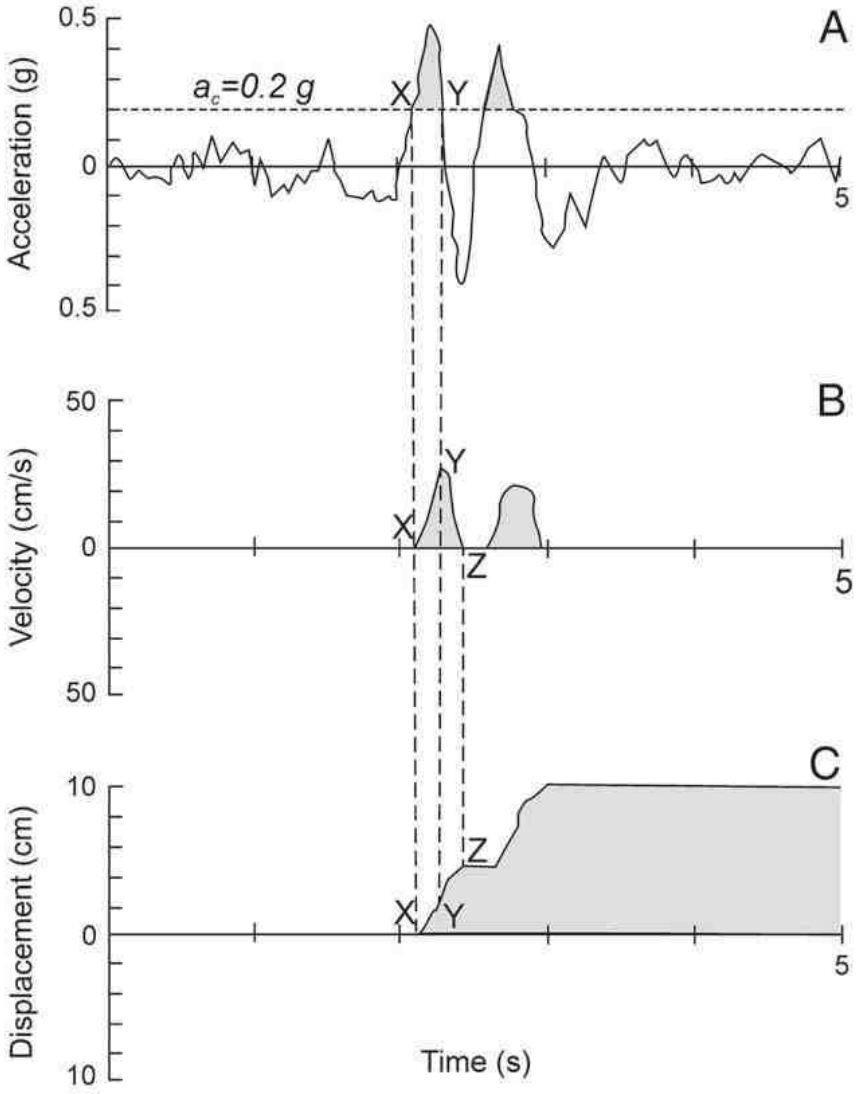

Figure 2-4 Illustration of the Newmark integration method of Wilson and Keefer (1983): A) Earthquake acceleration-time history with critical acceleration (dashed line) of 0.2 g shown; B) velocity of the landslide versus time; C) displacement of landslide versus time. Points X, Y, and Z are for reference between plots. (Jibson, 2011: 46)

2.2.4 Simplified Newmark analysis

Rigorous Newmark analysis (described above) requires a full seismic acceleration time history, and is generally only applicable for site-scale analysis. A range of regression models have been produced with which to predict Newmark displacements as a function of various ground motion parameters (Jibson, 1993, Jibson et al., 1998, Jibson

et al., 2000, Jibson, 2007, Ambraseys and Menu, 1988). Parameters used include earthquake moment magnitude, M_W, Arias intensity, I_a (m s^{-1}) (Arias, 1970), and critical acceleration ratio ($\frac{a_c}{PGA}$), which is the ratio of a_c to PGA. The different models, sizes of samples used to fit them and their goodness-of-fit are summarised in Table 2-1. Of all published examples, models from Jibson (2007) have been fitted using the largest number of individual strong motion records from the largest number of different earthquakes. Within the datasets a mixture of different site conditions is represented, including 10% of records on hard rock, 27% on soft rock, 49% on stiff soil and 14% on soft soil. The models have been fitted for a_c values from 0.05 to 0.40 g, the range of practical interest for seismic slope stability problems. These models therefore provide the most globally representative solution for simplified rigid block analysis. Of these, number 5 (in Table 2-1) provides the highest goodness-of-fit and lowest standard deviation. Here the combination of critical acceleration ratio and moment magnitude is used to account for both the amplitude of seismic accelerations and the duration of seismic shaking. The increase in shaking duration with earthquake magnitude means that larger earthquakes generally produce larger displacements for the same critical acceleration ratio (Figure 2-5). The model also provides a clear control on when displacement does and does not occur, as no displacement is predicted when $a_c \geq PGA$ ($FS \geq 1$); unlike models 6 and 7 where the dependence on I_a means that small displacements are predicted when $a_c \geq PGA$ (Jibson, 2011). The simplicity and low computational requirement of these simplified models has led to their widespread use in regional scale seismic landslide hazard models (e.g.: Jibson et al., 2000, Miles and Keefer, 2009) and rapid post-earthquake assessment (e.g.: Godt et al., 2009).

Table 2-1 Regression equations for predicting Newmark displacement

ID	Equation	Number of seismic records (Number of earthquakes)	R^2 goodness of fit	Source
1	$\ln D_N = 0.90 + \ln\left[\left(1-\frac{a_c}{PGA}\right)^{2.53}\left(\frac{a_c}{PGA}\right)^{-1.09}\right] \pm 0.30$	50 (11)	-	Ambraseys and Menu (1988)
2	$\ln D_N = 1.460 \ln I_a - 6.642\ a_c + 1.546 \pm 0.409$	11	0.87	Jibson (1993)
3	$\ln D_N = 1.521 \ln I_a - 1.993 \log a_c - 1.546$	555 (13)	0.83	Jibson et al. (1998), Jibson et al. (2000)
4	$\ln D_N = 0.215 + \ln[\left(1-\frac{a_c}{PGA}\right)^{2.341}\left(\frac{a_c}{PGA}\right)^{-1.438}] \pm 0.510$	2270 (30)	0.84	(Jibson, 2007)
5	$\ln D_N = -2.710 + \ln[\left(1-\frac{a_c}{PGA}\right)^{2.335}\left(\frac{a_c}{PGA}\right)^{-1.478}] + 0.424M_W \pm 0.454$	2270 (30)	0.87	(Jibson, 2007)
6	$\ln D_N = 2.401 \ln I_a - 3.481 \ln a_c - 3.230 \pm 0.656$	2270 (30)	0.71	(Jibson, 2007)
7	$\ln D_N = 0.561 \ln I_a - 3.833 \ln\left(\frac{a_c}{PGA}\right) - 1.474 \pm 0.616$	2270 (30)	0.75	(Jibson, 2007)

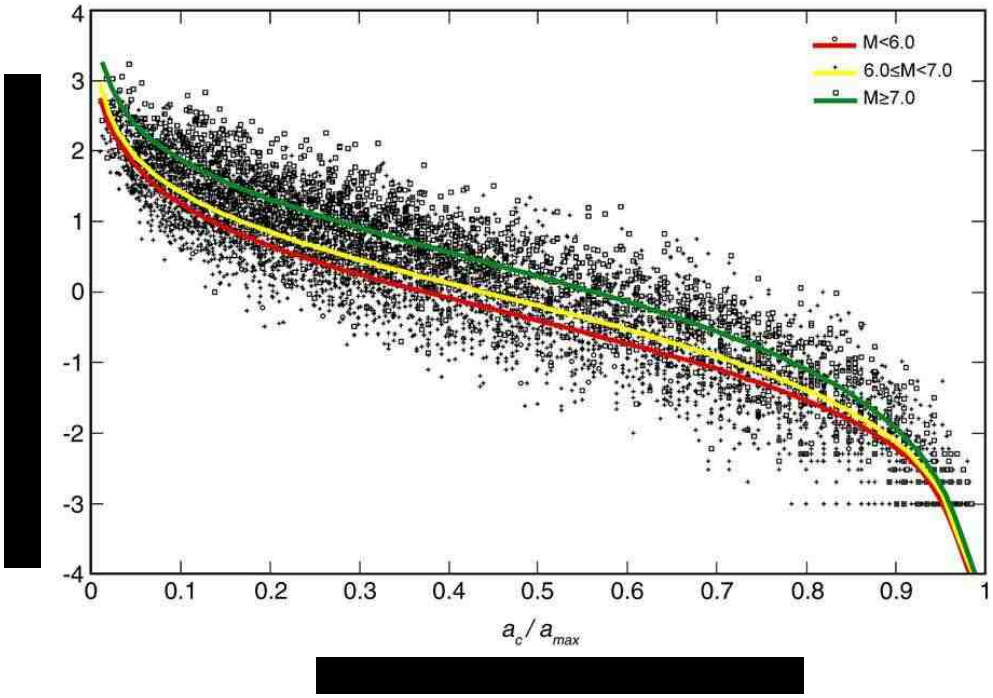

Figure 2-5 Plot of Newmark displacements as a function of critical acceleration ratio. The fitted data are separated into three magnitude groups, showing the influence of longer shaking durations associated with larger earthquakes (after Jibson, 2007: 214)

2.2.5 Interpretation of modelled displacements

While displacement itself may be significant when it takes place in and around engineered structures (e.g.: Blake et al., 2002), further analysis is required to determine the implications of displacement for hillslope failure. In rigorous Newmark analysis, strain- and strain-rate-softening rules built into the analysis can allow changes in FS to be analysed (e.g.: Wartman et al., 2005, Deng et al., 2011). In simplified Newmark analysis, the implications of displacements for stability have been previously evaluated in probabilistic terms or based on qualitative engineering judgement. Using data from the 1994 Northridge earthquake, Jibson et al. (2000) showed that spatial probability of landslide occurrence could be expressed as a function of locally predicted Newmark displacement, using a Weibull model. Qualitative landslide hazard categories selected through engineering judgement also reflect this relationship. However, shallow landslides are commonly triggered at lower displacement levels than deep-seated landslides (Jibson et al., 2000, California Geological Survey, 2008, Jibson and Michael, 2009).

2.2.6 The representativeness and accuracy of Newmark

The main simplifying assumptions of Newmark analysis are associated with the physical characterisation of landslide masses as rigid, plastic bodies, with displacement occurring along a discrete shear surface (Jibson, 2011). This in turn means that strain is distributed uniformly along the shear plane, no internal deformation occurs within the landslide mass and the shearing resistance does not evolve with strain (Chang et al., 1984, Newmark, 1965, Ambraseys and Menu, 1988, Makdisi and Seed, 1978). These assumptions have implications for both the extent to which Newmark represents the physical process and the accuracy of predicted displacements.

The performance of the Newmark method has been assessed using a combination of field data (Wilson and Keefer, 1983, Pradel et al., 2005, Strenk, 2010) and shaking table physical modelling experiments (Wartman et al., 2003, Wartman et al., 2005). Comparisons have also been made with the outputs of decoupled and coupled approaches (Lin and Whitman, 1986, Makdisi and Seed, 1978), which are extensions of the Newmark method and account for internal deformation within landslide masses (Rathje and Bray, 2000, Rathje et al., 1998, Strenk and Wartman, 2011). These investigations have shown that, although treating landslides as rigid bodies is valid for thin, stiff masses, it becomes increasingly invalid for larger landslides composed of softer materials (Jibson, 2011). The performance of the Newmark method has been found to be largely dependent on the tuning ratio: the ratio of the predominant frequency of the input motion to the natural frequency of the soil column (Figure 2-6). For thin, stiff landslides with a tuning ratio of 0.1 or less, the Newmark method yields accurate results when compared to analogue models, decoupled and coupled approaches. For deeper more deformable landslide masses with period ratios between 0.1 and 1, Newmark generally underestimates displacement. As tuning ratios continue to increase, Newmark again overestimates the displacement (Rathje et al., 1998, Rathje and Bray, 2000, Wartman et al., 2003, Kramer and Smith, 1997). Across the full range of tuning ratios, predicted displacements range from 27% to 255% of displacements observed on shear planes in clay physical models (Wartman et al., 2005).

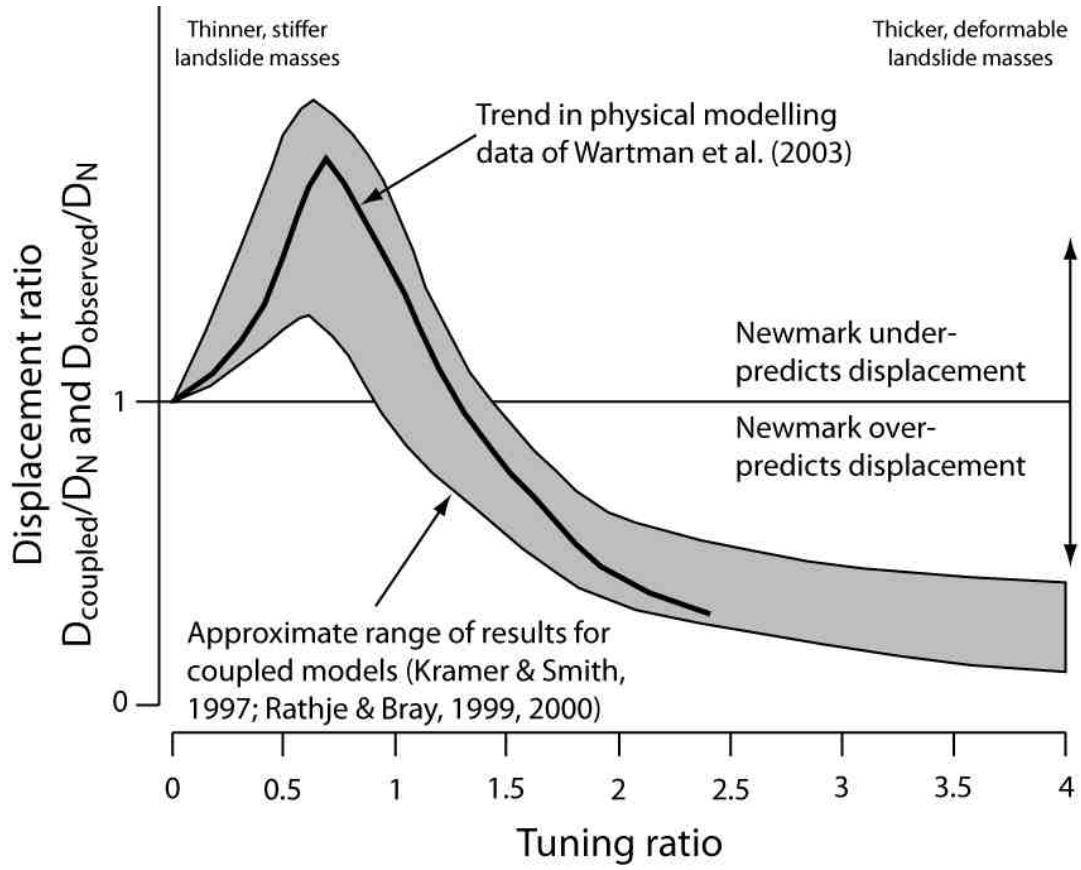

Figure 2-6 Plot showing the accuracy of predicted Newmark displacement, compared with displacements observed in physical and coupled analysis models, relative to the Tuning ratio (the ratio of the predominant frequency of the input motion to the natural frequency of the soil column), (after Wartman et al., 2003: 682)

While direct comparison of displacements is useful for determining the general accuracy of Newmark predictions, physical model experiments also allow the physical correctness of Newmark to be assessed. The main difference between Newmark rigid-block behaviour and that of real, strain-softening materials, is the decay in a_c that occurs with displacement (Kutter, 1989, Wartman et al., 2003, Wartman et al., 2005). The use of a strain-dependent degrading a_c therefore enhances the accuracy of displacement predictions (Wartman et al., 2005). Additionally, strain in physical materials does not localise uniformly on a single slip surface. This is more typically the case for shaking-induced failures (Ohishi et al., 1995), where deformations are distributed non-uniformly throughout the landslide mass and localise in a zone composed of multiple (2 or more) slip surfaces (Wartman et al., 2005). When compared to total measured displacements that include distributed deformation, Newmark more generally underpredicts the displacement (Wartman et al., 2005). However, as multiple slip surfaces develop with similar orientation in close proximity

to each other, a single sliding block can still provide a reasonable approximation of the failure geometry and mechanism (Wartman et al., 2005).

Due to the scarcity of well document landslide displacement case histories, few assessments of Newmark have been carried out using field data. Where available these studies generally suggest that displacements can be predicted within an order of magnitude of values observed in the field. In a study of landslide displacement induced by the 1979 Coyote Lake Earthquake (Californinia), Wilson and Keefer (1983) undertook Newmark analysis using seismic data from stations at 5 and 15 km distances from the site and material properties estimated from laboratory tests on similar rock types. The measured displacement of the landslide was 21 mm, while predicted displacements were 0.12 mm for the 5 km record and 27 mm for the 15 km record. Here the wide range of displacements is attributed to large uncertainties associated with material properties and ground accelerations. A study by Pradel et al. (2005) of a landslide displacement induced by the 1994 Northridge earthquake involved better quality ground motion data along with material properties determined through back analysis of previous failure of the slope and repeat shear box testing. Predicted displacements of 27-91 mm (average 46 mm) compare favourably to an observed displacement of 50 mm, with the range again due to uncertainty in material properties. Recent unpublished work, based on data from three additional landslide case histories, suggests that both simplified and rigorous Newmark approaches predict displacements within -100% to +150% of actual measured amounts (Strenk, 2010). Significantly, results also suggests that Newmark generally yields predictions of similar accuracy to decoupled and coupled methods, counter to the expectation that more complex and sophisticated methods should yield more accurate results (Strenk, 2010). However, these findings from field investigations should be interpreted carefully. The large uncertainties in ground motion and material properties used in the analyses make it difficult to identify the source of errors and thereby develop a general understanding of the accuracy of Newmark relative to field data.

An additional consideration for using the Newmark model is that the effects of seismically-induced changes in pore pressure are neglected. Although this assumption may be valid in dry conditions, and for slopes composed of impermeable, non-porous materials (Newmark, 1965, Makdisi and Seed, 1978), pore pressure generation during

earthquakes can have an important control on slope stability (Uzuoka et al., 2005, Zhang and Wang, 2007, Kramer, 1996). The Newmark model is therefore not applicable in these circumstances (Jibson, 2011), and the effects of dynamic pore pressures are not analysed in this study.

2.2.7 Summary

While a variety of techniques exist for analysing the performance of hillslopes during earthquakes, this investigation requires a model that can predict the cumulative effects if multiple earthquakes on hillslopes, but that is computationally simple enough to apply to large numbers of landslide masses. The Newmark sliding block is the only existing model that fits these criteria, providing a reasonable prediction of displacements due to seismic shaking, which can be associated with changes in hillslope stability by assuming strain-softening behaviour. While in reality deformation is distributed throughout landslide masses, the assumption of a discrete shear surface is not problematic in this case, as the regional-scale landslide activity being studied depends on the net stability of landslide masses rather than the distributed failure mechanics.

2.3 Regional-scale earthquake-triggered landslide activity

2.3.1 Regional-scale landslide data

Distributions of landslides triggered by earthquakes have been studied through the compilation and analysis of event-based landslide inventory maps (van Westen et al., 2006, Galli et al., 2008). These datasets record landslides triggered by a particular earthquake, and therefore provide a temporal snapshot of landslide activity. For most published studies, a single inventory of landslides is generated following an earthquake. Ideally the mapping is conducted using high resolution aerial imagery acquired immediately following the earthquake, controlling for landslides that occurred prior to the earthquake, so that the data can be attributed to seismic rather than aseismic processes (e.g.: Harp and Jibson, 1995a). However, practical limitations mean that there is often a lag between the main-shock and landslide mapping, such that inventories collected in the weeks, months and years after an earthquake may also include landslides that occurred subsequently. These single-snapshot inventories have been widely used to develop a spatial understanding of landslide distributions.

For a limited number of earthquakes, multi-temporal landslide maps have been generated, which capture the evolution of landslides before and/or following earthquakes (e.g.: Hovius et al., 2011, Lin et al., 2008b, Saba et al., 2010). While these data provide a temporal perspective of landslide activity, the time-scales covered by these studies are currently limited to a maximum of 7 years following large earthquakes.

The vast majority of published landslide inventories document the plan area of individual landslides (e.g.: Harp and Jibson, 1996, Liao and Lee., 2000, Malamud et al., 2004b, Dai et al., 2011, this study), and thus have much greater utility for geomorphic analysis than datasets where landslides are recorded as point locations (e.g.: Keefer, 2000). The area of landslides provides a useful metric for two-dimensional analysis of hazard (e.g.: Meunier et al., 2007) or vegetation disturbance (e.g.: Lin et al., 2005). Where landslide volumes are required for geomorphic analysis, these can also be estimated from landslide area (e.g.: Hovius et al., 2000, Hovius et al., 1997, Lavé and Burbank, 2004, Imaizumi and Sidle, 2007).

2.3.2 Landslide magnitude-frequency distributions

Landslide magnitude-frequency (MF) distributions characterise the relationship between the size of landslides and their frequency, providing a useful tool for assessing the completeness of landslide inventories (Brunetti et al., 2009) and modelling landslide activity (Korup et al., 2012, Malamud et al., 2004b). Area, volume or length generally provide the scale metric, while the frequency may be spatial or spatio-temporal. For earthquake-triggered landslides as well as for landslides resulting from other triggering mechanisms, a considerable body of research suggests a common form of magnitude-frequency distribution (Figure 2-7). Typically, inverse non-linear relationships between landslide size and frequency are observed (Figure 2-7, 2), and modelled using an inverse power-law (e.g.: Pelletier et al., 1997, Hovius et al., 1997, Hovius et al., 2000, Dai and Lee, 2001, Guzzetti et al., 2002, Malamud et al., 2004a, Malamud et al., 2004b, Van Den Eeckhaut et al., 2007). This distribution has been associated with self-organised criticality in the hillslope failure process (Turcotte and Malamud, 2004, Hergarten and Neugebauer, 2000), associated with the mechanics of landslide rupture and the geometry and abundance of discontinuities in soil and rock

(Brunetti et al., 2009, Stark and Guzzetti, 2009). For small landslides, many distributions exhibit a departure from power-law scaling, commonly termed the 'rollover' (Figure 2-7, 1). For complete landslide inventories, this rollover is accepted as a physical manifestation of the conditions of hillslope failure (Pelletier et al., 1997, Van Den Eeckhaut et al., 2007), thought to occur with the transition from cohesion controlled hillslope failure in shallow landslides to friction controlled failure in deep-seated landslides (Guzzetti et al., 2002, Stark and Guzzetti, 2009). However, in many datasets the rollover occurs artificially before this point due to censoring of smaller landslides, resulting from the mapping technique (Hovius et al., 1997, Hovius et al., 2000, Stark and Hovius, 2001, Brardinoni and Church, 2004). The position of the rollover can therefore be interpreted as indicating the limit of landslide size below which the datasets become incomplete (Guzzetti et al., 2002, Malamud et al., 2004b, Malamud et al., 2004a).

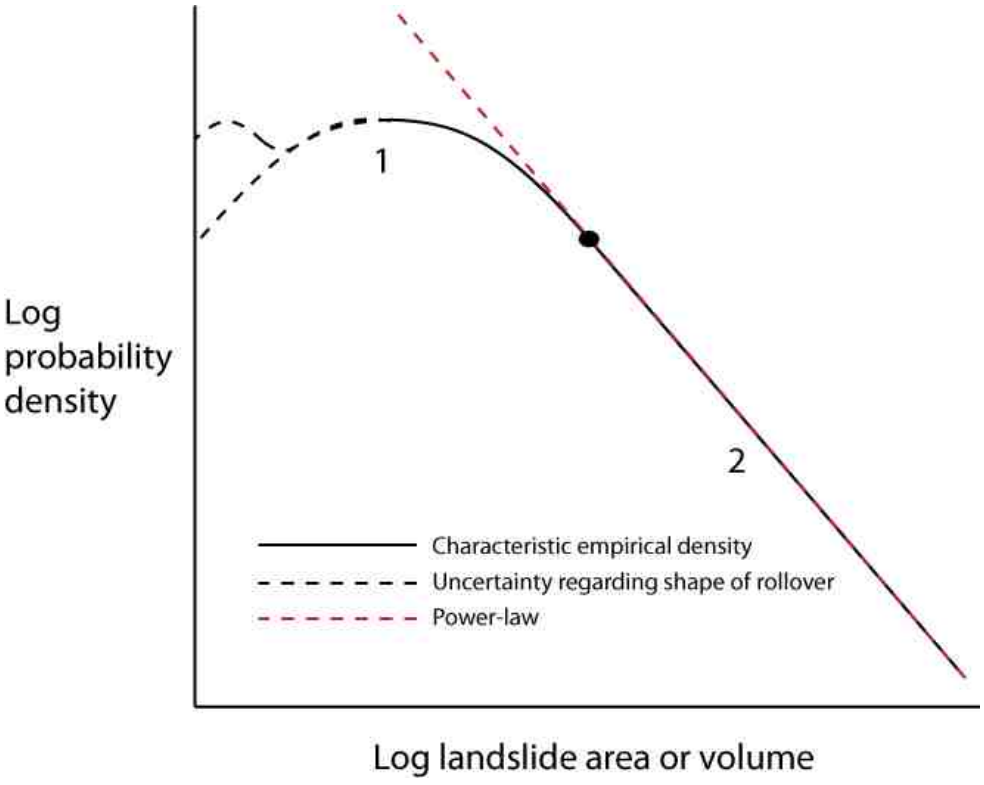

Figure 2-7 Illustration of characteristic landslide magnitude-frequency distribution ratio, which takes the form of a power-law decay in probability or freqeuncy for medium-large landslides, with a departure from this trend (or rollover) for smaller landslides.

Due to the uncertainties associated with the nature and shape of changes in scaling behaviour, landslide distributions are commonly simplified using a truncated inverse

power-law (e.g.: Korup et al., 2012, Hovius et al., 1997). It is important to note that two different approaches to characterising power-laws arise in the literature, which has led to some confusion when comparing landslide distributions (see Van Den Eeckhaut et al., 2007, Guzzetti et al., 2002). These are shown in the following equations, which give the probability of a landslide having a given size $p(x)$, as a function of x, where x_{min} is the minimum size of landslide modelled by the function and δ and α are the power-law scaling exponents.

Equation 2-12 (e.g.: Stark and Hovius, 2001, Stark and Guzzetti, 2009)

$$p(x) = \vartheta {x_{min}}^{\vartheta} x^{-\vartheta-1}$$

Equation 2-13 (e.g.: Clauset et al., 2009, Korup et al., 2012, Van Den Eeckhaut et al., 2007)

$$p(x) = \frac{\alpha - 1}{x_{min}} \left(\frac{x}{x_{min}} \right)^{-\alpha}$$

These two functions are equivalent and give the same results where $\alpha = \vartheta + 1$ or $\vartheta = \alpha - 1$. Throughout this thesis Equation 2-13 is used to characterise power-laws, and scaling exponents used are α values. Smaller α values represent a greater contribution from larger landslides, and vice-versa. Globally, empirical values of α range from around 1.4 to 3.4, with a central tendency around 2.3 to 2.5 (Van Den Eeckhaut et al., 2007, Stark and Guzzetti, 2009). This variability has been associated with environmental factors (Iwahashi et al., 2003, Guzzetti et al., 2002), and appears to reflect primary differences in landslide type, with rockfalls generally exhibiting larger α values ($2.5 \leq \alpha \leq 2.9$) than slides ($2.1 \leq \alpha \leq 2.4$) (Brunetti et al., 2009). Numerical modelling has linked α values more directly to hillslope material properties, suggesting that α is set by the capacity of material to support its own load in the absence of friction, and as cohesion increases (or friction angle decreases) α increases (Stark and Guzzetti, 2009).

2.3.3 The spatial distribution of earthquake-triggered landslides

Spatial analysis of landslide inventories has revealed characteristics of and factors influencing spatial distributions of earthquake-triggered landslides. This has been achieved by analysing landslide activity relative to the strength of seismic ground motions and the material and morphological characteristics of hillslopes.

At the global scale, the extent of the area affected by landslides, total number of landslides and total volume of landslide material mobilised, are all positively correlated with the magnitude of earthquakes (Keefer, 2002, Keefer, 1984, Malamud et al., 2004b, Rodríguez et al., 1999). Figure 2-8 shows these relationships from earthquakes distributed globally. All three relationships are log-linear and exhibit large residuals over an order of magnitude in the area affected, number and volume of landslides. The relationships can be understood in terms of the effect of increasing strength, duration and area affected by seismic ground motions with increasing magnitude (e.g.: Kramer, 1996, Abrahamson et al., 2008, Campbell and Bozorgnia, 2008, Campbell, 1981).The residuals are generally attributed to regional variability in other earthquake characteristics - such as earthquake depth and fault mechanism - and physiographic conditions – such as topography, lithology and climate (e.g.: Malamud et al., 2004b, Keefer, 2002).

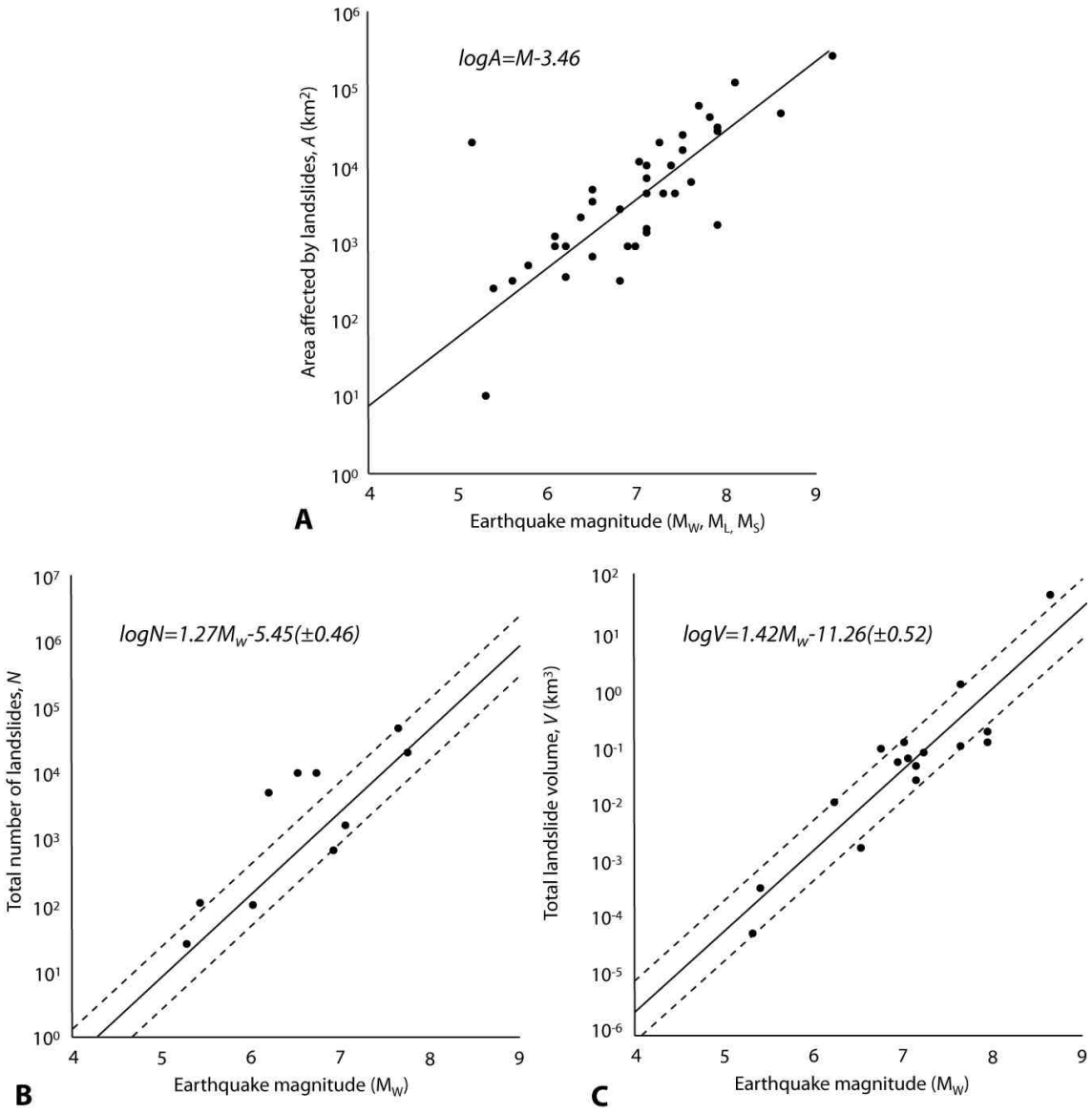

Figure 2-8 Plots showing observed relationships between earthquake magnitude and different metrics of landslide activity. Relationships between earthquake magnitude and A) area affected by landslides (after Keefer and Wilson, 1989), B) total number of landslides, and C) total landslide volume (after Malamud et al., 2004b) Each data point indicates an earthquake for which the area affect by landslides, total number of landslides or total landslide volume is known. Fitted relationships are given on the plots.

As seismic ground motions are not spatially uniform, regional patterns of landslide activity have also been investigated using two metrics, which have been termed landslide point density and landslide area density (e.g.: Dai et al., 2011). Landslide-point density is the number of landslides within a given unit area, while landslide-area density is the percentage area covered by the areas of landslides. Various authors have identified relationships between landslide density and proxy variables indicating the regional pattern of ground motions, including distributed PGA, Arias intensity and distance from seismic sources (e.g.: Meunier et al., 2007, Dai et al., 2011, Lee et al., 2008a, Meunier et al., 2013). These relationships appear to be regionally variable; for

example, Figure 2-9 shows relationships between landslide (area) density and vertical and horizontal components of PGA for the Northridge and Chi-Chi earthquakes (Meunier et al., 2007).

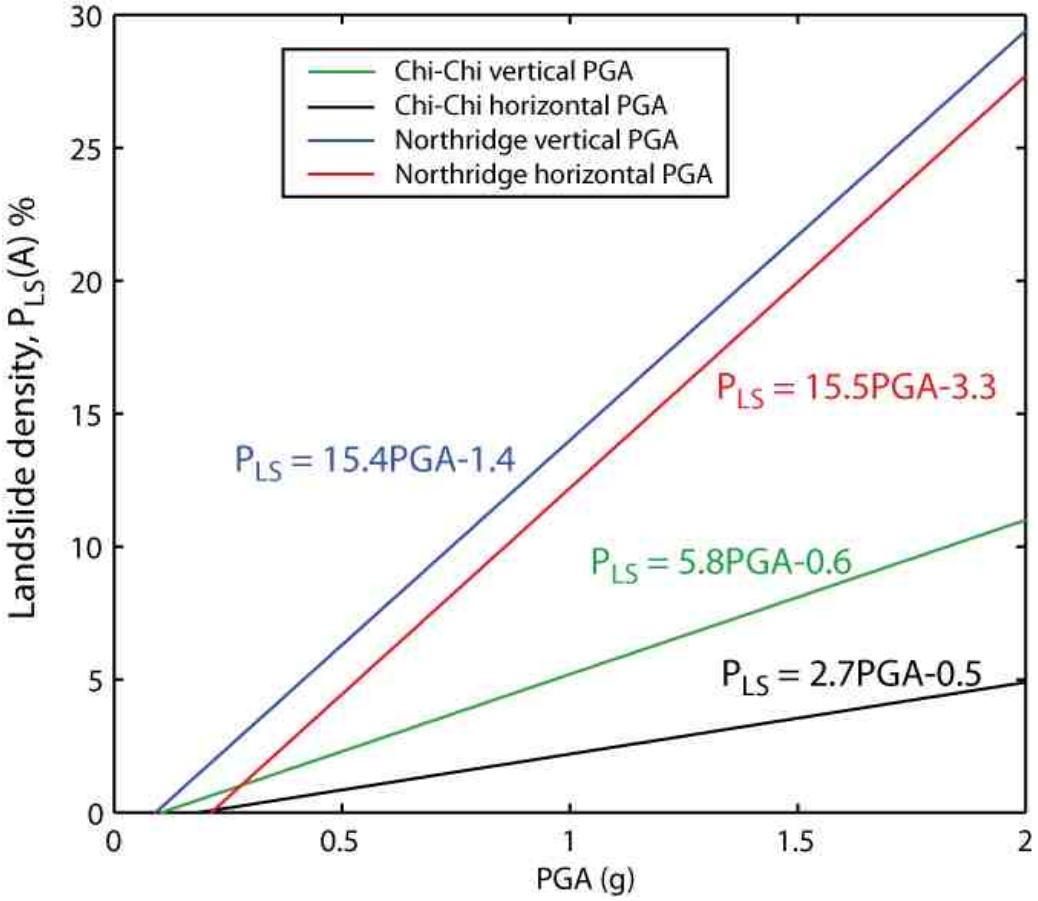

Figure 2-9 Relationships between landslide area density and PGA, constrained using inventories of landslides triggered by the 1994 Northridge earthquake (USA) and the 1999 Chi-Chi (Taiwan), (after Meunier et al., 2007)

The properties of seismic waves are also modified by topography. While topographic site effects are complex and difficult to separate from other effects such as surface layering, general patterns of ground motion modification at the ridge-valley scale have been identified (Davis and West, 1973, Bouchon, 1973, Wu et al., 1990, Benites et al., 1994, Meunier et al., 2008). Entering the base of topographic ridges, seismic waves undergo a combination of reflection back into the rock mass and diffraction along the free ground surface. This effect increases towards ridge crests giving rise to constructive interference and enhanced ground accelerations at topographic highs and convex knickpoints (Davis and West, 1973, Bouchon, 1973, Wu et al., 1990, Benites et al., 1994, Meunier et al., 2008). Results from two dimensional seismic wave field modelling using simple ridge-valley topography reveal a general pattern of

amplification that is most pronounced on the side of ridge crests facing away from the seismic source (150% of PGA in flat topography), with deamplification in valley bottoms and on the side of mountains facing towards the seismic source (60% of PGA in flat topography; Meunier et al. (2008)). This asymmetry of the PGA amplification pattern increases with increasing vertical incidence angle of seismic waves (Figure 2-10). The impact of topography is largest for S waves, but P waves also exhibit the same spatial amplification pattern. Topographic site effects have been attributed to the preferential occurrence of landslides on hillslopes orientated away from seismic sources (Meunier et al., 2008), along with their initiation near ridge crests and general occurrence across all parts of hillslope profiles, in contrast to rainfall-triggered landslides, which cluster around river channels (Densmore et al., 1997). While variability in hillslope material properties also modifies seismic waves at smaller scales in mountain ranges (Murphy et al., 2011b, Moore et al., 2011, Havenith et al., 2002), the lack of regional-scale data or proxy variables to constrain the spatial pattern means that relationships with regional scale landslide activity have not been investigated.

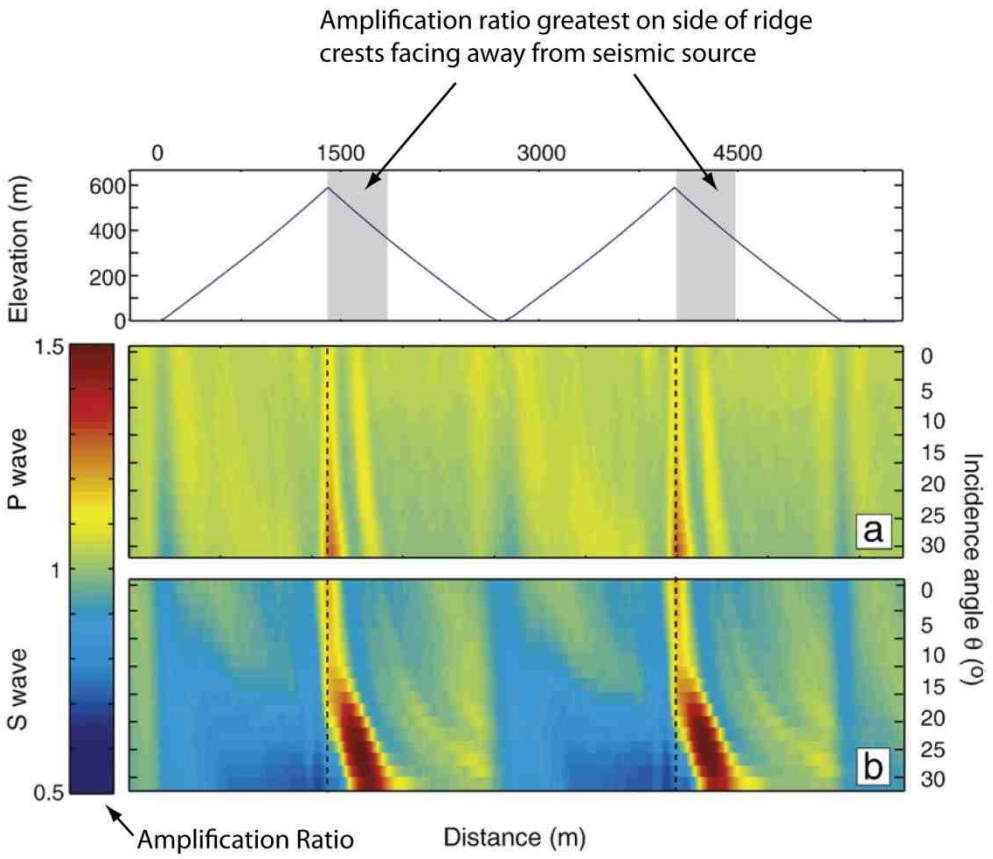

Figure 2-10 Patterns of P- and S-wave topographic amplification ratio modelled for a simplified topography composed of two adjacent triangular ridges (after Meunier et al., 2008: 228). The colour scale indicates the PGA with the topography normalised by the PGA without topography. The incidence angle of seismic waves is given with respect to the vertical (0^{o} indicates waves travelling vertically towards the Earth's surface, while 90^{o} indicates waves travelling horizontally).

Hillslope geometry and material properties determine the stability of hillslopes and therefore their likelihood of failure under seismic loading (Sections 2.1 and 2.2). Correspondingly, various studies have demonstrated a non-linear increase in landslide density with increasing slope gradient (e.g.: Keefer, 2000, Khazai and Sitar, 2004, Lee et al., 2008a, Dai et al., 2011). For example, Figure 2-11 shows relationships between landslide-point density and landslide-area density for the 2008 Wenchuan earthquake (Dai et al., 2011). Landslide density also varies by geology type (e.g.: Khazai and Sitar, 2004, Parise and Jibson, 2000, Keefer, 2000, Dai et al., 2011), indicating the influence of broad, regional variation in hillslope material properties. The aspect of hillslopes also appears to exert a stability control on landslide density, associated with the available heat and magnitude of diurnal heating and cooling cycles, which drive the physical breakdown of exposed bedrock (Mcfadden et al., 2005, Selby, 2005). The occurrence of earthquake-induced landslides on south-facing slopes during the Northridge earthquake (Meunier et al., 2008) and the Wenchuan earthquake (Parker,

2010, Chen et al., 2012b) has been attributed to this effect. While hillslope materials are highly spatially heterogeneous and anisotropic on smaller spatial scales, data is not currently available to resolve this level of local variability at the regional-scale for landslide inventory analysis.

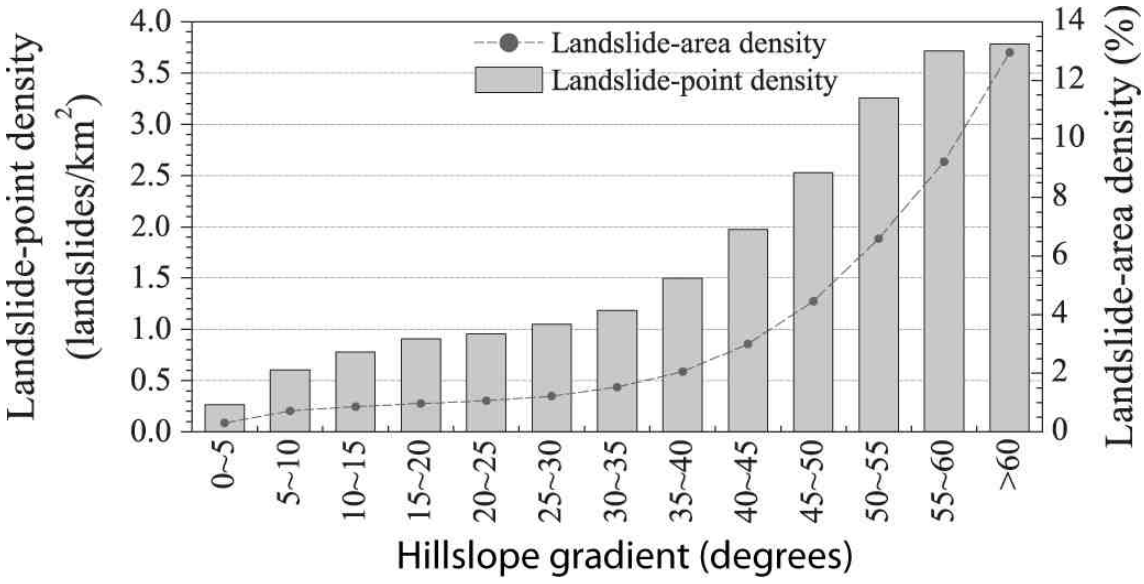

Figure 2-11 Relationship between landslide-point density, landslide-area density and hillslope gradient for the 2008 Wenchuan earthquake (after Dai et al., 2011: 892)

Figure 2-12 summarises factors influencing earthquake-triggered landslide density, separated into two groups: those pertaining to the strength of seismic ground motions and those pertaining to the stability of hillslopes. Proxy variables are given in red where they have been identified to represent these factors. Those factors that are known to influence landslide activity, but not constrained at the regional scale are shown in blue. Conceptually, regional-scale landslide activity can be understood in terms of a hierarchy of spatial scales over which the different factors influencing landslide density vary. Approximate bounds on these scales range from the global-scale variability with the size of different earthquakes to, site-scale variability in hillslope geometry and material properties. The major uncertainties in factors influencing landslide activity relate to site-scale variations in hillslope materials, which affect both hillslope stability and the local modification of seismic waves. These factors cannot be characterised using spatial proxies in the same way as other variables influencing landslide occurrence.

Numerous studies have produced models that combine different proxy variables influencing earthquake-triggered landslide occurrence, often to provide a synthesis of relationships for the purposes of landslide hazard assessment (e.g.: Yilmaz and Keskin, 2009, Lee et al., 2008a, Kamp et al., 2008, Garcia-Rodriguez et al., 2008, Lee and Evangelista, 2006, Ayalew and Yamagishi, 2005, Lin and Tung, 2004). However, currently available models have been produced through analysis of landslides specific to particular earthquakes or locations. As a result, a generalised understanding of ETL spatial distributions is lacking, along with models that are transferable between different earthquakes and regions.

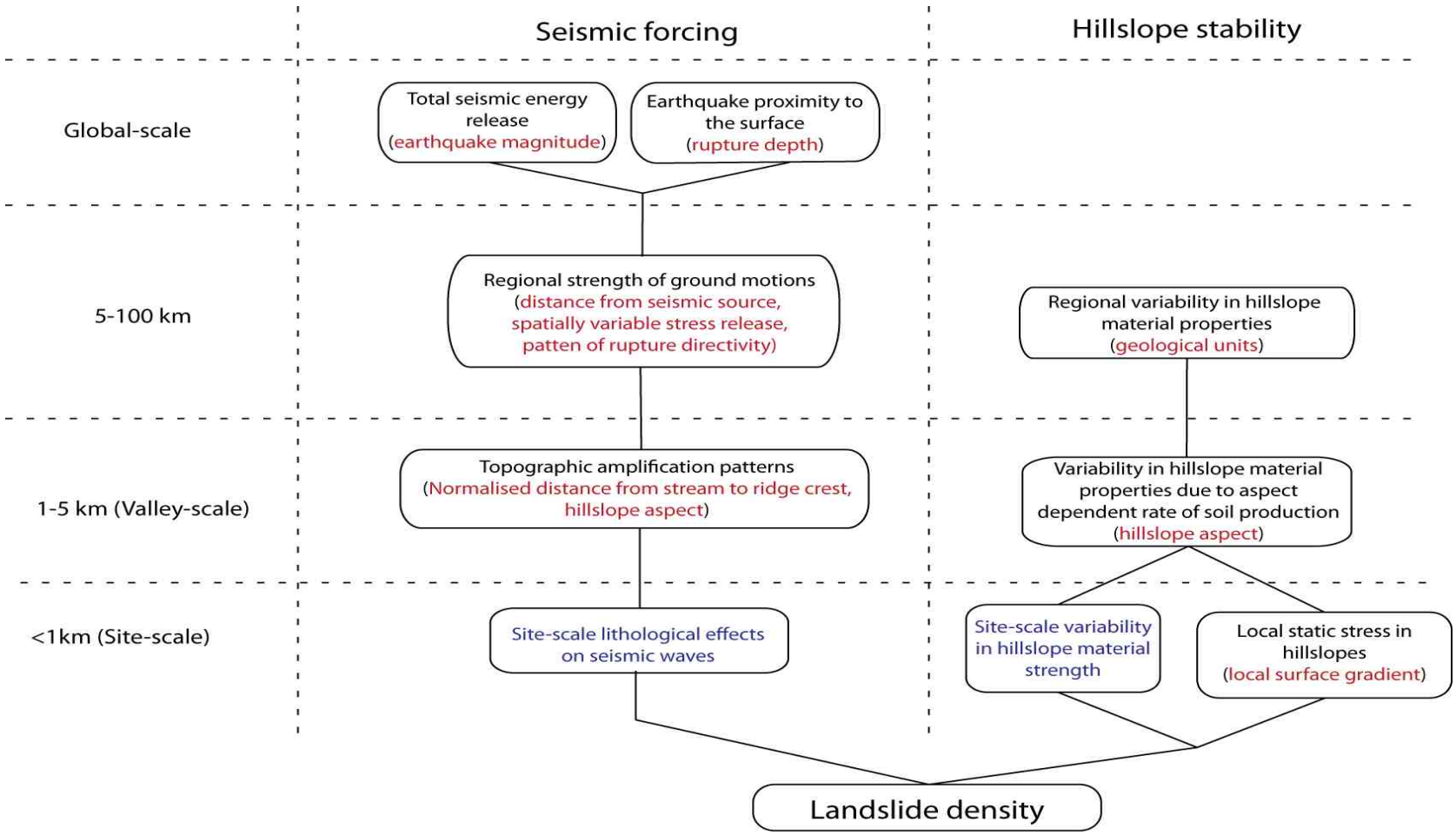

Figure 2-12 Conceptual model of factors controlling the density of earthquake-triggered landslides. Red text indicates where proxy variables have been identified to characterise these factors, while blue text indicates factors that have not been constrained using proxy variables

2.3.4 The temporal distribution of landslides associated with earthquakes

Spatial analyses of earthquake-triggered landslides provide an understanding of how landscapes respond to earthquakes at a single point in time but provide limited temporal information on landslide activity. However, multi-temporal landslide inventory studies have shown that, while large numbers of landslides occur co-seismically (i.e. during seismic shaking) many landslides also occur after large earthquakes. Observations from the 1999 Chi-Chi earthquake (Hovius et al., 2011, Lin et al., 2008b, Dadson et al., 2004, Shou et al., 2011) and the 2005 Kashmir earthquake (Saba et al., 2010), indicate elevated levels of landslide activity following these events that persist for several years. Hillslopes displayed an increased sensitivity to landslide triggering by rainfall, such that rainfall events following the earthquakes triggered more landslides than those preceding the earthquakes. This can be seen in Figure 2-12 (after Hovius et al., 2011), which shows results from the 367 km^2 Chenyoulan catchment, located between 10 and 20 km from the Chi-Chi earthquake coseismic fault. The time-series shows the new area of landslides recorded in 16 multi-temporal landslide maps, normalised for the strength of the storm forcing that triggered the landslides (the total water discharge from the catchment). Following the Chi-Chi earthquake, the area of landslides per unit volume of storm discharge exhibited a seven fold increase, which decayed to background levels over a period of ~6 years, with each subsequent typhoon triggering fewer landslides (Shou et al., 2011). As a result, the rate of landsliding (landslide area per unit area per year) was 13 times higher in the five years following the Chi-Chi earthquake than prior to the event (Lin et al., 2008b).

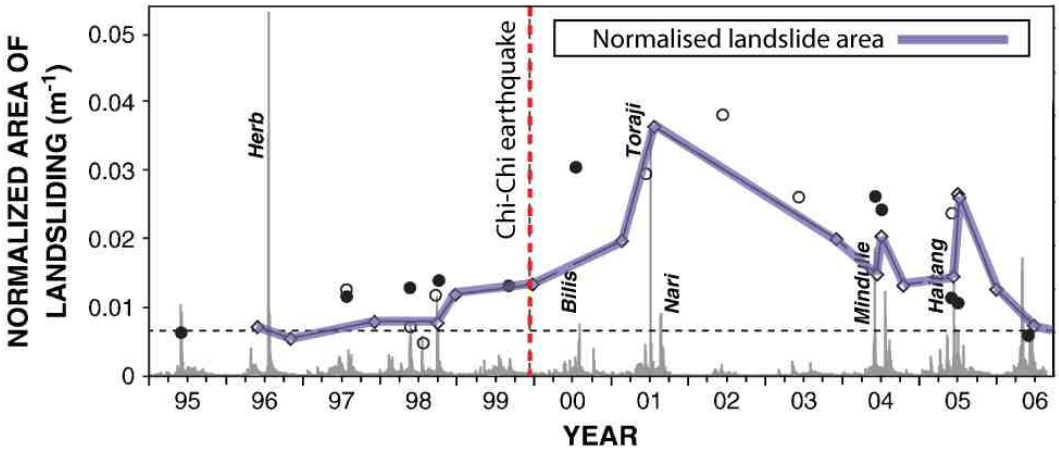

Figure 2-13 Time-series of landslide activity prior to and following the 1999 Chi-Chi earthquake (after Hovius et al., 2011: 351). The purple line indicates the newly mapped landslide area (recorded at 16 temporal snapshots), normalised for the strength of storm forcing. Shown in the background (grey bars) are hydrograph data, where the height is proportional to the discharge. Closed and open circles indicate suspended sediment levels, which are not the focus of the present discussion.

While results from the Kashmir earthquake have not been normalised for the strength of monsoon rainfall, a similar trend is apparent (Saba et al., 2010). The time-series in Figure 2-14 shows the new area of landslides recorded in 5 multi-temporal landslide maps, for a 36 km^2 sample area located ~10-15 km from the coseismic fault. Following the Kashmir earthquake the area of new landslides peaked and then returned to background levels within ~2 years. Preliminary results also suggest similar behaviour associated with the 2008 Wenchuan earthquake (Whadcoat, 2011, Tang et al., 2011), although a detailed temporal study has not yet been conducted.

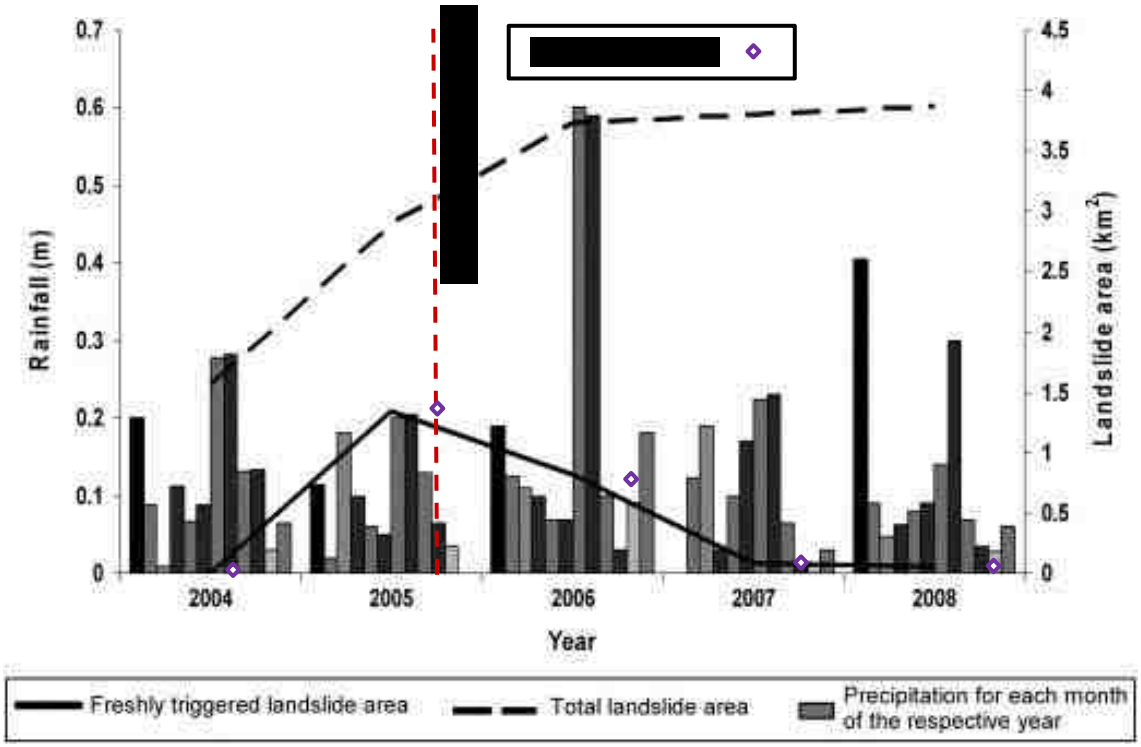

Figure 2-14 Time series of landslide activity and rainfall prior to and following the 2005 Kashmir earthquake (after Saba et al., 2010: 24). The solid black line incidates the newly mapped landslide area (recorded at 5 temporal snapshots). Note that the line originally plotted by Saba et al. (2010) places observations erroneously in the middle of each year, however the correct positions are indicated by the purple diamonds.

Post-seismic landslides represent a significant contribution to the total landslide activity associated with an earthquake. For example, data from Lin et al. (2008) show that post-seismic landslides make up 76% of the total area of landslides in the Chenyoulan catchment, triggered by and in the 5 years following the Chi-Chi earthquake. Similarly, for the 2008 Wenchuan earthquake, Whadcoat (2011) found that volumes of mobilised landslide material 5-10 months after the earthquake were over double those between 1 and 4 months after the earthquake. However, for the area studied by Saba et al. (2010), post-seismic landslides only contributed 15% to the total landslide area following the Kashmir earthquake.

Post-seismic landslides have been found to reflect the spatial distribution of earthquake ground motions and co-seismic landslides, but are also influenced by the spatial distribution of subsequent rainfall events. Hovius et al. (2011) has shown that the density distribution of typhoon-triggered landslides following the Chi-Chi earthquake reflects a combination of spatial patterns of mainshock PGA and typhoon rainfall intensity. Lin et al. (2008b) showed that hillslope gradient distributions of

landslides triggered by typhoons following the Chi-Chi earthquake are similar and have the same modal values as co-seismic landslide distributions.

While the majority of post-seismic landslides have been associated with rainfall-triggering and are largely unrelated to aftershocks (Hovius et al., 2011), it should be noted that the temporal resolution of landslide data in the above case studies is not sufficient to differentiate between landslides triggered by aftershocks and rainfall. As seismicity decays rapidly via a power law following large earthquakes (e.g.: Shcherbakov et al., 2005a, Shcherbakov et al., 2004, Adamaki et al., 2011), the highest rates of landslide activity associated with aftershocks will occur immediately following the mainshock. Without repeated landslide mapping over intervals of hours to days following the mainshock, the true contribution of aftershocks remains unknown.

These observations have, to date, been explained conceptually as the result of the disturbance to hillslope materials produced by large earthquakes, which recovers with time as subsequent landslide-triggering events occur (Saba et al., 2010, Hovius et al., 2011, Lin et al., 2008b). However, the nature and mechanics of this behaviour remains poorly understood. For example, it is unclear from a conceptual point of view why large earthquakes should prime the landscape for future landsliding, while large numbers of landslides are triggered coseismically. Why, when many hillslopes fail, do other hillslopes remain unfailed but primed for future failure? Similarly, why do subsequent landslide-triggering events following a large earthquake result in a decay in landslide activity, and how is their effect different to that of the mainshock earthquake? These questions are addressed in the Chapters that follow.

2.4 Summary

Although hillslope material strength is a primary control on the stability of slopes, this represents a major element of uncertainty in current spatial models of regional-scale ETL landsliding. Hillslopes composed of brittle materials undergo progressive failure, such that their strength and stability evolves through time, prior to failure. Temporal changes in landslide activity following large earthquakes suggest that the evolution of hillslope strength may have an important influence on spatial and temporal patterns of regional-scale ETL activity. However, the temporal coverage of ETL data is limited to sub-decal timescales and insufficient to develop a detailed understanding of how

landslide activity evolves through time. Developing a better understanding of temporal aspects of landslide activity, and how these are influenced by hillslope failure processes, therefore requires the integration of hillslope progressive failure into models of regional-scale landslide activity.

In order to understand temporal patterns of ETL activity, it is important to first have a clear understanding of spatial patterns of ETL activity. A variety of different factors have been found to influence spatial distributions of landslides and currently available spatial models are specific to particular earthquakes or regions. Therefore, a first step is to establish an understanding of ETL spatial distributions that is transferrable between different earthquake and regions. Developing this understanding is therefore the focus of the next two Chapters of this thesis.

Chapter 3 - Study areas and datasets

This chapter presents the study areas and earthquake-triggered landslide datasets used in analysis in Chapters 4 and 5. Five earthquake-triggered landslide events were chosen to investigate and statistically model the influence of static landscape conditions on earthquake-triggered landslide activity and test for the influence of hillslope memory using multi-temporal landslide inventories. The level of detail with which each earthquake-triggered landslide event is reviewed reflects the analysis undertaken. The region affected by the 1929 Buller and 1968 Inangahua earthquakes in New Zealand provides the primary case study for building an understanding of factors influencing landslide spatial distributions, and testing for the influence of hillslope memory. These events provide a rare example of two M_w > 7 earthquakes for which ground accelerations affected an overlapping region, and where aerial imagery for mapping landslides was acquired following both events. This creates the opportunity to investigate landscape characteristics that influence hillslope failure probability as well as factors influencing failure probability through time (namely the influence of the first earthquake on the distribution of landslides triggered by the second earthquake). In order to provide the foundations for this analysis, a detailed review of these events is undertaken. This covers details of landslide data acquisition along with a review of earthquake characteristics, geology, topography, and precipitation conditions, which have been found to influence landslide occurrence in previous investigations.

Three additional ETL datasets are also presented, which are used to build on analysis of the New Zealand earthquakes and develop a generalised understanding of earthquake-triggered landslide spatial distributions. For the 1994 Northridge, 1999 Chi-Chi and 2008 Wenchuan earthquakes, landslide inventories had been generated in previous investigations. To provide a widely representative dataset, these events were selected to encompass a range of different earthquake magnitudes (6.7<M_w<7.9) in regions of different climate, topography, geology and seismic history.

3.1 1929 Buller and 1968 Inangahua earthquakes, New Zealand

3.1.1 Geological setting

The 1929 Buller and 1968 Inanagahua earthquakes occurred in the north-west Nelson region of New Zealand's South Island, around 50 km north-west of the Alpine Fault. The region is characterised by north-east trending, uplifted basement-cored ranges and down-faulted depressions filled with alluvial sediments, separated by steeply dipping, north-striking active reverse faults on which the earthquakes occurred (Suggate and Lensen 1968; Anderson et al. 1994). The area affected by earthquake-triggered landslides is lithologically diverse, composed of rocks from Pre-Cambrian to Quaternary age, and is the product of a complex tectonic history. Geological unit and structure data were acquired from the New Zealand QMAP (Quarter-million Map) series of 1:250,000 scale geological maps produced by GNS Science (Nathan et al., 2002, Rattenbury et al., 1998, Rattenbury et al., 2006). The geology of the region is broadly classified into five tectonostratigraphic terrane units, which are useful for providing a broad indication of regional variations in lithology and material types (Figure 3-1).

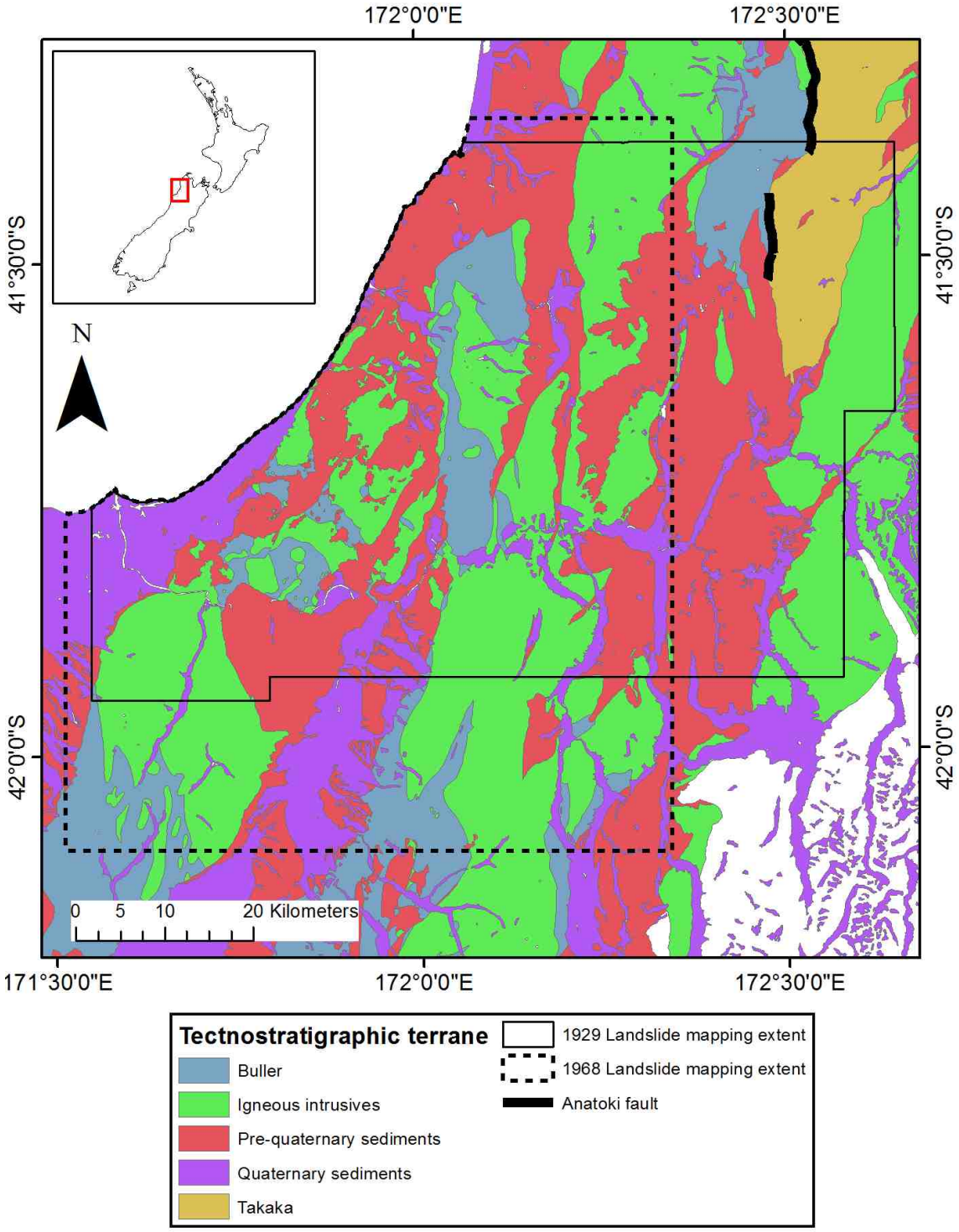

Figure 3-1 Map of tectonostratigraphic units of the north-west Nelson Region, produced by combining geological maps published in Rattenbury et al. (2006), Nathan et al. (2002) and (Rattenbury et al., 1998).

The Buller Terrane consists of all rocks older than the middle Devonian that lie to the west of the Anatoki fault. The terrane is predominantly composed of a sedimentary sequence of Ordovician, continent derived, quartz-rich turbidites, overlain by black shale, siltstone and quartz sandstone. To the east of the Anatoki fault lies the Takaka Terrane. This structurally-complex unit contains a wide variety of rock types, with

evidence of formation through two major depositional cycles during the Cambrian and Devonian periods. Major rock groups include volcanic and volcaniclastic arc-related sedimentary rocks and their metamorphosed equivalents, a prominent melange unit, and an overlying succession of clastic and carbonate sedimentary rocks. (Nathan et al., 2002, Rattenbury et al., 1998, Rattenbury et al., 2006). Within both the Buller and Takaka units are igneous intrusions, which were emplaced during the Paleozoic and Mesozoic (Nathan et al., 2002, Rattenbury et al., 1998).

The Buller and Takaka units are overlain by Cretaceous to Quaternary sediments, which are variably consolidated. These are classified into two groups: Quaternary sediments include hillslope colluvium and talus, peats, and unconsolidated to partly-consolidated fluvial and debris-flow deposits in the valley floors. Pre-Quaternary sediments include mudstones, sandstones, conglomerates, and limestones that have generally undergone some deformation and rock uplift (Nathan et al., 2002, Rattenbury et al., 1998, Rattenbury et al., 2006).

3.1.2 Topographic data

For the analysis of these two events, topographic data were derived from a DEM provided by GNS at 10 m pixel resolution (GNS Science, 2011b), using heights interpolated from 20 m contours based on 1:50,000 scale topographic data (NZ Topo Map, 2012). The elevation of the study area ranges from sea level to around 1800 m (See Figure 3-2).

3.1.3 Climate

The northwest Nelson region has a moist sub-tropical mid-latitude marine climate, according to the Koppen climate classification system (Kottek et al., 2006). Along the west coast the climate is primarily dependent on exposure from weather systems from the Tasman Sea, which brings high levels of precipitation of 1600-4100 (mean of 2500) mm/year across the combined landslide mapping extent (Hijmans et al., 2005). Mean annual rainfall is highly variable across the region, with high levels along the orographic relief of the west coast and increasingly drier conditions inland to the east (NIWA, 2011). Temperature follows a similar pattern with summer daytime temperatures of 17 - 22^{o}C (10 - 14^{o}C in winter) along the west coast, rising to 20-26^{o}C

(10-15^{o}C in winter) in the Moutere depression towards to the town of Nelson, with lower temperatures in higher altitude mountain regions (NIWA, 2011).

3.1.4 The 1929 Buller earthquake

At 2247 GMT on 16th June 1929 (1017 New Zealand Mean Time on 17th June) the Buller earthquake (also known as the Murchison earthquake) occurred in the north-west Nelson region of New Zealand's south island (Figure 3-2). The earthquake's epicentre was located at 41.7^{o}S, 172.2^{o}E (Dowrick, 1994, Anderson et al., 1994).

The surface wave magnitude of M_s = 7.8 is well determined from 16 observations (Dowrick and Smith, 1990, Dowrick, 1991). Using the waveform inversion techniques of Baker and Doser (1988) and McCaffrey and Abers (1988), Doser et al. (1999) estimated a seismic moment of 93 x 10^{18} ± 7 x 10^{18} Nm and 98 x 10^{18} (-10 x 10^{18}/+40 x 10^{18}) Nm, corresponding to the moment magnitude M_w = 7.3. However, it is likely that this is an underestimate as not all the moment release and source complexity of the earthquake has been modelled due to the insufficient bandwidth of instruments operating at the time. M_w = 7.7 can be inferred from the M_s using regression relationships from Dowrick and Rhoades (1998). Therefore, for the purposes of this study the magnitude is taken as M_w = 7.7. This is unlikely to be an underestimate, and the magnitude conforms with M_s-M_w relationships for other New Zealand earthquakes.

Surface faulting from the earthquake was observed along an 8 km length of the White Creek fault (Fyfe, 1929, Henderson, 1937). This length of observed faulting is much shorter than would be expected for an earthquake of this magnitude (Dowrick, 1994). The combination of a sparsely populated epicentral region, steep terrain and thick vegetation meant no systematic attempt to map surface faulting was carried out following the earthquake. Ground motion intensities (Dowrick, 1994) and landsliding (Pearce and O'Loughin, 1985, Hancox et al., 1998) suggest a rupture extending at least 50 km to the north of the epicentre. From back analysis of data from global seismic stations Doser et al. (1999) found that the total source duration suggested a unilateral rupture length of 30-40 km, while the mapped geological trace of the White Creek fault extends around 120 km (Stirling et al., 2002, Stirling et al., 2000). Location of the epicentre to the south of the fault suggests that the rupture propagated north.

The faulting mechanism was a combination of reverse thrust, with the hanging wall to the east, and left-lateral strike-slip along a strike of 15^{o}. The magnitudes of observed vertical and horizontal surface displacement are in the range 3.1- 4.5 m vertical, and around 1.6 m horizontal (Berryman, 1980). Henderson (1937) estimated a dip of 60 - 70^{o} based on surface displacement observations. Using this range along with the above displacement values, (Anderson et al., 1993) estimated a rake of 59^{o} – 72^{o}. Elastic dislocation modelling (Haines, 1991) suggests rupture on a thrust fault dipping about 45^{o} east. Estimates of strike, dip and rake generated through back analysis of data from global seismic stations are similar to those estimated from surface and geodetic information (Doser et al., 1999). Doser et al. (1999) inferred a focal depth of 9 ± 3 km.

In order to provide a 3-dimensional model of the seismic source for analysis in Chapter 4, the surface fault line and fault parameters of the White Creek fault used in the New Zealand probabilistic seismic hazard model were used (Stirling et al., 2007, Stirling et al., 2000, Stirling et al., 2002). This model is shown in Figure 3-2, and assumes a fault plane dipping at 45^{o} from the surface to a maximum depth of 12 km, with a 100^{o} dip direction. Note that across much of the study area for the present investigation the location of the surface fault rupture is well constrained from surface mapping. In addition to the main shock epicentre, epicentres of three 1929 aftershocks of Mw >= 6 recorded in the New Zealand earthquake catalogue (GeoNET, 2011) are also shown.

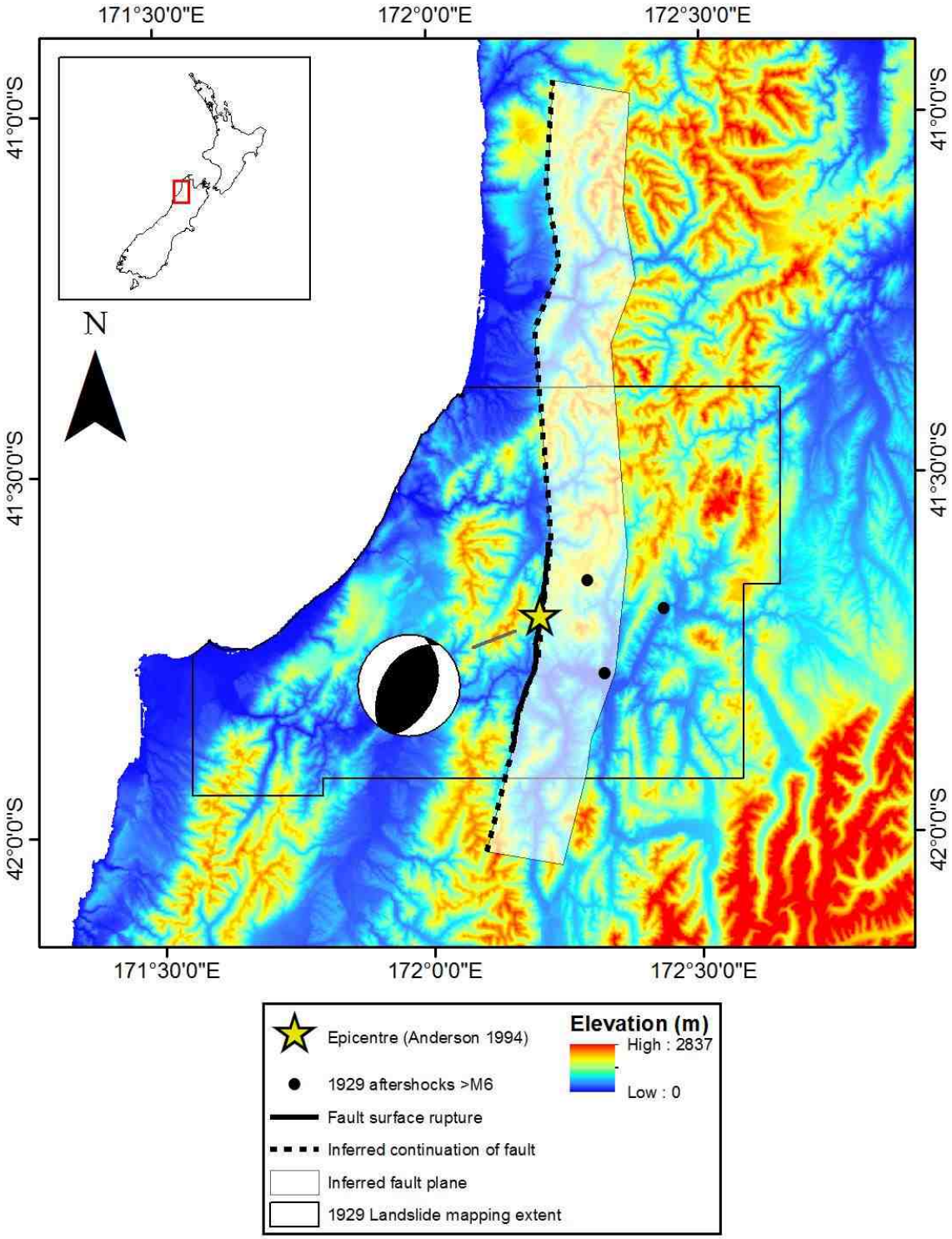

Figure 3-2 Map of the 1929 Buller earthquake epicentre , focal mechanism (Dowrick, 1994, Anderson et al., 1994), fault and locations of major aftershocks (GeoNET, 2011). Both the mapped extent of the fault rupture (Dowrick, 1994) and its inferred continuation along the White Creek fault (Stirling et al., 2007, Stirling et al., 2000, Stirling et al., 2002) are shown.

Limited instrumented seismic records exist for the 1929 earthquake, with only two stations located within 10^{o} of the White Creek Fault, at Christchurch (~200 km south-west) and Wellington (~230 km north-east). However, Dowrick (1994) generated estimates of Modified Mercalli Intensities (MMI) based on observations of building damage, in accordance with the 1992 revision of the New Zealand version of the MMI scale (New Zealand Society for Earthquake Engineering, 1992), using criteria set out for pre-earthquake code buildings. Dowrick (1994) used these to derive isoseismals for MMI <= 9, however an MMI 10 region could not be assigned from building damage observations due to the low population density. Hancox et al. (2002) modified Dowrick's original map to assign a region of MMI 10 based on observations of large landslide occurrence (Figure 3-3).

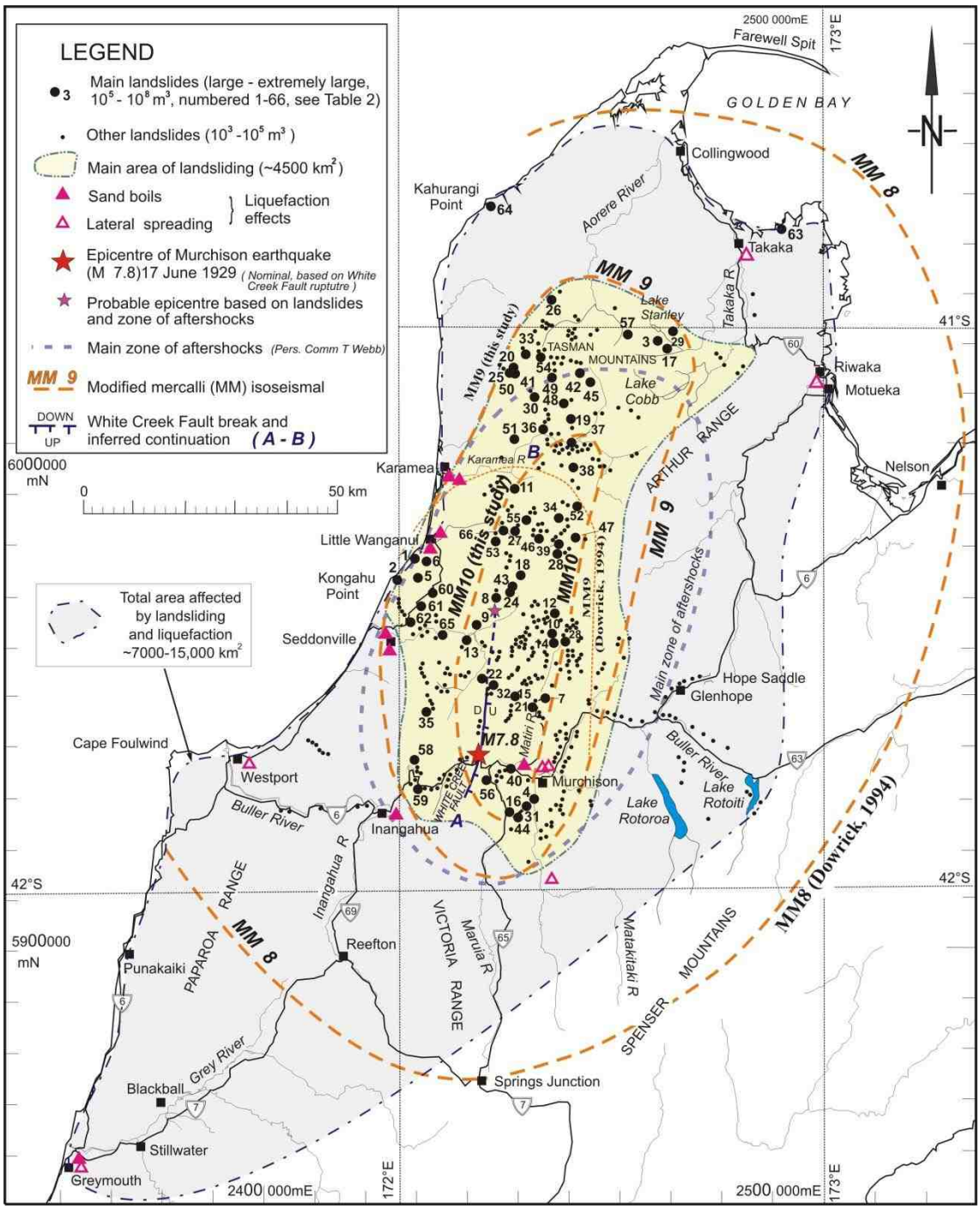

Figure 3-3 Map of locations of large landslides triggered by the 1929 Buller earthquake and MMI isoseismals inferred from building damage and landslide observations (Hancox et al., 2002: 65)

3.1.5 The 1968 Inangahua earthquake

At 1724 GMT on 23rd May 1968 (0524 on 24th May New Zealand Standard Time) the Inangahua earthquake also occurred in the north-west Nelson region of New Zealand's south island. It was the first large (M_w >= 7) earthquake to occur in the region since the 1929 Buller earthquake. The earthquake's epicentre has been located at 41.76°S, 171.96°E ± 10 km (Anderson et al., 1994).

The magnitude of the earthquake was first determined via the local magnitude, M_L = 6.7 (e.g.: Adams and Lowry, 1971). Later Dowrick and Smith (1990) determined the surface wave magnitude M_s = 7.4 through back analysis of global seismic data. Uncertainties regarding geometry of the fault plane, discussed below, have resulted in uncertainties in the estimation of the moment magnitude. Anderson et al. (1993) determined the seismic moments 6.9 x 10^{19} Nm for a fault plane projecting to the surface near the Lyell fault and 4.6 x 10^{19} Nm for their preferred seismological source model. These correspond to moment magnitudes of M_w = 7.2 and M_w = 7.1 respectively. Therefore, for the purposes of this study the magnitude is taken as M_w = 7.1.

The Inangahua fault was originally assumed to be the source of the Inangahua earthquake (e.g.: Adams and Lowry, 1971), where several short fragmented surface fault displacements were observed following the event. However, this source is inconsistent with the pattern of uplift that occurred during the earthquake (Anderson et al., 1994). Seismological and geodetic analysis of the earthquake and its associated deformation suggest that most of the moment was released on a single fault plane trending northeast (25^o), dipping northwest at ~45^o, and extending around 30 km in length to a depth of 10 - 15 km (Anderson et al., 1993). The focal depth of the earthquake is estimated at between 6 and 15 km, with a best fit depth of 10 km (Anderson et al., 1993). The coseismic fault plane predicted by Anderson et al. (1993) extends to within ~1 km of the ground surface, with the up-dip projection to the surface a few kilometres to the west of the Lyell Fault, suggesting a potential candidate for the seismic source. This single, planar fault source is likely a simplification, as geological data suggest the rupture may have occurred along three segments of a bent or splayed north-west-dipping fault (Anderson et al., 1994). However, insufficient data exists to further constrain the source (Anderson et al., 1994). The style of faulting is predominantly reverse thrust, with possibly a small component of either right- or left-lateral strike slip (Adams and Lowry, 1971, Robinson et al., 1975, Anderson et al., 1994). In order to generate the observed surface deformation, Anderson et al. (1994) estimated that 4 – 6 m of displacement must have taken place on the fault.

The source-time function indicates that the earthquake was a multiple event consisting of a small earthquake of M_w = 6.5 followed by a larger event of M_w = 7.0 (Anderson et

al., 1994). However, data are not sufficient to resolve either the spatial separation of these two earthquakes or a difference in mechanism between them. In addition to the main shock, a large number of aftershock epicentres, consistent with this source model, were recorded following the earthquake across a similar range of depths to the main shock (84% falling between 4 and 14 km). The aftershock distribution indicates that the main shock originated at the north-eastern end of an elongated region of aftershock epicentres, suggesting that the rupture propagated towards the southwest (Anderson et al., 1994). The source model and parameters used in this analysis (Figure 3-4) are taken from the best fit model of Anderson et al. (1994).

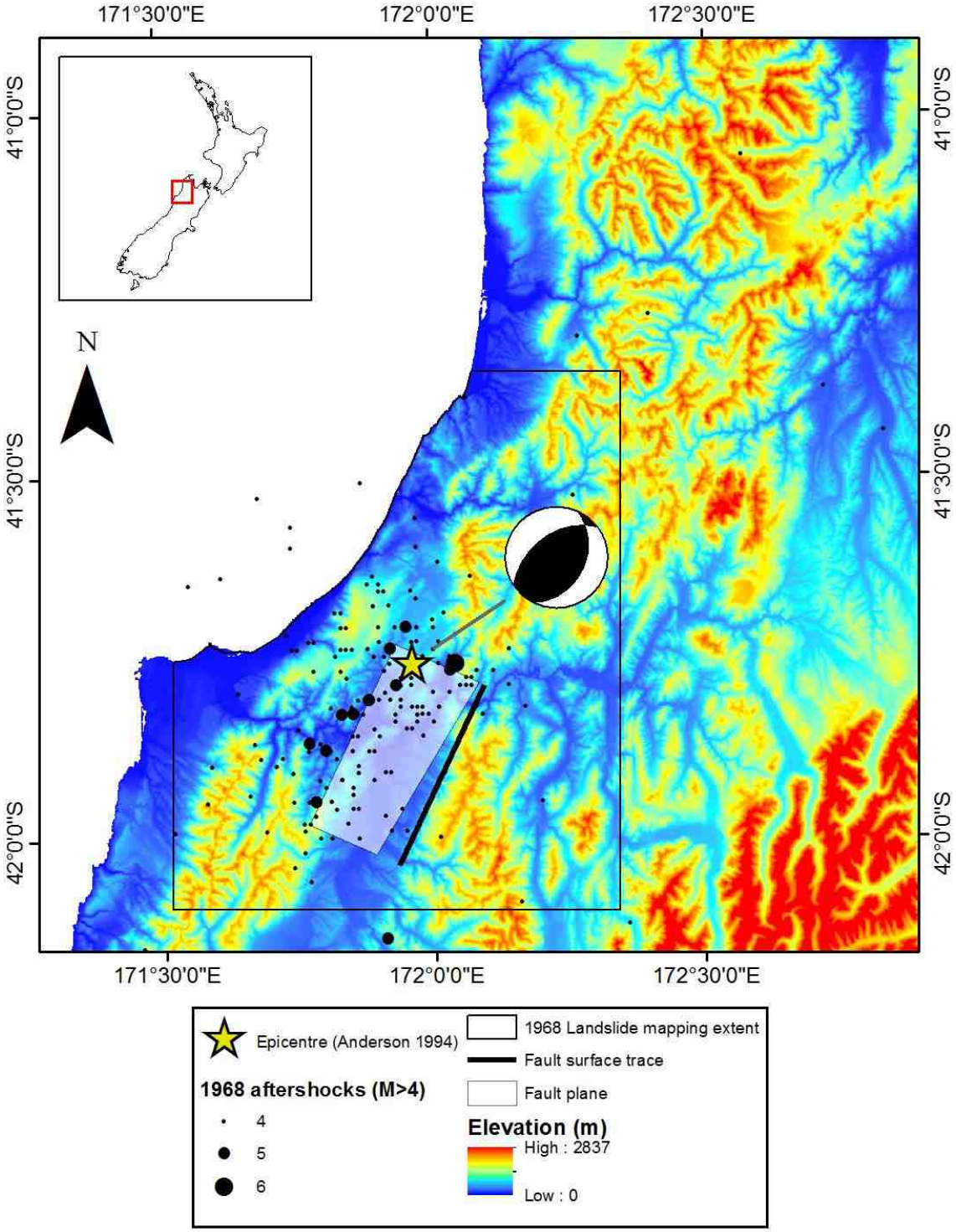

Figure 3-4 Map of the 1968 Inangahua earthquake epicentre , focal mechanism, fault model and aftershocks (data from Anderson et al., 1994)

Felt reports, newspaper and descriptive accounts have been used to derive intensity data using the MMI scale of (Dowrick, 1996). These data have been used to derive isoseismals (Downes, 1995), shown in Figure 3-5.

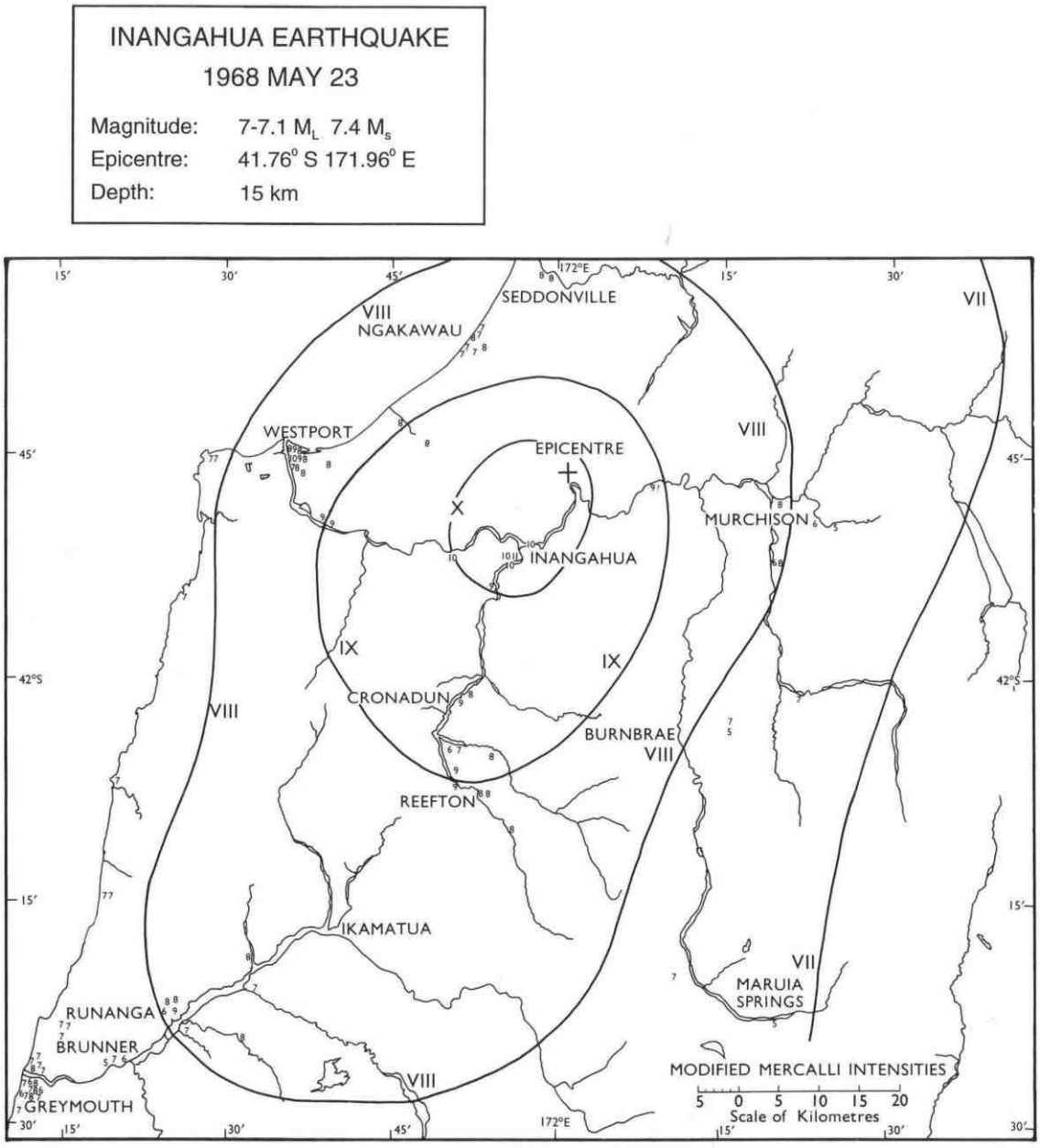

Figure 3-5 Isoseismal map for the 1968 Inangahua earthquake (Downes, 1995: 68)

3.1.6 Event comparison

Characteristics of the spatial distribution of landslides triggered by these earthquakes are analysed and compared in Chapters 4 and 5. It is important to understand how these events relate to each other spatially, and how the ground conditions at the time of the earthquakes are likely to differ in ways that should be considered in analysis. A comparison of earthquake characteristics can be summarised as follows:

- The epicentres of the 1929 and 1968 earthquakes are located 21 km apart and at their closest point the surface expressions of the coseismic faults lie 7 km apart.

- The earthquakes have nearly identical focal mechanisms (Anderson et al., 1994, Anderson et al., 1993), although the faults dip in opposite directions.

- The fault ruptures propagated in different directions, with the 1929 rupture propagating north along the fault and the 1968 rupture propagating southwest. Isoseismal maps from the two earthquakes reflect expected patterns of directivity resulting from these patterns of rupture propagation, with strong shaking in regions towards which the rupture propagated (north of the 1929 epicentre and southwest of the 1968 epicentre).

- The 1929 earthquake (M_w = 7.7) had a higher magnitude than the 1968 earthquake (M_w = 7.1), resulting in generally stronger shaking intensity distributed over a larger area.

- Both earthquakes have a focal depth of ~ 10 km.

- According to isoseismal maps published in Downes (1995), an area of 3505 km^2 was affected by MMI 8 ground motions in both earthquakes, 2287 km^2 of which is included in the overlap area of the two landslide maps, and an area of 584 km^2 was affected by MMI 9 or greater, all of which is included in the overlap area (Figure 3-6)

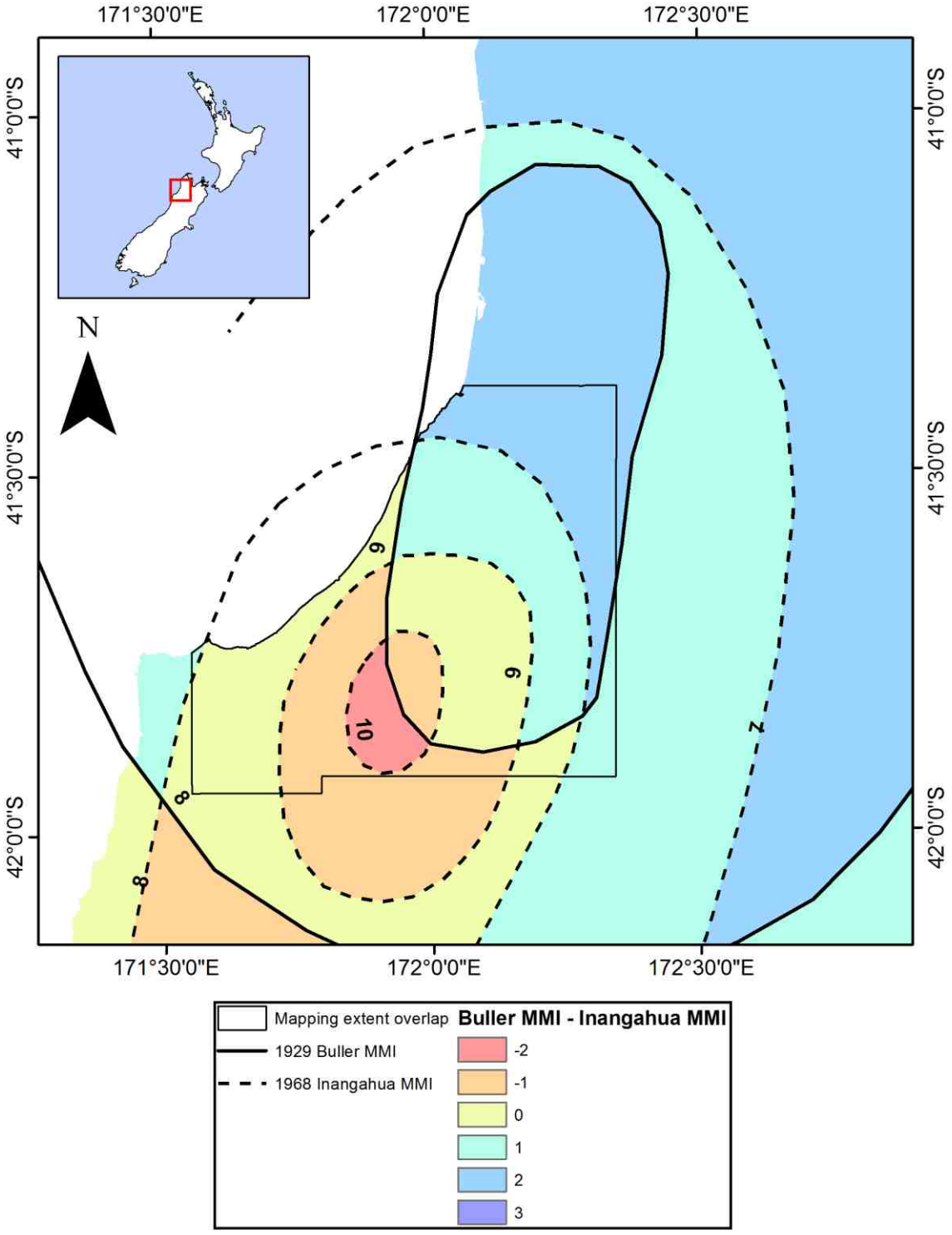

Figure 3-6 Map of MMI difference for the 1929 Buller and 1968 Inangahua earthquakes (1929 MMI – 1968 MMI), using data from Downes (1995). Combined areas affected by ground accelerations for both earthquakes and included in the study area are 2287 km^2 for MMI 8 and 584 km^2 for MMI 9. Colour scale indicates the difference in the shaking intensity of the two events.

Ground water levels and antecedent rainfall conditions affect the stability of hillslopes through pore pressure generation (Selby, 2005). From an analysis of the landslides and modified Mercalli intensity data for four New Zealand earthquakes, Dellow and Hancox (2006) suggested that wet conditions increase levels of landslide damage by the

equivalent to an increase in seismic ground motion of two MMI units over dry conditions, and that on average areas affected by earthquake-triggered landslides are greater in winter than in summer. Rainfall data for the region are available through the National Institute of Water and Atmospheric Research (NIWA, 2011), with complete records from selected gauging stations for both 1929 and 1968. The Karamea gauging station is located closest to the study area with a complete record for both earthquakes (Figure 3-7). Additionally, Hijmans et al. (2005) provide distributed mean monthly and annual rainfall totals, interpolated from gauging station data (1950-2000) at 1 km^2 resolution (Figure 3-7).

Figure 3-8 shows the monthly distribution of rainfall based on spatial mean values across the study area (Hijmans et al., 2005) and data from the gauging station at Karamea, with monthly means and monthly totals for the years of the Buller (1929) and Inangahua (1968) earthquakes. In terms of mean monthly rainfall totals across the area of landslide mapping, summer months (December to February) generally experience less rainfall with a minimum of 122 mm in February. Levels rise through the Autumn (March to May) and remain high (> 200 mm) through the winter and spring. This overall annual pattern is generally echoed in the Karamea record, although Karamea has generally lower rainfall than the majority of the study area. The Karamea record suggests that both months in which earthquakes occurred were wetter than the 1950-2000 average, with June 1929 receiving 307 mm (May-June 1929 received 406 mm) and May 1968 receiving 275 mm (April-May 1968 received 525). If levels of rainfall at the Karamea gauge reflect observations across the study areas, this suggests similar ground moisture conditions for the months of both earthquakes.

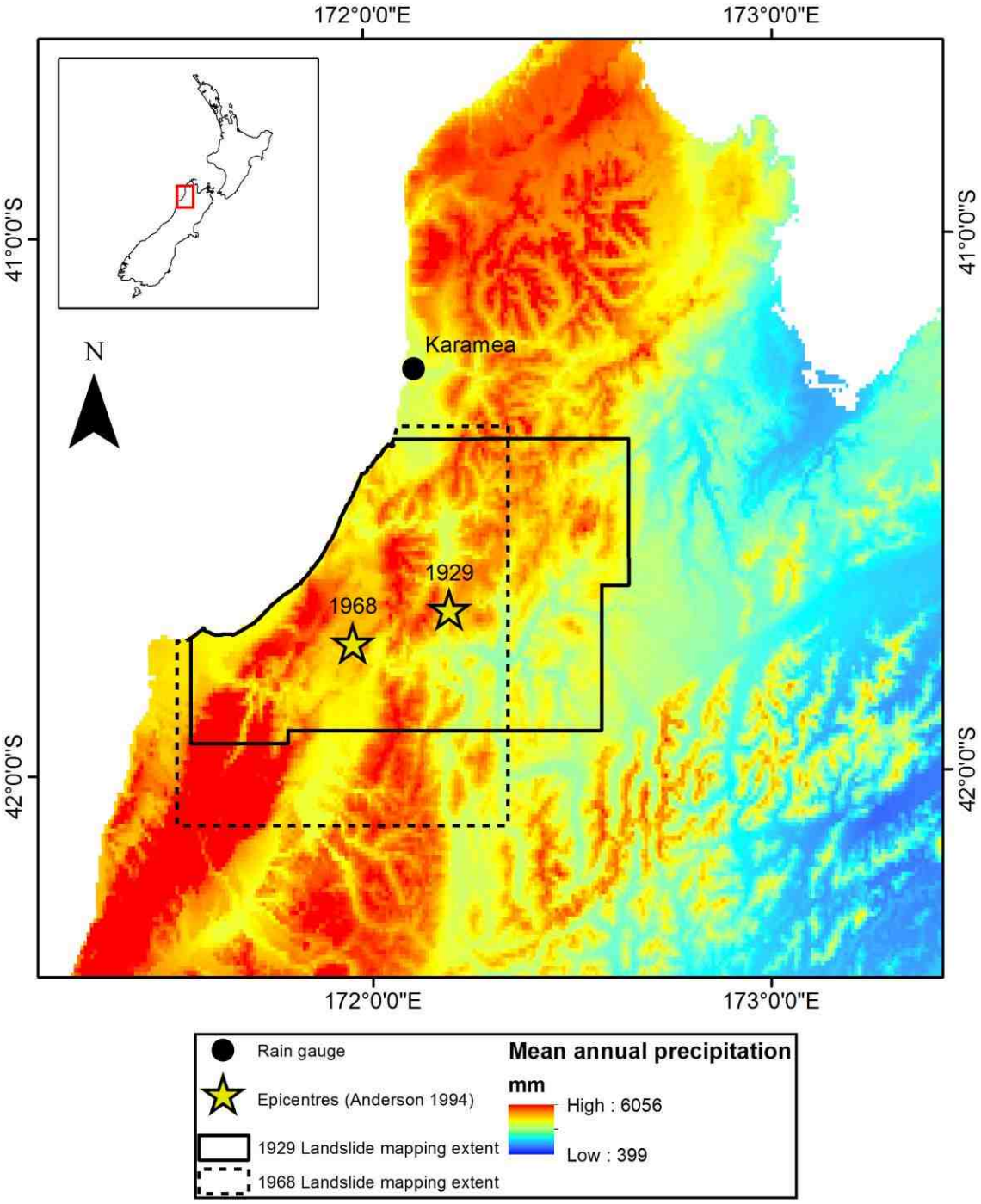

Figure 3-7 Map showing distributed mean annual precipitation for the study area estimated at 1 km^2 resolution, based on records from the period 1950-2000, and interpolated as a function of latitude, longitude and elevation (data from Hijmans et al., 2005). The location of the Karamea rain gauge is indicated, which provides a complete record of precipitation for both earthquakes.

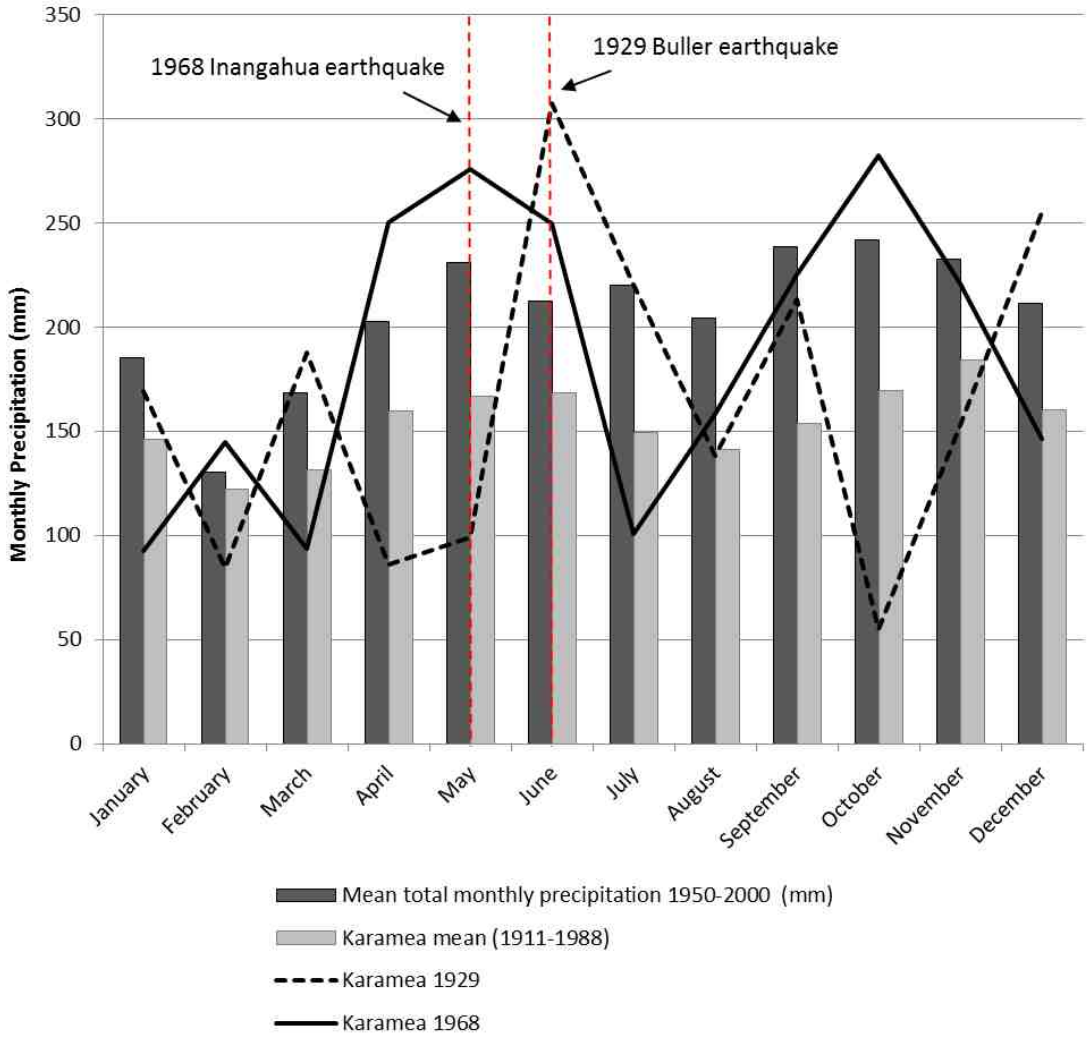

Figure 3-8 Plot showing the annual distribution of rainfall for the study area based on long-term mean values and data from 1929 and 1968. Mean monthly precipitation totals for the area of landslide mapping are estimated from interpolated mean monthly data for the period 1950-2000 (Hijmans et al., 2005). These correlate with mean monthly totals at the Karamea rain gauge for the period 1911-1988, suggesting that data from the Karamea gauge is reflective of precipitation across the study area. Monthly totals for the years of the earthquakes suggest similar ground water conditions for June 1929 (Buller earthquake) and May 1968 (Inangahua earthquake).

3.1.7 Landslide mapping

Landslide maps were originally produced for both events by Graham Hancox from GNS Science. Landslides triggered by the 1929 Buller earthquake were identified on 1:86,000 scale panchromatic aerial images (Table 3-1) taken in February 1968 through stereoscopic interpretation, together with ground photos taken in 1929 and aerial images taken in 1937 for some areas. Landslide polygons (outlining the full extent of the landslide source, runout and deposit) were plotted by hand onto 1:50,000 scale NZMS 260 paper topographic maps. Landslides triggered by the 1968 Inangahua earthquake were identified on 1:66,000 scale panchromatic aerial images (Table 3-1) taken in November 1974 through stereoscopic interpretation, together with aerial

oblique and ground photos taken in 1968 and 1969. Landslide mapping was further validated based on observations from fieldwork undertaken throughout 1968 and 1969 by Graham Hancox. Landslide polygons (outlining the full extent of the landslide source, runout and deposit) were plotted in CorelDraw onto 1:50,000 scale NZMS 260 topographic maps. For both inventories, landslides were identified using defined parameters for air photo interpretation of landslides (e.g.: Nichol and Wong, 2005, Liu et al., 2002) and mapped down to a minimum size of ~10,000 m^2. In order to differentiate between landslides triggered by the two earthquakes, comparison was made between landslide scars visible in the November 1974 and February 1968 aerial photographs, along with terrestrial photos taken in 1929 (Henderson, 1937) and field mapping (Hancox, 1969). Where landslide scars attributed to the 1929 earthquake displayed evidence of further failure, enlargement and deposition following 1968, these areas were included in the 1968 dataset.

Table 3-1 Source and details of imagery used for landslide mapping for the 1929 and 1968 earthquakes

Source: New Zealand Aerial Mapping (http://www.nzam.com/)
Imagery for mapping of 1929 Buller earthquake-triggered landslides
Survey Number: SN 2033, February 1968 **Contact Print Scale**: 1:86,000 Run 4029 Photos 9-56 Run 4030 Photos 6-66 Run 4031 Photos 68-85 Run 4032 Photos 15-38 Run 4033 Photos 18-31
Imagery for mapping of 1968 Inangahua earthquake-triggered landslides
Survey Number: SN 3777 **Acquisition period:** November 1974 **Contact Print Scale**: 1:60,000 Run A-Photos 1-7 Run B-Photos 1-7 Run C-Photos 1-9 Run D-Photos 1-9 Run E-Photos 1-10 Run F-Photos 4-6 Run G-Photos 4-10 Run H-Photos 6-12 Run I-Photos 9-12 Run J-Photos 7-11

For this study, these data were digitised and imported into GIS software by the author. Field reconnaissance and historical imagery were then used to conduct further validation and correction of mapping errors. This included rectifying delineation inaccuracies, and identifying landslides that had been attributed to the wrong event or features that had been double-mapped in both inventories. Key to the mapping methodology is the slow rate of post-landslide re-vegetation in the region, which allows landslides to be identified in imagery acquired long periods after the initial failure. This is emphasised by oblique aerial imagery acquired in 2011, in which landslides triggered by the 1929 earthquake are still clearly distinguishable (Figure 3-9). Older, relic features, such as the Tidal Creek (Lake Hanlon) landslide (see Nathan et al., 2002, Rattenbury et al., 1998), were found to be thickly obscured by older vegetation and clearly distinguishable from more recent failures. Observations in the period since the 1968 Inangahua earthquake from various field expeditions by New Zealand geologists (Pearce and O'Loughin, 1985, Hancox, 2011), and during field validation carried out by R. Parker in 2011, suggest a lack of widespread landsliding resulting from heavy rainstorms or other processes during interseismic periods. This suggests that the majority of landslides in the terrain, and therefore captured in the datasets, are associated with seismic events - either co-seismic landslides or post-seismic landslides occurring soon after the earthquakes. This combined with low levels of historical seismicity prior to the 1929 earthquake (GeoNET, 2011), suggests minimal errors associated with the inclusion of pre-1929 landslides in the datasets.

Landslides maps for the 1929 and 1968 earthquakes are shown in Figure 3-10 and Figure 3-11 respectively. For the 1929 earthquake, 4074 landslides have been mapped across an area of 4222 km^2, while 1159 landslides have been mapped across an area of 4288 km^2 for the 1968 earthquake.

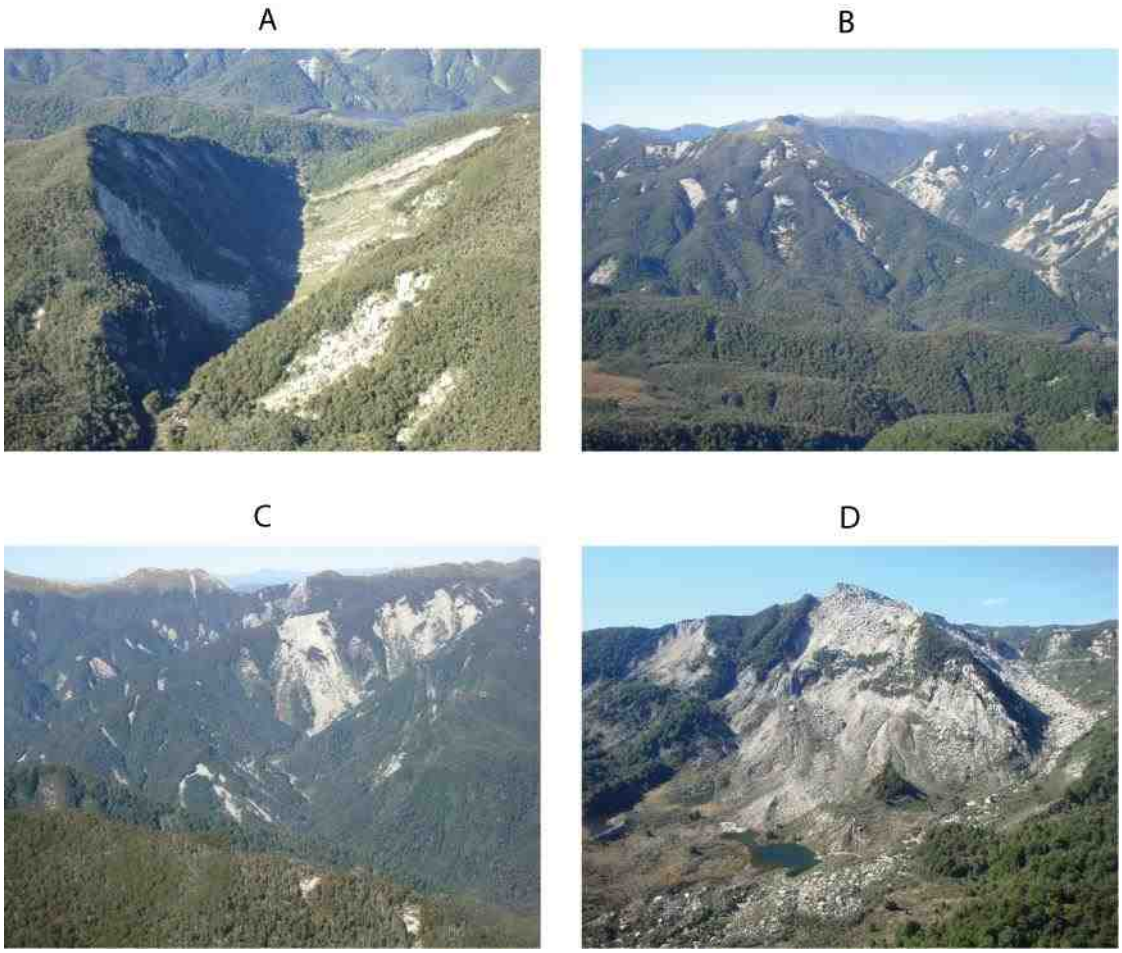

Figure 3-9 Oblique aerial images of landslides triggered by the 1929 Buller earthquake, taken in May 2011 at locations indicated in Figure 3-10. Despite the intervening period of 82 years, failure scars from the 1929 landslides were still clearly visible in 2011.

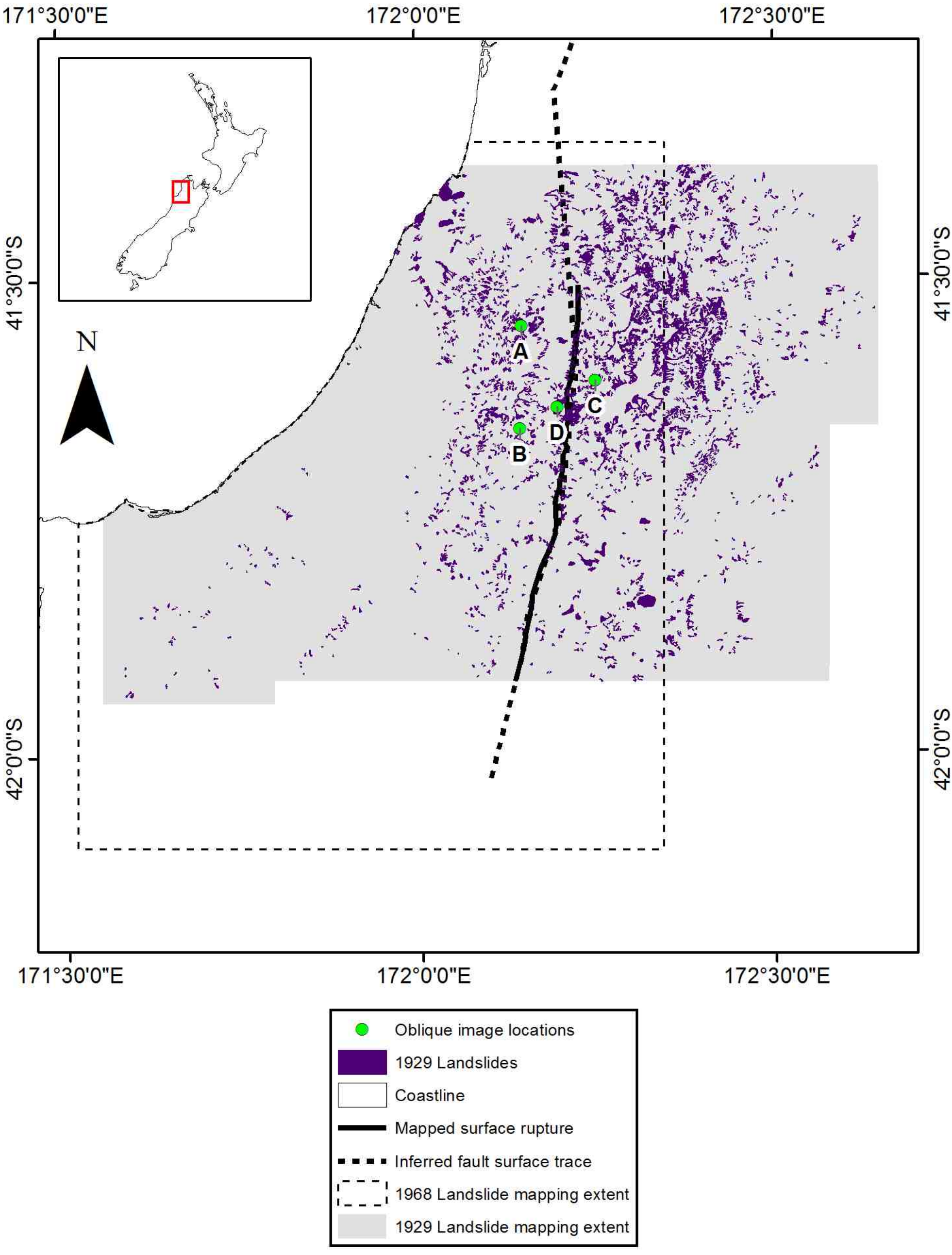

Figure 3-10 Map of landslides (full landslide areas including source, runout and deposit) triggered by the 1929 Buller earthquake. The locations of oblique aerial images shown in Figure 3-9 are indicated.

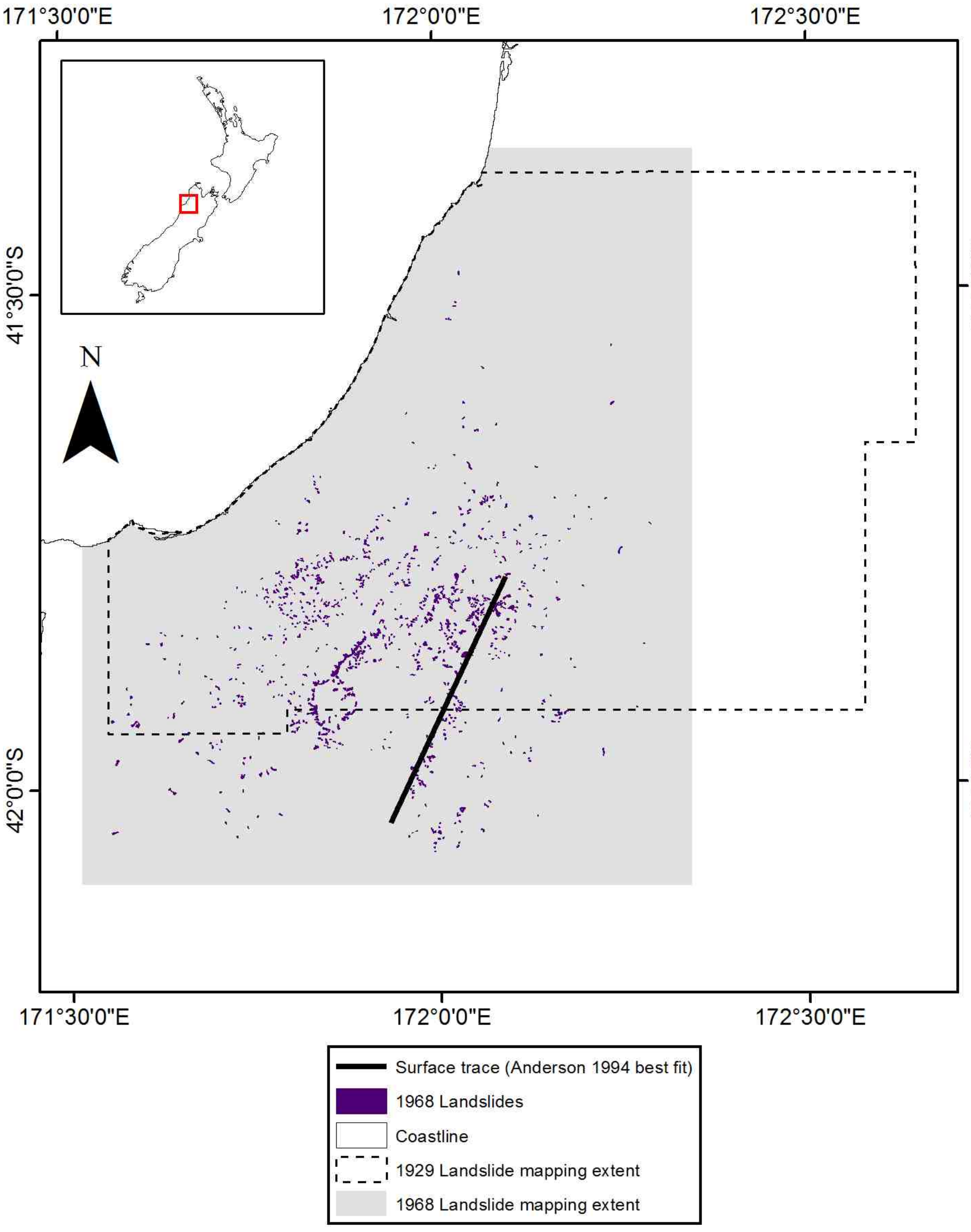

Figure 3-11 Map of landslides (full landslide areas including source, runout and deposit) triggered by the 1968 Inangahua earthquake

3.1.8 Separation of landslide source areas

The full area of landslide source, runout and deposit captures the result of both the hillslope failure process and the behaviour of landslide material during transit and deposition downslope. As the focus of this investigation is on the initial failure and detachment of material, separation of the landslide source from areas of runout and deposition is required. While landslide scars are clearly visible in the aerial imagery used to map landslides, individual features within the landslides are not. In order to provide an approximation of landslide source zones, these were delineated using an algorithm based on the DEM. Using an approach conducted in previous studies, landslide areas with elevations above the median elevation for each landslide were extracted, such that the upper half of each landslide is considered the source area and the lower half the runout and deposit (e.g.: Parise and Jibson, 2000, Jibson et al., 2000, Capolongo et al., 2002, Lee et al., 2012). This process is illustrated in Figure 3-12, for a region of high landslide density resulting from the 1929 earthquake.

The use of this technique is based on the principle that a landslide source area undergoes failure and the material travels and is deposited downslope, and that areas of the original source and areas of runout and deposition are distributed evenly relative to elevation. It should be noted that the technique does not account for variability in hillslope gradient and water content, and the presence or absence of physical features known in influence runout such as gullies, stream channels, roads and trees, or different landslide types or process (Guthrie et al., 2010). These factors are likely to alter how source and runout areas are distributed across the landslide elevation profile. For instance, landslides on steep slopes with high water content are likely to have longer runout distances relative to their original source dimensions as compared to landslides on shallow slopes with lower water content. Errors associated with the technique will vary for landslides of different types and with different characteristics. In the absence of higher resolution imagery and detailed field mapping at the time of the earthquakes, the outputs of this process cannot be validated quantitatively. However, this technique is widely used and previous authors have found it to provide a reasonable approximation (Parise and Jibson, 2000, Jibson et al., 2000, Capolongo et al., 2002, Lee et al., 2012).

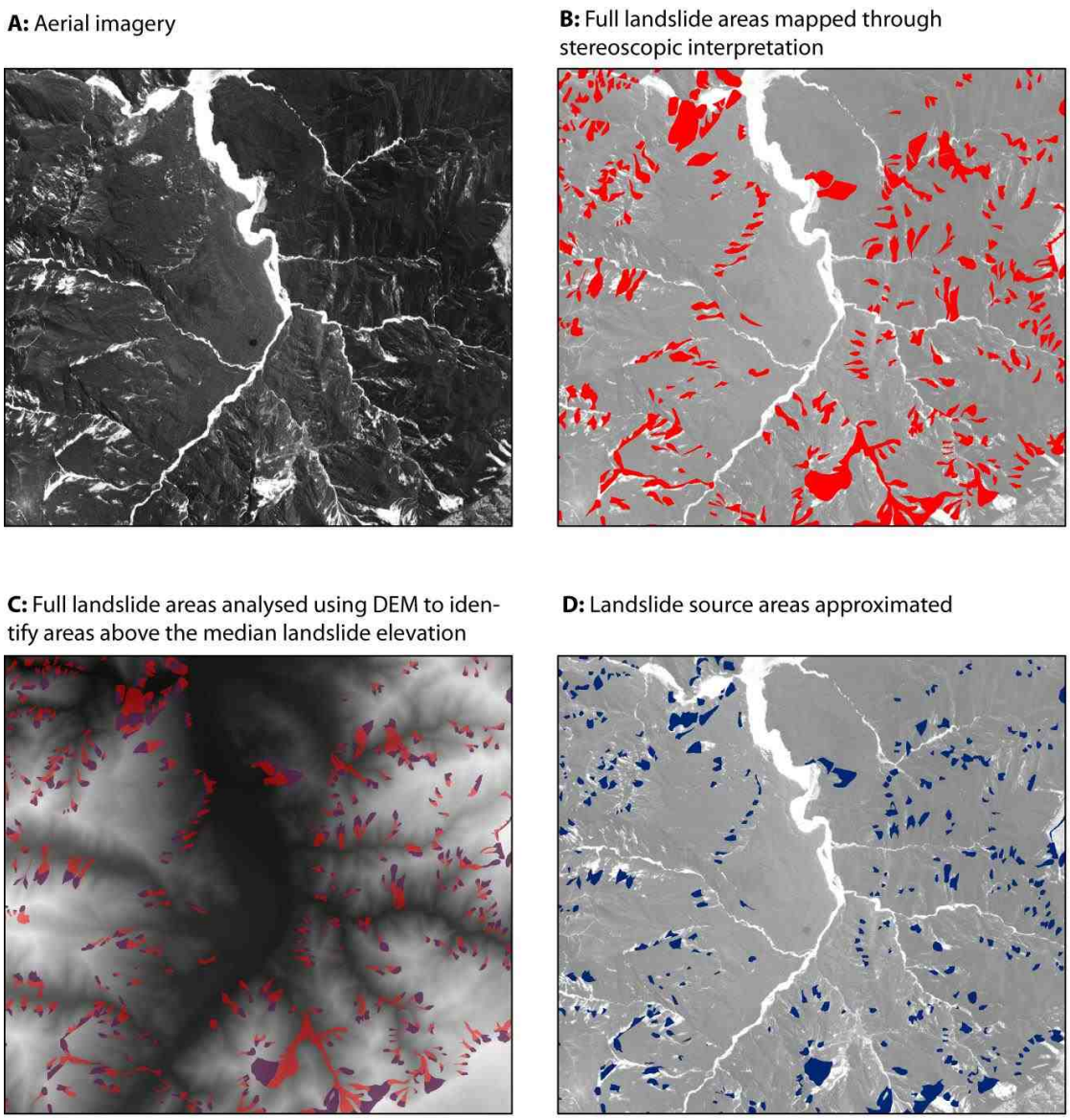

Figure 3-12 Illustration of landslide source area extraction technique for a 10x10 km sample area, showing landslides triggered by the 1929 Buller earthquake.

3.2 Comparative earthquake-triggered landslide datasets

Landslide inventories for the 1994 Northridge, 1999 Chi-Chi and 2008 Wenchuan earthquakes were obtained from previous studies. Analysis of these events focusses on the influence of topographic, earthquake and ground motions characteristics on landslide occurrence. A summary of information relevant to this analysis is provided for each earthquake below. Firstly, two global datasets are described which allow direct comparison between these events and the 1929 and 1968 landslide datasets.

While a regional DEM was available for the New Zealand earthquakes, in order to provide a consistent dataset for analysis of all five events, topographic data was obtained from the ASTER Global DEM (GDEM) dataset (N.A.S.A. Land Processes Distributed Active Archive Center, 2011). This data is generated from ASTER stereo pairs and gives complete global coverage at 30 m resolution. GDEM has an average absolute vertical accuracy of 0.2 m, with an accuracy of 17 m at the 95% confidence level (Tachikawa et al., 2011). Compared to the Shuttle Radar Topography Mission (SRTM) dataset (Jarvis et al., 2008), GDEM exhibits lower levels of noise and provides a better representation of slope gradient, particularly of steep topographic ridges, V-shaped valleys, and contrasts between steep slopes and gentle valley floors (Hayakawa et al., 2008). This makes GDEM the most appropriate global dataset for landslide analysis, owing to relationships between hillslope gradient and stability (see Section 2.1.4).

The USGS Shakemap Atlas (Allen et al., 2008) contains map data of peak ground motions and intensity, termed "ShakeMaps", for recent and historical earthquakes distributed globally. Each map has been produced using the Shakemap methodology (Wald et al., 1999, Wald et al., 2005), with constraints from macroseismic intensity data, instrumental ground motions, regional topographically-based site amplifications, and published earthquake-rupture models. In general, ground motions are well constrained near seismic recording stations and uncertainty increases with distance from seismic stations where ground motion prediction equations must be relied upon (Wald et al., 2008). Shakemaps were available for all events with the exception of the 1929 Buller earthquake, which occurred prior to the establishment of seismic recording stations in the region. Input data range from dense station coverage for the Northridge and Chi-Chi earthquakes, to sparser coverage for the Wenchuan and Inangahua earthquakes. Maps of spatial uncertainty in ground motions are provided for each earthquake in the relevant appendices.

3.2.1 1994 Northridge earthquake

The M_w = 6.7 Northridge earthquake had a focal depth of 18 km (USGS, 1994) and resulted from a reverse thrust fault displacement, with minor components of strike-slip (Wald et al., 1996, Shen et al., 1996). The earthquake affected the San Fernando

Valley and adjacent mountains, in Southern California. A total of 11,111 landslides that occurred on the morning of the earthquake have been mapped over an area of 3973 km^2 (Harp and Jibson, 1995a, Harp and Jibson, 1996), shown in Figure 3-13. Landslides were mapped by hand through interpretation of 1:60,000-scale aerial photographs, acquired within 8 hours of the mainshock. The minimum size of mapped landslides is reported as 1-2 m in width, and it is estimated that over 90% of the total areal extent of landslides has been mapped (Harp and Jibson, 1995a, Harp and Jibson, 1996). Supplementary information regarding available fault models and Shakemap PGA uncertainty are provided in Appendix A ii.

3.2.2 1999 Chi-Chi earthquake

The M_w = 7.6 Chi-Chi earthquake had a focal depth of 8 km, and also resulted from a reverse thrust fault displacement, with minor components of strike-slip (Shin et al., 2000, Shin and Teng, 2001). The earthquake affected the mountainous region of central west Taiwan. 9272 landslides that occurred in the first 6 days following the earthquake have been mapped by Liao and Lee. (2000), across an area of 10,513 km^2 (Figure 3-14). Landslides were mapped manually through interpretation of 10 m SPOT satellite imagery, acquired before and following the earthquake. The minimum size of mapped landslides mapped is reported as 625 m^2. Supplementary information regarding available fault models and Shakemap PGA uncertainty are provided in Appendix A iii.

3.2.3 2008 Wenchuan earthquake

The M_w = 7.9 Wenchuan earthquake had a focal depth of 12.8 km (Larson et al., 2012), and also resulted from a combined reverse-thrust and strike-slip displacement (Shen et al., 2009). The earthquake affected the Longmen Shan mountains to the west of the Sichuan Basin, in western China. This event is the largest recorded continental thrust earthquake and produced much larger numbers and densities of landslides than the events described above. 73,367 landslides that occurred within the first 8 months following the earthquake have been mapped by Parker (2010) and Whadcoat (2011), across an area of 12,350 km^2. Comparisons with field evidence (Liu-Zeng et al., 2009), fault models (Shen et al., 2009), and SAR analysis (de Michele et al., 2010), and with independent landslide maps compiled by hand from imagery and aerial photographs

(Dai et al., 2011), suggest that the mapped area covers the majority of coseismic slip and represents a significant sample of the main impact zone of the earthquake. Landslides were mapped using a semi-automated classification technique, by processing SPOT-5 images using a combined spectral and topographic algorithm. This technique is prone to issues associated with landslide scar coalescence, where multiple landslides are mapped as a single feature, and fragmentation, where a single landslide is mapped as multiple features. This can result in errors when extracting landslide source areas via the technique described in Section 3.1.7, and when analysing the geometry of individual landslides. In order to minimise these errors, mapped landslides were visually checked against available satellite imagery. Where coalescence and fragmentation could be identified, these errors were manually corrected. This resulted in an increase in the total number of landslides to 74,498 (Figure 3-15). Supplementary information regarding available fault models and Shakemap PGA uncertainty are provided in Appendix A iv.

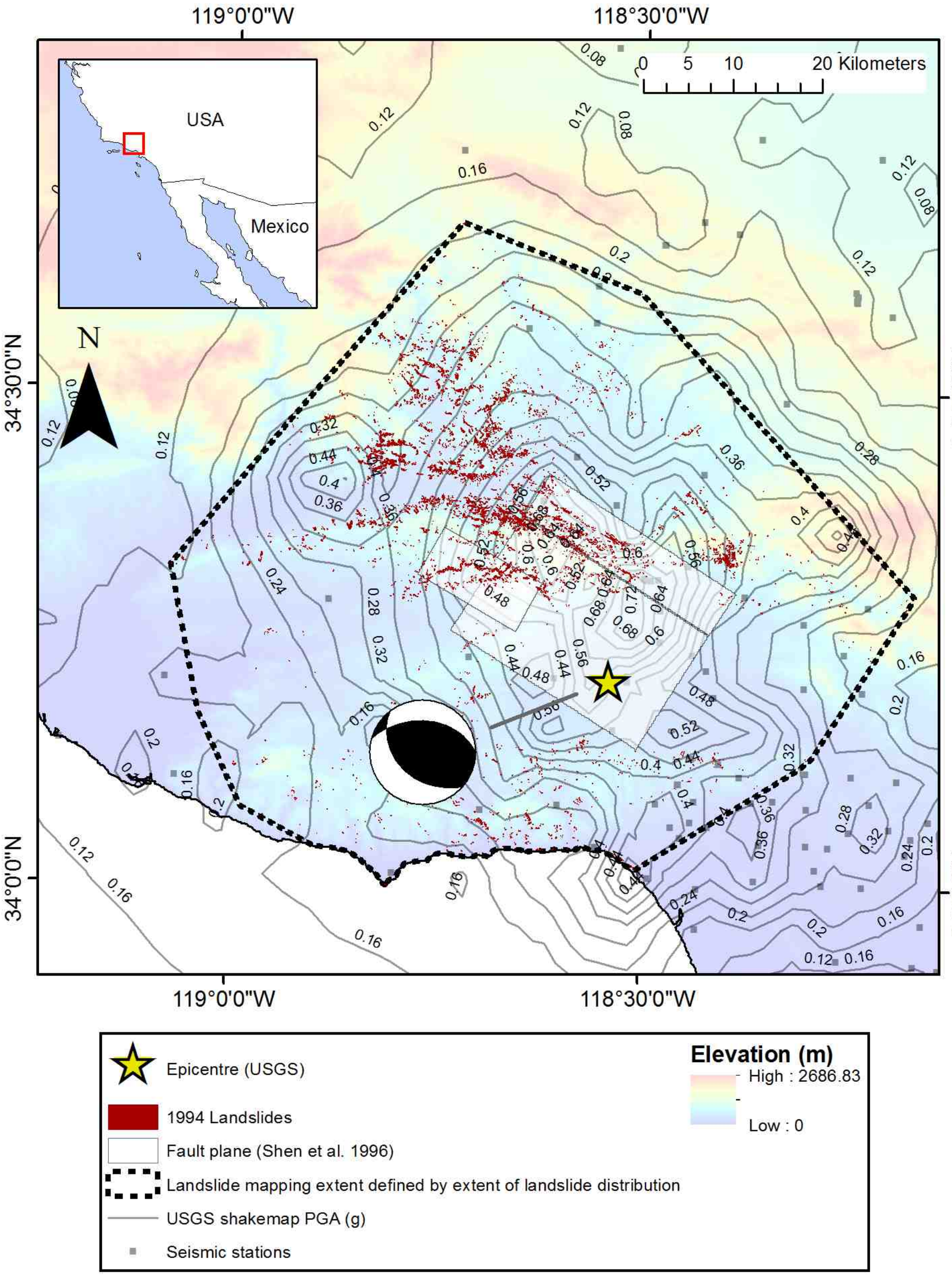

Figure 3-13 Landslide inventory map for the 1994 Northridge earthquake (Harp and Jibson, 1995a), showing the areal extent of landslides, topography (N.A.S.A. Land Processes Distributed Active Archive Center, 2011), earthquake epicentre (Wald et al., 1996, Shen et al., 1996, Hudnut et al., 1996), focal mechanism (Larson et al., 2012), fault plane (Shen et al., 1996) and maximum PGA isoseismals (Allen et al., 2008)

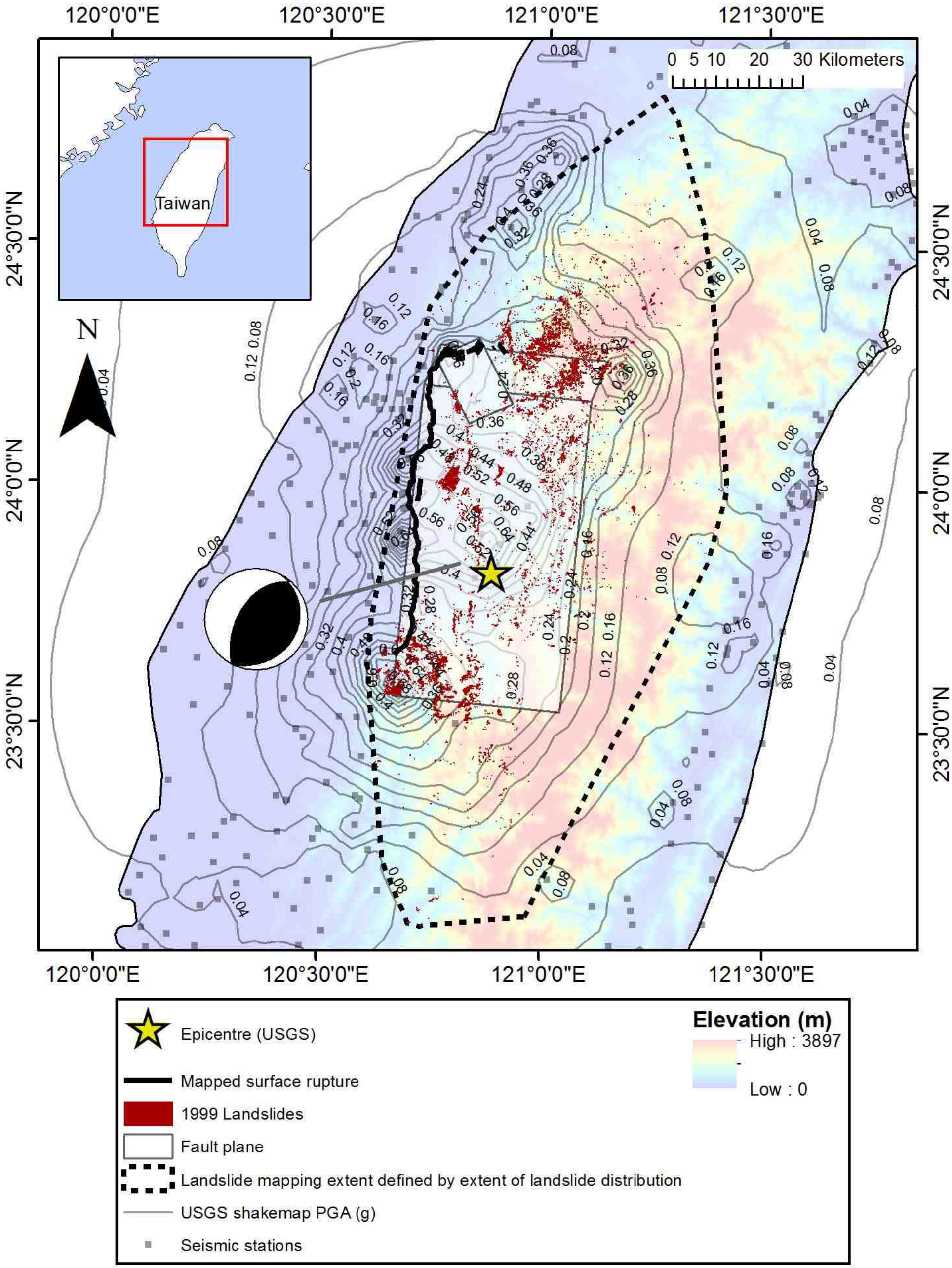

Figure 3-14 Landslide inventory map for the 1999 Chi-Chi earthquake (Liao and Lee., 2000), showing the areal extent of landslides, topography (N.A.S.A. Land Processes Distributed Active Archive Center, 2011), earthquake epicentre (Shin et al., 2000, Shin and Teng, 2001), focal mechanism (Larson et al., 2012), fault plane (Wu et al., 2001) and maximum PGA isoseismals (Allen et al., 2008)

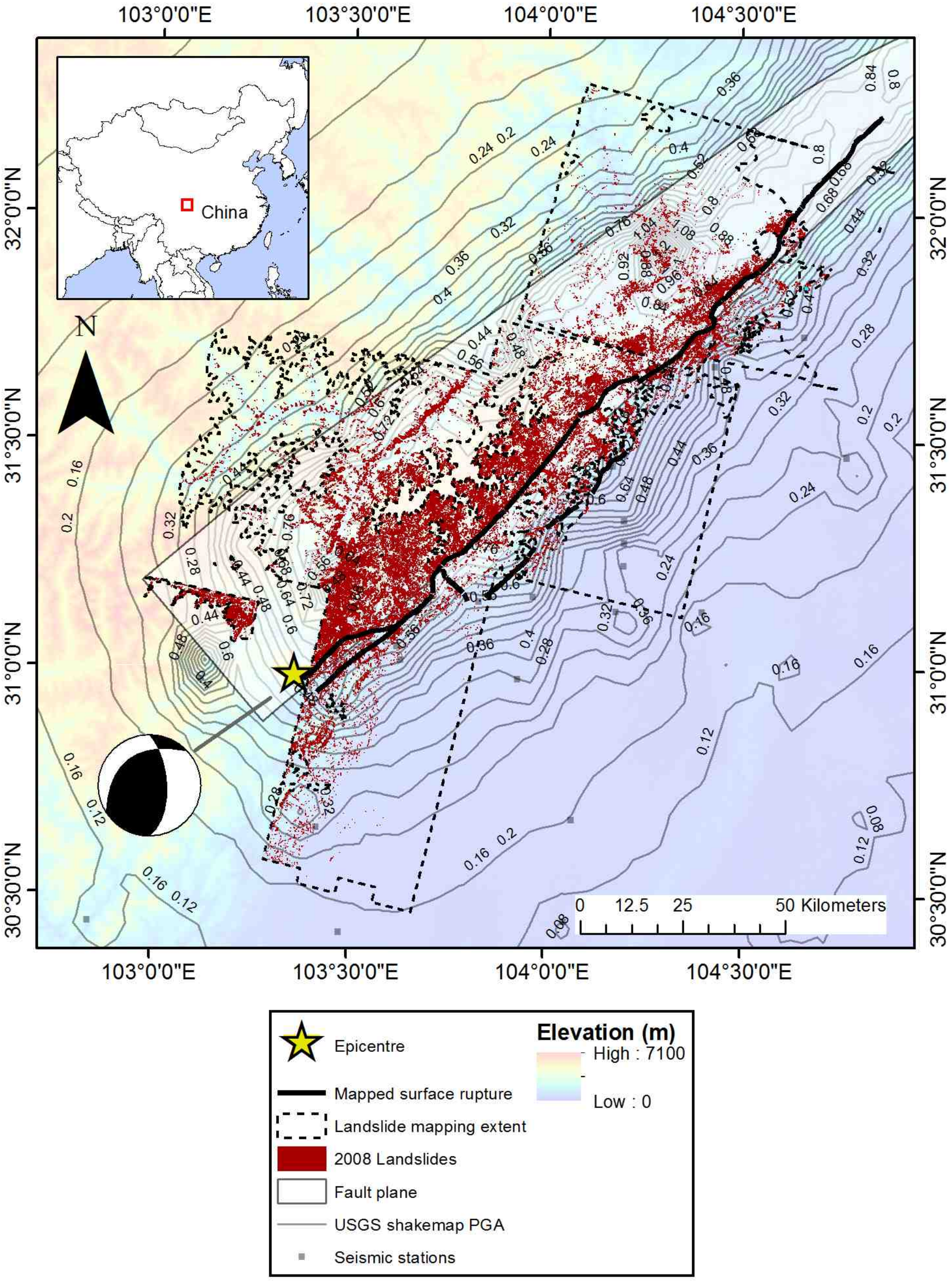

Figure 3-15 Landslide inventory map for the 2008 Wenchuan earthquake (Parker, 2010, Whadcoat, 2011), showing the areal extent of landslides, topography (N.A.S.A. Land Processes Distributed Active Archive Center, 2011), earthquake epicentre , focal mechanism (Larson et al., 2012), fault plane (Shen et al., 2009) and maximum PGA isoseismals (Allen et al., 2008)

3.3 Landslide dataset comparison

Table 3-2 summarises earthquake and landslide distribution characteristics for all five earthquakes. The combination of all five events provides a dataset for investigating landscape characteristics controlling the spatial distribution of landslides, which are common between earthquakes. However, as mapping methodologies and mapping time periods differ, the limitations of the data must be understood and controlled for in analysis where possible.

3.3.1 Landslide inventory completeness

The completeness of landslide inventories can be estimated through analysis of landslide magnitude-frequency distributions (Guzzetti et al., 2002, Malamud et al., 2004b, Malamud et al., 2004a). These are shown in Figure 3-16, which has been generated by calculating frequency-density (frequency divided by bin size) across logarithmically spaced bins of landslide area (after Malamud et al., 2004a, Malamud et al., 2004b). All five datasets display characteristic log-linear relationships between area and frequency for larger landslides, with a rollover away from this trend for smaller landslides (Pelletier et al., 1997, Hovius et al., 1997, Hovius et al., 2000, Dai and Lee, 2001, Guzzetti et al., 2002, Malamud et al., 2004a, Malamud et al., 2004b, Van Den Eeckhaut et al., 2007). Table 3-2 gives the landslide area rollover inflection for each dataset, which has been determined visually from Figure 3-16. For landslide areas larger than these thresholds, the area-frequency relationship can be described using a power-law, given by Equation 2-13 [1]. α values fitted using the algorithm published by Clauset et al. (2009), are also given in Table 3-2. These all fall towards the centre of the range of α values reported globally (Van Den Eeckhaut et al., 2007).

The position of the rollovers is interpreted as indicating the limit of landslide size below which the datasets become incomplete. For both the Buller and Inangahua earthquakes the rollover begins at landslide areas ~11,000 m^2, which is consistent with the fact that these datasets were produced using the same mapping methodology. For

[1] $p(x) = \frac{\alpha-1}{x_{min}}\left(\frac{x}{x_{min}}\right)^{-\alpha}$

the Wenchuan earthquake there is a distinct peak frequency at a landslide area of ~300 m^2. This discrete threshold is an artefact of the automated landslide mapping technique, in which features smaller than 300 m^2 were removed, due to uncertainties in distinguishing landslides at this scale from other ground features. (Parker, 2010). However, the distribution begins to depart from a power-law prior to this at ~10,000 m^2. For the Northridge earthquake a smoother, curved rollover occurs, beginning at ~900 m^2. For the Chi-Chi earthquake dataset the rollover is less distinct still, beginning at ~10,000 m^2, with a peak frequency at landslide areas ~1000 m^2. As the magnitude-frequency distributions are consistent for the Buller and Inangahua earthquakes, no correction is required to ensure the comparability of these datasets to each other. However, in order to use all five inventories in a combined analysis, landslides smaller than 11,000 m^2 must be removed from the datasets, as this is the smallest landslide size for which all datasets appear to be complete.

Table 3-2 Summary details of earthquake-triggered landslide datasets

Earthquake	Date	Country	Location	Earthquake magnitude (M_w)	Focal depth (km)	Number of mapped landslides	Extent of mapped area (km^2)	Period of mapping coverage after earthquake	Landslide magnitude-frequency distribution rollover (landslide area in m^2)	Power-law scaling exponent (α)
Buller	16/06/1929	New Zealand	41.7°S, 172.2°E	7.7	9 ± 3	4,074	4,222	39 years	11,000	2.68
Inangahua	23/05/1968	New Zealand	41.76°S, 171.96°E	7.1	10	1,159	4,288	6.5 years	11,000	2.85
Northridge	17/01/1994	USA	34.21°N, 118.54°W	6.7	18	11,111	3,973	<8 hours	900	2.62
Chi-Chi	21/09/1999	Taiwan	23.85° N, 120.82°E	7.6	8	9,272	10,513	6 days	10,000	2.29
Wenchuan	12/05/2008	China	31.0°N, 103.4°E	7.9	12.8	74,498	12,356	1-8 months	10,000	2.08

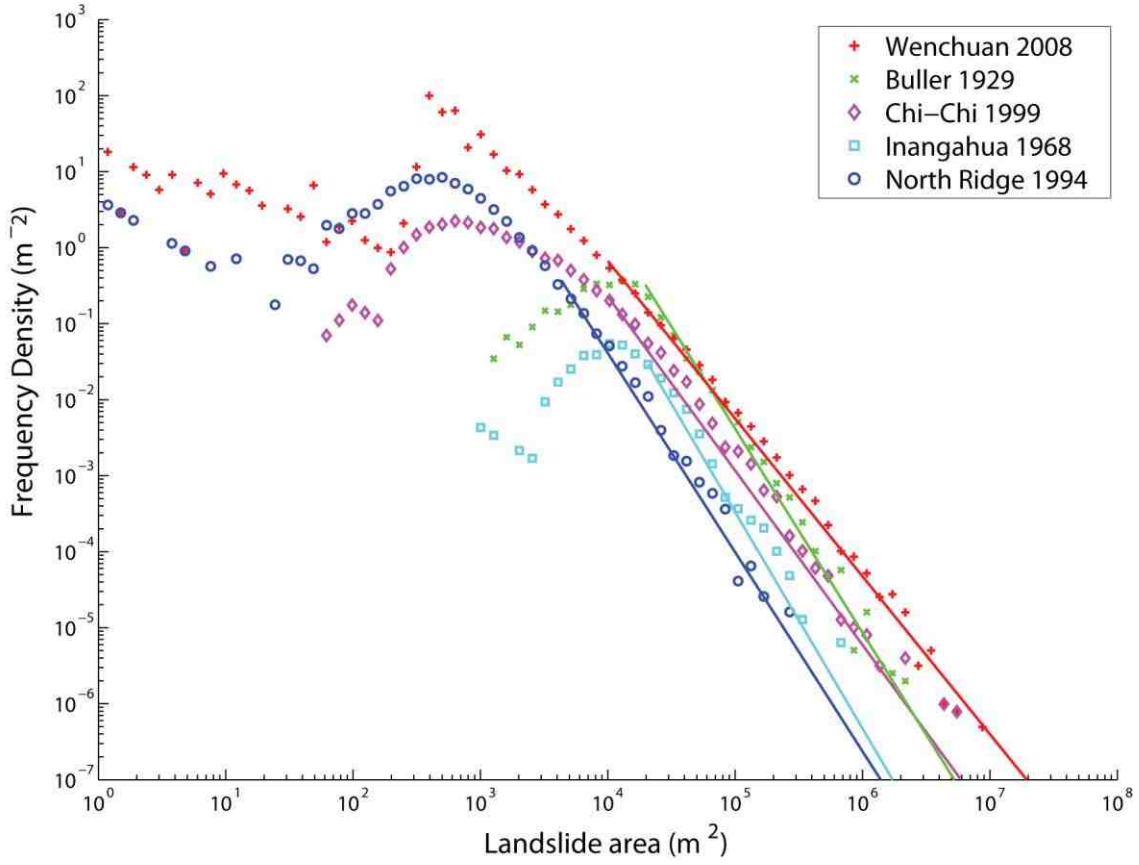

Figure 3-16 Landslide frequency density as a function of landslide area for the Buller earthquauke, Inangahua earthquake, Northridge earthquake, Chi-Chi earthquake and Wenchuan earthquake landslide inventories. Data points represent the frequency-density (frequency divided by bin size calculated across logarithmically-spaced bins, after Malamud et al. (2004a), Malamud et al. (2004b)), while the solid lines show the fitted power-laws (using parameters given in Table 3-2), up to the points of rollover initiation.

3.3.2 Timing of landslide data acquisition

The period between the earthquake and acquisition of imagery for landslide mapping is important to consider, in order to determine the extent to which datasets capture post-seismic landslides, triggered by subsequent aftershocks and rainfall events, in addition to co-seismic landslides. For the Northridge earthquake, the contribution from post-seismic landslides will be minimal, as imagery for mapping was acquired on the morning of the earthquake (within 8 hours of the mainshock). For the Chi-Chi earthquake, landslides triggered by aftershocks and rainfall in the 6 days following the earthquake will also be included in the dataset. As post-seismic landslides following the Chi-Chi earthquake have been associated with subsequent typhoons, and as the first typhoon did not occur until 11 months after the earthquake (Hovius et al., 2011),

contributions from rainfall-triggered landslides in the first 6 days are should be minimal. Due to the lack of studies into the temporal distribution of landslides triggered by aftershocks, the extent to which this affects the dataset cannot currently be determined.

For the Wenchuan, Buller and Inangahua datasets, the data were collected after a longer interval following the earthquakes. As a result these inventories will include larger numbers of post-seismic landslides and therefore overestimate the impact of co-seismic landslides. For the Wenchuan earthquake, data from Whadcoat (2011) show that, for a 1500 km^2 sample area, the total area of landslides mapped 8 months after the earthquake was 142% of the area of landslides mapped 1 month after the earthquake. The Wenchuan inventory is therefore likely to overestimate total landslide areas by about 42%. While multi-temporal mapping of landslides is not available for the Buller and Inangahua earthquakes, the studies reviewed in Chapter 2 suggest that post-seismic landslides may contribute an increase in the total landslide area in the range of 15-76% (Saba et al., 2010, Hovius et al., 2011, Lin et al., 2008b). Observations made by Graham Hancox during several months of fieldwork in 1968-1969 following the Inangahua earthquake suggest that the New Zealand study area is less prone to post-seismic landslides than other regions. Few post-seismic failures were observed, with the exception of minor retrogression of soil and regolith materials around the head scarps of co-seismic landslides (Hancox, 2011), and similar behaviour is also thought to have occurred following the 1929 earthquake (Hancox, 2011). The contribution from post-seismic landslides is therefore likely to be at the lower end of the 15-76% landslide area range. As the spatial distribution of post-seismic landslides generally reflects that of co-seismic landslides (Dadson et al., 2004, Hovius et al., 2011, Lin et al., 2008b, Whadcoat, 2011), the datasets should provide a reasonable representation of the distribution of co-seismic landslides relative to different landscape characteristics, despite contributions from post-seismic landslides.

3.4 Summary

Landslide inventories that provide snapshots of landslide activity following five major earthquakes have been presented. The relative completeness of the datasets and the likely impact of variable timescales of data acquisition have been established. While

the landslide inventories vary in their mapping methodology and temporal coverage, they provide the most accurate available dataset for a combined analysis of landslides triggered by different earthquakes in different regions, in order to develop a generalised understanding of ETL spatial distributions.

Chapter 4 - Spatial models of earthquake-triggered landslide probability

While spatial distributions of ETLs have been studied extensively, a generalised, albeit simplified model, which describes ETL spatial distributions in a manner transferable between different earthquakes and regions is currently lacking. If the spatial and temporal evolution of regional-scale ETL activity is to be studied in more detail, then this knowledge gap must be addressed. This chapter presents an analysis of spatial distributions of ETLs from the datasets presented in Chapter 3, using logistic regression models to investigate the influence of multiple variables influencing hillslope failure probability. The conceptual and statistical basis for the modelling is first established, and challenges associated with the format of available data are addressed. The spatial distributions of landslides triggered by the 1929 Buller and 1968 Inangahua earthquakes are first considered in detail, by testing the influence of proxies for factors shown to influence landslide distributions. The aim of this analysis is twofold: firstly, underlying relationships controlling hillslope failure probability are identified, and the relative importance of different factors is determined in order to identify the most important variables that define system behaviour; secondly, these models provide the basis for testing for the influence of hillslope memory in landslide distributions, the results of which are presented in Chapter 5. The behaviour of the models is tested using all five landslide inventories and generalised hillslope failure probability models are fitted to data from all five events.

4.1 Methodology: Hillslope failure probability modelling

There is a large body of literature exploring controls on the spatial distribution of earthquake-triggered landslides. All these studies first involve processing the data, in order to convert maps of landslide areas or locations into a format suitable for statistical analysis. This commonly involves the calculation of landslide point density or landslide area-density within discrete zones representing regions with similar hillslope stability or seismic forcing characteristics. In calculating landslide density, the response variable for analysis is continuous, indicating the percentage of hillslopes that fail within a given area. This approach is suitable for the majority of studies which consider the influence of variables on landslide occurrence individually using simple statistics designed to model the influence of a single predictor variable (e.g. PGA) on a single

continuous response variable (e.g. landslide density). However, as multiple factors influence the spatial distribution of landslides, bivariate approaches can only provide partially explanations. This problem can be solved by analysing hillslope failure probability using multiple regression models.

4.1.1 Introduction to logistic regression

Logistic regression is a type of regression analysis used for predicting the outcome of a categorical response variable (Cox, 1958, Walker and Duncan, 1967) and is widely used in biomedical research (Hosmer and Lemeshow, 2000) and increasingly in the earth sciences (e.g.: Atkinson et al., 1998, Garcia-Rodriguez et al., 2008, Gorsevski et al., 2006, Perkins, 1997, von Ruette et al., 2011) as a method of modelling probability. In the case of binomial logistic regression the dependent variable (Y) is binary (0 and 1). By convention 1 indicates the occurrence of an event of interest while 0 indicates non-occurrence. Logistic regression is used to estimate the coefficients (b, b_i …) for predicting the probability that $Y = 1$, given the values of one or more predictor variables (x, x_i …), using the logistic, or log-odds function:

Equation 4-1: (Chen et al., 2012a)

$$P(Y = 1) = \frac{1}{1 + e\left(-(b_0 + b_1x_1 + b_2x_2 + b_3x_3 \dots b_nx_n)\right)}$$

The function has an unlimited range for x, while P is restricted to the range 0 to 1. Use of this function in logistic regression prevents predicted probabilities from exceeding 1 or falling below 0. The regression coefficients are estimated by the method of maximum likelihood. Logistic regression carries many of the normal assumption of ordinary least squares regression. These include the following (Chen et al., 2012a: Chapter 3):

- No important variables are omitted from the model
- No extraneous variables are included in the model
- The independent variables are measured without error
- The observations are independent

- The independent variables are not linear combinations of each other

Additionally it is also assumed that conditional probabilities are a logistic function of the independent variables, i.e.: the log-odds of probability is a linear combination of the independent variables. This assumption is best understood by considering the linear form of the model equation:

$$\ln\left(\frac{P(Y=1)}{1-P(Y=1)}\right) = b_0 + b_1x_1 + b_2x_2 + b_3x_3 \ldots b_nx_n$$

Where $\ln\left(\frac{P(Y=1)}{1-P(Y=1)}\right)$ is the log-odds of probability, expressed as a linear function of the independent variables. Note that logistic regression carries no assumptions regarding the distribution of either the response or predictor variables. This means that predictor variables can be continuous or categorical.

Alternatives to logistic regression include the probit model and discriminant analysis. However, these techniques are generally more difficult to implement in analysis and rely on additional assumptions being met (Harrell, 2001). Although probit regression assumes as similar shape to the logistic function, it involves more cumbersome calculations and there is no natural interpretation of its regression parameters (Harrell, 2001). Discriminant analysis assumes that predictor variables are normally distributed and that jointly the predictors have a multivariate normal distribution. As a result the technique cannot be used with categorical predictors. Additionally, even when all assumptions are met, logistic regression is virtually as accurate as the discriminant model (Harrell and Lee, 1985).

Logistic regression has been widely used as a method to model landslide spatial probability (e.g.: Yesilnacar and Topal, 2005, Dai and Lee, 2003, Garcia-Rodriguez et al., 2008, von Ruette et al., 2011). A first challenge in applying logistic regression to modelling landslide probability is in establishing how the principles of probability and probability modelling can be applied to hillslope failure, and along with this how landslide inventory maps should be converted to a binary variable for analysis.

4.1.2 Landslide probability

Probability is the number of times an event occurs divided by the number of times an event could occur, within a given time-frame. When using inventories of landslides triggered by a particular event, the time-frame is the period over which landslides are triggered by that event. For co-seismic landslides this is generally assumed to be the duration period of seismic shaking, however, where landslides have been mapped later after an earthquake this period also includes additional time following the earthquake.

A common approach to analysing landslide spatial probability is to adopt the landslide area-density principle (e.g.: Meunier et al., 2008, Meunier et al., 2007) in which landslide probability is defined as the size of the area covered by landslides divided by the total area of interest. However, the total area covered by landslides is not only the sum of landslide source areas, but also the area of material run-out and deposition, which are the product of different physical mechanisms. In investigating hillslope failure, landslide probability is better defined as the sum of landslide source areas (A_{LS}) divided by the total area of interest (A_t).

Equation 4-2

$$P_{ls}(A) = \frac{\sum A_{LS}}{\sum A_t}$$

Where $P_{ls}(A)$ is the landslide source area probability, which is also:

i. The proportion of the area of interest covered by new landslide source areas following a given earthquake (landslide area density)

ii. The probability that any location in the area of interest undergoes failure during (or shortly following) a given earthquake

For each of the landslide inventory datasets, landslide source areas were therefore separated from the full landslide areas prior to analysis, using the methodology described in Section 3.1.8.

4.1.3 Matrix grid sampling of variables for analysis

In order to model the relationship between $P_{ls}(A)$ and multiple independent variables, the landscape must be divided into discrete areas of equal sizes to provide individual

observations for analysis. These areas must be classified to indicate the presence or absence of landslide source areas (i.e.: whether or not hillslope failure has occurred) and associated with values of each of the predictor variables. This was achieved by dividing the landscape based on the areas of individual pixels at the available DEM grid scale (e.g.: Dai and Lee, 2003, Lee et al., 2008a, Lee et al., 2008b). This approach captures the minimum scale of variability in predictor variables, set by variables derived from the DEM, and other predictor variables with coarser resolutions can be sampled at the DEM resolution. For predictor variables derived directly from the DEM, such as local hillslope gradient or distance and directional variables calculated using Euclidean functions, no resampling is required prior to analysis. Predictor variables at coarser resolution raster or in vector formats, such as polygons from geological mapping, incrementally contoured data such as isoseismals and coarsely gridded precipitation data, were resampled to the DEM grid resolution. Here the majority resampling approach was used, in which DEM pixels are classified by the class representing the majority (>= 50 %) of their plan area (ESRI, 2012). For the response variable, pixels were classified based on whether the majority of their area fell inside (Y=1) or outside (Y=0) of a landslide source zone.

4.2 Landslide probability models for the 1929 Buller and 1968 Inangahua earthquakes

The 10 m pixel resolution of the New Zealand DEM was found to produce very large datasets, which proved computationally impractical. The raw DEM raster was therefore resampled to 30 m resolution using a bilinear convolution, and this grid size was used for analysis. The bilinear method is appropriate for continuous data of this type (ESRI, 2012) and the 30 m resolution is the same as the GDEM elevation data (N.A.S.A. Land Processes Distributed Active Archive Center, 2011) used for analysis in Section 4.3. As 30 m DEM pixels are much smaller than the zones sampled from the predictor variables, edge errors associated with predictor variable resampling are minimal. Landslide source areas smaller than the 900 m^2 pixel area are censored by the resampling and therefore are not included in this analysis. These areas only account for 0.03% and 0.15% of the total landslide source areas for 1929 and 1968 respectively, and therefore removing them has little effect on the spatial pattern of landslides being analysed. Unless otherwise stated, all DEM derivatives used in analysis were calculated

at this resolution. While slope gradients calculated using the 30 m DEM will be lower than those calculated from the 10 m DEM, these errors are spatially consistent for both datasets. The extent of analysis was limited to the coverage overlap area for the 1929 and 1968 landslide datasets, covering 2,804 km^2 and comprising of 3,115,601 individual grid cell observations. This provides a consistent sample area for the two events, allowing the landslide distributions to be analysed side-by-side and for the influence of hillslope memory to be tested.

4.2.1 Response variables

Response variables were generated from landslide source zones extracted from the 1929 and 1968 landslide inventories (Figure 4-1). As the mapping methodology and distribution of mapped landslide areas is consistent for both datasets no correction for mapping resolution was required and all landslide source areas >900 m^2 were included in the analysis.

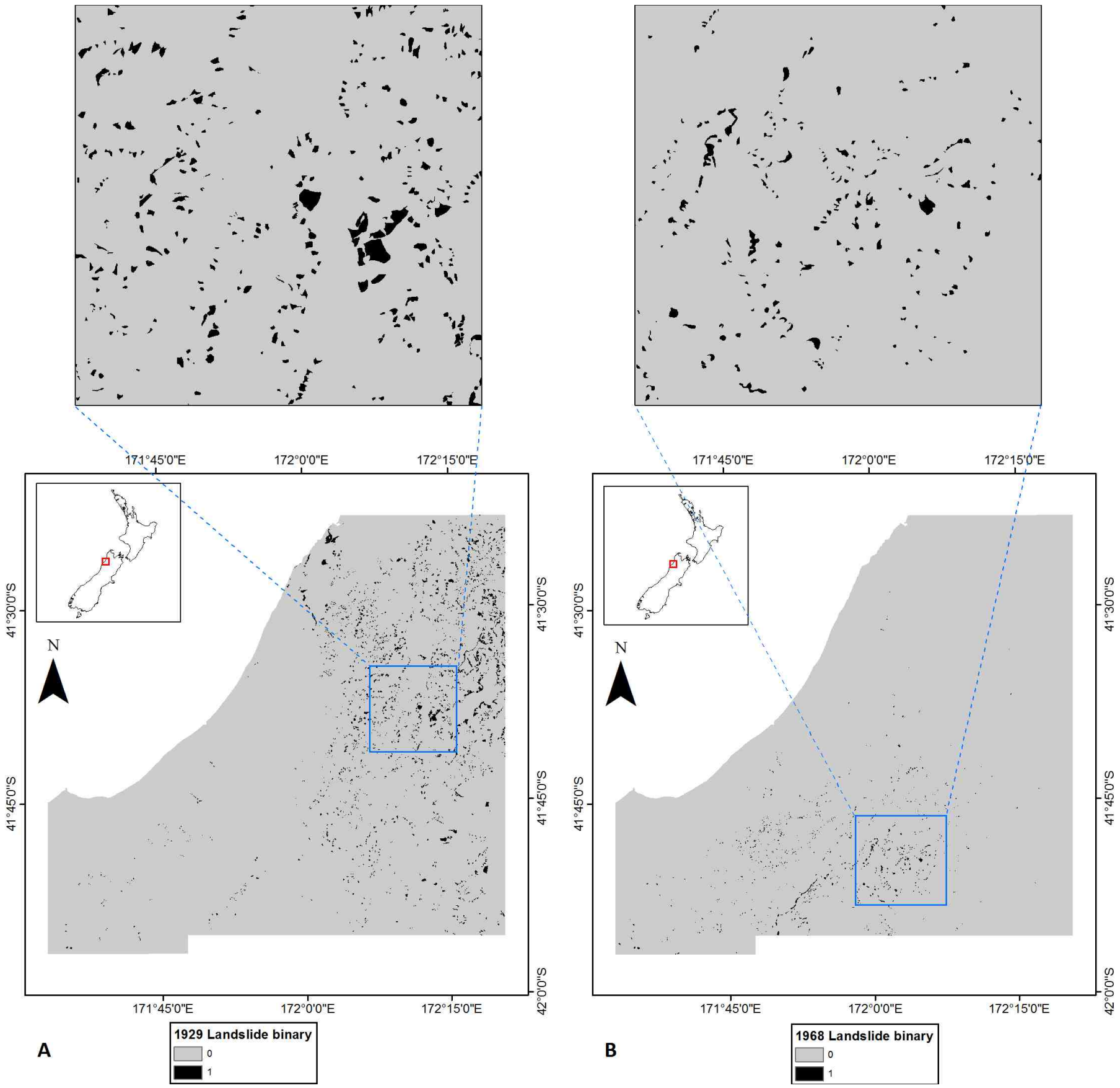

Figure 4-1 Landslide binary grids for the 1929 Buller earthquake (A) and 1968 Inangahua earthquake (B), using landslide source areas extracted using the methodology outlined in Section 3.1.8. The areal extent is limited to the landslide mapping overlap region for the two events. The outset maps provide zoomed-in sections of the data to show the level of spatial detail.

4.2.2 Predictor variables

The following predictor variables represent the hierarchy of factors influencing landslide probability at different spatial scales (Section 2.3.3) and are generated from the thematic datasets presented in Section 3.1. At the regional-scale (across distances of ~5-100 km) the strength of seismic ground motions, is commonly expressed as an inverse function of distance from the seismic source (e.g.: Kramer, 1996, Campbell, 1981, Campbell and Bozorgnia, 2008, Abrahamson et al., 2008), and spatial patterns of landsliding have been associated with this regional signal (Meunier et al., 2007, Meunier et al., 2013). Various different features have been used to constrain the seismic source in strong motion predictive relationships including the following (Kramer, 1996):

- Epicentre
- Hypocentre
- Fault rupture line or surface projection in the case of bind faults
- Fault rupture plane
- High-stress release zone of the fault rupture plane, or surface projection of the high-stress release zone of the fault rupture plane.

The point locations of the epicentre and hypocentre provide a poor characterisation of the seismic source for larger (M_w>7) earthquakes, where rupture may occur across length scales of 10s to 100s of kilometres. Accordingly, fault models were used to constrain the seismic sources for the 1929 and 1968 earthquakes (Stirling et al., 2007, Stirling et al., 2002, Anderson et al., 1994). For both events, distance variables were generated relative to the fault rupture lines and the fault rupture planes. Distances variables were calculated as 2-dimensional Euclidean distances between the centroid of each DEM pixel and the nearest location on these features. Distance variables for the 1929 and 1968 earthquakes are shown in Figure 4-2 and Figure 4-3 respectively.

In order to account for the closer proximity of the fault and enhanced rupture directivity effects in hanging wall areas (e.g.: Abrahamson and Somerville, 1996, Somerville et al., 1997, Abrahamson et al., 2008), hanging wall and foot wall areas were described using a binary indicator variable. For the 1929 earthquake, regions to the east of the fault line were classified as hanging wall areas (Figure 4-4 A). For the

1968 earthquake regions to the northwest of the extended strike of the fault line were classified as hanging wall areas (Figure 4-4 B).

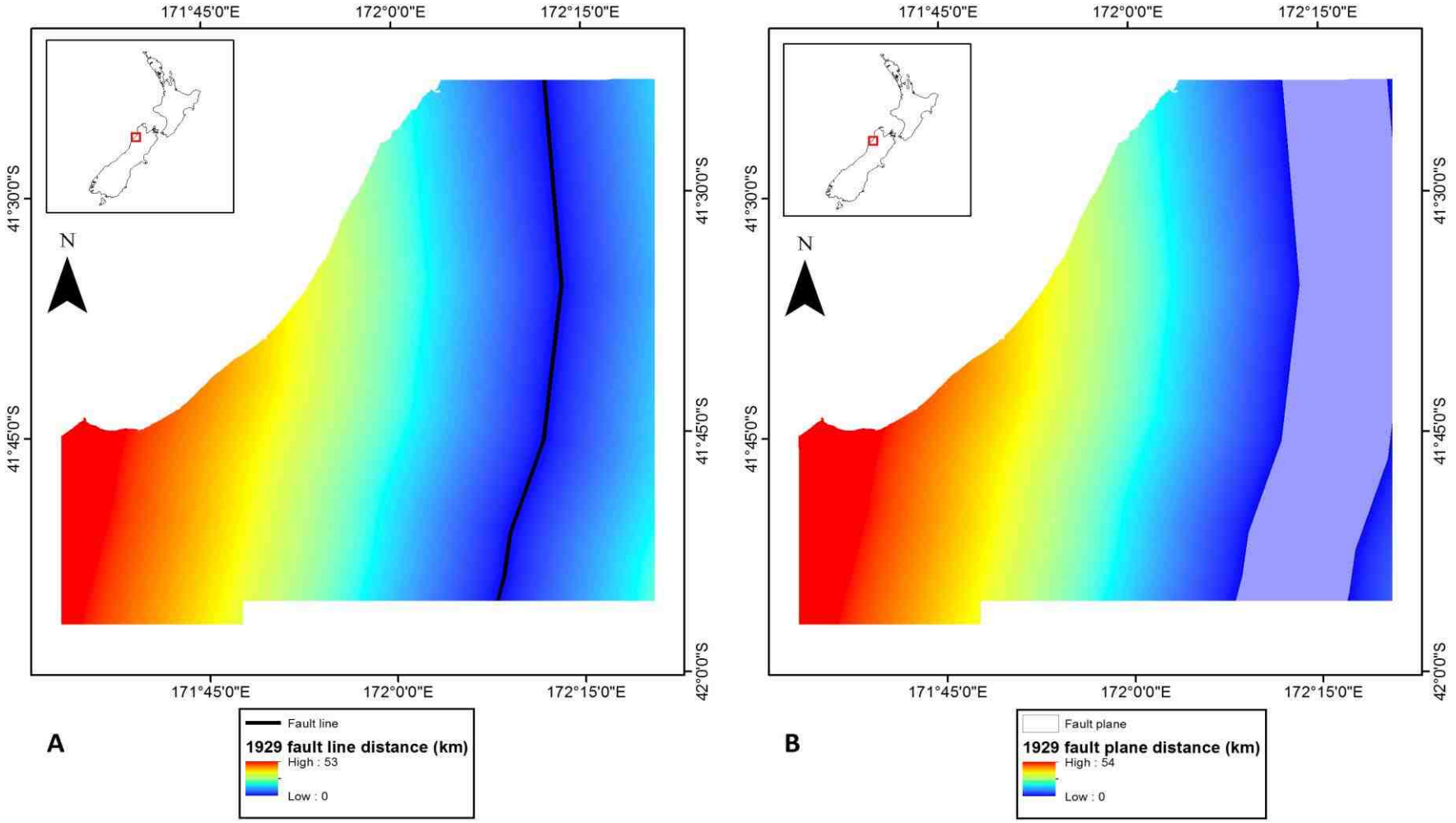

Figure 4-2 Maps of fault line distance (A) and fault plane distance (B) for the 1929 earthquake, using the fault model provided by Stirling et al. (2007), Stirling et al. (2002)

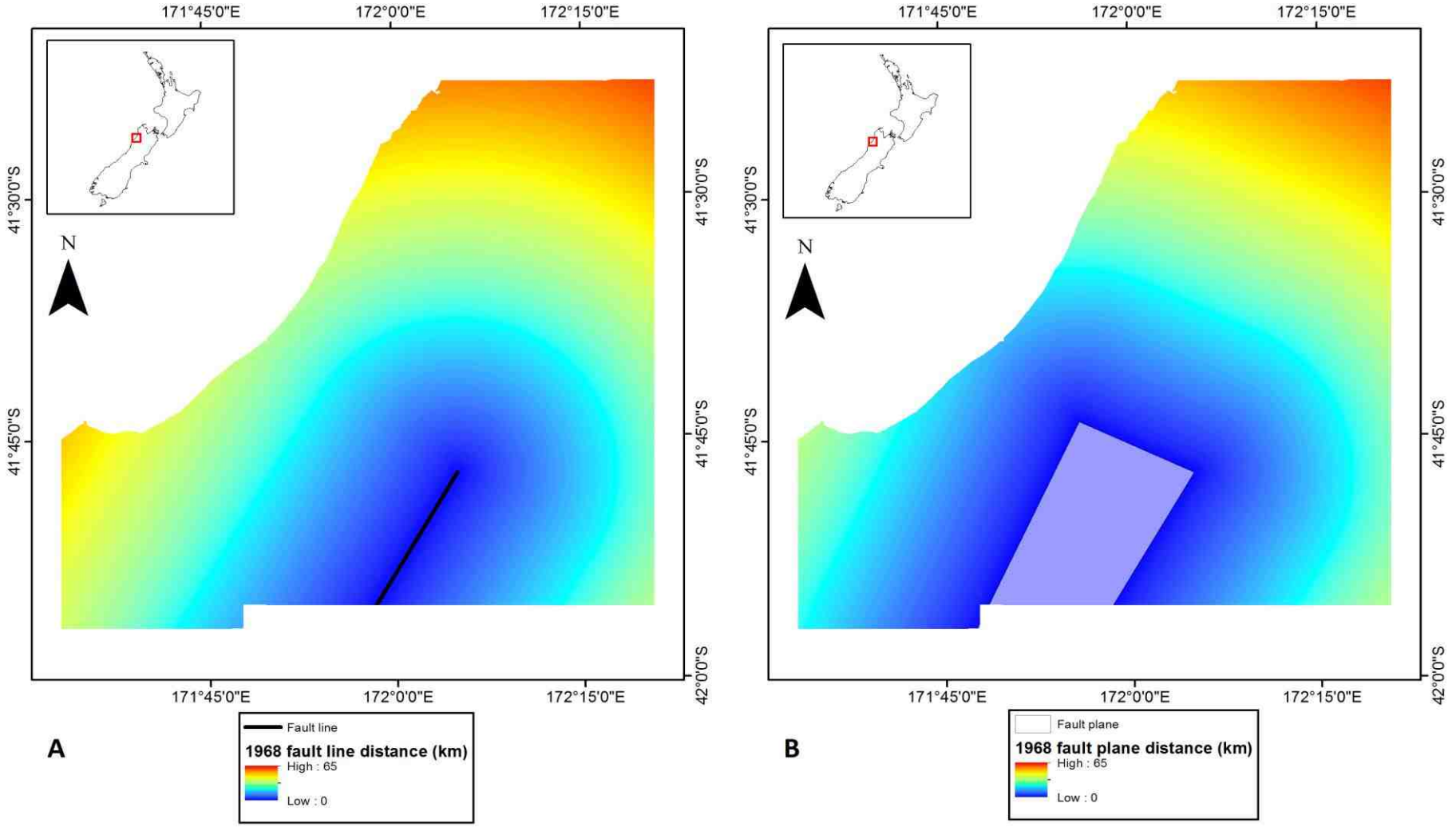

Figure 4-3 Maps of fault line distance (A) and fault plane distance (B) for the 1968 earthquake, using the fault model provided by Anderson et al. (1994)

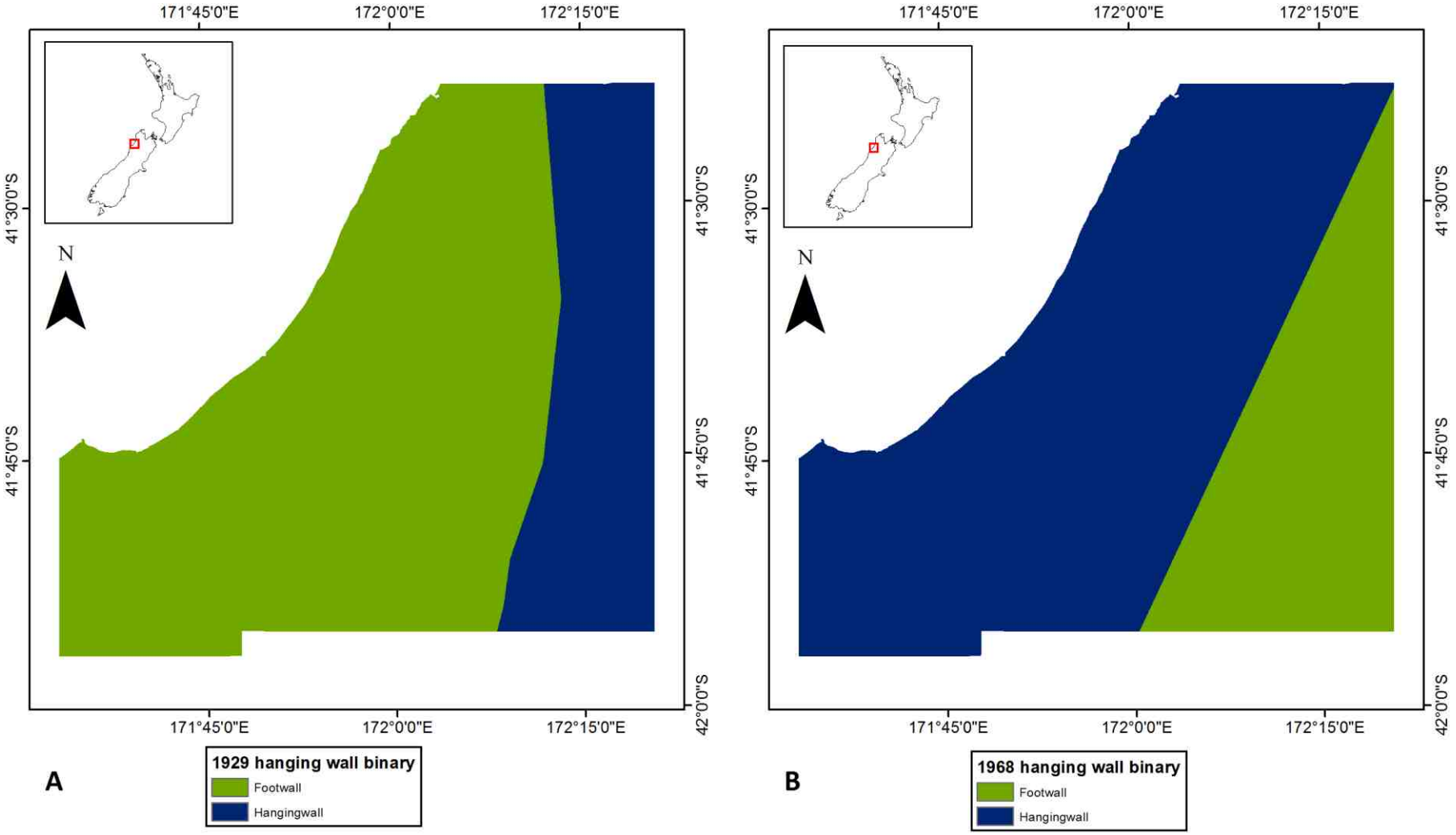

Figure 4-4 Maps of hanging wall binary variables for the 1929 (A) and 1968 (B) earthquakes

4.2.2.1 Normalised distance from stream-channel to ridge crest

The normalised distance from stream-channels to ridge crests is used to evaluate variability in failure probability at different positions on hillslopes, associated with valley-scale patterns of topographic ground motion modification (e.g.: Meunier et al., 2008). In order to produce this variable, the ridge and stream networks in the landscape must be known. The stream network was defined using ArcGIS hydrological analysis on the DEM, corrected for hydrological sinks (ESRI, 2012). The drainage area threshold used to define the stream channels was based on the relationship between local slope and upslope area (Montgomery, 2001, Meunier et al., 2008). On landslide dominated hillslopes, where gravitational processes dominate, local hillslope gradient is dependent on the upslope area producing runoff through a point (Meunier et al., 2008). Through identification of characteristic breaks in the local slope-upslope area scaling relation, this transition from hillslope domain to fluvial domain can be defined. Meunier et al. (2008: 223) defined this threshold as:

- 3.2 ±1 km^2 for the Finisterre Mountains of Papua New Guinea
- 1.1 ±0.3 km^2 for central west Taiwan
- 0.89 ±0.2 km^2 for the Santa Susanna Mountains in California
- 1.5 ±0.5 km^2 for western Southern Alps of New Zealand

For the study area for Buller and Inangahua earthquakes this relationship is shown in Figure 4-5. The humped feature at 0.08 km^2 was found to define a reasonable threshold for definition of the fluvial network. While this threshold is around an order of magnitude lower than values defined by Meunier et al. (2008), stream channels extracted at this level were found to closely reflect the limits of the fluvial network on the ground and in aerial photographs. Note that applying this uniform threshold across the landscape does not account for variability in slope lengths, which is a likely source of error (Meunier et al., 2008).

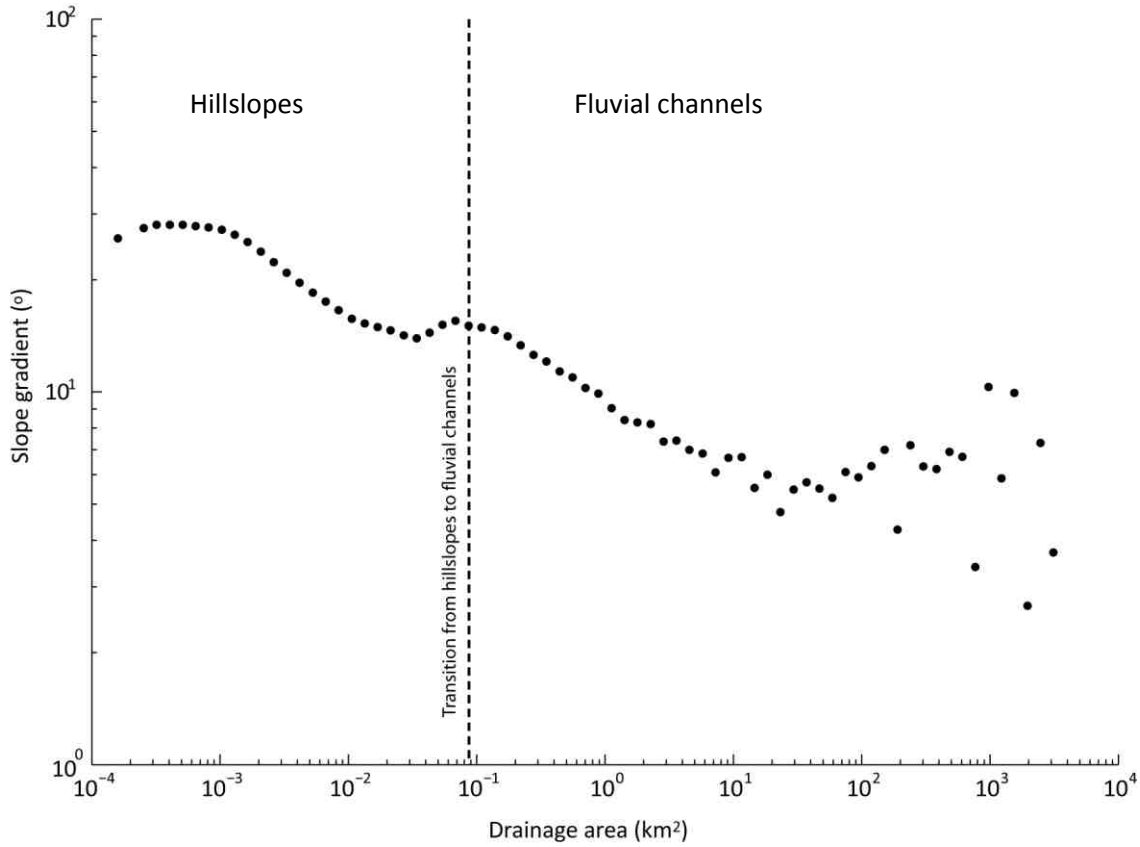

Figure 4-5 Plot of local hillslope gradient against upslope area for the study region. Filled circles show the mean gradient measured in the direction of steepest descent within logarithmically spaced bins of upslope area. The humped feature is interpreted as indicating a break in the scaling relationship, and transition from hillslopes to fluvial channels.

Definition of topographic ridgelines is more challenging than extraction of the fluvial network, primarily due to the lack of automated techniques for incorporating this into GIS software. To overcome this, ridgelines were defined as drainage divides lying on upwardly convex ground. To delineate these features across the whole DEM, all individual drainage basins were first generated by defining pour points immediately upstream of every confluence in the stream network. Then local total curvature (the second derivative of elevation) was calculated for all cells in the DEM. Ridgelines were generated by extracting all drainage divides that crossed upwardly convex cells.

Horizontal distances from streams (d_{st}) and ridges (d_r) were calculated as two-dimensional Euclidean distances from the centroid of each DEM pixel. The normalised distance from ridge to stream (NDS) was then calculated using the method of Meunier et al. (2008: 224):

Equation 4-3:

$$NDS = \frac{d_{st}}{d_{st} + d_r}$$

Where NDS varies from 0 for cells located in the stream network increasing to 1 for cells located on the ridgeline. A sample of NDS for the study region is shown in Figure 4-6. While fill correction effects in low lying basin areas have resulted in some errors in the ridge-stream network, these represent regions with low levels of landslide occurrence across a small proportion of the study area and therefore have little influence on the fitted models.

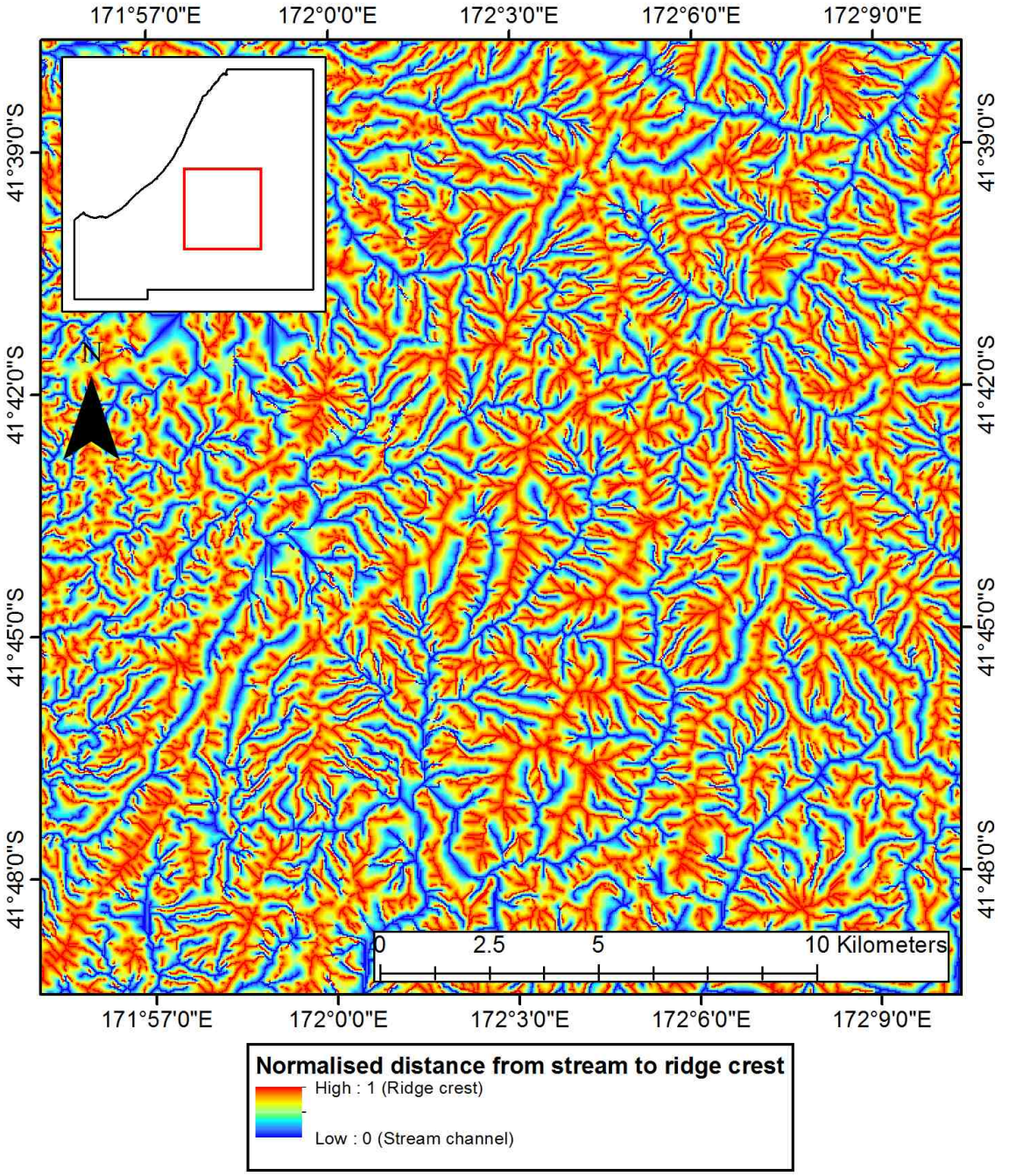

Figure 4-6 Map of normal distance from stream to ridge crest variable, used to characterise valley-scale patterns of topographic amplification and damping of seismic waves. Inset shows the location within landslide mapping overlap region

4.2.2.2 Hillslope orientation with respect to the seismic source

The direction hillslopes face with respect to the seismic source has also been associated with valley-scale patterns of topographic ground motion modification (Meunier et al., 2008). This was calculated in the horizontal plane with respect to the closest points on the fault lines for each earthquake. First, local hillslope aspect (As) was calculated for all cells. Next, for each cell the direction to the seismic source (Dir) was calculated as the Euclidean direction from the closest point on the fault line to the

centre of each cell. Then, orientation with respect to the seismic source, (IA) was calculated as:

Equation 4-4

$$IA = \begin{cases} \sqrt{\left(\left(\sqrt{(Dir - As)^2}\right) - 360\right)^2}, \sqrt{(Dir - As)^2} > 180 \\ \sqrt{(Dir - As)^2}, \sqrt{(Dir - As)^2} \leq 180 \end{cases}$$

Where IA varies from 0 indicating that the hillslope aspect is oriented directly away from the seismic source, to 180 indicating the hillslope aspect is oriented directly towards the seismic source. Samples of these variables for the 1929 and 1968 earthquakes are shown in Figure 4-7.

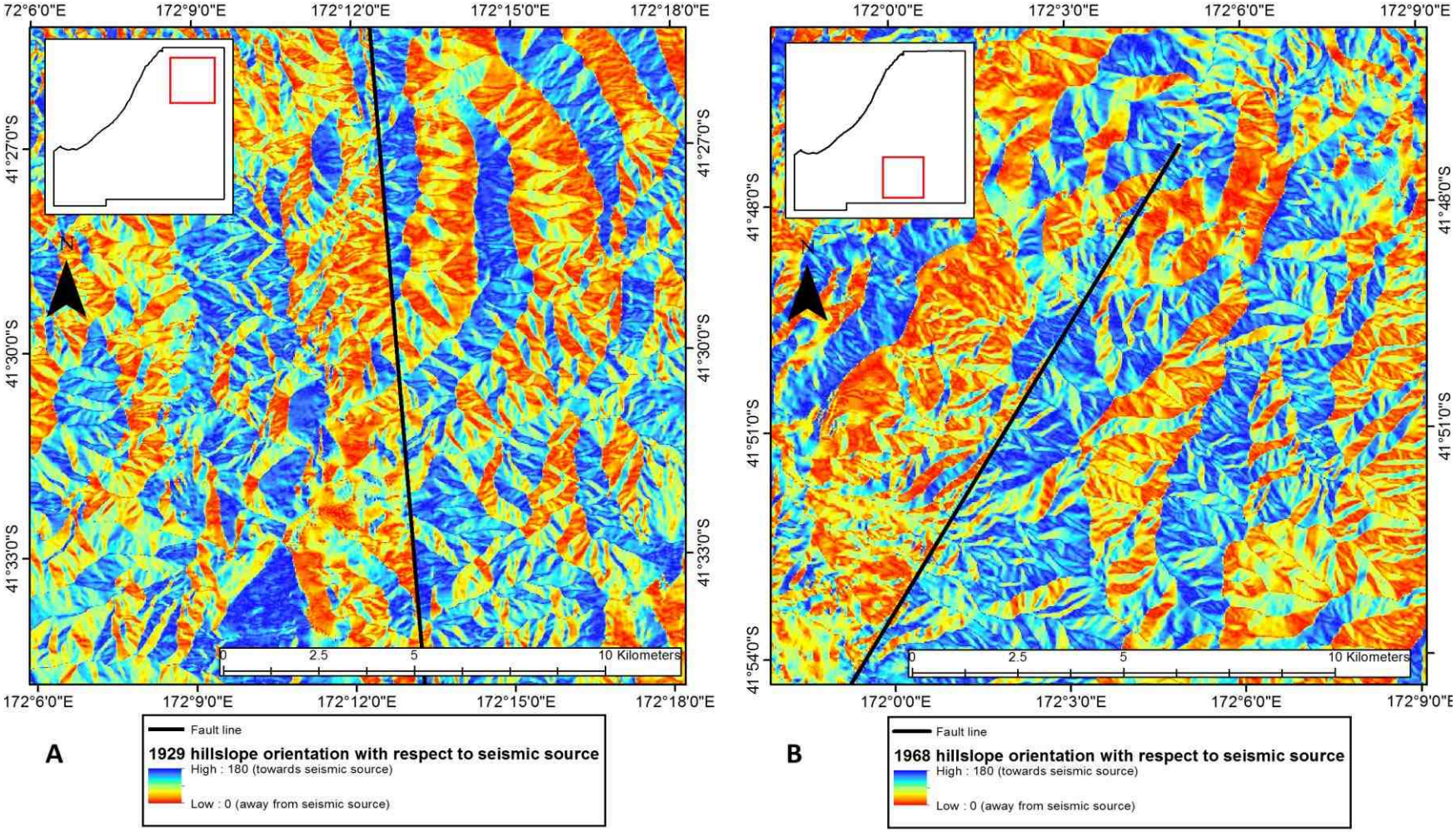

Figure 4-7 Maps of hillslope orientation with respect to the 1929 (A) and 1968 (B) seismic sources (fault lines). Inset maps show the location within the 1929 and 1968 landslide mapping overlap area.

4.2.2.3 Local hillslope gradient

Local hillslope gradient is closely related to the distribution of normal and shear stresses, which define the stability of hillslopes (Section 2.1.3). Local hillslope gradient in the direction of steepest descent (SL) was calculated for each analysis cell (Figure 4-8)

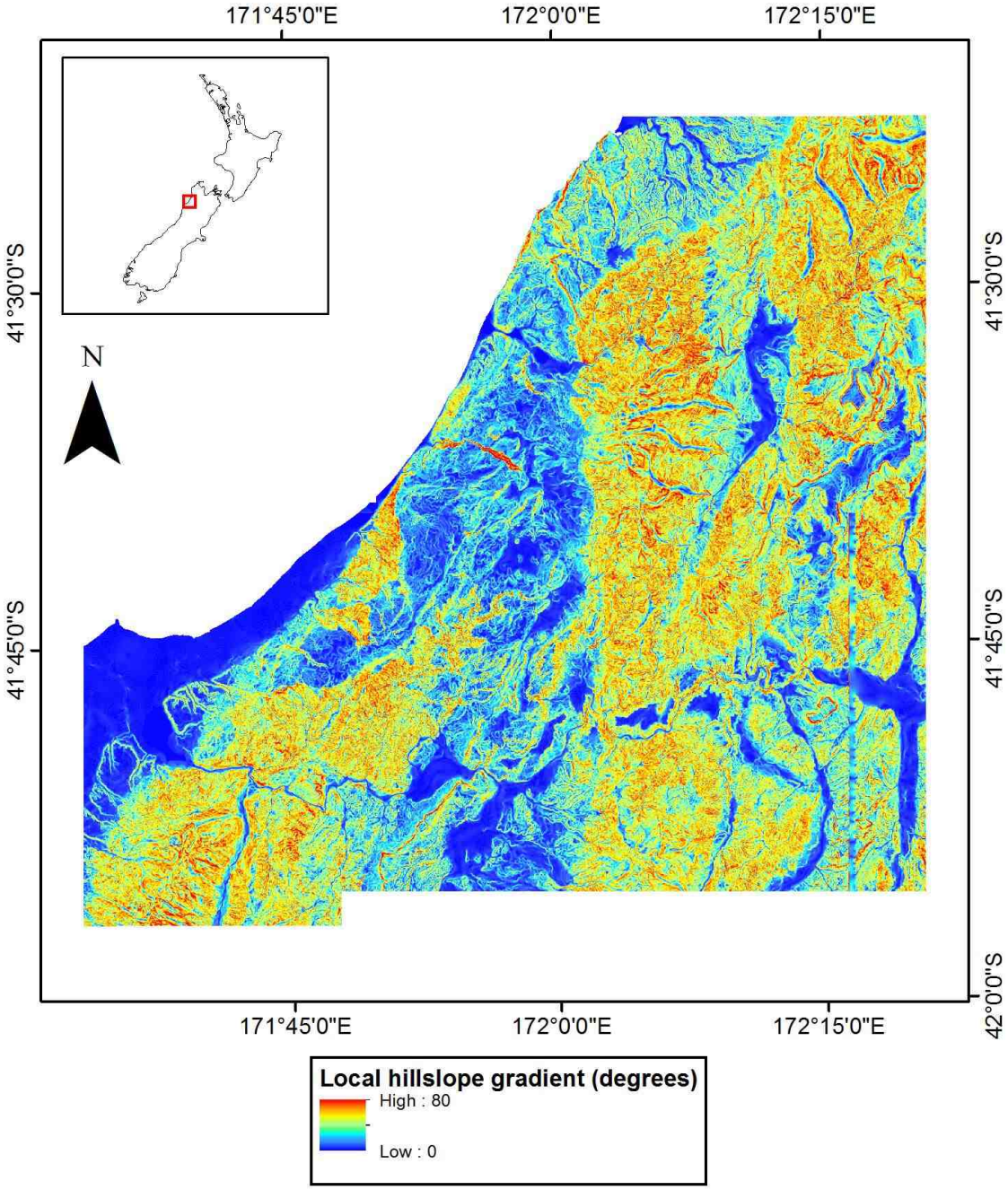

Figure 4-8 Map of local hillslope gradient variable. Inset map show the location within the 1929 and 1968 landslide mapping overlap area.

4.2.2.4 Local relief

Although slope stability at individual locations in the landscape is dependent on the local gradient and therefore shear stress, stability may also be dependent on the local relief. Gravitationally-induced shear stresses increase with the local height of hillslopes and rock mass strength decreases when considered at increasing spatial scales due to the net influences of spatially distributed discontinuities (Bieniawski and Vanheerden, 1975, Schmidt and Montgomery, 1995). If this is the case, failure is more likely to occur

where steep gradients and high shear stresses are sustained over larger scales. In order to provide an index of relief to account for this effect, two variables were generated. First, each individual drainage basin was delineated as outlined in Section 4.2.2.1. Then the range and standard deviation of elevation were calculated for each individual drainage basin. Grid cells were then assigned these values for the drainage basin within which they were located. Maps of drainage based elevation range (ER) and standard deviation (ES) are shown in Figure 4-9 A and B, respectively.

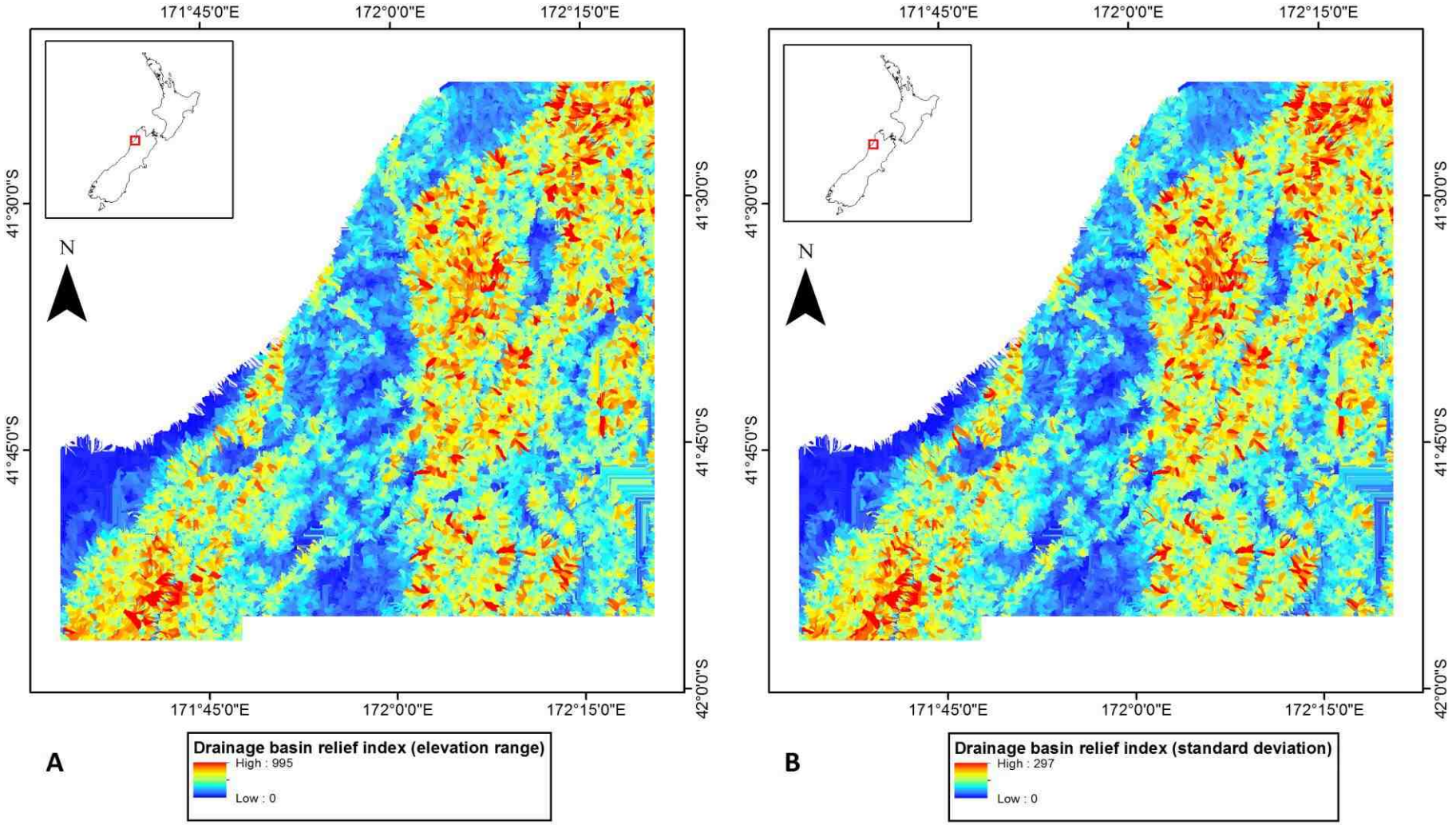

Figure 4-9 Maps of relief variables: A) Drainage basin elevation range (ER), B) Drainage basin elevation standard deviation (ES)

4.2.2.5 Regional geology

Different rock types display varying levels of susceptibility to earthquake-triggered landsliding, which have been analysed by comparing patterns of landsliding in different mapped geological units (Parise and Jibson, 2000, Khazai and Sitar, 2004, Ohlmacher and Davis, 2003). Geological maps provide a classification of materials according to their age and the structural unit within which they occur, rather than providing a direct indicator of variations in material properties. This is the case for the tectonostratigraphic units by which the geology of the study area is classified (Rattenbury et al., 1998, Nathan et al., 2002, Rattenbury et al., 2006). However, as these units provide an indication of variations in lithology and the degree of material consolidation, they can be used as a proxy for first-order variation in hillslope material properties. Therefore, cells were classified by geological units from the QMAP dataset to provide a variable for analysis (Figure 4-10A). The amalgamation of units is somewhat arbitrary, as each contains a wide range of different lithologies and materials with specific geotechnical characteristics. However, in the absence of spatially distributed data on material properties, this is currently the only practical approach for accounting for material variations in analysis of landslide distributions.

4.2.2.6 Orientation of dominant structures

The orientation of dominant structures in hillslope materials, such as joints, lithological boundaries and bedding cleavages, each exhibit a control on the stability of rock masses (Hoek et al., 2002, Selby, 2005, Moore et al., 2009). Data on structural orientations is not usually available at the regional scale. The QMAP dataset contains a high density of point recordings of azimuth and inclination attributes describing rock defect, fabric and strata orientation (Rattenbury et al., 2006, Nathan et al., 2002, Rattenbury et al., 1998). These data were processed in combination with topographic data to infer the regional pattern of dominant structural orientation relative to hillslopes. To carry out this analysis, the terrain was first separated into individual geological units, as the distribution of dominant structures for each unit is independent. In order to interpolate the point structural measurements to estimate the regional structural pattern, Theissen polygons were generated using the point locations of structural measurements for each individual unit, with each polygon area assigned the structural azimuth and dip of its source point. Theissen polygon sets for

each individual unit were then merged to create a complete distributed map of structural domains (Figure 4-10 A). In order to identify regions with out-of-slope dipping, the azimuth (Az) and dip (Dip) of geological structures were then compared with the local aspect (As) and gradient (SL) of the surface topography. For each cell, values of azimuth and dip were assigned from the interpolated Theissen polygon areas. First, the difference between geological structure azimuth and hillslope aspect (Or_{dif}) was calculated using:

Equation 4-5

$$Or_{dif} = \begin{cases} \sqrt{\left(\left(\sqrt{(Az-As)^2}\right)-360\right)^2}, \sqrt{(Az-As)^2} > 180 \\ \sqrt{(Az-As)^2}, \sqrt{(Az-As)^2} \leq 180 \end{cases}$$

Where $Or_{dif} = 0$ indicates hillslope aspect and structural azimuth are the same and $Or_{dif} = 180$ indicates that hillslope aspect and structural azimuth are opposite. Next, the difference between geological structure dip and hillslope gradient (Dip_{dif}) was calculated using:

Equation 4-6

$$Dip_{dif} = SL - Dip$$

Finally, a binary variable was generated to indicate grid cells containing dip slopes (DS), defined where azimuth was within ± 30^o of aspect, and hillslope gradient was steeper than the geological dip angle (Figure 4-10B).

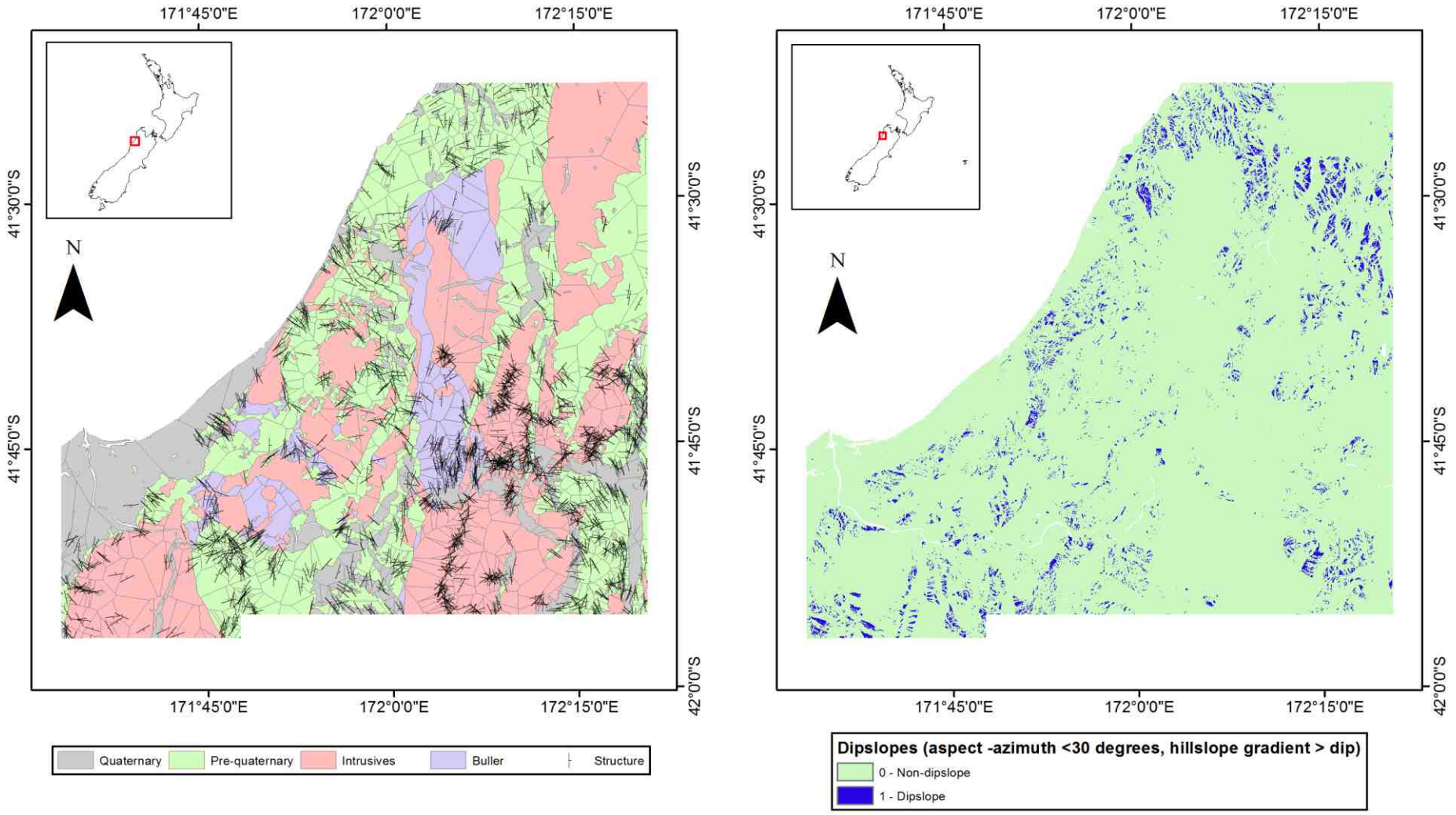

Figure 4-10 Maps of structural domains within geological units (A) and dip slope binary variable (B)

4.2.2.7 Distance from mapped faults

Hillslope material strength is controlled in part by strain localisation and associated weakening (Petley and Allison, 1997, Hoek, 2000). This same process also occurs at the orogen-scale to create a characteristic damage structure around individual fault zones (e.g.: Mooney et al., 2007, Lockner et al., 2009). Such structure results in geomorphically relevant strength variations over many orders of magnitude normal to the faults, which has been associated with the maximum height and gradient of hillslopes that the rock can support (Grant-Taylor, 1964) and the high order topography of actively deforming orogens (Koons et al., 2012). Existing tectonic strain data for the region is of insufficient detail to resolve strain localisation along faults (Beavan and Haines, 2001, Beavan, 2011). Detailed fault mapping has been carried out in the region and compiled for the New Zealand active fault database (GNS Science, 2011a). In order to estimate the regional pattern of strain dependent material variations, a variable of 2-dimensional Euclidean distance from all mapped faults was generated (FDA). This variable is shown in Figure 4-11.

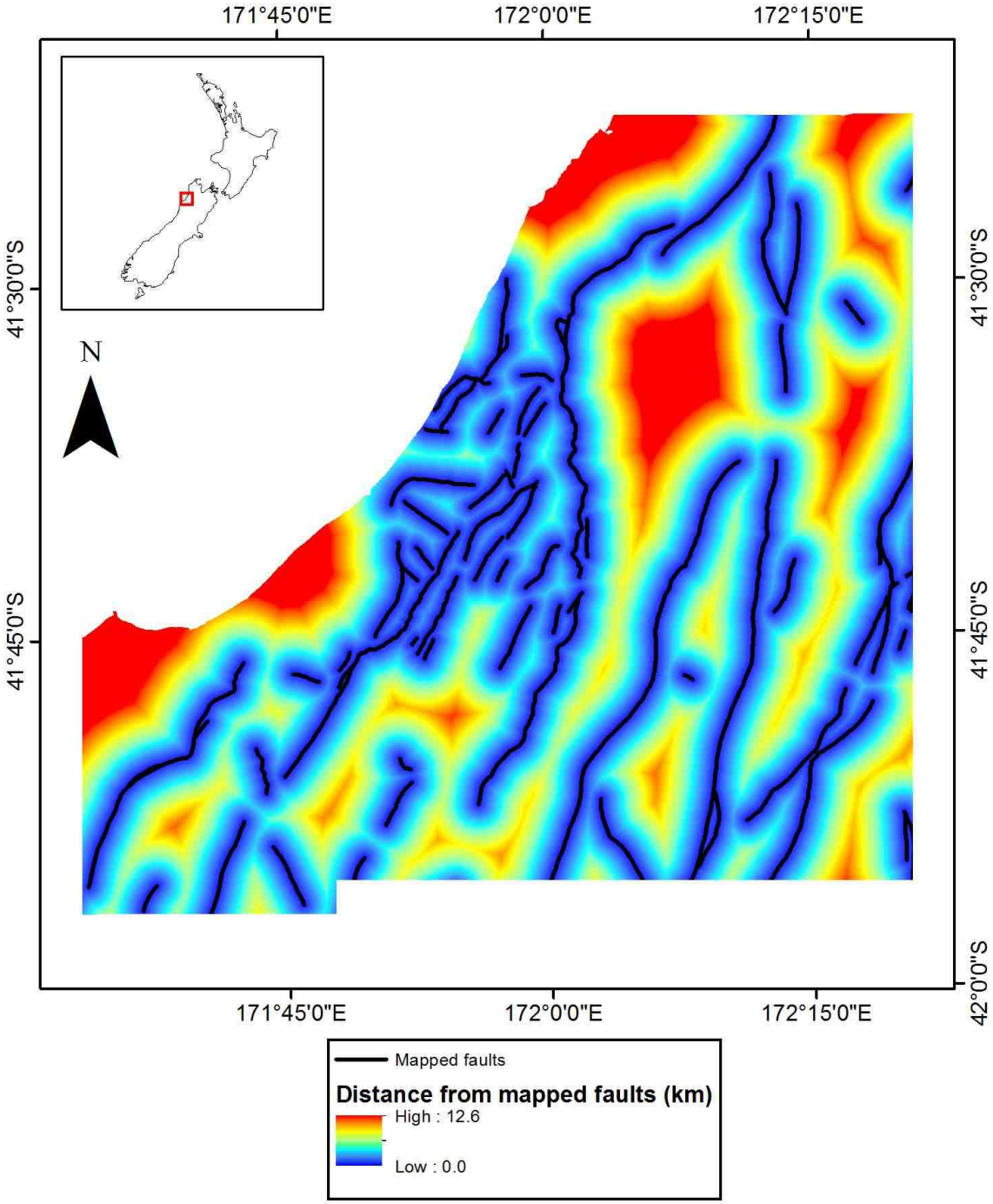

Figure 4-11 Map of distance from mapped faults in the New Zealand active fault database, used to estimate the regional pattern of strain dependent material variations

4.2.2.8 Solar insolation

In order to account for variable insolation, which influences in available energy to drive the physical breakdown of expose bedrock, the annual solar radiation for each DEM pixel was estimated using the ArcGIS Area Solar Radiation tool, based on a uniform sky diffuse radiation model (ESRI, 2012). The map of solar radiation (SR) is shown in Figure 4-12.

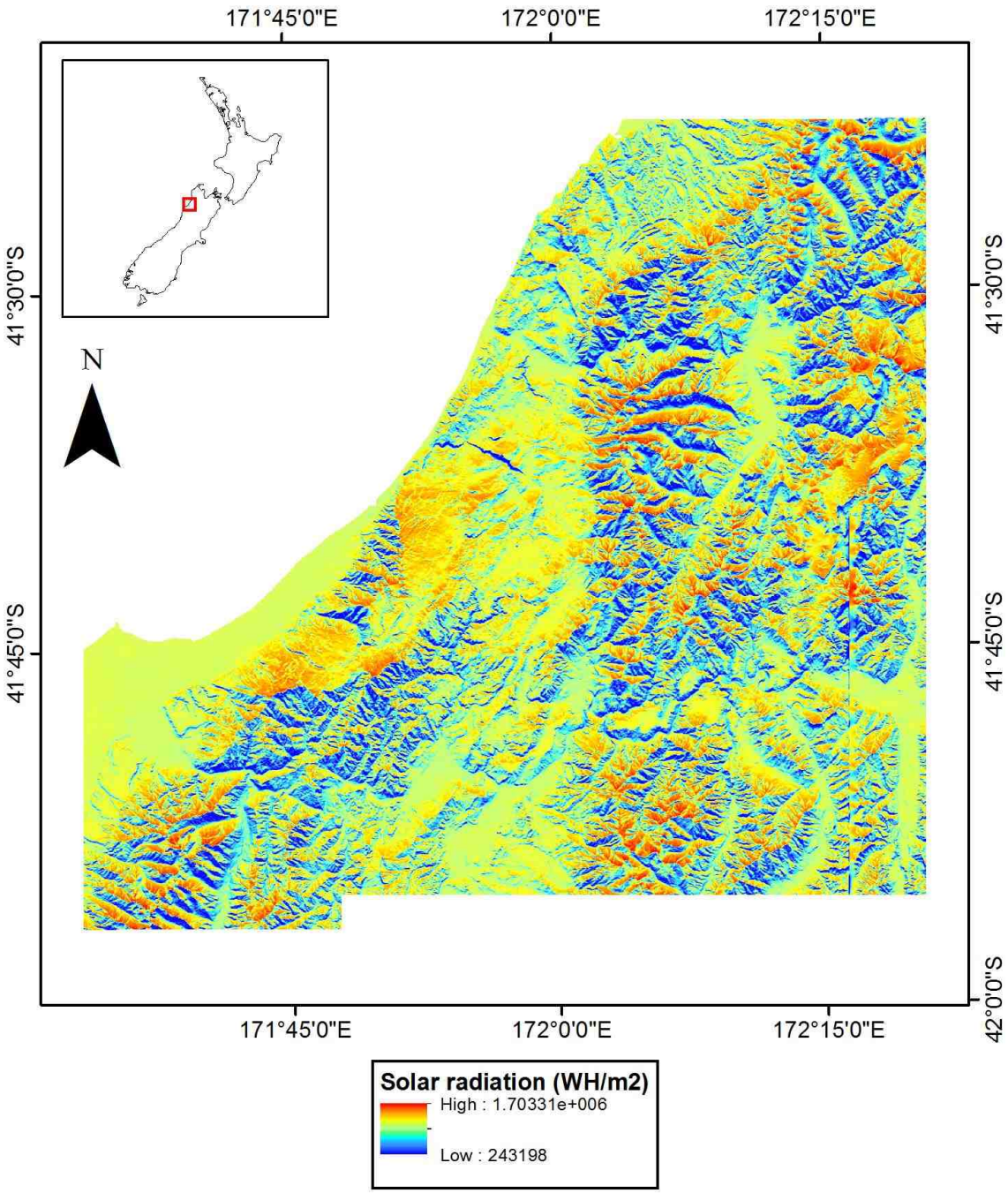

Figure 4-12 Map of annual solar radiation variable, produced using a uniform sky diffuse radiation model.

4.2.2.9 Precipitation

Precipitation conditions affect hillslope stability through their influence on pore water pressures, which reduce effective stress levels (Iverson, 2000). In order to account for spatial variability in precipitation, data from Hijmans et al. (2005) was used to estimate antecedent precipitation totals for each grid cell, for the 3 months and 6 months prior to each earthquake (Figure 4-13 and Figure 4-14). Note that these variables are based on mean interpolated values for the period 1950-2000 and are therefore intended to reflect relative spatial variations rather than absolute values for the years of the earthquakes.

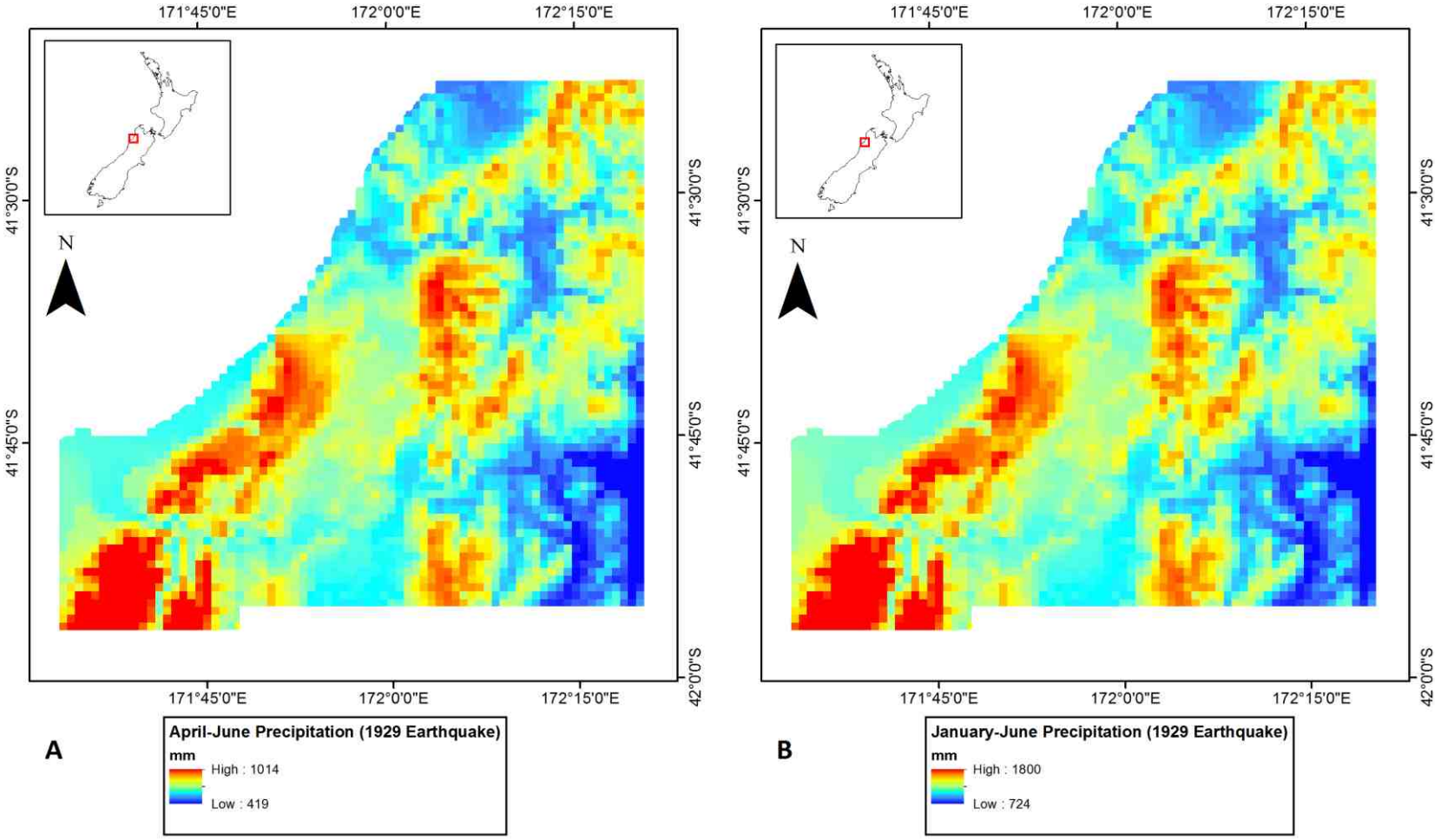

Figure 4-13 Maps of gridded precipitation variables for the 1929 Buller earthquake. A) Mean gridded precipitation total for the months April to June, for the period 1950-2000, B) Mean 900 m gridded precipitation total for the months January to June, for the period 1950-2000. Variables reflect spatial variability in antecedent precipitation prior to the 1929 earthquake. (Data from Hijmans et al., 2005).

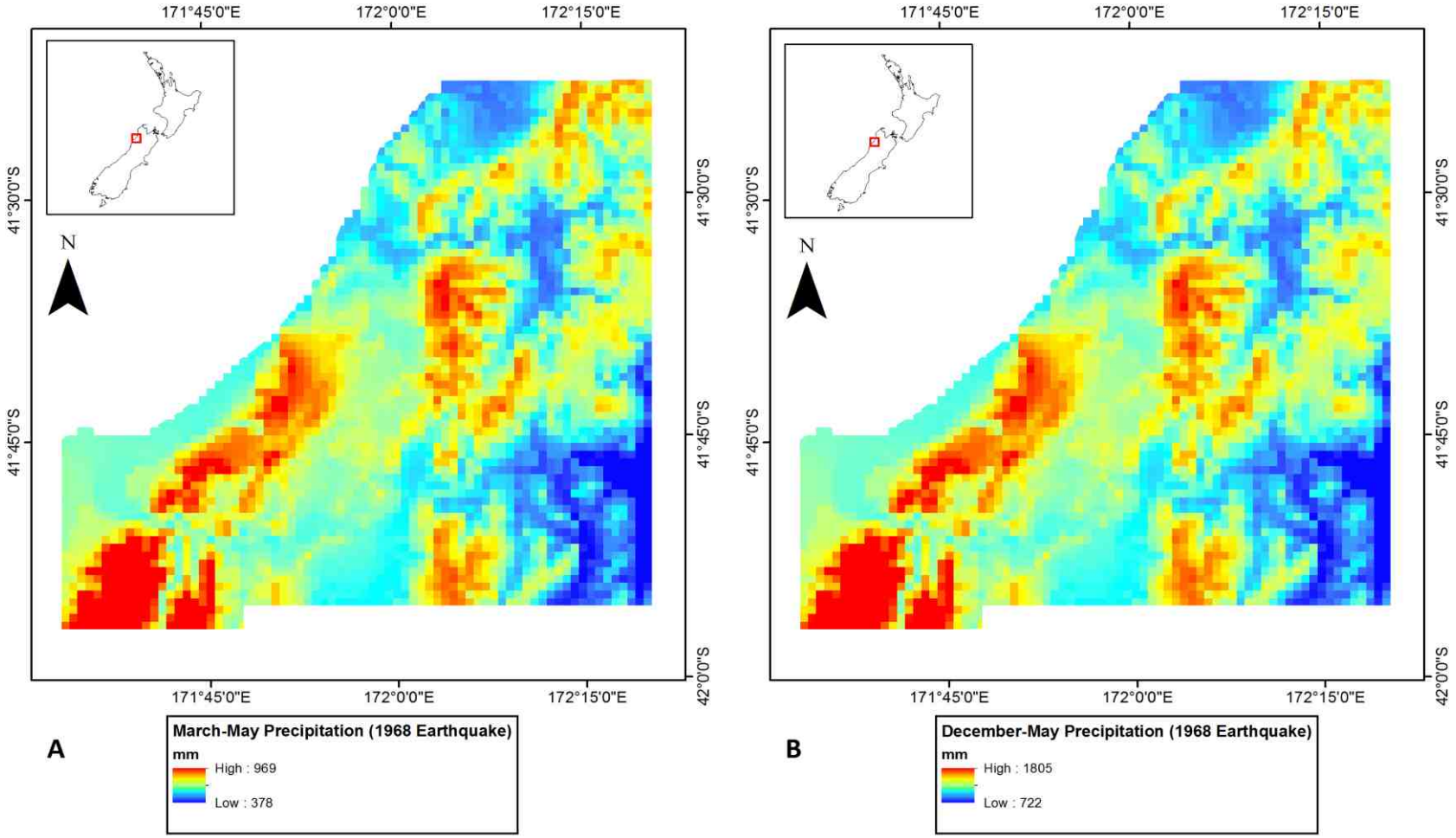

Figure 4-14 Maps of gridded precipitation variables for the 1968 Inangahua earthquake. Maps of A) Mean gridded precipitation total for the months March to May, for the period 1950-2000, B) Mean 900 m gridded precipitation total for the months December to May, for the period 1950-2000. Variables reflect spatial variability in antecedent precipitation prior to the 1968 earthquake. (Data from Hijmans et al., 2005).

4.2.3 Variables summary

Table 4-1 summarises the response and predictor variables generated for analysis. For each event FLD, FPD, IA and NDS are variables characterising the local seismic forcing, while SL, ED, ES, GT, DS, FDA, SR, $PD3$ and $PD6$ characterise the local stability of hillslopes.

Table 4-1 Variables used to logistic regression analysis for the 1929 Buller and 1968 Inangahua earthquakes

Variable ID	Description	
Response Variables		
$\boldsymbol{LS(A)_{1929}}$	1929 landslide source area binary	
$\boldsymbol{LS(A)_{1968}}$	1968 landslide source area binary	
Predictor Variables		
$\boldsymbol{FLD}$	Coseismic fault line distance (km)	Seismic forcing
$\boldsymbol{FPD}$	Coseismic fault plane distance (km)	
$\boldsymbol{HW}$	Coseismic hanging wall binary	
$\boldsymbol{IA}$	Local hillslope orientation with respect to coseismic source (incidence angle of seismic waves)	
$\boldsymbol{NDS}$	Normalised distance from stream channel to ridge crest	
$\boldsymbol{SL}$	Local hillslope gradient (degrees)	Hillslope stability
$\boldsymbol{ER}$	Drainage basin elevation range (m)	
$\boldsymbol{ES}$	Drainage basin elevation standard deviation (m)	
$\boldsymbol{GT}$	Geology (tectnostratigraphic terrane)	
$\boldsymbol{DS}$	Dip-slope binary	
$\boldsymbol{FDA}$	Distance from all mapped faults (km)	
$\boldsymbol{SR}$	Local annual solar radiation (WH/m^2)	
$\boldsymbol{PD3}$	Earthquake month plus previous 2 months spatially distributed precipitation (mm)	
$\boldsymbol{PD6}$	Earthquake month plus previous 5 months spatially distributed precipitation (mm)	

4.2.4 Model fitting

While there are various automated procedures for selecting appropriate combinations of variables for use in generalised linear models (Furnival and Wilson, 1974, Lawless and Singhal, 1978, Lawless and Singhal, 1987a, Lawless and Singhal, 1987b, Hosmer and Lemeshow, 2000), automated techniques were not used to fit models in this investigation. This is because these techniques lack input from the scientific knowledge

and understanding of the analyst, and models produced through automated techniques may therefore provide a good statistical fit whilst being scientifically implausible (Greenland, 1989). Rather, models were constructed manually, guided by goodness-of-fit statistics and the understanding of earthquake-triggered landslide events presented in previous chapters. Separate models for the two earthquakes were fitted in parallel, in order to identify a set of common predictor variables describing the spatial probability of landsliding. McFadden's Pseudo R^2 was used as a guide to goodness-of-fit and p-values generated by logistic regression were used to test the statistical significance of relationships (Chen et al., 2012a). McFadden's Pseudo R^2 is calculated as:

Equation 4-7:

$$R^2 = 1 - \frac{\ln \hat{L}\,(M_{full})}{\ln \hat{L}\,(M_{intercept})}$$

Where $\ln \hat{L}\,(M_{full})$ is the log likelihood of the full model and $\ln \hat{L}\,(M_{intercept})$ is the log likelihood of the model without any predictors. R^2 values indicate the level of improvement offered by the full model over the model without its predictors. p-values generated by logistic regression indicate the probability of obtaining the chi^2 statistic if there is no effect of the predictor variables on the response variable. Predictor variables were only included in the model if they provided an improvement in R^2, were significant at the 0.05 level, and produced consistent and physically plausible relationships to seismic and hillslope processes, in the case of both earthquake datasets. During the fitting process multiple variable combinations were iteratively tested. The final model presented below represents the version producing the best fit whilst meeting the above criteria.

4.2.5 Buller and Inangahua earthquake-triggered landslide probability models

For the 1929 and 1968 earthquakes, hillslope failure probability can be modelled via the following equation:

Equation 4-8

$$P_{LS}(A) = \frac{1}{1 - e\left(-\begin{pmatrix} c_{intercept} + c_{FPD}\,FPD + c_{NDS}\,NDS + c_{FPD\cdot NDS}(FPD \cdot NDS) \\ +c_{SL(G)}\,SL + c_{ES}\,ES + c_{SR}\,SR + c_{DS}\,DS \end{pmatrix}\right)}$$

where the variables in red characterise the local seismic forcing and the variables in blue characterise the local stability of hillslopes. Logistic regression coefficients are indicated by c followed by the predictor variable ID subscript. Coefficients and fit statistics for this model are given in Table 4-2 (1929) and Table 4-3 (1968). Coefficients are given in log-odds units, indicating the change in the log-odds of probability per unit change in the predictor variables. In addition to predictor variable coefficients, coefficient standard errors, z-values (coefficients divided by standard errors), p-values for the full models and individual predictors, and the 95% confidence intervals of the predictors are also given. Both the full models and all individual predictor variables are statistically significant beyond the 0.01 level.

Table 4-2 Logistic regression statistics for the 1929 Buller earthquake model

Variables in red characterise the strength of the seismic forcing
Variables in blue characterise the local stability of hillslopes

Number of observations	3116647
Likelihood ratio chi^2	110670.28
Model p-value	0.00
Pseudo R^2	0.187

					95% confidence interval	
Variable	**Coefficient**	**Standard error**	**z-value**	**p-value**	**Lower bound**	**Upper bound**
FPD	-0.0606	0.0016	-37.67	0.00	-0.0637	-0.0574
NDS	1.1811	0.0203	58.31	0.00	1.1414	1.2208
$FPD * NDS$	-0.0288	0.0023	-12.60	0.00	-0.0332	-0.0243
$SL\ (GT = 1)$	0.0824	0.0006	146.25	0.00	0.0813	0.0835
$SL\ (GT = 2)$	0.0657	0.0005	132.40	0.00	0.0647	0.0667
$SL\ (GT = 3)$	0.0968	0.0005	189.89	0.00	0.0958	0.0978
$SL\ (GT = 4)$	0.1040	0.0013	77.99	0.00	0.1014	0.1066
SR	0.0054	0.0002	28.51	0.00	0.0050	0.0058
ES	0.0078	0.0001	66.70	0.00	0.0076	0.0081
DS	0.3478	0.0157	22.13	0.00	0.3170	0.3786
$Intercept$	-7.6669	0.0316	-242.36	0.00	-7.7289	-7.6049

Table 4-3 Logistic regression statistics for the 1968 Inangahua earthquake model

Variables in red characterise the strength of the seismic forcing
Variables in blue characterise the local stability of hillslopes

Number of observations	3116650
Likelihood ratio chi^2	34392.70
Model p-value	0.00
Pseudo R^2	0.248

Variable	Coefficient	Standard error	z-value	p-value	95% confidence interval	
					Lower bound	Upper bound
FPD	-0.2283	0.0072	-31.80	0.00	-0.2424	-0.2142
NDS	1.2995	0.0519	25.05	0.00	1.1978	1.4011
$FPD * NDS$	-0.0892	0.0105	-8.50	0.00	-0.1097	-0.0686
$SL\ (GT = 1)$	0.0868	0.0013	66.29	0.00	0.0842	0.0893
$SL\ (GT = 2)$	0.0982	0.0012	83.99	0.00	0.0959	0.1005
$SL\ (GT = 3)$	0.1079	0.0012	91.50	0.00	0.1056	0.1103
$SL\ (GT = 4)$	0.1499	0.0021	72.23	0.00	0.1458	0.1539
SR	0.0037	0.0005	7.63	0.00	0.0027	0.0046
ES	0.0022	0.0003	6.88	0.00	0.0016	0.0029
DS	0.1388	0.0439	3.16	0.00	0.0527	0.2250
$Intercept$	-7.9556	0.0746	-106.60	0.00	-8.1018	-7.8093

Figures 4-16 to 4-22 show observed (black dots) and predicted (red lines) $P_{LS}(A)$ values relative to values of individual predictor variables. In order to account for the uneven distribution of data relative to the predictor variables, mean predicted and observed probability was calculated for each predictor within 20 equal frequency (5%) bins. Note that predicted values on these plots are the product of all predictor variables, such that the red lines do not appear as smooth functions. However, the plots are useful for visualising variability in $P_{LS}(A)$ and assessing the fit of the models.

The seismic forcing variables FPD and NDS influence landslide probability individually, but also have a combined influence as an interaction variable ($FPD \cdot NDS$). FPD derives a negative coefficient indicating that landslide probability decreases with distance from the seismic source (Figure 4-15). NDS derives a positive coefficient, indicating that landslide probability increases with normalised proximity to ridge crests, or that landslide probability is higher for locations closer to ridge crests than those closer to river channels (Figure 4-16). $FPD \cdot NDS$ also has a significant influence in both models, with landslide probability decreasing with increasing $FPD \cdot NDS$. This indicates that the influence of NDS decreases with increasing FPD. In other words the

proportional effect of topographic amplification in increasing failure probability diminishes with distance from the seismic source. For each of these variables, the default logistic transformation was found to produce a good fit to observed data, without the need for additional transformations.

Variables FLD, HW and IE that also characterise the seismic forcing are not included in the models. In the case of IE, this variable was not found to exhibit a significant influence on landslide probability in any of the model combinations tested. FLD and HW were found to be significant, but only when used in place of FPD. As FLD and FPD both relate to distance from the seismic source, these variables are highly co-linear. However, FPD was found to be more effective than FLD in increasing the model R^2 value. As FPD indicates distance from the fault plane, hanging wall areas are assigned lower values due to their closer proximity. This in turn accounts for higher ground accelerations experienced in these areas so that HW is no longer required in the model. For both events FPD was found to produce a greater increase in R^2 than the combination of FLD and *HW*.

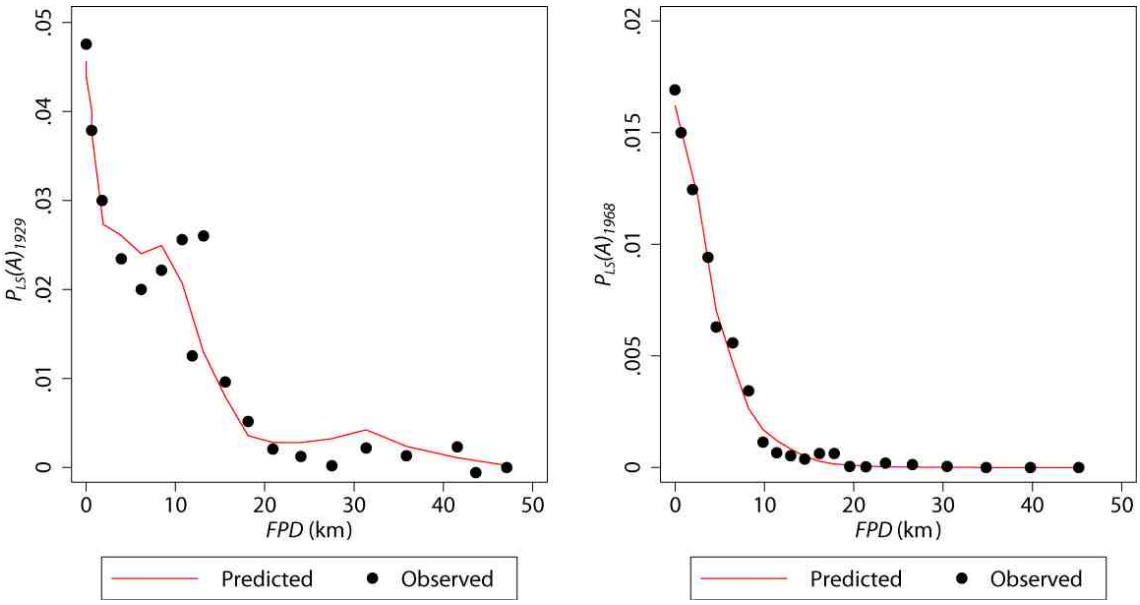

Figure 4-15 Plots of observed and predicted hillslope failure probabilities for the 1929 ($P_{LS}(A)_{1929}$) and 1968 ($P_{LS}(A)_{1968}$) earthquakes relative to the distance from the earthquake coseismic fault planes (FPD)

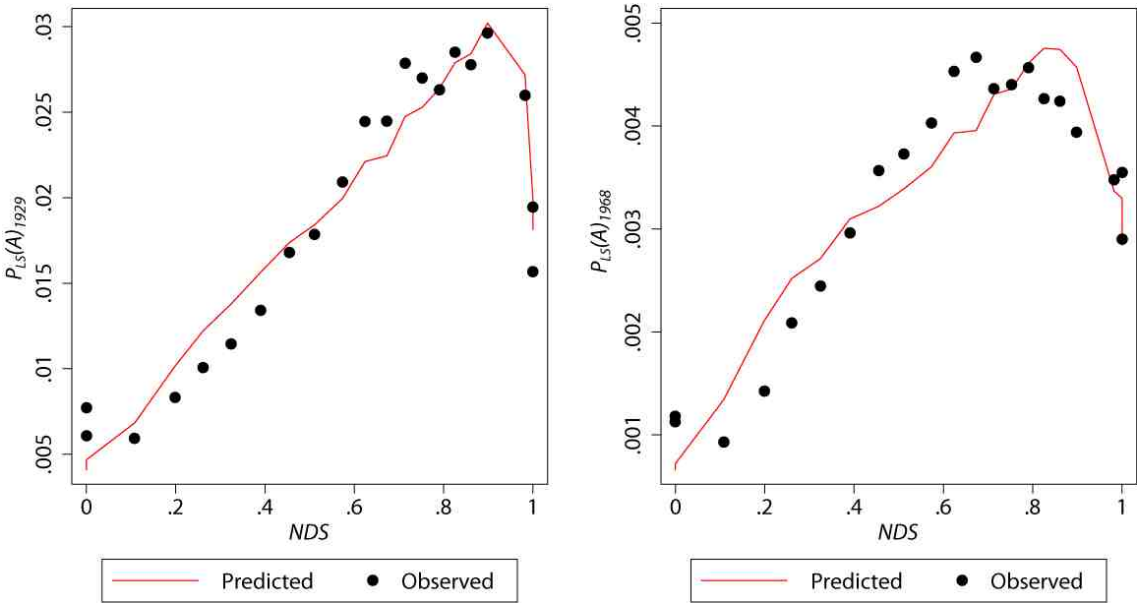

Figure 4-16 Plots of observed and predicted hillslope failure probabilities for the 1929 ($P_{LS}(A)_{1929}$) and 1968 ($P_{LS}(A)_{1968}$) earthquakes relative to the relative to the normalised distance from stream channels to ridge crests (NDS)

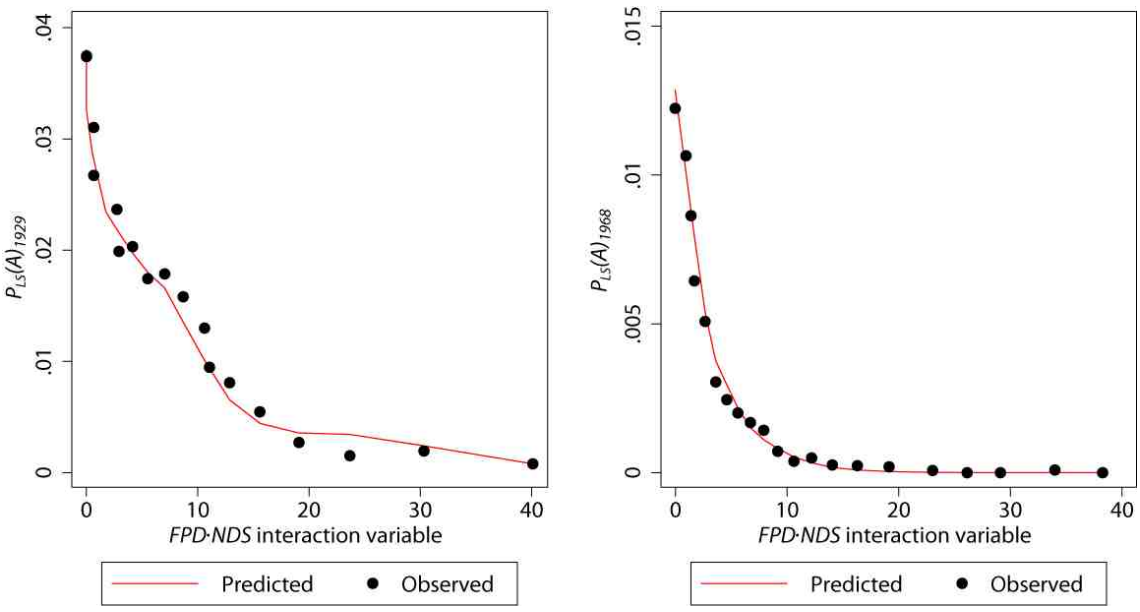

Figure 4-17 Plots of observed and predicted hillslope failure probabilities for the 1929 ($P_{LS}(A)_{1929}$) and 1968 ($P_{LS}(A)_{1968}$) earthquakes relative to the variable $FPD \cdot NDS$

The static stability of hillslopes is characterised in the models by the variables SL, GT, SR, ES and DS. GT was found not to perform well as an individual variable in the model, with its derived indictor variables on the whole not being statistically significant. However, GT was found to impart a statistically significant effect on the coefficient of SL, and is therefore included in the model as an interaction variable allowing the coefficient for SL to vary for different geological units. For all units SL displays a positive coefficient, indicating that landslide probability increases with slope gradient. Probability curves for different geological units are shown in Figure 4-18. Observed and predicted values match closely for the Buller, Intrusives and Pre-Quaternary sediments units, however the fit is poor for high slope gradients in the Quaternary sediments. This is likely due to the very low frequency of data in these sectors, resulting in high sensitivity to stochastic variability and outlying values.

DS exhibits significant positive coefficients indicating higher landslide probability on dip slopes. ES displays significant positive coefficients indicating increasing landslide probability with increasing relief. While ES and SL exhibit colinearity with a correlation coefficient of 0.58, the inclusion of ES still results in a substantial increase in the R^2 value. SR displays a significant, positive coefficient, indicating increasing landslide probability with increasing annual solar radiation incident on the hillslope. Note that for ES and SR, the individual relationships are less clear in the plots of predicted and observed values (Figure 4-20 and Figure 4-21). This indicates that the effect of these

variables, particularly SR, is to improve the fit of the model by increasing the predictive validity of other variables in the model. Such variables are commonly termed 'suppressor variables' (e.g.: Smith, 1992, Woolley, 1997), and their effect can be understood as explaining residual variance not explained by other variables. In other words, while the probability of failure may be predominantly determined by FPD, SL and GT, it is modified to a lesser extent by SR and ES.

Other variables, ER, FDA, $PD3$ and $PD6$, that also potentially influence hillslope stability are not included in the model. FDA, $PD3$ and $PD6$ were found not to exhibit significant influence on the model in any of the variable combinations tested. ER was found to be significant, however ER and ES are highly co-linear, and ES was found to produce a greater increase in the R^2 value. Again the default logistic transformation was found to produce a good fit to observed data. A slight improvement in overall fit could be attained using multiple cubic spline variables in place of SL, however this also resulted in several of the additional coefficients being insignificant.

During the model fitting, grid cells with $SL > 58$ were found to produce numerical problems associated with the very low frequency of data at high values. This amounted to an area of 1.3 km^2 (less than 0.05% of the study area). In this range the relationship between hillslope gradient and failure probability was found to exhibit a rollover, suggesting a decrease in failure probability with gradient. It is unclear whether this behaviour is real or an artefact of the low data frequency and/or the limitation of mapping landslides on steep slopes from aerial imagery. As the logistic function cannot model a humped relationship, and as SL this is one of the dominant variables in the model, these data were removed from the analysis.

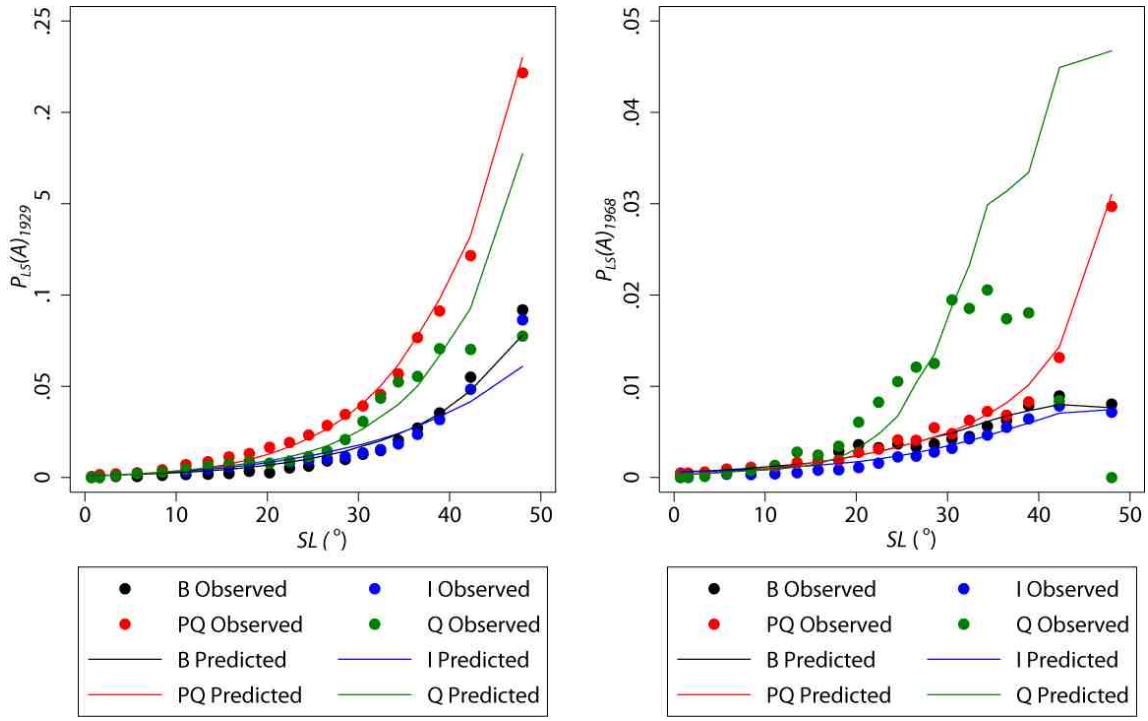

Figure 4-18 Plots of observed and predicted $P_{LS}(A)_{1929}$ and $P_{LS}(A)_{1968}$, relative to SL, separated by GT zones (B=Buller, I=Igneous Intrusions, PQ=Pre-quaternary, Q = Quaternary)

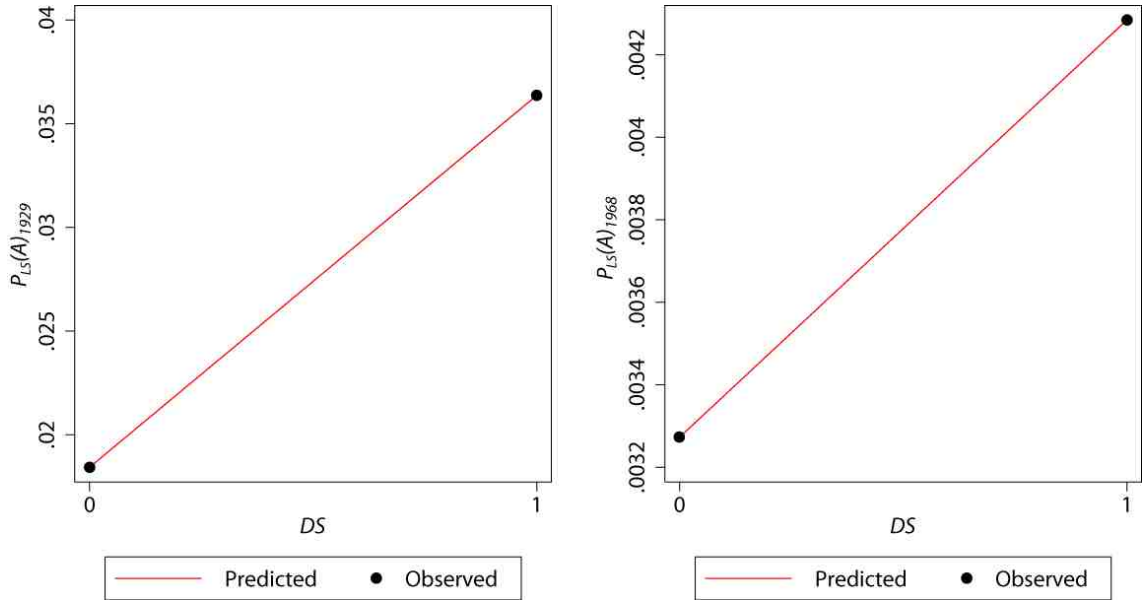

Figure 4-19 Plots of observed and predicted $P_{LS}(A)_{1929}$ and $P_{LS}(A)_{1968}$, relative to DS. Note that dipslopes (DS = 1) have the higher probability.

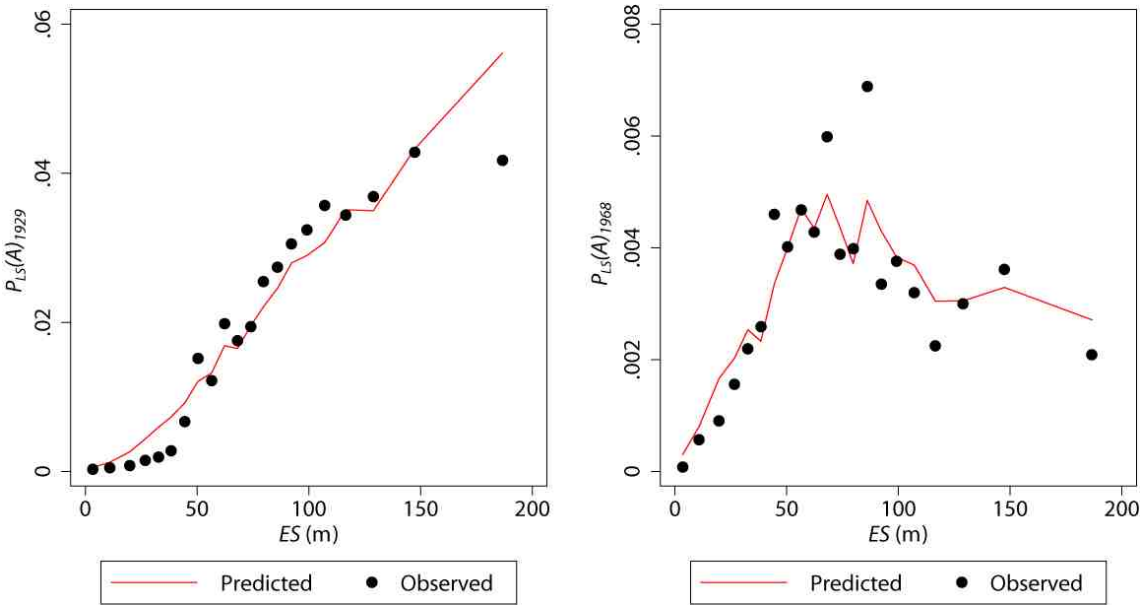

Figure 4-20 Plots of observed and predicted $P_{LS}(A)_{1929}$ and $P_{LS}(A)_{1968}$, relative to ES

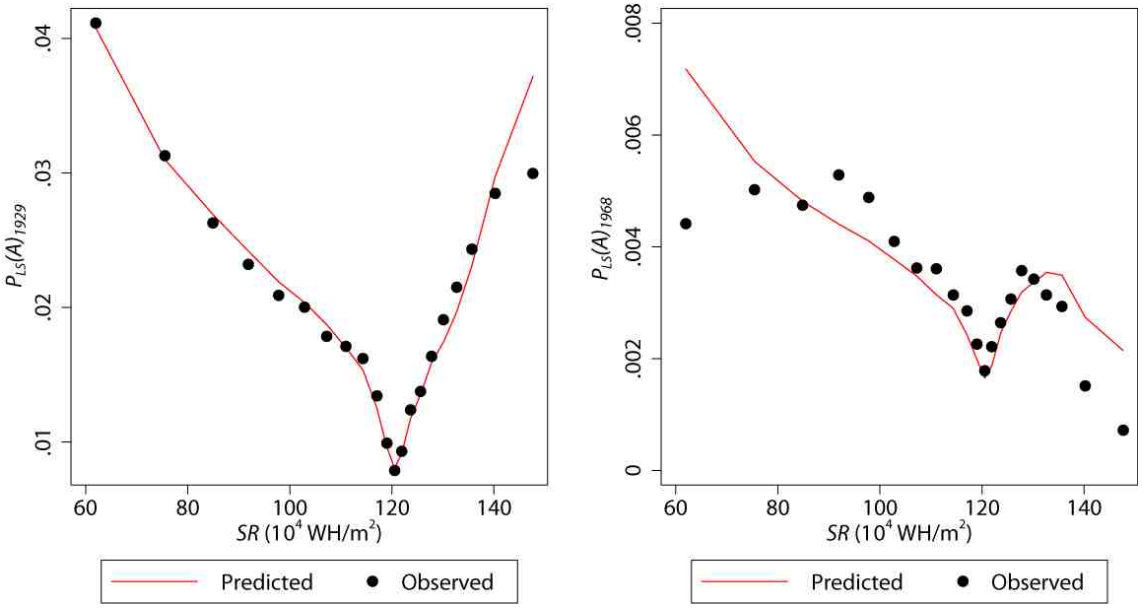

Figure 4-21 Plots of observed and predicted $P_{LS}(A)_{1929}$ and $P_{LS}(A)_{1968}$, relative to SR

4.2.6 Coefficient variability

For both events the sign attached to each of the coefficients (i.e.: whether the coefficient is positive or negative and thus whether the variable has the effect of increasing or decreasing landslide probability) is the same. The values of coefficients vary between the two event models, as shown in Figure 4-22. Since the effect of individual predictors is co-dependent on the effect of all other predictors, it is difficult to attribute variability of individual coefficients to particular factors. This variability is

in part due to differences in the overall magnitude of the earthquakes. The higher intercept value for 1929 indicates the higher overall failure probability produced by the higher magnitude earthquake and the larger negative FPD coefficient indicates a more gradual decrease in probability per unit distance from the seismic source. Larger positive 1929 coefficients for SR, ES and DS are also likely to result from the higher overall failure probability for the 1929 event. Coefficients for NDS are similar, suggesting that the increase in failure probability due to topographic amplification is reasonably consistent. The larger negative $FDP \cdot NDS$ coefficient for 1968 suggests that the strength of the topographic amplification effect decreases more quickly with distance in the lower magnitude 1968 earthquake. SL coefficients are similar for both events, although the relative strength of the coefficient for Intrusives unit is slightly lower for 1929 than 1968.

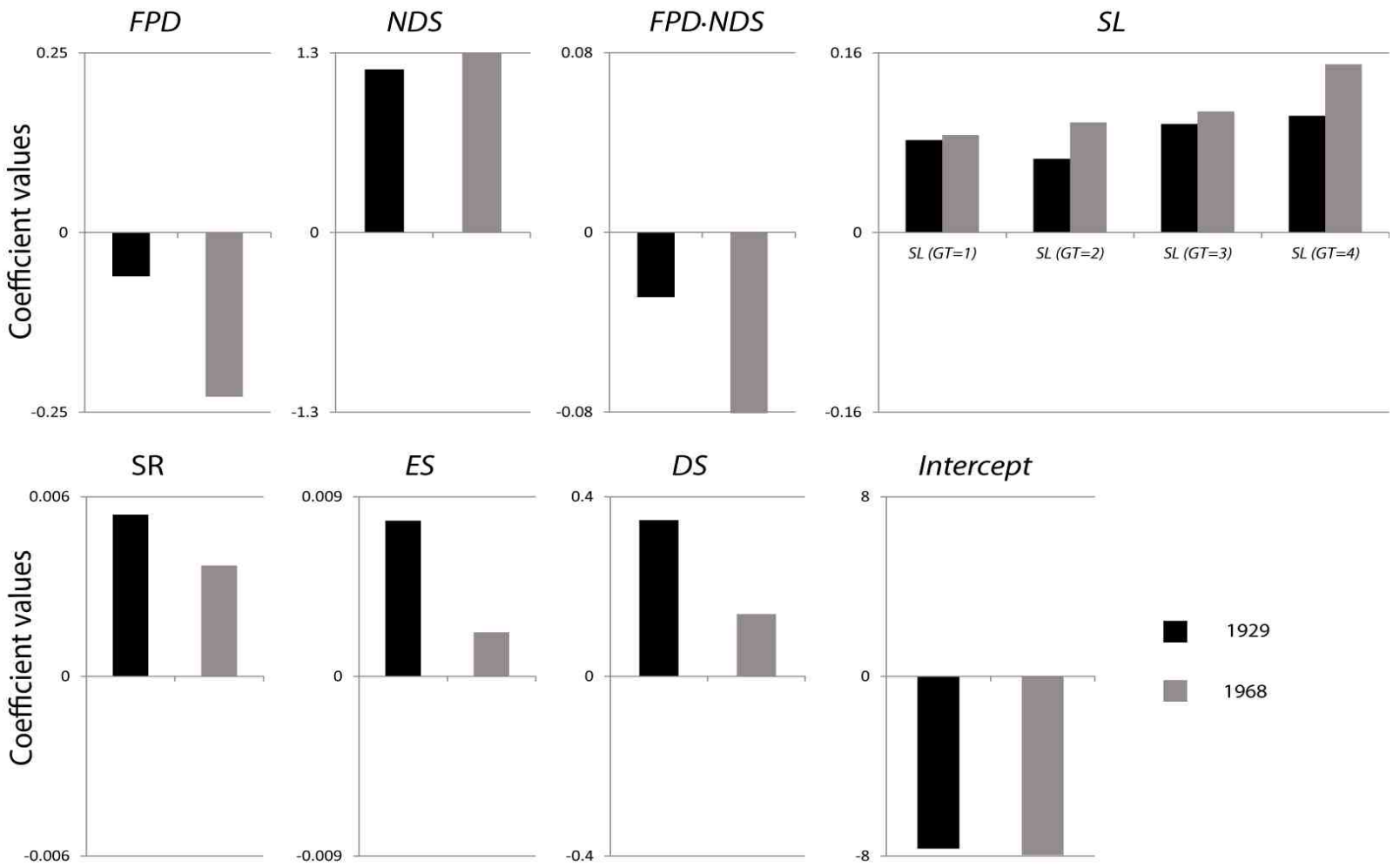

Figure 4-22 Comparison plots of predictor coefficients for the 1929 and 1968 probability models. Note that the axes have different scales as the coefficients are not normalised and vary over a large scale between predictor variables

4.2.7 Predicted and observed probability comparison

Figure 4-23 shows a comparison of predicted and observed probability calculated across 100 equal frequency (1%) bins. These values have been plotted on logit (log-odds) scales, reflecting the mechanics of logistic regression: fitting linear correlation in log-odds space. At high values both models exhibit a close fit to the line of equality. At low values the 1929 model produces slightly over-predicted probabilities, while the 1968 model exhibits departure from equality with under-predicted probabilities. It is likely that these errors at the lower limit of the distribution of probabilities are at least in part statistical artefacts of low data frequency and near-zero probability values.

Figure 4-24 and Figure 4-25 show predicted probability values projected spatially, alongside the landslide source binary grids used to fit the models. The spatial projection of predicted failure probability closely reflects the spatial distributions of landslide source areas. For the 1929 earthquake, some of the large coastal landslides in the northwest of the study area occur outside of the region of higher failure probabilities. This may be due to the influence of coastal erosion on hillslope stability in these areas, which is not accounted for in the model.

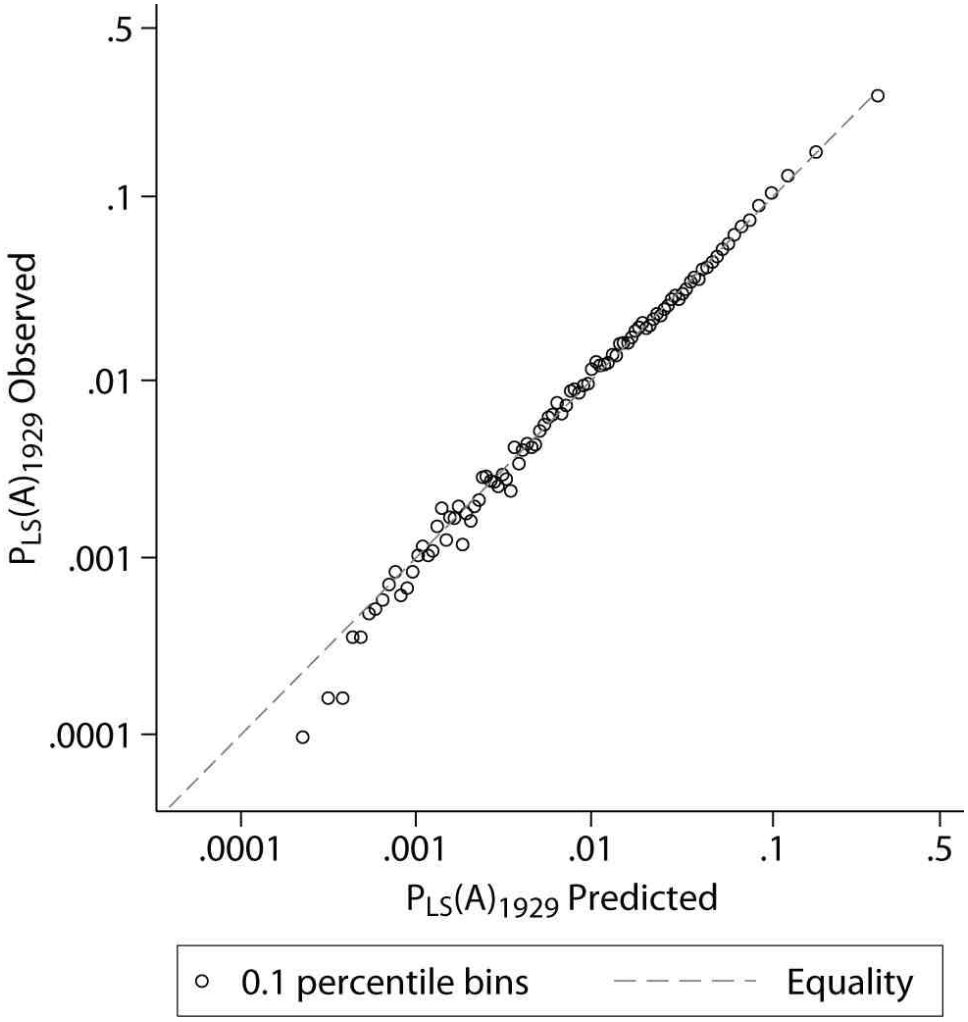

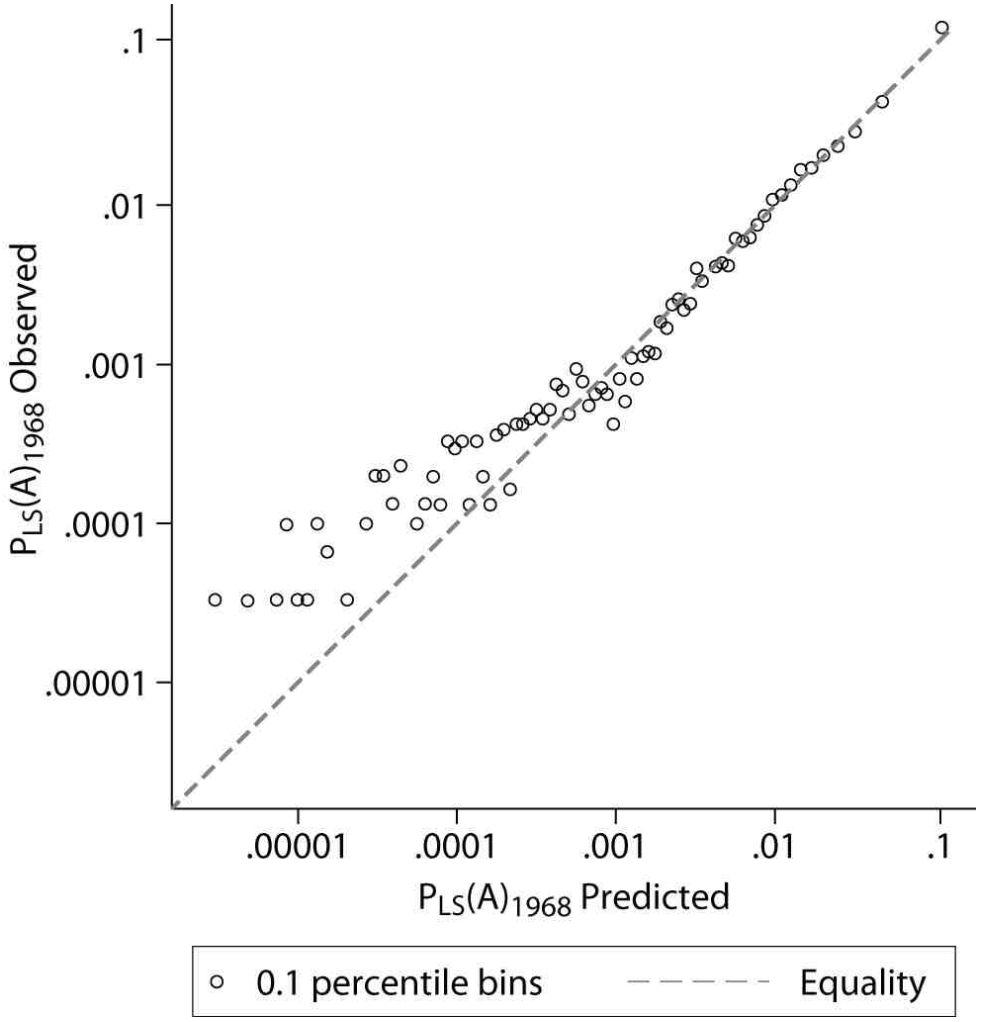

Figure 4-23 Plotted comparison of predicted and observed probability for the 1929 Buller and 1968 Inangahua earthquakes, sampled within 100 equal frequency (1%) bins widths. The dotted line indicates the line of equality. The data are plotted on logit (log-odds) scales.

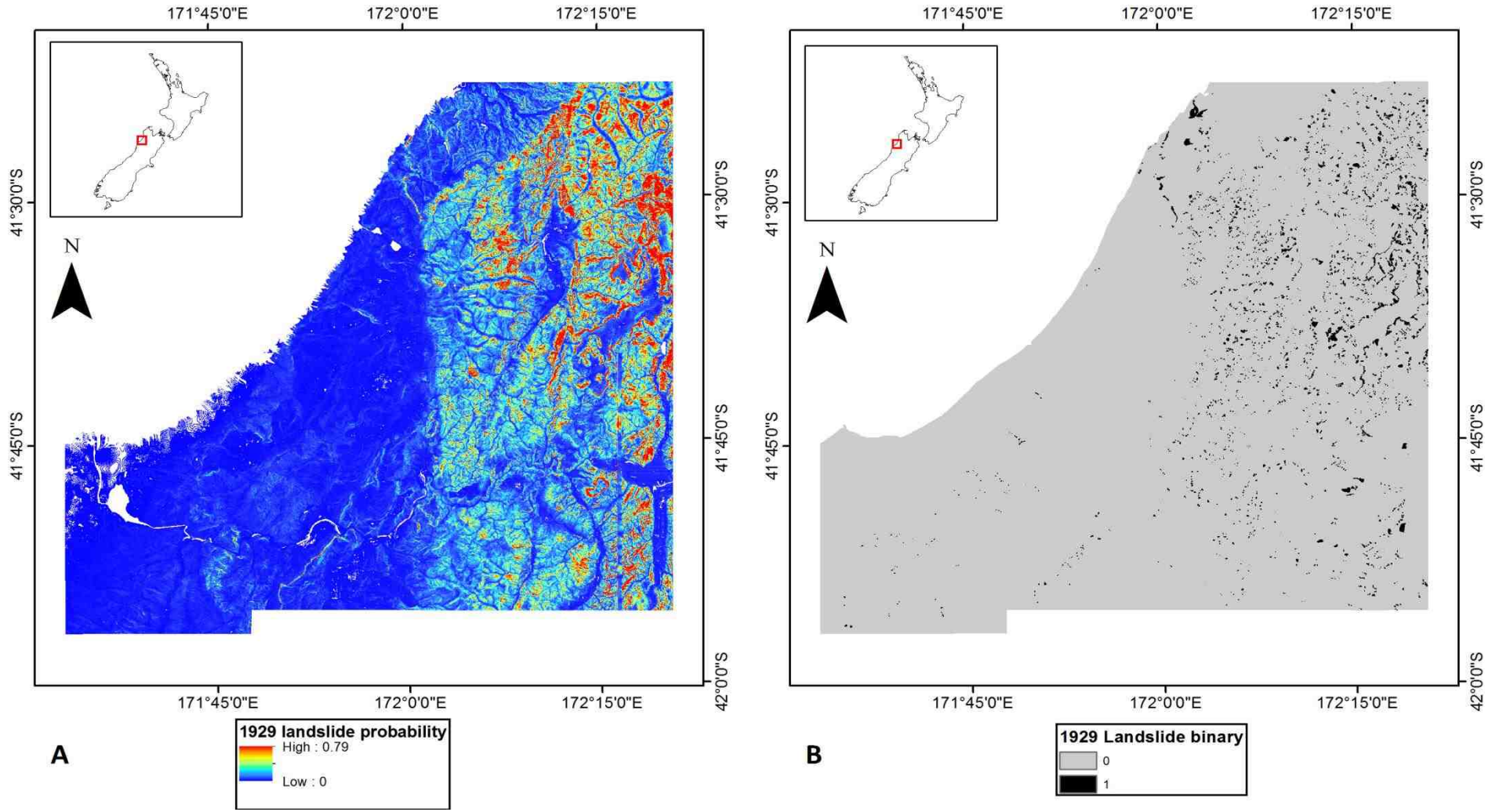

Figure 4-24 Map projected predicted probabilities (A) and observed landslide source locations (B) for the 1929 earthquake.

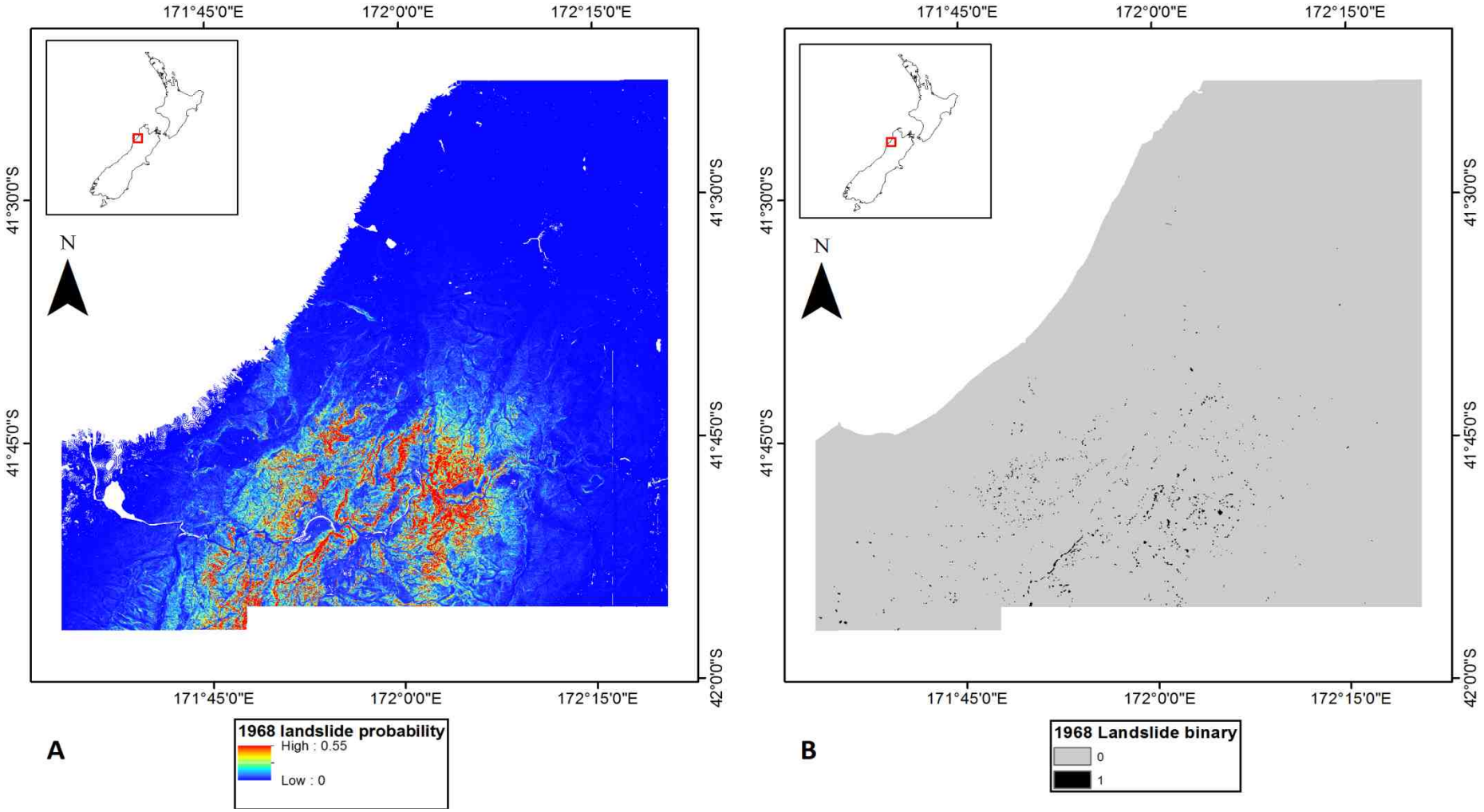

Figure 4-25 Map projected predicted probabilities (A) and observed landslide source locations (B) for the 1968 earthquake.

4.2.8 Model fit breakdown

Each predictor variable accounts for some part of the improvement in fit, although not all variables contribute equally. It is important to establish the relative contribution of different predictor variables to the fit of the models and thus the relative importance of different factors in determining hillslope failure probability. In order to achieve this, beginning with the full models presented above, the variable contributing the least increase in the R^2 value was repeatedly removed from the model and the model refitted. This process was carried out for both the 1929 and 1968 models and the R^2 values were recorded for each refinement. Figure 4-26 shows the ranked order of variable combinations and evolving values of R^2 resulting from this experiment. For both events, FPD, SL and GT are primary variables accounting for the majority of the model fit. Whilst the rank order of $FPD \cdot NDS$, DS, SR, NDS and ES differs, all these variables appear to be secondary in defining the spatial distribution of $P_{LS}(A)$. For 1929, the initial increase in R^2 produced by FPD is much lower than in 1968. This suggests that less variability is accounted for by FPD in 1929. Given the large scale and less well-constrained rupture in this event, the lower level of fit may be due to the effect of unresolved rupture complexity.

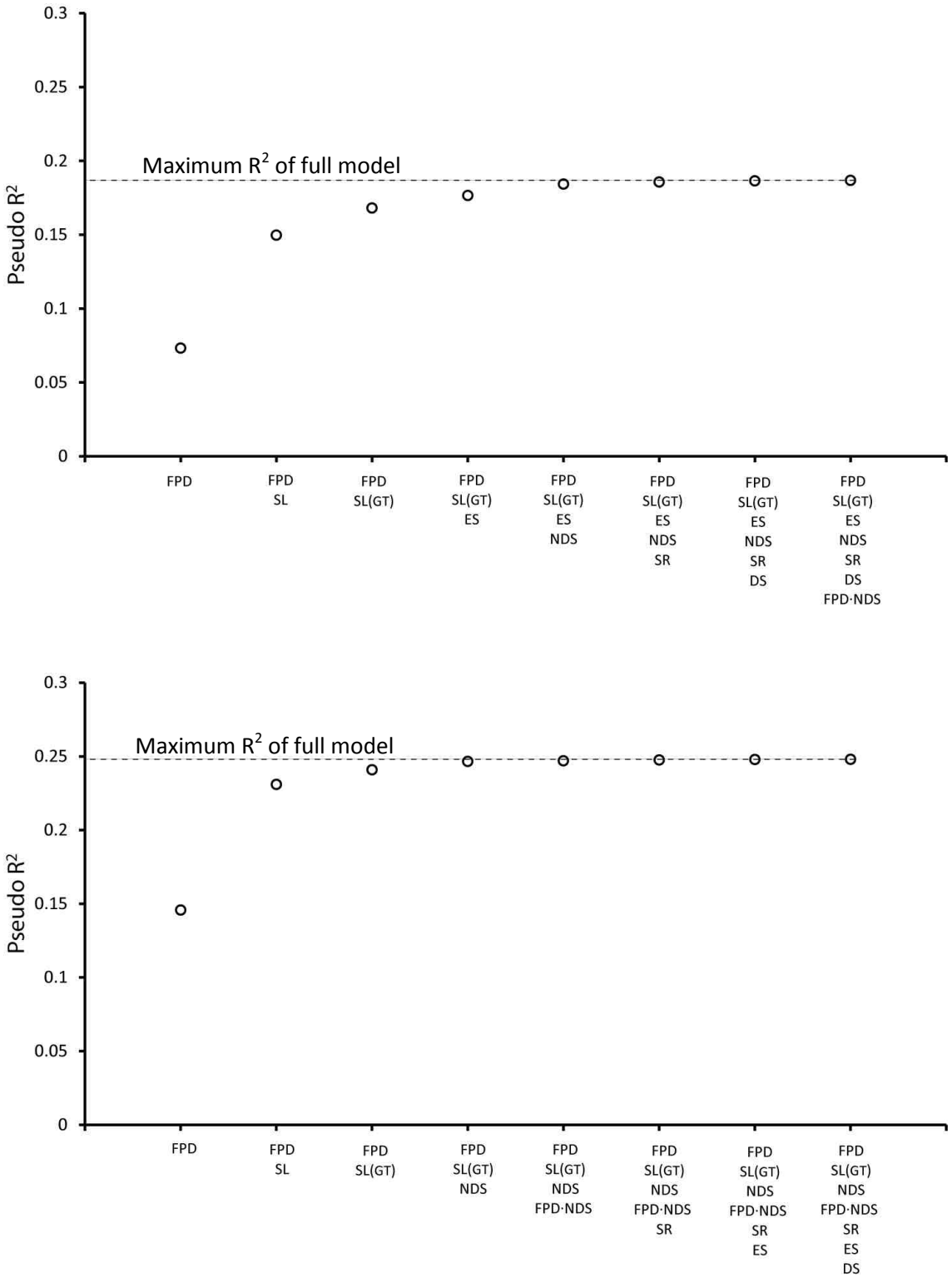

Figure 4-26 Plots showing the relative contribution of predictor variables to the fit of the 1929 and 1968 hillslope failure probability models. 1929 (top) and 1968 (bottom) model fit breakdown: sequence of model input predictors and resulting pseudo-R^2 goodness of fit values, produced by sequetially removing the least contributing predictor variable.

4.2.9 Discussion of model components and implications

The spatial probability distributions of landslides triggered by the 1929 and 1968 earthquakes can both be described using the logistic regression model given in Equation 4-8. The major influences upon the model behaviour are the distance of sites from the seismic source and the local hillslope gradient, where the underlying influence of hillslope gradient is dependent on geology. Secondary are the effects of topographic amplification, solar radiation, hillslope structural domains and local relief, which modify failure probability to a lesser extent. The influence of the model variables corresponds with that expected, based on their physical relationships to seismic and hillslope processes. The findings from this analysis have a number of similarities with the results of previous investigations but also notable differences.

The negative correlation between landslide probability and distance from the seismic source is commensurate with the attenuation of seismic ground accelerations (Campbell and Bozorgnia, 2008), and fits with the results of other ETL studies (e.g.: Meunier et al., 2007, Dai et al., 2011, Lee et al., 2008a). While the decision of how to characterise the seismic source is somewhat arbitrary, the use of the fault plane provides the most physically accurate fault characterisation and the best fitting model, without the need to include an additional variable to account for differences between the hanging wall and footwall. The positive correlation between failure probability and NDS corresponds with expected valley-scale patterns of topographic amplification and damping. The decay in the amplification effect with distance from the seismic source can be related to both the general lowering of relief and a change in the incidence angle of seismic waves. The change in wave incidence angle with increasing horizontal distance from coseismic faults results in a shift of topographic amplification peaks away from ridge crests (Meunier et al., 2008). The expected result of this is that failures will occur lower on hillslopes, resulting in the reduced influence of NDS with increasing fault distance. While the NDS variable accounts for the position of cells in the stream-ridge profile, it does not account for the local relief and therefore the severity of the topographic amplification effect (Benites et al., 1994). This corresponds with the greater influence of NDS in high relief areas close to the fault, than in lower relief, coastal areas that occur at greater distances from the source.

Positive correlation between failure probability and hillslope gradient fits with the associated increase in local shear stresses (Section 2.1.4). A major difference in this model to similar published models of ETL susceptibility (e.g.: Lee et al., 2008a, Xu et al., 2012, Li et al., 2012) is that the influence of geology is not to modify landslide probability directly, but rather by changing the relationship between landslide probability and hillslope gradient. As the topography and lithology of landscapes are not independent, owing to the relationship between the strength of hillslope material and the maximum gradient and relief that hillslopes can sustain (e.g.: Hoek, 2000, Schmidt and Montgomery, 1995), it is logical that the influence of these variables should be coupled. The increase in failure probability with the local relief between drainage divides can be associated with the increase in gravitationally-induced shear stresses with the local height of hillslopes and the associated decrease in rock mass strength at increasing spatial scale (Culmann, 1866, Schmidt and Montgomery, 1995).

Although hillslope aspect is a common variable used in landslide susceptibility models, its influence is generally attributed to a combination of topographic effects on seismic waves, structural influences on hillslope stability and local climatic differences affecting the physical breakdown of hillslope material (Chen et al., 2012b, Dai et al., 2011, Lee et al., 2008a, Lee and Min, 2001). As a result, statistical relationships between aspect and landslide probability will be specific to particular earthquakes and regions. By separating the individual seismic, structural and climatic components that influence the aspect of landslides, model relationships derived here are more likely to be representative of other earthquakes and regions. The positive correlation between solar radiation and hillslope failure probability, and higher failure probability for slopes with out-of-slope dipping structures agree with the expected influence of these variables (Mcfadden et al., 2005, Selby, 2005, Moore et al., 2009, Hoek et al., 2002). When these effects are controlled for in analysis, the orientation of hillslopes relative to seismic sources, associated with topographic effects on ground accelerations (e.g.: Meunier et al., 2008), was not found to exhibit a significant influence on landslide probability. This may indicate that, when seismic waves interact with complex surface topography, this site effect may be weaker than suggested by results of seismic waves field experiments using simplified topography (Meunier et al., 2008).

Spatially distributed precipitation variables do not exhibit a significant influence on failure probability. This may suggest that rainfall and associated variability in pore-pressures have little influence on ETL activity, which may be true for well-drained sections of hillslope positioned high on mountainsides. As localised pore-pressure generation is highly dependent on surface and sub-surface hydrology (Montgomery et al., 1997, Wilson and Dietrich, 1987, Fannin and Jaakkola, 1999), and rainfall data represent long-term mean conditions rather than data at the time of the earthquakes, these variables may not accurately characterise the influence of rainfall on hillslope stability. In the absence of distributed pore-pressure data with which to compare the landslide distribution, understanding hydrological influences on ETL activity remains an area of uncertainty. Similarly, no significant relationship was observed between landslide probability and the distance of sites from mapped faults. While zones of weakened and damaged material occur around fault zones (e.g.: Mooney et al., 2007, Lockner et al., 2009), local hillslopes may have already adjusted to these conditions. Mapped faults generally track along valleys, suggesting that erosional processes have already removed material weakened by faulting, which therefore exerts little influence on present day hillslope processes.

The consistency with which the model describes the spatial distribution of ETLs for both events suggests that this combination of underlying relationships can be applied generally to earthquakes in the region. In other words, landslides triggered by earthquakes in this area are sampled from this same spatial distribution of hillslope failure probability. The variables exhibiting a more minor influence in the model have greater potential to describe characteristics of the landslide distribution specific to these events and to this region. By removing these variables and identifying the major influences on failure probability, the model can be made less event-specific and more transferrable between different earthquakes and regions. The combination of the distance of sites from the seismic source and the local hillslope gradient, with influence dependent on geology, therefore provide a candidate variable subset for a generalised ETL probability model.

4.3 General earthquake-triggered landslide probability models

In order to test whether the major influences on ETL probability in the Buller and Inangahua earthquakes can provide the basis for a generalised model of ETL spatial probability, logistic regression models were fitted using data from all five earthquakes presented in Chapter 3. The individual datasets were processed via the methodology outlined in Section 4.1. The 30 m pixel resolution of the ASTER GDEM dataset was used to define the analysis grid and provide elevation data for all events. To ensure a comparable level of completeness in the landslide datasets, landslides smaller than 11,000 m^2 were removed from the analysis (see Section 3.3.1). The models presented in this section therefore predict $P_{LS}(A)$ for landslides of area greater than or equal to 11,000 m^2.

For each grid cell landslide binary variables, distances from the nearest point on the coseismic rupture plane and local hillslope gradient were calculated. For this analysis, distances were calculated in three dimensions in order to account for inter-event variability in rupture depth, in addition to the horizontal site distance. To account for differences in the total size of the earthquakes and duration of shaking, M_w was also included as a predictor variable. Additionally, for all but the 1929 earthquake, values of peak ground acceleration were also sampled using USGS Shakemap maximum PGA isoseismals. Table 4-4 summarises the response and predictor variables generated for analysis.

Table 4-4 Variables used in logistic regression analysis for all earthquake events

Variable ID	Description
$\boldsymbol{LS}$	Landslide source binary
$\boldsymbol{M_w}$	Earthquake moment magnitude
$\boldsymbol{FPD}$	3-dimensional distance from the nearest point on the coseismic fault rupture (km)
$\boldsymbol{PGA}$	Peak ground acceleration (g) – 1968, 1994, 1999, 2008 only
$\boldsymbol{SL}$	Local hillslope gradient (degrees)

For each earthquake the spatial extent of analysis was limited to the total coverage area of landslide mapping. Note that for the 2008 Wenchuan earthquake, for around 5% of the study area the GDEM elevation dataset was found to contain errors and voids resulting from cloud interference. These regions were clipped from the DEM and

removed for analysis. Data from all five events were combined as described in Table 4-5. In order to account for the different size of areas covered by the landslide inventories for the different earthquakes, when fitting the models presented below observations were inversely weighted by the frequency of observations for each earthquake. This was achieved using the analytical weights feature in Stata (Gould and StataCorp, 1994). While generally applied in cases of linear regression, the technique is appropriate in this case to ensure that the individual earthquake datasets contributed equally to modelled relationships and to avoid dominance by the larger datasets for the Chi-Chi and Wenchuan earthquakes (Cox, pers coms).

Table 4-5 Landslide inventory mapping coverage areas and sample sizes used in analysis

Earthquake	Coverage area (km^2)	Number of observations (30 m grid cells)
1929 Buller	4,222.53	4,691,700
1968 Inangahua	4,288.03	4,764,477
1994 Northiridge	3,973.77	4,415,300
1999 Chi-Chi	10,513.20	11,681,333
2008 Wenchuan	11,465.49	12,739,433
Total	34,463.02	38,292,244

4.3.1 Earthquake magnitude, seismic source distance and hillslope gradient model

For all five earthquakes, $P_{LS}(A)$ can be modelled as a function of M_w, FPD and SL via Equation 4-9. Coefficients and fit statistics for this model are given in Table 4-6.

Equation 4-9

$$P_{LS}(A) = \frac{1}{1 - e\left(-\left(c_{intercept} + c_{M_w} M_w + c_{FPD} FPD + c_{SL} SL\right)\right)}$$

where variables in red characterise the seismic forcing and the variables in blue characterise the stability of hillslopes. Coefficients for both the distance and hillslope gradient components of the model were found to vary for the different events. The coefficients of the distance component (FPD) range from 0.09 to 0.18 for the five earthquakes, and these differences were found to be statistically significant beyond the 0.01 level. This indicates variability in the rate at which $P_{LS}(A)$ decays with distance from the seismic source. Coefficients of the hillslope gradient component (SL) also vary between 0.07 and 0.1, and again these differences were found to be

statistically significant beyond the 0.01 level. While allowing for variability in coefficients allows the model to over-fit to these particular datasets, both the FPD and SL coefficient variability appears to be logically plausible. As demonstrated in Section 4.2.6, the relationship between $P_{LS}(A)$ and hillslope gradient varies by geology, which will be reflected in the SL coefficients for different regions. In the case of SL coefficients for the 1929 and 1968 earthquakes, differences may be due to the spatial locations of the earthquakes, such that the SL relationships are dominated by different geology types. Rates of seismic wave attenuation with distance from sources vary globally depending on near-surface structures, surface lithology and earthquake magnitude (e.g.: Campbell and Bozorgnia, 2008). While it may be possible to constrain FPD coefficient variability using additional variables and variable interactions, modelling the seismic wave attenuation characteristics of these different regions is beyond the scope of this investigation. Rather, the use of PGA data in place of seismic source distance in the following section accounts for variability associated with different attenuation characteristics.

Table 4-6 Logistic regression statistics for earthquake magnitude, seismic source distance and hillslope gradient model

Variables in red characterise the strength of the seismic forcing
Variables in blue characterise the local stability of hillslopes

Number of observations	38292244
Likelihood ratio chi^2	856569.8300
Model p-value	0.0000
Pseudo R^2	0.2114

					95% confidence interval	
Variable	**Coefficient**	**Standard error**	**z-value**	**p-value**	**Lower bound**	**Upper bound**
M_w	1.7443	0.0210	83.21	0.00	1.7032	1.7854
$FPD(1929)$	-0.0898	0.0003	-259.55	0.00	-0.0905	-0.0891
$FPD(1968)$	-0.1760	0.0011	-163.78	0.00	-0.1781	-0.1739
$FPD(1994)$	-0.1702	0.0019	-91.10	0.00	-0.1739	-0.1666
$FPD(1999)$	-0.1589	0.0007	-228.97	0.00	-0.1602	-0.1575
$FPD(2008)$	-0.1081	0.0004	-271.99	0.00	-0.1089	-0.1073
$SL(1929)$	0.0880	0.0002	488.94	0.00	0.0876	0.0883
$SL(1968)$	0.1035	0.0005	219.24	0.00	0.1026	0.1044
$SL(1994)$	0.0928	0.0008	120.69	0.00	0.0913	0.0943
$SL(1999)$	0.0851	0.0003	297.88	0.00	0.0846	0.0857
$SL(2008)$	0.0718	0.0002	360.50	0.00	0.0714	0.0722
$Intercept$	-18.6080	0.1609	-115.62	0.00	-18.9234	-18.2925

4.3.2 Earthquake magnitude, PGA and hillslope gradient model

Where distributed ground motion data are available for the 1968, 1994, 1999 and 2008 earthquakes, the ground motion proxy variable FPD can be replaced with PGA, to provide a more direct link between $P_{LS}(A)$ and ground acceleration:

Equation 4-10

$$P_{LS}(A) = \frac{1}{1 - e\left(-\left(c_{intercept} + c_{M_w} M_w + c_{\ln PGA} \ln PGA + c_{SL} SL\right)\right)}$$

Here moment magnitude is included to account for differences in shaking duration. Duration tends to increase with earthquake magnitude (Jibson, 2007), and has been shown to influence seismically-induced displacements in landslide masses (Jibson, 2011, Jibson, 2007). Although the natural logarithm transformation of PGA is not required to satisfy model assumptions, it was found to improve the fit of the model and correct for non-linearity in the model log-odds space.

Coefficients and fit statistics are given in Table 4-7 where the coefficient for PGA is allowed to vary by event, while Table 4-8 shows values where the PGA coefficient is held constant. When held constant, a PGA coefficient of 2.5 is attained. When allowed to vary, values range from 1.8 to 4.3, with the 2008 and 1968 events producing the minimum and maximum values respectively. This indicates that the slope of the relationship for PGA varies between earthquakes. However, coefficients for the 1994 and 1999 events are similar with values of 2.6 and 2.8 respectively. Given that the 1994 and 1999 earthquakes were much more densely instrumented with seismic stations and therefore have better constrained Shakemaps than the 1968 and 2008 events, the outliers may be in part a reflection of error associated with this uncertainty. Coefficients for 1994 and 1999 are therefore more likely to provide an accurate representation of the relationship between $P_{LS}(A)$ and PGA. Allowing the PGA coefficient to vary in turn affects the M_w coefficient. This suggests that in the fixed PGA coefficient model, $c_{M_w}$is in part accounting for the variable relationship between $P_{LS}(A)$ and PGA. c_{M_w} in the variable-PGA coefficent model is therefore more likely to be representative of the relationship between $P_{LS}(A)$ and shaking duration associated with M_w.

Figures 4-27 to 4-31 show mapped probabilities derived using coefficients from Table 4-6 (A) and Table 4-8 (C), along with binary grids showing the locations of landslide source areas used to fit the models (B). The spatial distribution of predicted probabilities generally reflects the distribution of discrete hillslope failures. For cases where both PGA and distance based models have been fitted, differences in the spatial distribution of probabilities are evident. These are likely due to inaccuracies in defining the location of fault ruptures and the large uncertainties in regional PGA data.

Table 4-7 Logistic regression statistics for Earthquake magnitude, PGA and hillslope gradient model

Variables in red characterise the strength of the seismic forcing
Variables in blue characterise the local stability of hillslopes

Number of observations	34660262
Likelihood ratio chi^2	478048.77
Model p-value	0.00
Pseudo R^2	0.191

					95% confidence interval	
Variable	**Coefficient**	**Standard error**	**z-value**	**p-value**	**Lower bound**	**Upper bound**
M_w	1.5492	0.0181	85.51	0.00	1.5137	1.5847
$\ln(PGA)$	2.5042	0.0071	353.77	0.00	2.4903	2.5181
$SL(1968)$	0.0804	0.0004	203.20	0.00	0.0796	0.0811
$SL(1994)$	0.1050	0.0006	161.89	0.00	0.1038	0.1063
$SL(1999)$	0.1011	0.0002	418.28	0.00	0.1007	0.1016
$SL(2008)$	0.0588	0.0002	270.58	0.00	0.0584	0.0592
$Intercept$	-17.1010	0.1387	-123.34	0.00	-17.3728	-16.8292

Table 4-8 Logistic regression statistics for Earthquake magnitude, PGA and hillslope gradient model, with PGA interaction term

Number of observations	34660262
Likelihood ratio chi^2	492377.74
Model p-value	0.00
Pseudo R^2	0.196

Variable	Coefficient	Standard error	z-value	p-value	95% confidence interval Lower bound	95% confidence interval Upper bound
M_w	1.0422	0.0200	52.04	0.00	1.0029	1.0814
$\ln PGA(1968)$	4.2826	0.0217	197.34	0.00	4.2401	4.3251
$\ln PGA(1994)$	2.6235	0.0273	96.15	0.00	2.5700	2.6769
$\ln PGA(1999)$	2.7911	0.0119	234.16	0.00	2.7677	2.8144
$\ln PGA(2008)$	1.8030	0.0091	197.47	0.00	1.7851	1.8209
$SL(1968)$	0.0970	0.0005	206.16	0.00	0.0961	0.0980
$SL(1994)$	0.0963	0.0008	122.31	0.00	0.0947	0.0978
$SL(1999)$	0.1104	0.0004	312.83	0.00	0.1097	0.1111
$SL(2008)$	0.0582	0.0002	271.02	0.00	0.0578	0.0586
$Intercept$	-13.3081	0.1533	-86.82	0.00	-13.6085	-13.0000

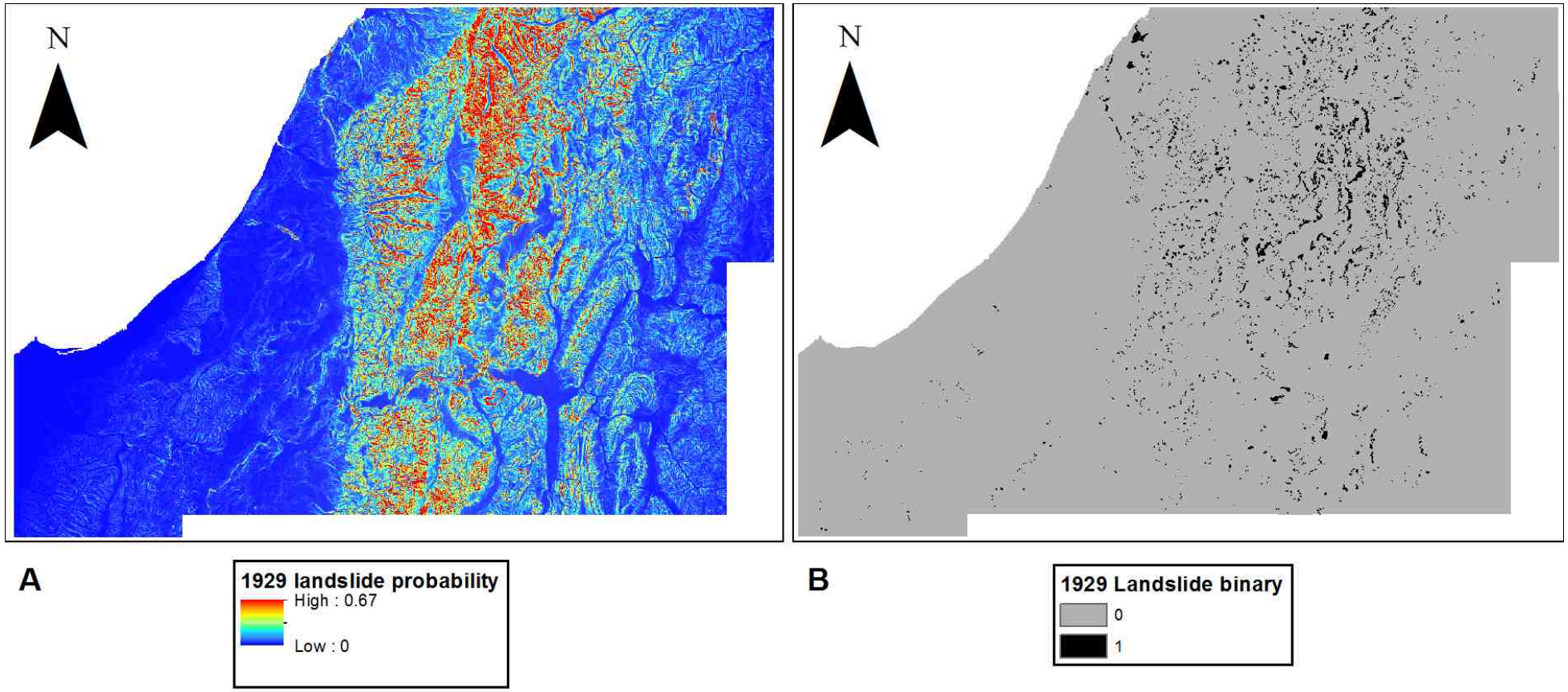

Figure 4-27 Map projected probability values for the 1929 Buller earthquake, derived using coefficients from Table 7 (A) and binary grid showing the location of landslide source areas used to fit the model (B)

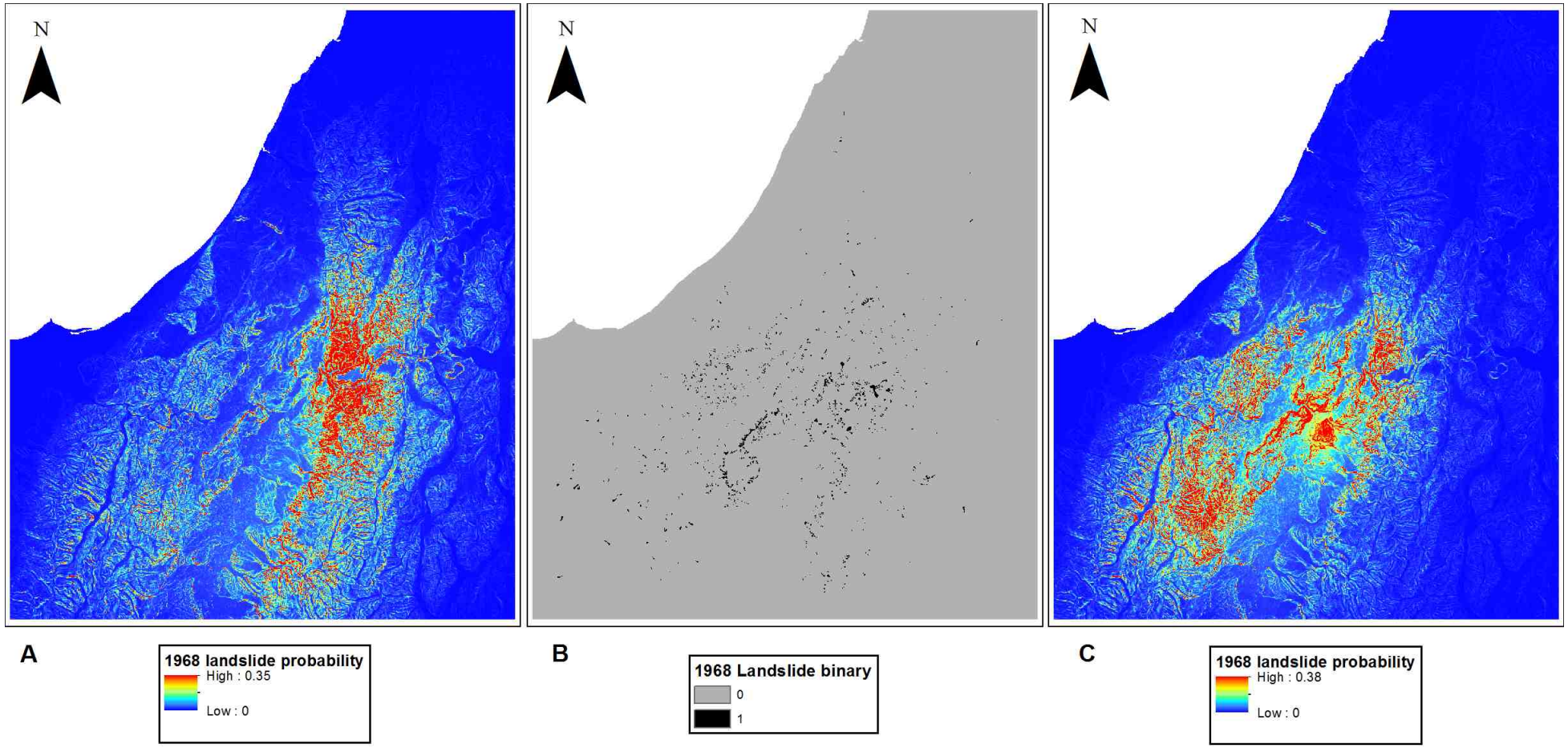

Figure 4-28 Map projected probability values for the 1968 Inangahua earthquake, derived using coefficients from Table 7 (A) and Table 9 (C), and binary grid showing the location of landslide source areas used to fit the models (B)

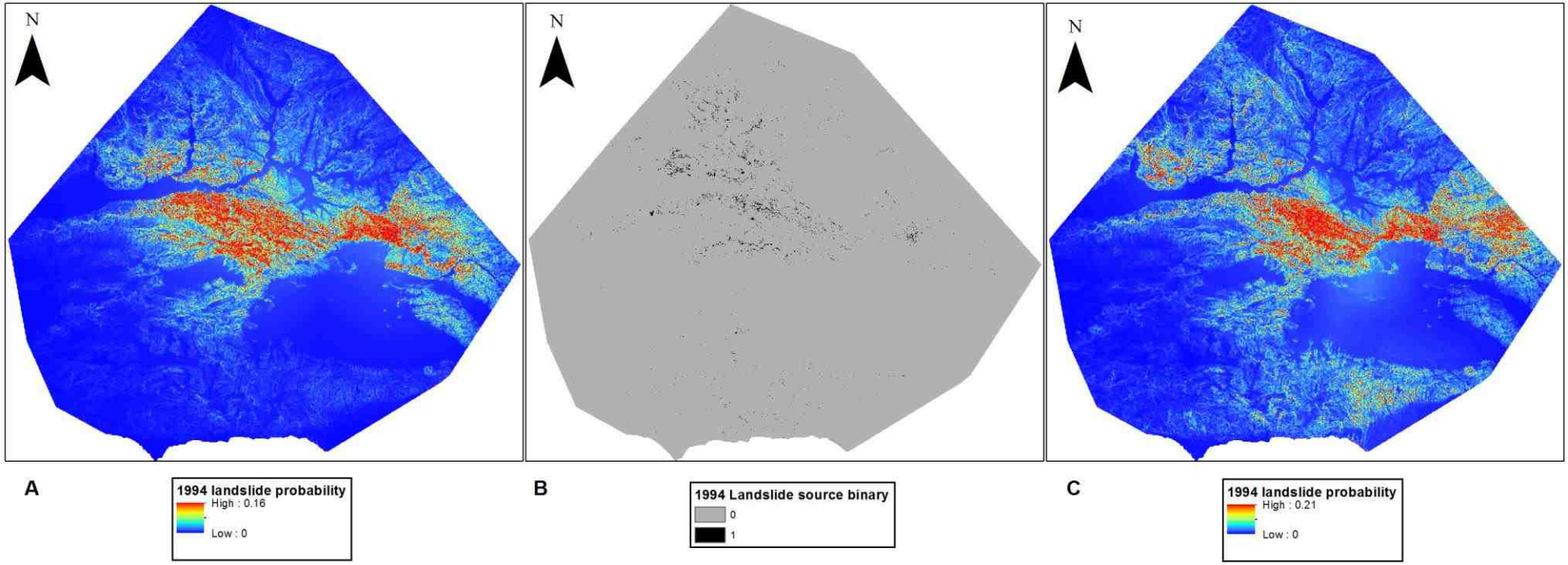

Figure 4-29 Map projected probability values for the 1994 Northridge earthquake, derived using coefficients from Table 7 (A) and Table 9 (C), and binary grid showing the location of landslide source areas used to fit the models (D)

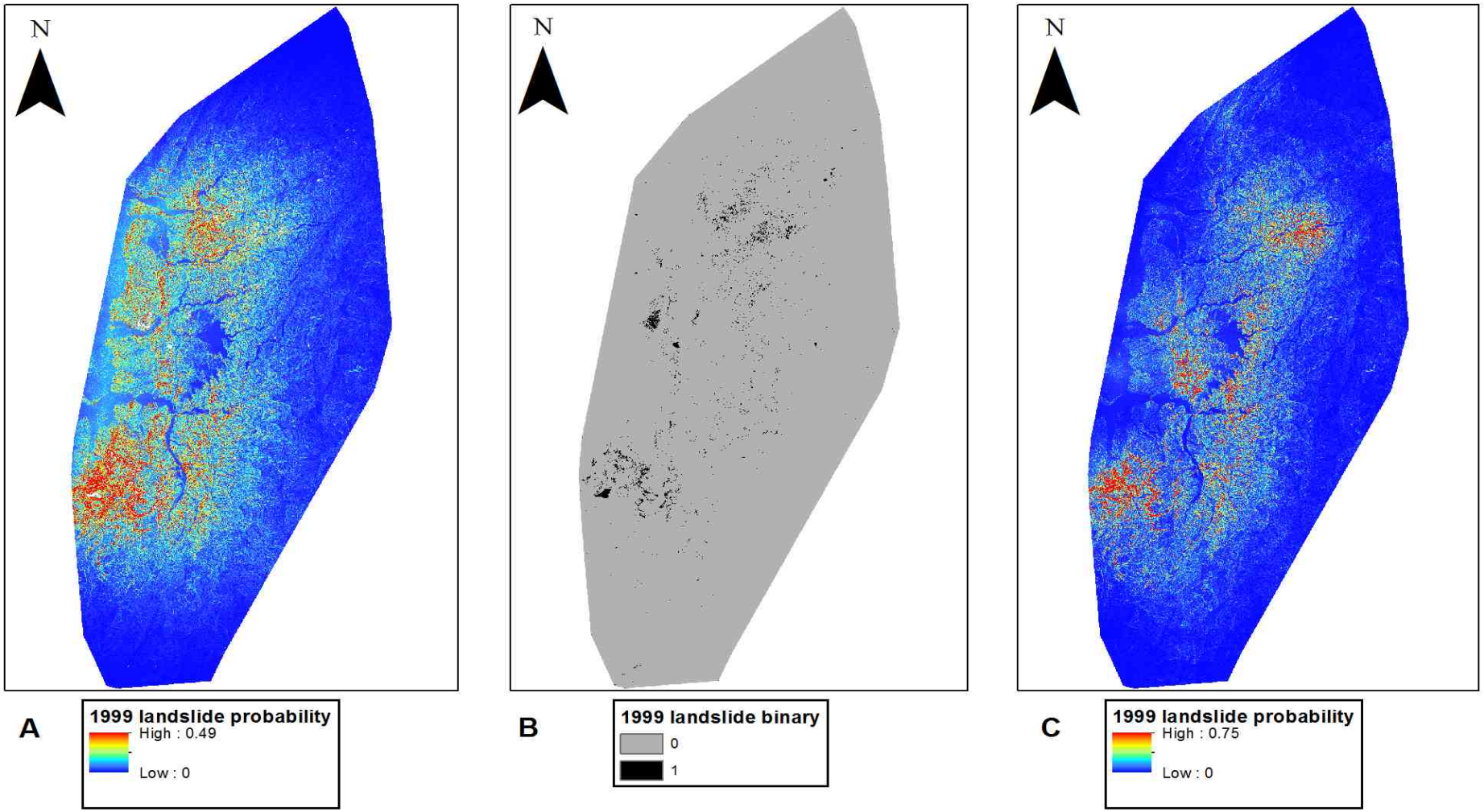

Figure 4-30 Map projected probability values for the 1999 Chi-Chi earthquake, derived using coefficients from Table 7 (A) and Table 9 (C), and binary grid showing the location of landslide source areas used to fit the models (B)

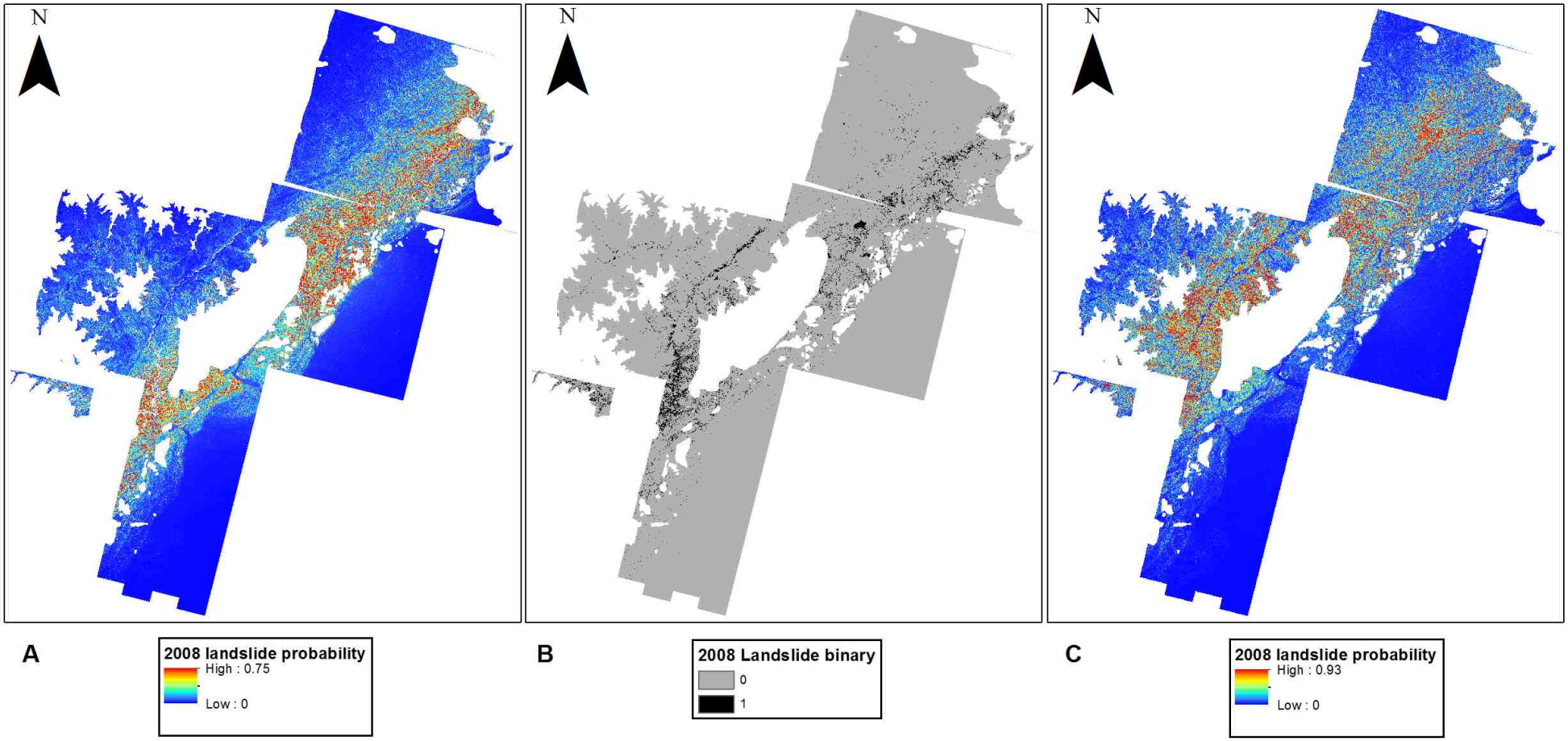

Figure 4-31 Map projected probability values for the 2008 Wenchuan earthquake, derived using coefficients from Table 7 (A) and Table 9 (C), and binary grid showing the location of landslide source areas used to fit the models (B)

4.4 Discussion and Summary

A general model describing the spatial distribution of earthquake-triggered landslides has been derived using data from the five ETL datasets. The spatial probability of hillslope failure is described as a function of the earthquake moment magnitude and the local site PGA and hillslope gradient. Although the values of model coefficients vary between earthquakes, the nature of relationships is consistent for all events, and can be linked physically to the response of hillslopes to seismic ground motions. While other variables accounting for the influence of lithology, topographic site effects, structural controls on hillslope stability and solar radiation are omitted from the model, the effect of these factors was found to be only secondary at this scale of investigation. The simplicity of this model means this it is transferrable between different earthquakes and regions.

As the datasets used to fit the model were limited to landslide areas >11,000 m^2, the validity of the model is limited to these larger landslides. Such larger, deeper failures will generally represent landslides with sliding mechanisms that shear into bedrock beneath. Data used to fit the models will also include some contribution from post-seismic landslides, particularly for the Wenchuan, Buller and Inangahua earthquakes. The main implication of this is that probabilities of coseismic hillslope failure predicted using the general model will be overestimated, particularly when using coefficients specific to these three events. As the analysis was weighted so that all five events contribute equally to the models, this effect will be buffered by the influence of the Northridge and Chi-Chi data. Despite these limitations, the model has substantial potential for use in ETL hazard assessment, as a means for first-order prediction of ETL spatial probability using freely available global data. Though estimates are likely to be conservative and are limited to landslides with an area >11,000 m^2.

Although the focus of previous investigations has been to analyse the predictive capabilities of such models, they can also provide insight into longer-term spatial and temporal patterns of ETL activity. The model cannot be used to determine the discrete locations of hillslope failures, but can used to estimate how often hillslopes with different characteristics might be expected to fail in response to sequences of earthquakes. However, in this respect the model current also has a fundamental

limitation. Although the influences of hillslope shear stress and seismic ground accelerations are captured, in the absence of available data there is no component to account for hillslope material strength. Therefore, neither the spatial distribution nor the temporal evolution of hillslope material strength is included in the model. While the model can be used to describe the spatial distribution of failure probability for individual earthquakes, it cannot be used to analyse how hillslope damage or memory accrued from previous events, associated with strain-accumulation and progressive failure, might influence future events. However, having constrained the influence of these static conditions on hillslope response, this spatial understanding can now be used to investigate how hillslopes undergoing brittle deformation might respond to multiple earthquakes.

Chapter 5 - Hillslope failure and regional-scale landslide activity

In order to investigate how hillslope memory associated with progressive failure affects regional-scale ETL activity, the results of Chapter 4 must be reconciled with an understanding of how hillslopes respond to earthquakes at the site-scale. This chapter establishes a conceptual model using the Newmark sliding block, which provides a simplified but physically accurate conception of earthquake-induced hillslope failure. The model is used to infer the role of hillslope memory in the spatial patterns of landslide activity, and uses further analysis of data from the 1929 and 1968 earthquakes to test this hypothesis. From the model, a mechanism of potential temporal variability in landslide propensity is identified, providing the justification for numerical modelling undertaken in Chapter 6. In Appendix B a short paper summarising the model is provided, which was presented at the 2012 International Symposium on Earthquake-Induced Landslides (Parker et al., 2013).

5.1 Hillslope failure via seismically-induced strain

5.1.1 The failure cycle

By modifying the Newmark model to incorporate strain-softening as a result of permanent displacements (e.g.: Wartman et al., 2005, Kutter, 1983, Crawford and Curran, 1982), hillslope failure can be understood as the product of cumulative, seismically-induced changes in hillslope stability. Building on this it is possible to consider the temporal behaviour of a section of hillslope subjected to multiple earthquakes with return periods of hundreds to tens of thousands of years (depending on the regional seismicity). Over these timescales, one must assume that a section of hillslope fails on multiple occasions in response to the multiple earthquakes that occur. Figure 5-1 illustrates the behaviour of a single section of hillslope, modelled as a Newmark sliding block that experiences a time series of earthquakes. The hillslope undergoes a cycle in which the shear strength decays from its peak towards its residual level via strain-softening, in response to earthquake ground accelerations, until it reaches the point of failure. Each time the hillslope fails, the weakened material of the landslide mass is assumed to be unobstructed and evacuates the shear surface. A new, stable section of hillslope is then formed, where the topography is defined by the

previous shear surface. As the new section of hillslope has yet to experience strain-softening, the shear strength effectively resets to its peak level and the process restarts. This process of repeated weakening and failure is termed the 'failure cycle'.

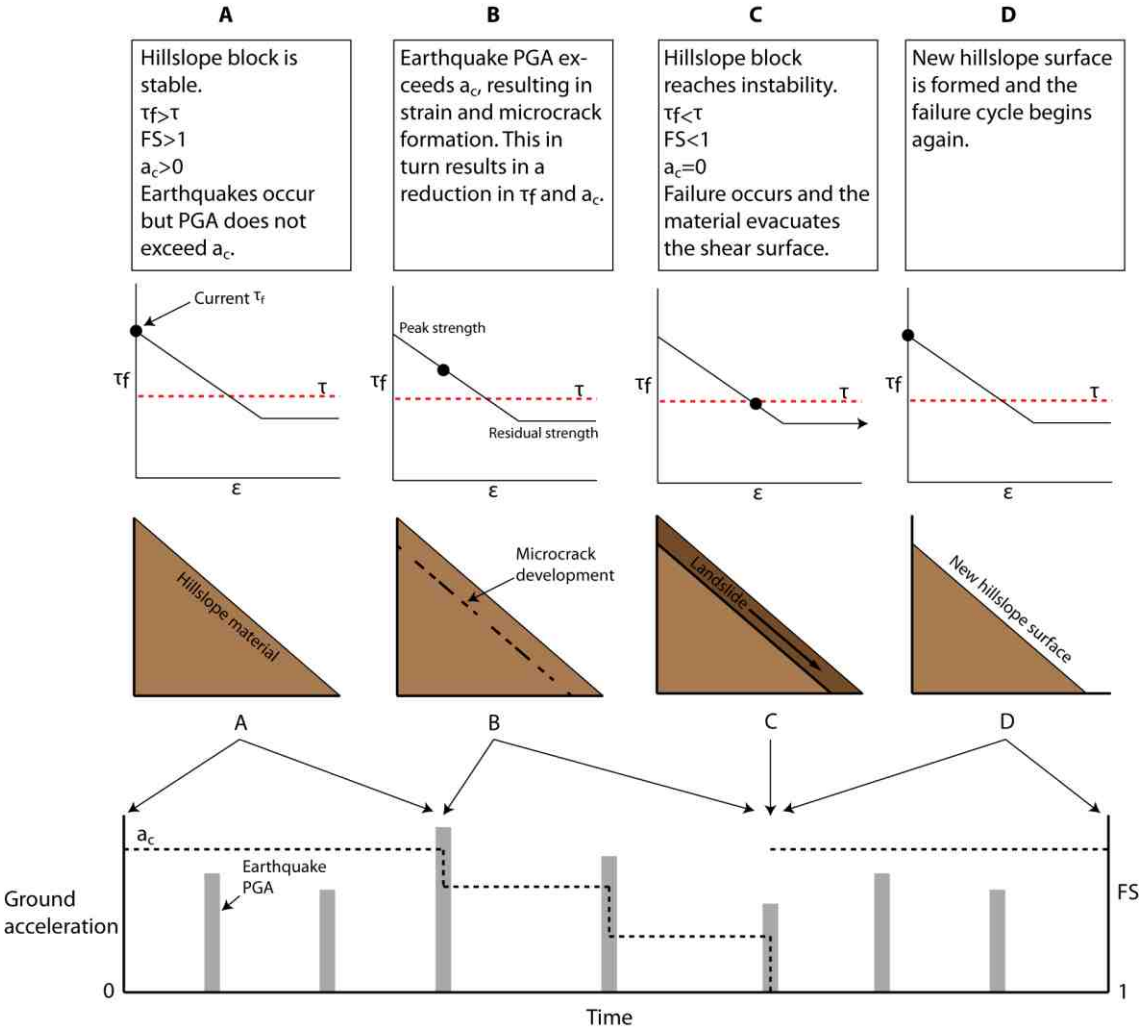

Figure 5-1 Illustration of the failure cycle occurring in a single section of hillslope, modelled as a Newmark sliding block that experiences a time series of earthquakes. A: Initially τ_f at its peak is greater than τ such that the section of hillslope is stable. During this stage earthquakes occur, but the peak ground acceleration (PGA) does not exceed the critical acceleration (a_c), such that no permanent deformations occur in the hillslope material, i.e. any deformation will be elastic and recoverable. B: Earthquake accelerations begin to exceed (a_c), resulting in permanent deformation and softening, such that each time a_c is exceeded, FS and a_c decrease. C: The hillslope reaches the point of instability – shear strength is less than shear stress, $FS < 1$ and a_c is effectively 0 – and failure occurs. D: Following failure a new hillslope surface is formed, where the topography is defined by the previous shear surface and the section of hillslope is once again stable - the shear strength is greater than the static stress, $FS > 1$ and $a_c > 0$.

5.1.2 Failure cycles in populations of potential landslide masses

In order to extrapolate this model to the regional scale of 10^2 – 10^5 km^2 over which earthquakes can trigger landslides (Keefer, 2002, Rodríguez et al., 1999, Keefer, 1984), the behaviour of multiple sections of hillslope must be considered. This can be

achieved by considering a hypothetical landscape with hillslopes composed of a population of potential landslide masses (PLMs), which are again modelled as Newmark sliding blocks that undergo strain-softening (Figure 5-2). A single ridge-to-stream hillslope profile may comprise of a single PLM or multiple PLMs of different sizes, which will determine the size of landslides that occur on that hillslope. Commensurate with the distribution of triggered landslides (e.g.: Stark and Guzzetti, 2009, Brunetti et al., 2009, Malamud et al., 2004b) the magnitude-frequency distribution of PLMs must scale over several orders of magnitude, and PLMs will have a range of hillslope gradients as defined by the topography.

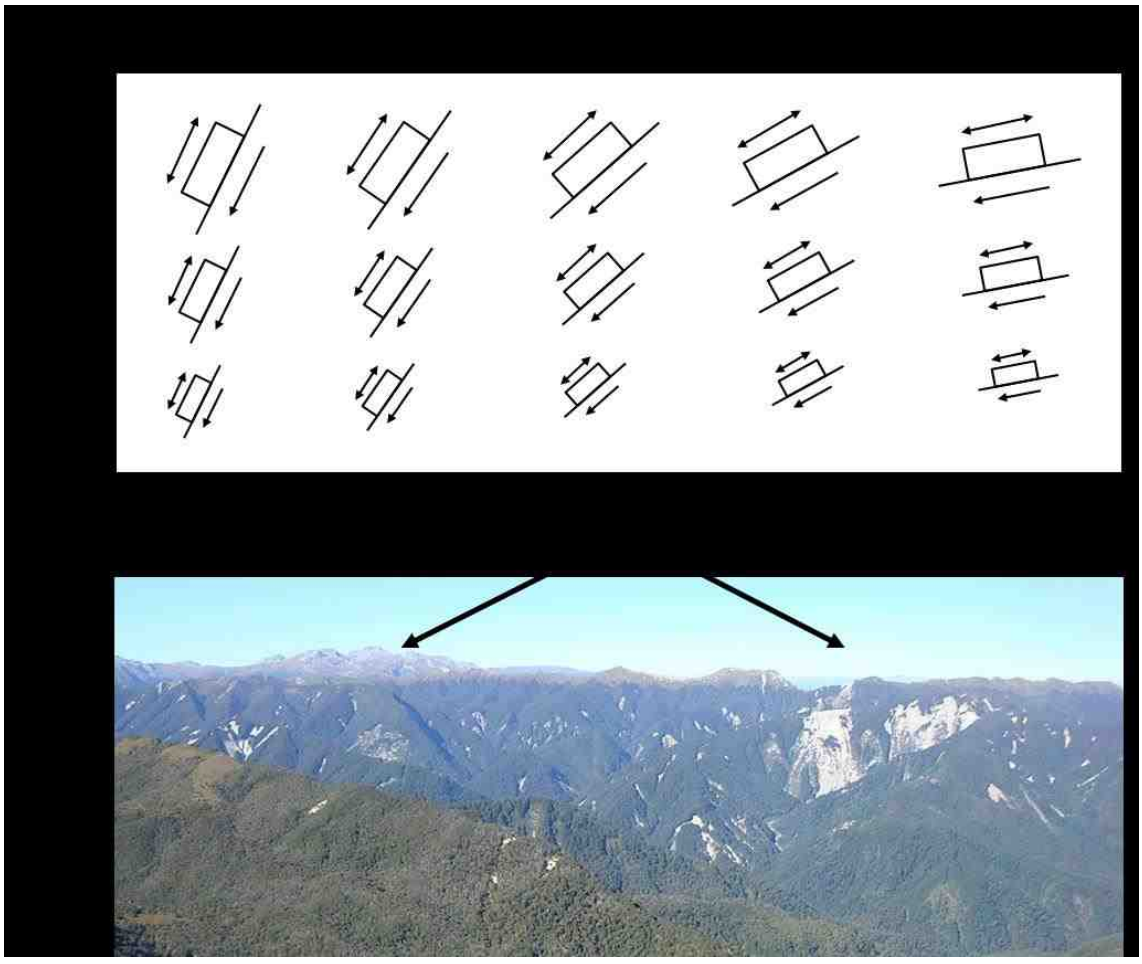

Figure 5-2 Illustration of a hypothetical landscape with hillslopes composed of a population of potential landslide masses, modelled as strain-softening Newmark sliding blocks with a range of gradients and different scales. Each section of hillslope can be thought of as a PLM at some stage in the failure cycle. The PLMs have a range of different gradients, defined by the topography, and different scales commensurate with the magnitude-frequency distribution of landslides that occur. At any point in time some hillslope sections will be close to the point of failure with low FS values, while others will be more stable.

As the thickness and downslope length of landslide masses is positively correlated (e.g.: Hovius et al., 1997, Brunetti et al., 2009, Guzzetti et al., 2008, Stark and Guzzetti, 2009, Korup, 2006), for larger landslide masses there is greater potential for strain to

be distributed non-uniformly throughout a larger zone of material. In order to produce the same reduction in shear strength, more displacement is thus likely to be required for larger PLMs. As internal deformations within landslide masses are not modelled by the Newmark method, shear strength is assumed to decay with shear strain (shear displacement divided by downslope PLM length) rather than shear displacement, in order to account for this effect. To generate the same net reduction in strength, longer PLMs must undergo larger displacements than shorter PLMs; i.e. maintaining the same displacement to length ratio or strain. This increase in displacement required for failure with landslide size is reflected in differences in observed displacement thresholds for small, shallow and large, deep-seated landslide masses (e.g.: Jibson et al., 2000, California Geological Survey, 2008, Jibson and Michael, 2009).

As in Section 5.1.1, it is assumed that at the point of failure the failed material evacuates the shear surface, and the shear strength resets to its peak value. Of course, as detachment and failure of material occurs, new hillslope surfaces are also formed from deposition of this material downslope, which in turn forms part of new PLMs. In order to isolate the effect of material strength evolution without imposing ill-constrained assumptions regarding material transport and surface modification from secondary processes, mobilisation and deposition is not modelled. Rather, it is assumed that all sections of hillslope are spatially independent of one another and that landslide material is simply removed from the system each time hillslope failure occurs. Topography is a static component in the model, such that the geometry of hillslopes does not change as failures occur, i.e.: the form of failure is that of a pseudo-infinite slope. This assumption is not unreasonable for a steady-state landscape, in which erosion keeps pace with incision and uplift, and may be particularly valid for landscapes dominated by earthquake-triggered landslides as opposed to rainfall-triggered landslides. While landslides triggered by rainfall cluster in valley bottom areas (Megahan et al., 1978), landslides triggered by earthquakes and post-seismic rainfall events are more distributed across all parts of hillslope profiles (Hovius et al., 2011), producing roughly planar, uniform hillslopes (Densmore and Hovius, 2000).

Each PLM has the following characteristics, which determine its behaviour in response to seismic accelerations (Figure 5-3):

1. A peak strength, τ_{fp} (which is the maximum shear resistance)

2. A residual strength, τ_{fr} (this is the lowest shear strength a PLM can exhibit. However, failure ($FS < 1$) will occur before the residual strength is reached as long as the shear stress exceeds the residual strength)

3. A rate of material strength decay with permanent strain, k ($\frac{\Delta\tau_f}{\Delta\varepsilon}$)

4. A slope gradient, β (which determines the static shear stress)

5. A downslope length, l (which determines the relationship between displacement and strain)

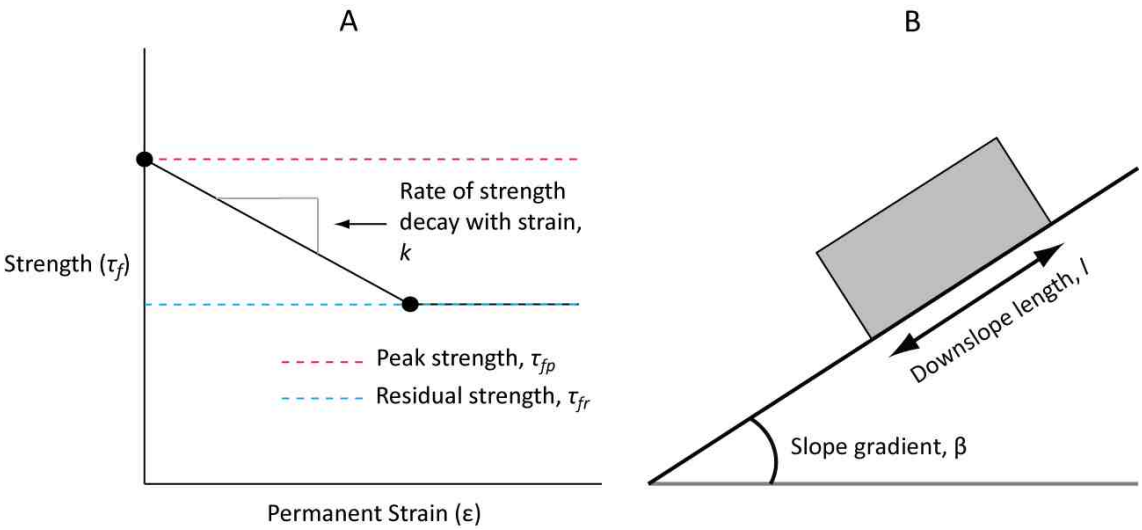

Figure 5-3 Illustration of potential landslide mass (PLM) characteristics that determine the response to seismic accelerations. A: PLM stress-strain relationship; B: Schematic diagram of PLM geometry.

5.1.3 Model assumptions and limitations

This model provides a simplification of the mechanics controlling regional-scale patterns of ETL activity in landscapes formed of brittle materials. As no model will capture the full complexity of ETL processes, it is important to establish the limits of the model and its appropriateness for use in this investigation.

In terms of the geotechnical basis of hillslope behaviour, the model carries many assumptions from the infinite-slope and Newmark methods. By characterising all landslides as translational, sliding blocks, the model is valid for failures that exhibit this form and movement mechanism. The model does not account the influence of circular

or irregular failure geometries and does not apply to landslides with different movement mechanisms that are not addressed in this study, such as topples or tensile detachments. As the infinite-slope model does not consider the influence of lateral stresses on hillslope stability, PLMS cannot interact spatially. Material in adjacent slopes is known to exert stabilising forces, the removal of which can result in instability (e.g.: Milledge, 2008, Chen, 1981, Dietrich et al., 2007). However, the assumption of spatial independence means that cases of failure retrogression or cascading failure of adjacent hillslopes are not considered. This is an appropriate simplification for this investigation, as the influence of temporal changes in hillslope stability via progressive failure is the focus, rather than changes in topography and ambient stress distributions.

Although horizontal seismic accelerations are the only forcing that drives hillslope failure in the model, landslide mass response is also affected by other directional components of ground accelerations (e.g.: Harp and Jibson, 1995b, Zhang et al., 2013, Moore et al., 2011, Wasowski et al., 2013), which are not considered here. Using the Newmark model to predict displacements also carries additional inaccuracies, outlined in Section 2.2.3. Results from previous investigations and those presented in Chapter 4 suggest that horizontal accelerations, and Newmark displacements derived from them, strongly reflect the distribution of landslides at the regional-scale (Meunier et al., 2007, Jibson et al., 2000, Jibson et al., 1998). Therefore, spatial and temporal patterns of landslides predicted using the model should be representative of real landslide activity.

Although increasing the pore-pressure in a Newmark sliding block model will temporarily reduce the FS for as long as the pore-pressure remains elevated, once pore-pressure drops FS will return to its previous level. Permanent changes in FS, associated with displacements induced by pore-pressure, are not and cannot be simulated using the Newmark approach. Therefore, the model cannot be used to investigate the temporal-evolution of landslide activity in response to precipitation events or seismically-induced changes in pore-pressure. However, the model can be used to suggest how the propensity for landslides triggered by changes in pore-pressure evolves in response to earthquake accelerations. For example, this can be achieved by posing the following question: following a reduction in FS due to

seismically-induced strain, what change in pore-pressure would be required to further reduce FS to less than 1? For simplicity, the numerical simulations presented in Chapter 6 only consider failure induced by seismic accelerations. However, this concept is revisited in Chapter 7 when discussing post-seismic rainfall-triggered landslides.

The major modification made to the Newmark approach is that shearing resistance evolves with shear strain. Although this is characterised using a single shear strength value that decays with the total strain across the PLM, in real materials strain localises and different segments experience strength decay at different points in time (Petley et al., 2005b, Petley et al., 2005a). This investigation is concerned with the stability of the whole landslide mass and whether or not slope failure occurs, rather than the distributed failure mechanics within individual PLMs. It is therefore appropriate to analyse the stability of each PLM in terms of a single FS value. As a consequence of this, it is also assumed that hillslopes at or close to $FS = 1$ do not undergo time-dependent cascading failure under gravity (Petley et al., 2005b, Petley et al., 2005a) and therefore do not fail once seismic shaking has stopped.

The stress-strain behaviour for all PLMs is assumed to be the same, with no change in material properties with landslide depth and confining pressure. This means that all hillslope failures occur via the same brittle deformation process, and there is no transition toward more ductile behaviour for very large landslides with deep shear surfaces (Hudson and Harrison, 1997). As the fate of failed material is not considered and the shear strength of hillslopes is assumed to reset to its peak following failure, the model is specific to landslides where failure occurs in previously unsheared brittle materials. The model is not representative of landslide activity associated with the remobilisation of previously failed material accumulated on hillslopes, nor does it apply to areas in which landslides form in ductile materials.

In order for failure to occur, the static shear stress must be greater than the residual strength. Where the residual strength is greater than the static shear stress, the PLM will never reach the point of failure, although it will continue to experience plastic deformation with no further strength loss each time a_c is exceeded. Some gently sloping hillsides on which reactivating landslides experience repeated displacements in

response to seismic accelerations may be interpreted as exhibiting this behaviour (e.g.: Cole et al., 1998). While the model can potentially be used to investigate cases of reactivating landslides at residual strength, these do not produce the hillslope failures that are the focus of this investigation.

While this model is both generalised and represents a specific type of failure mechanism, it is also widely applicable to ETLs. Physically, the model represents the key components of the triggering process of first-time ETLs via brittle failure of rock. When applied at the regional-scale the Newmark approach produces predicted displacements that correlate empirically with patterns of ETL activity. As such, the model can provide an appropriate tool for investigating the effect of hillslope material memory on spatio-temporal patterns of landslide activity associated with earthquakes, within the limits outlined above.

5.2 Interpretation of earthquake-triggered landslide distributions

Now that a model linking the site-scale evolution of hillslope progressive failure to regional-scale ETL activity has been proposed, it is possible to revisit a number of empirical observations and explore how they relate to the model corollaries. This can provide evidence to establish the validity of the model and identify how the model should be applied to address the research questions.

5.2.1 Spatial patterns of landslide density

Over time, PLMs with different characteristics will progress through the failure cycle at different rates in response to ground accelerations. In this section the ways in which different PLM and seismic wave characteristics contribute to the rate at which PLMs progress through the failure cycle (hereafter termed the "progression rate") are examined, allowing analysis of observed characteristics of landslide distributions. Local factors controlling the progression rate can be broken down qualitatively into those pertaining to material properties, those governed by static stresses associated with slope geometry and those controlled by the magnitude and duration of seismic accelerations. The effect of each of these is discussed, assuming that the other factors remain constant.

In terms of PLM material properties, the peak strength and rate of strength decay control the progression rate. PLMs with lower peak strength must undergo less weakening to reach the point of failure compared with PLMs with higher peak strength. PLMs with a higher rate of strength decay have a higher progression rate than those with lower rates of strength decay. Differences in hillslope failure probability observed for different geological units (Parise and Jibson, 2000, Khazai and Sitar, 2004, Ohlmacher and Davis, 2003) may be interpreted in terms of variations in material stress-strain behaviour that define strength-decay due to deformation (e.g.: Plumb, 1994, Hoek et al., 2005, Liang et al., 2007).

As a general approximation, PLMs with steeper gradients have larger shear stresses, meaning that the static FS is lower than for PLMs with shallow gradients. In terms of the Newmark model this corresponds to a lower critical acceleration value, resulting in displacement occurring under lower ground accelerations, and larger displacements developing under strong accelerations. Larger displacements result in greater strain-softening and thus greater reductions in FS. Thus for each earthquake, steeper PLMs experience a greater reduction in relative strength (and thus stability) than do shallower PLMs. Over time this translates to a higher progression rate for steeper PLMs. This is reflected in observed patterns of increasing failure probability with hillslope gradient, common to all earthquakes analysed in Chapter 4. However, hillslope gradient and peak strength are unlikely to be independent as higher shear strength is required to support steeper slopes. Observed relationships between landslide probability and hillslope gradient will therefore also reflect this interaction.

As the amplitude of seismic accelerations increases, critical acceleration thresholds are exceeded in a larger number of PLMs. As accelerations continue to increase above critical acceleration levels, the displacement produced by each seismic wave also increases. Further, as the duration of accelerations above the critical acceleration increases, the cumulative displacement generated also increases. For each earthquake PLMs in regions experiencing seismic accelerations with higher amplitudes and longer durations have a higher progression rate and thus a higher proportion of PLMs that fail. This is reflected in observed patterns of increasing landslide probability with PGA and earthquake magnitude observed for all five earthquakes analysed in Chapter 4.

The results of Chapter 4 indicate increasing failure probability with the amplitude of seismic accelerations and local hillslope gradient, with variations in relationships for different geological units. According to the approach used here, the probability that a hillslope fails in any given earthquake reflects relative spatial variations in progression rate. Predicted spatial probabilities can therefore be understood as providing a spatial metric of progression rate and strain-softening resulting from the triggering earthquake; areas of hillslope with high failure probability having a higher progression rate than areas with low probability. This is also supported by observed relationships between estimated Newmark displacements and spatial landslide probability (Jibson et al., 2000).

5.2.2 The influence of hillslope memory on landslide activity

While current landslide models, including those developed in Chapter 4, are capable of expressing spatial patterns of hillslope failure probability, their lack of consideration of hillslope material memory represents a potentially large source of uncertainty. According to this conceptual model, whether or not a section of hillslope fails in an earthquake depends on the state of the PLM in its failure cycle at the onset of shaking. As earthquakes also drive PLMs through the failure cycle, memory of previous earthquakes will be important in determining which hillslopes undergo failure. This means that for two identical and sequential earthquakes (with the same spatial pattern of ground accelerations), failure will occur for different subsets of PLMs. The apparently stochastic nature of landslide occurrence and the inability of current models to identify the particular hillslopes that undergo failure, may in part result from not knowing the condition of each PLM within its own failure cycle at the onset of shaking.

Combined with this, generally smaller areas of the landscape experience failure than do not, even in regions identified as having extreme landslide susceptibility. For example, Figure 5-4 shows $P_{LS}(A)$ plotted by hillslope gradient for areas within 5 km of the seismic source, for the five events analysed in Chapter 4. Note that the data is truncated at 60^{o} due to a lack of data for steeper slopes. Within this region of high ground acceleration, at 40^{o} gradient a maximum of only 10% of hillslopes underwent failure, and even at 60^{o} no more than 50% failed. This implies that the majority of

PLMs are not sufficiently unstable, or close to failure at the onset of seismic shaking, to reach the point of failure as a result of the earthquake excitation. However, PLMs that do not fail may have experienced a major reduction in their FS, and thus would require less loading to bring them to the point of failure. By this reasoning the population of unfailed hillslopes should contain a memory of past events, which can be tested using landslide inventories for sequential earthquakes.

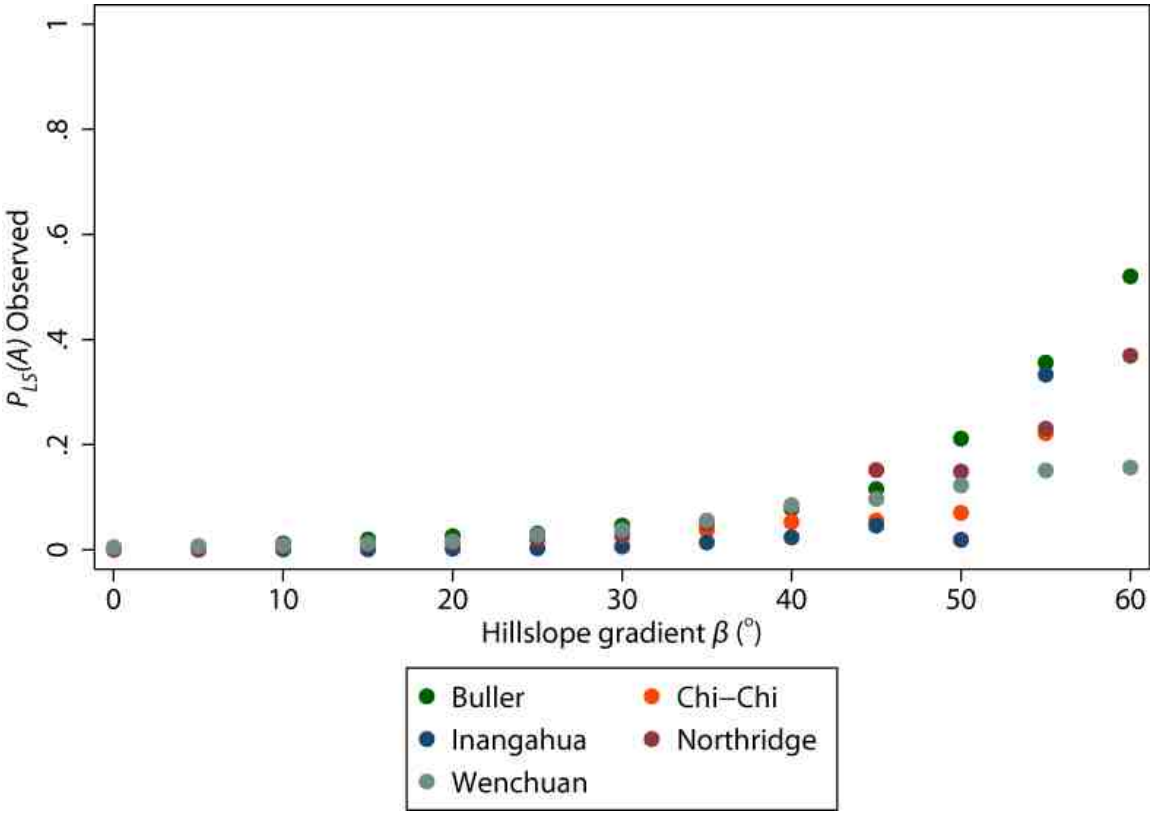

Figure 5-4 Landslide density ($P_{LS}(A)$) plotted by hillslope gradient (5° bins) for areas within 5 km of the seismic source, for the Buller, Inangahua, Chi-Chi, Wenchuan and Northridge earthquakes.

5.2.3 Formulation and testing of a landscape memory hypothesis

Testing for the influence of hillslope material memory on landslide activity is required to establish the validity of this conceptual model. If the model is correct and landslide distributions are partially controlled by strain accumulated through time, then evidence of memory should be present. The datasets from the 1929 Buller and 1968 Inangahua earthquakes, which occurred in close spatial proximity and generated landslide-triggering seismic accelerations across an overlapping region, provide the basis for testing this hypothesis. If the landscape exhibits memory, then areas of hillslope that did not reach the point of failure in the 1929 earthquake but in which a_c was exceeded, should have undergone strain-softening and therefore be capable of

reaching the point of failure under weaker seismic accelerations in the 1968 earthquake. Of the areas of hillslope that were affected by the 1929 earthquake but did not fail, there should be an anomaly in the empirical probability of landslide occurrence during the 1968 earthquake, which is correlated with the expected spatial pattern of seismic strain-softening during the 1929 earthquake. This can be tested by examining the difference between observed and predicted failure probabilities for the 1968 earthquake, relative to the failure probability for the 1929 earthquake, for hillslopes that did not fail in 1929 (Figure 5-5).

The performance of the 1968 logistic regression model in describing the patterns of landslide activity varies significantly with the distribution of 1929 hillslope failure probabilities. For 1929 failure probabilities in the range 0.000~0.003 (Figure 5-5 Sector 1) observed 1968 failure probabilities are generally equal to or less than predicted values, while for 1929 failure probabilities in the range 0.003~0.02 (Figure 5-5 Sector 2) observed 1968 failure probabilities are generally greater than predicted failure probabilities. Note that these residuals exceed the 95% confidence interval lower and upper bound of expected stochastic variability. For 1929 failure probabilities in the range 0.02~0.3 (Figure 5-5 Sector 3) observed and predicted 1968 failure probabilities again converge. The shape of the failure probability curve reflects the fact that the results of the two failure probability models are partially correlated where their input variables are the same, but are also partially decoupled due to the different locations of their seismic sources. These three sectors are shown spatially in Figure 5-6, overlain by the locations of 1968 landslides.

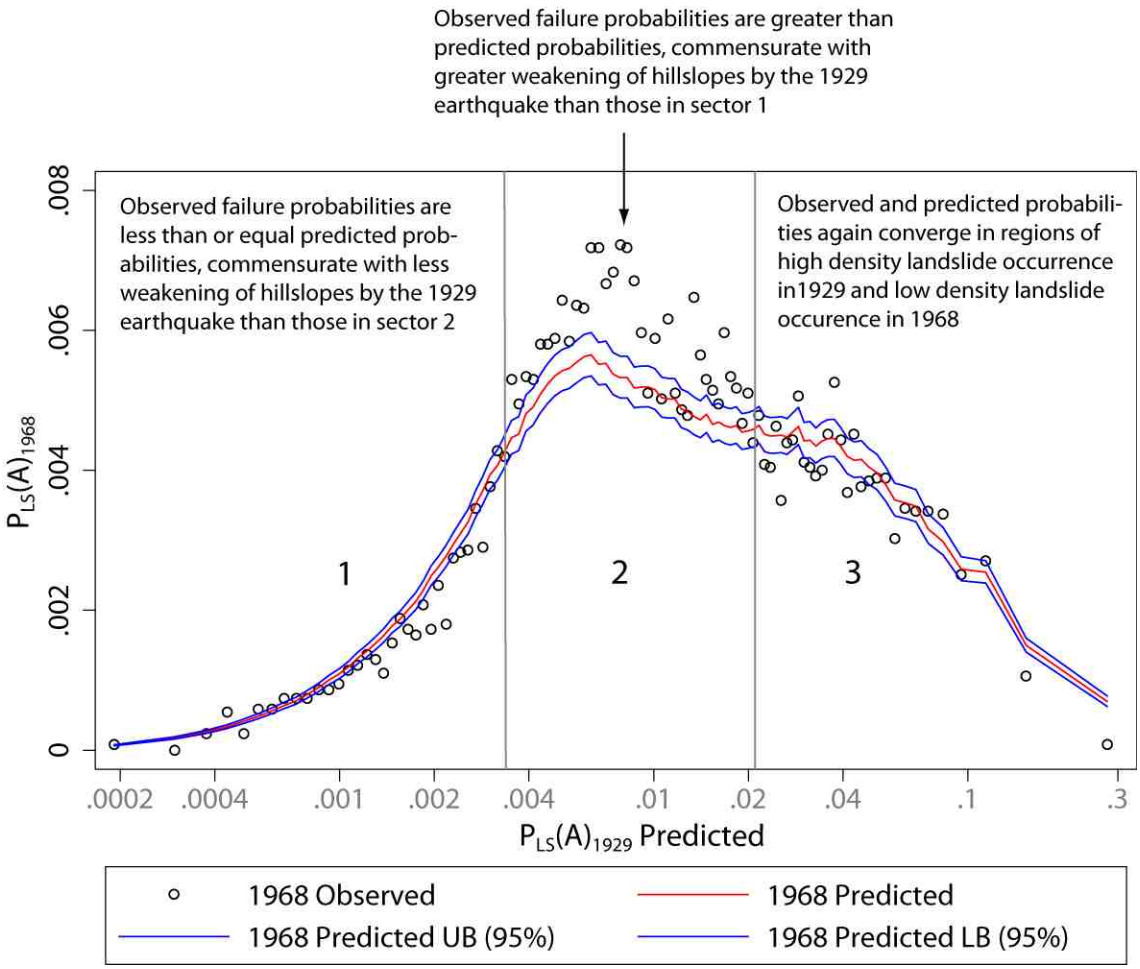

Figure 5-5 Plotted comparison of observed and predicted hillslope failure probability for the 1968 Inangahua earthquake distributed by predicted probability for the 1929 earthquake, for hillslopes that did not fail in the 1929 earthquake. The variable of predicted failure probability for the 1929 earthquake ($\hat{P}_{LS}(A)_{1929}$, Figure 4-24) was divided into 100 equal frequency (1%) bins, such that each bin contains the same number of observations. Within each bin, the mean predicted (Figure 4-25 A) and observed (Figure 4-25 B) failure probabilities for the 1968 earthquake were calculated. These means represent the proportion of hillslopes that, having not failed in the 1929 earthquake, did fail in the 1968 earthquake. The differences between observed and predicted probabilities show where the distribution of landslides departs from that predicted by the probability model, which does not account for the influence of hillslope memory. Where the black circles fall above the red line, observed probability is greater than that predicted by the fitted model, and vice-versa. Note that regions of Quaternary sediments were removed from this analysis as these regions generally represent low-lying topography and exhibit low levels of landslide occurrence, which in turn resulted in uncertainty in fitted coefficients. A logarithmic x-axis is used to account for the spread of the binned data.

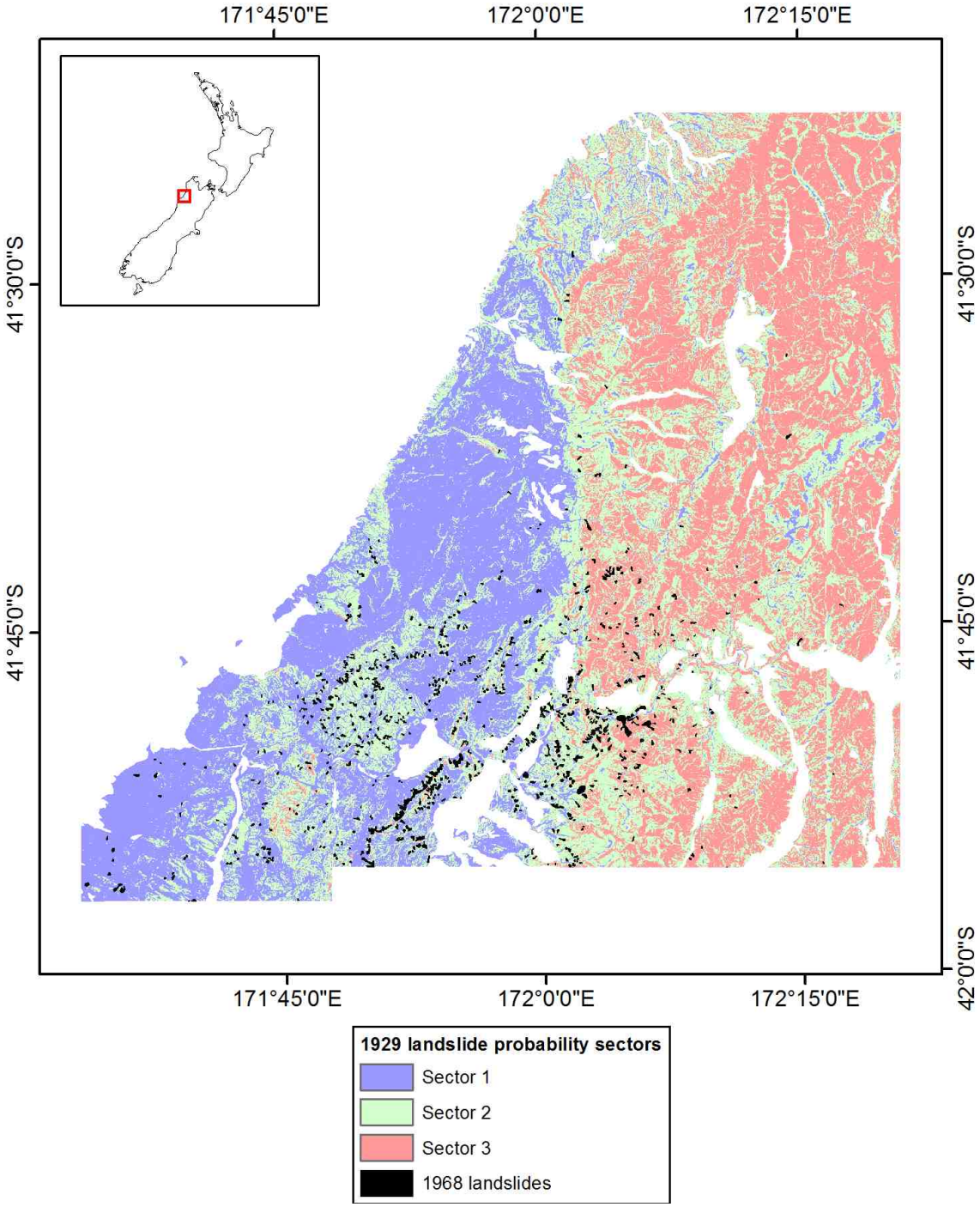

Figure 5-6 Map of delineated sectors of the 1929 landslide probability space in Figure 5-5, overlain by mapped landslides from the 1968 earthquake. Sector 1: observed 1968 landslide probabilities are generally equal to or less than predicted values; sector 2: observed 1968 landslide probabilities are generally greater than predicted probabilities; sector 3: observed and predicted 1968 landslide probabilities are roughly equal.

The pattern of failure probability residuals in sectors 1 and 2 reveal that expected if hillslopes that did not fail in 1929 had been weakened and were more susceptible to failure in 1968. Of hillslopes that had a higher predicted probability of failure in 1929 but did not fail, a larger than expected proportion failed in 1968, suggesting that these hillslopes were weakened by strain accumulated in 1929. However, the convergence of

observed and predicted 1968 failure probabilities in sector 3 is counter to the expected pattern, suggesting that hillslopes that would have experienced the most progression through the failure cycle in 1929 do not show increased sensitivity to earthquake-triggered landsliding.

If this signal shown is due to hillslope memory, the convergence of failure probabilities in sector 3 may be an artefact of data acquisition. Landslides from the 1968 earthquake are likely to have been unidentifiable in areas already heavily disturbed by landsliding from the 1929 earthquake. This will particularly be the case if 1968 landslides occurred on hillslopes that had already failed in 1929. Additionally, very few 1968 landslides would have been expected in regions of sector 3, owing to the large distances from the 1968 seismic source. This would have in turn made 1968 landslides in sector 3 more difficult to identify and more likely to be censored from the mapping. Thus an underestimation of 1968 failure probability could be reasonably expected in areas of highest 1929 failure probability. Conversely, if not due to errors in the landslide data, this result may suggest that hillslopes with the highest failure probability in 1929 experienced no increase in landslide propensity. This may appear contrary to the conceptual model, as unfailed hillslopes in areas of high 1929 probability are expected to have undergone significant weakening. However, when the large number of 1929 failures in sector 3 occurred, only the most stable hillslopes would have remained stable. If the high critical acceleration thresholds of these hillslopes were not exceeded, then no change in landslide propensity would be expected. In addition to suggesting the priming of hillslopes for future landsliding, the results may therefore also reveal more complex elements of the regional-scale hillslope response.

As no systematic errors in appear in the model relationships between landslide probability and the predictor variables, another possible explanation is that a temporal change in some other factor, which was not constrained in analysis, is driving this pattern of errors. A potential candidate could be a difference in the spatial distribution of precipitation and ground water conditions between the earthquakes. If the hillslopes in sector 2 experienced wetter conditions in 1968 than in 1929, while hillslopes in sectors 1 and 3 did not, then this could explain their enhance susceptibility to landsliding. The absence of distributed precipitation data for the time of the

earthquakes means that this cannot be tested quantitatively. However, an isolated increase in the susceptibility of sector 2 hillslopes would require these areas to be separated spatially from those in sectors 1 and 3, which is not the case. Therefore, at this stage, the hillslope memory effect of accrued damage from the 1929 earthquake is considered to be the most likely explanation for the anomaly in landslides triggered by the 1968 earthquake.

5.3 A mechanism of temporal changes in landslide propensity

While evidence from landslide datasets appears to support the conceptual model, current data can only provide a limited insight into the effect of hillslope failure processes on regional-scale ETL activity. This is primarily due to the limited temporal coverage of landslide inventories and difficulties in controlling for the influence of both earthquake and rainfall events that trigger landslides. However, the model can be used to hypothesise how hillslope memory may influence landslide activity in response to sequences of earthquakes, by considering how the aggregate behaviour of populations of landslide masses may evolve with time.

The total proportion of landslide masses that fail in a particular earthquake depends on the population of PLMs primed for failure – those sufficiently close to failure prior to the earthquake that they will reach the point of failure as a result of the earthquake. Critically, this population may not necessarily be of a constant size. As PLMs progress through the failure cycle at different rates, and as strong seismic events cause the simultaneous failure and reset of multiple PLMs, there is potential for variability in the number and area of PLMs primed for failure. The result of changes in this population is a variability in landslide propensity through time and therefore in the aggregate sensitivity of landscapes to earthquake-triggered hillslope failure. This is illustrated in Figure 5-7 by considering hypothetical stability (FS) distributions. In A, the PLM population has high levels of accumulated strain, with lower FS values and a larger subset primed for failure in the next earthquake. Therefore, the landscape is in a more sensitive state with higher landslide propensity. In B, PLMs have low levels of accumulated strain, fewer are primed for failure and the landscape is in a less-sensitive state. Landslide propensity is lower and the same earthquake will trigger fewer

landslides. However, as earthquakes occur the cluster of PLMs in B may accumulate strain and move into the failure zone, resulting in an increase in landslide propensity.

How landslide propensity evolves through time will depend on the influence of different magnitude earthquakes in moving PLMs into the failure zone via strain accumulation, and out of the failure zone via hillslope failure. If more PLMs move into the failure zone than reach the point of failure during a given earthquake, landslide propensity will increase, and vice-versa.

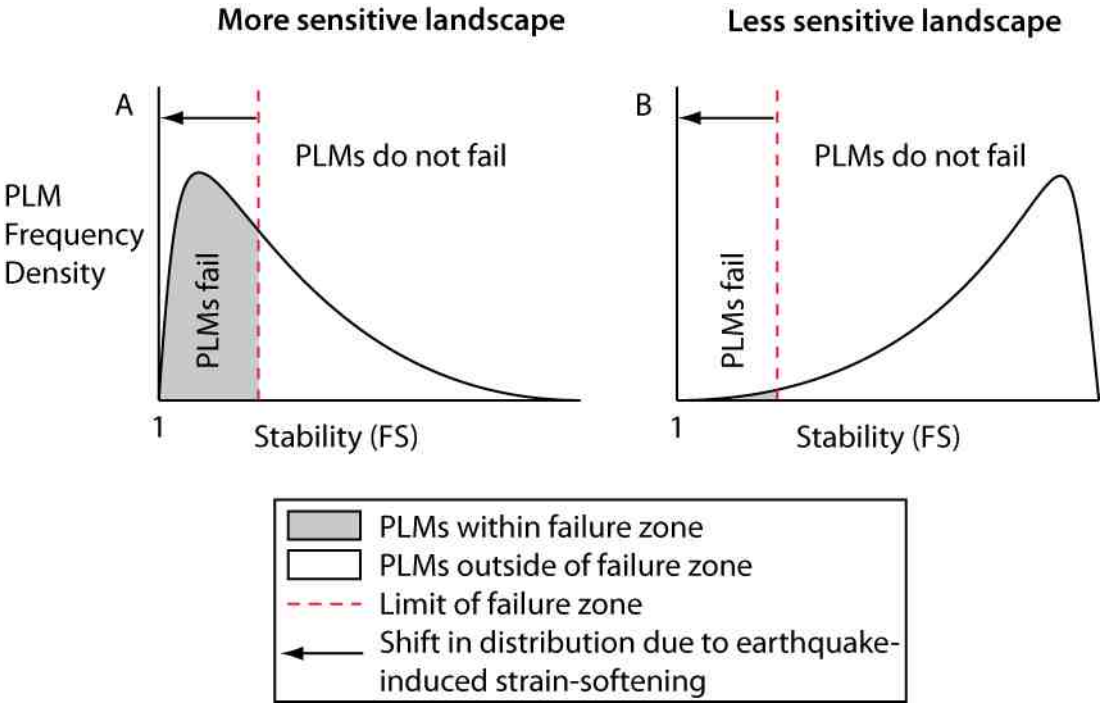

Figure 5-7 Hypothetical stability (FS) histograms for a landscape in more sensitive and less sensitive states. The frequency distributions represent the stability of a population of PLMs, while the failure zone represents the range of stability values within which PLMs will fail during the next large earthquake. A: a large subset of PLMs is primed for failure and will fail in the next large earthquake. B: the subset of PLMs primed for failure is smaller and therefore the same earthquake will trigger fewer landslides.

5.4 Summary

The conceptual model outlined in this chapter provides a means of understanding observed patterns of regional-scale ETL activity in terms of the evolution of strain-dependent hillslope failure. Although the conception of landslide processes provided by the model is simplified, it possesses the key mechanisms controlling earthquake-triggered hillslope failure in brittle materials. The model has been used to suggest how spatial patterns of landslide probability (Chapter 4) are the product of differences in the relative rate at which hillslopes with different characteristics undergo failure. The

apparent stochastic nature of ETL activity has been linked to the inability of current models to determine the stage of different hillslopes in their failure cycle. The time-dependent behaviour of the landscape predicted by the model is reflected in further analysis of landslide distributions for the Buller and Inangahua earthquakes, suggesting that the first earthquake may have primed hillslopes for failure during the second earthquake.

An interesting hypothesis arising from the above discussion is that regional-scale landslide propensity may vary through time, depending on the pattern of strain accumulation within the population of PLMs in hillslopes. Changes in landslide propensity due to this mechanism provide a potential explanation for observed global variability in levels of landslide activity associated with earthquakes of similar magnitude (Section 2.3.3), and temporal changes in landslide activity following large earthquakes (Section 2.3.4). However, this temporal behaviour cannot be studied in detail using current empirical data. By simulating the behaviour of this system numerically, the following chapter seeks to build a better understanding of the landscape response to large earthquakes, by investigating how and to what extent landslide propensity varies through time.

Chapter 6 - Numerical modelling of regional-scale landslide activity

The conceptual model proposed in Chapter 5 suggests that a model of regional-scale landslide activity that incorporates hillslope progressive failure may be capable of producing temporal variability in the sensitivity of landscapes to earthquake-triggered landsliding. However, due to the limited temporal coverage of empirical data, the nature and intensity of this variability is currently unknown. Using the model developed in Chapter 5, this chapter uses numerical simulations to explore ways in which landslide propensity, in hillslopes formed of brittle materials, may change through time in response to earthquakes. From the outset, it is important to emphasise that the purpose of this modelling is not to recreate particular events or series of events, but rather to understand how landslide populations in hillslopes behave and what model outputs can tell us about the performance of real landscapes in response to earthquakes. While this modelling approach could be developed into a fully spatial simulation, the focus here is not towards exploring spatial variability in the behaviour of landslide distributions, which was covered in Chapter 4. Rather a population of hillslopes is modelled using a single set of spatial characteristics (a single hillslope gradient and distance from the seismic source). The model is used to explore how levels of accumulated strain in landslide populations evolve in response to earthquakes and the resulting temporal variability in landslide propensity. This Chapter outlines the model framework, calibration and an assessment of variability in landslide propensity at two temporal scales: (1) the response to individual large earthquakes, and (2) long-term patterns of variability in response to synthetic time series of multiple earthquakes. The implications of the model outputs for understanding the behaviour of real landscapes are then discussed in detail in Chapter 7.

6.1 Model architecture

The modelling approach is a preliminary attempt to simulate the aggregate behaviour of populations of evolving landslide masses in the hillslopes of active mountain ranges. The model is composed of two elements: 1) a hillslope component in the form of a population of PLMs; and, 2) an earthquake component in the form a magnitude-frequency distribution and seismic wave attenuation function. This section describes the underlying algorithms and framework.

6.1.1 Hillslope component: potential landslide mass population

As proposed in Chapter 5, PLMs in hillslopes are modelled as a population of Newmark sliding blocks that undergo strain-softening behaviour. Each PLM is assumed to behave as an independent infinite slope block. The static FS of each PLM is:

Equation 6-1

$$FS = \frac{\tau_f}{\tau}$$

where τ_f is the total basal shear strength of the shear plane, and τ is the total stress acting along the shear plane. τ is defined as a function of the PLM gradient, β (see Section 2.1.3):

Equation 6-2

$$\tau = \tan\beta$$

By defining τ in this manner, it is assumed that FS is independent of the depth of the failure plane, and the requirement of imposing poorly constrained estimates of landslide material density and failure plane depth is eliminated. τ_f is similarly defined as a static coefficient of friction, equivalent to:

$$\tau_f = \tan\phi$$

Newmark displacements (D_N, cm) are determined using the simplified Newmark model, derived by Jibson (2007):

Equation 6-3

$$ln\, D_N = -2.710 + log[\left(1 - \frac{a_c}{PGA}\right)^{2.335} (\frac{a_c}{PGA})^{-1.478}] + 0.424M_w$$

This is the most accurate of available models for estimating Newmark displacements at large scales, while avoiding the impractical computational demands of the Newmark approach (Section 2.2.3). In order to simulate strain-softening of the hillslope material, the basal shear strength (τ_f) evolves as strain accumulates within the landslide mass. As discussed in Section 5.1.2, the model assumes that material weakening is a function of strain ($\varepsilon = \frac{D_N}{l}$) rather than displacement (D_N). τ_f therefore decays as a function of

strain (ε) from the peak strength (τ_{fp}) to the residual strength (τ_{fr}) at a constant rate set by the parameter k (Figure 6-1).:

Equation 6-4

$$\tau_{f[n+1]} = \begin{cases} \tau_{fp} - \varepsilon\, k\,, & \tau_{f[n]} > \tau_{fr} \\ \tau_{fr}, & \tau_{f[n]} \leq \tau_{fr} \end{cases}$$

This strain-weakening function is a simplification of the curved geometry commonly seen for Earth material stress-strain behaviour (Petley and Allison, 1997), and assumes distinct transitions between elastic, strain-weakening and residual phases. In accordance with the Hooke's law, no permanent displacement occurs prior to the point at which peak strength is exceeded, after which permanent displacements occur and shear strength decays as a linear function of strain. Although the stress-strain behaviour of rock is highly variable (Jaeger et al., 2008, Bell, 2000), as long as there is a decay from $\tau_f = \tau_{fp}$ to $\tau_f = \tau$, then hillslope failure will take place. Therefore, a constant rate of strength decay is assumed for simplicity.

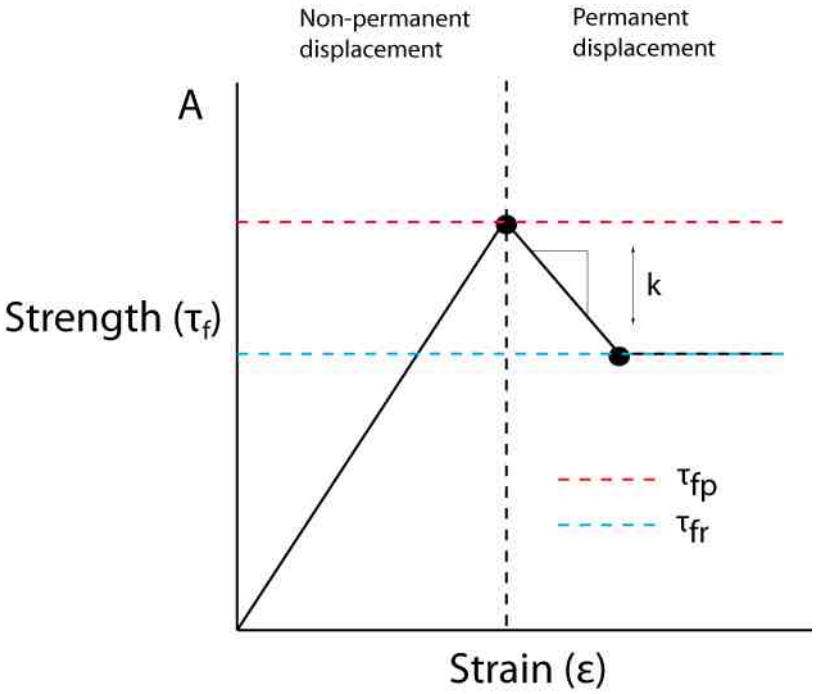

Figure 6-1 Model parameters τ_{fp}, τ_{fr} and k, illustrated on an idealised stress-strain curve.

ε is irreversible and increases cumulatively through each failure cycle. Failure occurs when $\tau_f < \tau$, such that $FS < 1$. Once failed, τ_f resets to τ_{fp}, ε resets to zero and the PLM retains the same gradient and length. Note that as Equation 6-3 predicts the total

displacement produced by each earthquake based on a_c at the onset of shaking, τ_f is recalculated after each earthquake rather than evolving continuously with strain. An artefact of this is that Newmark displacements are underestimates of those that would actually occur if strain-softening were fully incorporated into the rigorous Newmark model. However, the effect of this on PLM behaviour is compensated for by calibrating τ_{fp} and k, as described in Section 6.2.

When a slope reaches the point of failure, a proportion of the strength decay (εk) predicted for that earthquake may be left 'unused' i.e.: the PLM reaches $FS < 1$ before the full amount of strain for that earthquake has occurred, such that $\varepsilon k - (\tau_{f[n]} - \tau) > 0$. In this case, the residual strength decay may be carried over to the next model iteration, i.e.: the underlying potential landslide mass. If the earthquake PGA is less than the critical acceleration for the PLM at peak strength, $a_c(\tau_{fp})$, then no residual strength decay is carried over, as the ground acceleration is not sufficient to deform the new, undamaged hillslope. However, if the PGA is greater than the critical acceleration for the PLM at peak strength, then strength decay is carried over as follows. The total strength decay that the earthquake would produce for the PLM at peak strength, $\varepsilon k_{\tau_{fp}}$, is calculated using Equation 6-3 and Equation 6-4. This is then down-scaled according to the proportion of strength decay left 'unused', and subtracted from τ_{fp} to give τ_f for the next iteration:

Equation 6-5

$$\tau_{f[n+1]} = \begin{cases} \tau_{fp} - \left(\varepsilon k_{\tau_{fp}} \dfrac{\varepsilon k - (\tau_{f[n]} - \tau)}{\varepsilon k} \right), & PGA > a_c(\tau_{fp}) \\ \tau_{fp}, & PGA \leq a_c(\tau_{fp}) \end{cases}$$

When subjected to a series of earthquakes, each PLM experiences progression through the failure cycle and undergoes failure each time $\tau_f < \tau$. This full process is illustrated in Figure 6-2. As discussed in Section 5.1.3, hillslope gradients do not change during the simulation, such that the topography is assumed to remain constant.

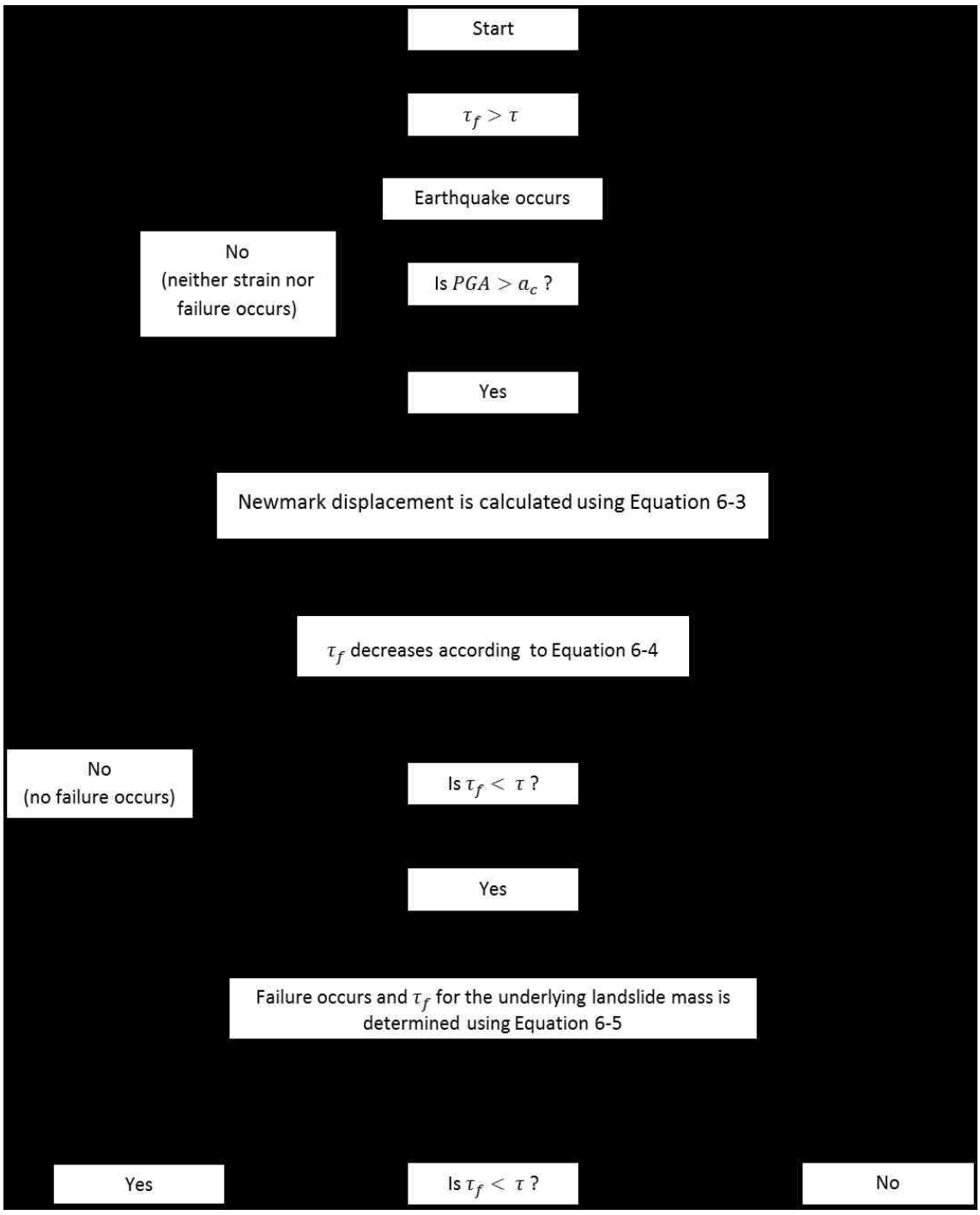

Figure 6-2 Flow diagram of the full failure cycle simulation sequence

6.1.2 PLM magnitude-frequency distribution

The distribution of failed landslide mass (FLM) areas inevitably reflects the distribution of PLM areas. When using a power-law distribution of PLM areas, the distribution of FLM areas also exhibits a power-law, corresponding with characteristic landslide magnitude-frequency distributions (Pelletier et al., 1997, Hovius et al., 1997, Hovius et al., 2000, Dai and Lee, 2001, Guzzetti et al., 2002, Malamud et al., 2004a, Malamud et al., 2004b, Van Den Eeckhaut et al., 2007). The PLM magnitude-frequency (MF)

distribution is characterised using a bounded inverse power-law (Equation 2-13[2]), using the method provided by Clauset et al. (2009). The distribution is valid over the interval A_{min} : A_{max} (m^2). Landslide areas ($A_{L,}$ m^2) are defined by selecting *n* equally spaced quantiles from a power-law distribution, using the inverse cumulative form of Equation 2-13[2]:

Equation 6-6

$$A_L = A_{min}(1 - r_n)^{\frac{-1}{\alpha_{PLM}-1}}$$

where α_{PLM} is the power-law scaling exponent and r_n is a vector of the interval 0 to $1 - (\frac{A_{max}}{A_{min}})^{1-\alpha_{PLM}}$, at spacing 1/n. α_{PLM} is calibrated in Section 6.2.1, based on the model output value α_{FLM}, the scaling exponent for the distribution of FLMs. Although different values of n and A_{max} are used in the modelling, A_{min} is set to 11,000 m^2, corresponding to the limit on landslide size used when fitting hillslope failure probability models (Section 4.3).

6.1.3 PLM geometry

In order to generate and analyse model outputs, it is important that various components of the landslide geometry can be defined. Components of geometry important to this investigation are:

1. Landslide source area, A_{LS} (m^2) - as used in Chapter 4 to define landslide probability. Note that A_{LS} differs from the full landslide area (A_L), which includes zones of runout and deposition in addition to the source area.

2. Landslide mass downslope length, l (m), which is required for calculation of shear strains.

Scaling relationships between A_L, A_{LS} and l have received limited quantitative study, so here were defined using data from the five landslide inventories. For each individual landslide, full landslide areas were first calculated. Landslide source areas were then

[2] $p(x) = \frac{\alpha-1}{x_{min}}\left(\frac{x}{x_{min}}\right)^{-\alpha}$

extracted via the methodology outlined in Section 3.1.8. Finally, landslide source lengths were estimated by measuring the long-axis of each individual landslide source zone, which visual inspection of the landslide data showed to be generally representative of the landslide source length in the downslope direction.

A_{LS} increases proportionally with A_L, as shown in Figure 6-3. A linear model fitted to this data using least-square regression shows that on average landslide source areas are just less than half of full landslide areas. This relationship reflects the link between A_{LS} and A_L imposed by using the median landslide elevation to extract the landslide source area. The relationship can be expressed as:

Equation 6-7

$$A_{LS} = 0.459\, A_L$$

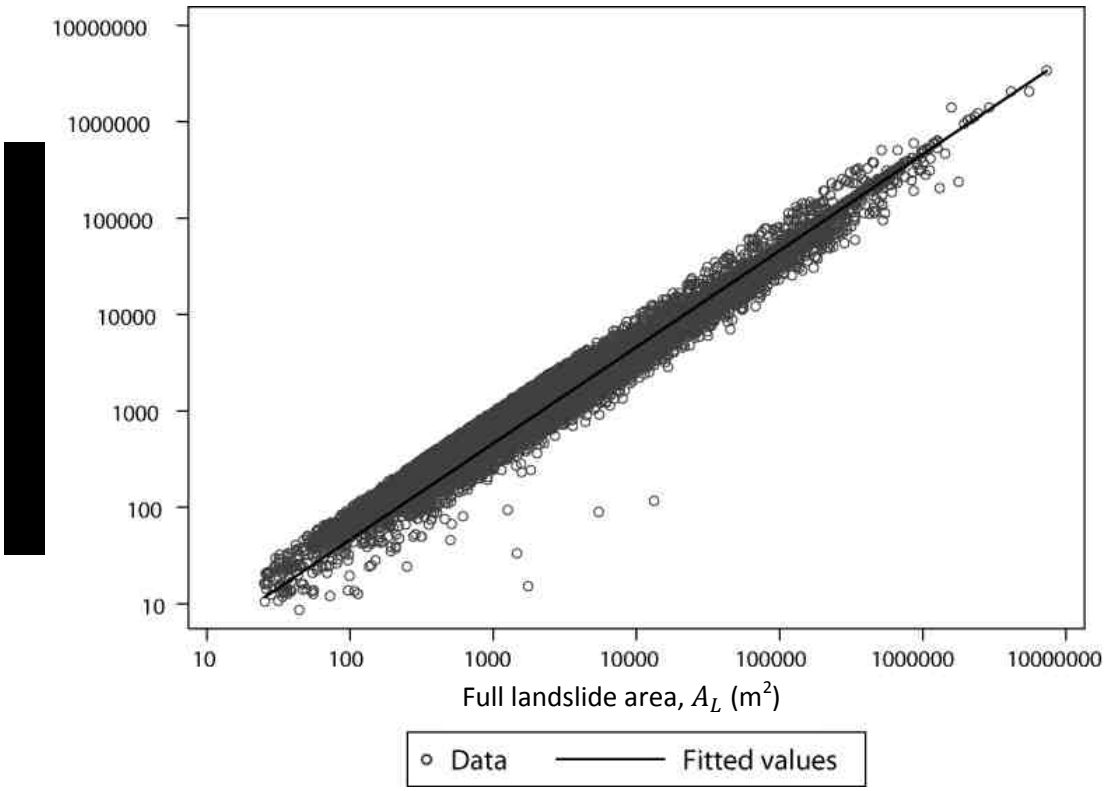

	A_{LS}
A_L coefficient	0.459
t-value	1,227.52**
R^2	0.96
Number of observations	68,596

** *p*<0.01

Figure 6-3 Scatter plot of relationship between full landslide area (A_L) and landslide source area (A_{LS}), and regression output statistics

l was found to increase in proportion to $\sqrt{A_{LS}}$, corresponding to:

$$A_{LS} \sim l^2$$

The relationship and fitted regression is shown in Figure 6-4, and the relationship can be expressed as:

Equation 6-8

$$l = 1.973 \sqrt{A_{LS}}$$

The coefficient of 1.973 suggests that on average the length of landslides is roughly double the width.

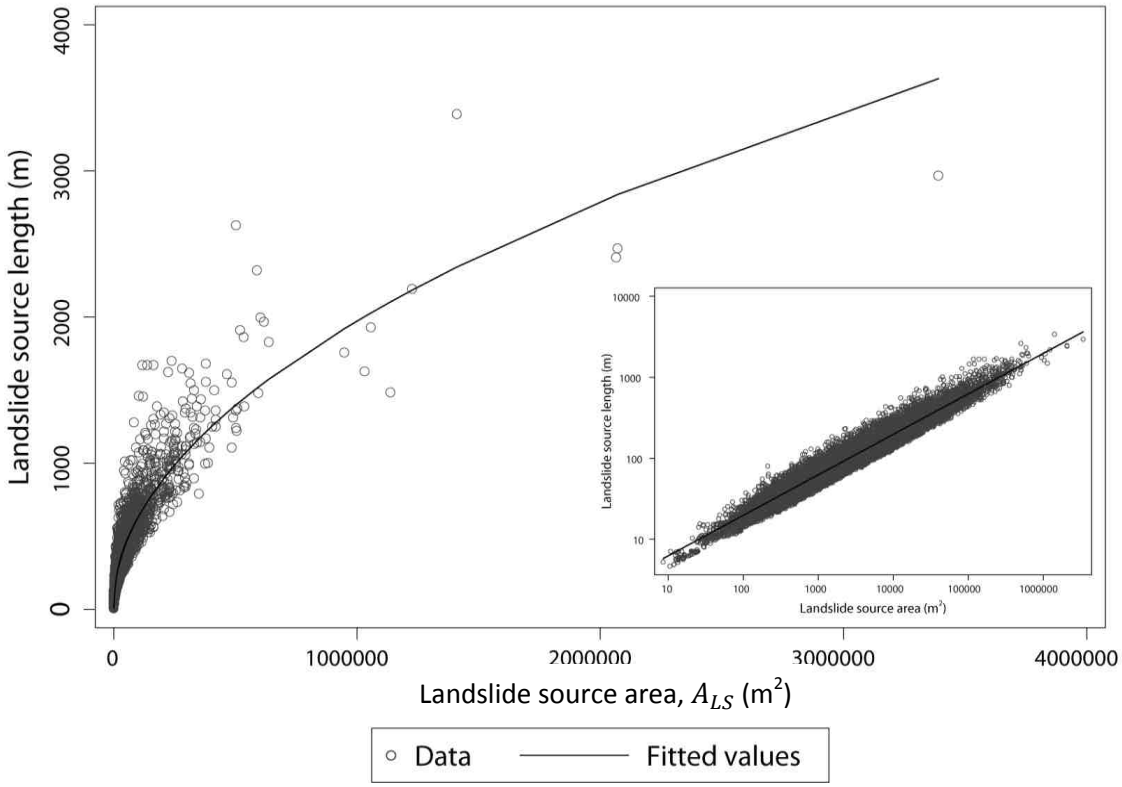

	l
$\sqrt{A_{LS}}$ *coefficient*	1.973
t-value	1,077.77**
R^2	0.94
Number of observations	68,596

** p<0.01

Figure 6-4 Scatter plot of relationship between landslide source area (A_{LS}) and landslide source length (l), and regression output statistics

6.1.4 Seismic component: Earthquake magnitude and PGA time series

The response of PLMs to earthquakes is dependent on the earthquake magnitude and PGA (Equation 6-3). The model therefore requires the generation of synthetic time series for these variables.

The Gutenberg-Richter (GR) recurrence law is the standard approach for modelling earthquake magnitude distributions (e.g.: Bak et al., 2002, Olami et al., 1992, Stafford, 2011). For engineering and probabilistic hazard assessment purposes, this is commonly defined as a doubly-bounded exponential distribution (Cornell and Van Marke, 1969). The probability distribution function (PDF), cumulative distribution function (CDF) and the inverse CDF can be expressed as:

Equation 6-9: Earthquake magnitude PDF

$$f_M(m) = \frac{\delta exp\big(-\delta(m - m_{min})\big)}{1 - exp\big(-\delta(m_{max} - m_{min})\big)}$$

Equation 6-10: Earthquake magnitude CDF

$$F_M(m) = P(M < m | m_{min} \leq m \leq m_{max}) = \frac{1 - exp\big(-\delta(m - m_{min})\big)}{1 - exp\big(-\delta(m_{max} - m_{min})\big)}$$

Equation 6-11: Earthquake magnitude inverse CDF

$$m = m_{min} - \frac{1}{\delta}\ln\Big(1 - F_M(m)\Big(1 - exp\big(-\delta(m_{max} - m_{min})\big)\Big)\Big)$$

Where m is the earthquake magnitude, and m_{min} and m_{max} are the minimum and maximum magnitudes generated. $\delta = \ln(10)\, b$, where b is the GR b-value. The upper and lower magnitude thresholds are imposed to prevent prediction of non-zero probabilities for magnitudes up to infinity, and to eliminate very small earthquakes that greatly increase the computational demands of the model whilst having little effect on hillslope stability. m_{max} is commonly governed by geological criteria, which define the maximum magnitude a region is capable of generating (e.g.: Kijko, 2004). b describes the relative likelihood of large and small earthquakes. As b increases, the number of higher magnitude earthquakes decreases compared to those of lower magnitudes. Across large areas and over long time scales $b \sim 1$ (Kulhanek, 2005), although spatial and temporal variations in b have been identified (Wiemer et al., 1998, Gerstenberger et al., 2001). Globally b-values range between 0.5 and 1.5 (e.g.: Bayrak et al., 2002, Kulhanek, 2005), with variations ascribed to differences in crustal stress levels, material heterogeneity (Mogi, 1962), and thermal gradients (Warren and Latham, 1970). Temporal variations include lower b-values prior to large earthquakes and higher b-values following large earthquakes (Suyehiro et al., 1964). Large departures from b~1 (up to b~2.5) are also observed during earthquake swarms (Kulhanek, 2005, Scholz, 1968), although this behaviour is generally associated with volcanic activity (Hainzl and Fischer, 2002).

For the purposes of this study, it is important to set upper and lower magnitude bounds appropriately, to maintain computationally practical numbers of model iterations. m_{min} was set to magnitude 4, which represents the approximate magnitude

of the smallest earthquakes observed to trigger landslides (Keefer, 2002). m_{max} was set to magnitude 8, which represents the approximate maximum observed magnitude for continental earthquakes (e.g.: Rodgers and Little, 2006, Xu et al., 2009). The occurrence of earthquakes is treated as time-independent, such that b is constant with time and magnitudes are selected independently from the GR distribution. Figure 6-5 shows the PDF for $m_{min} = 4$, $m_{max} = 8$, $b = 1$. In order to generate synthetic time series of earthquake magnitudes using Equation 6-11, uniformly distributed random numbers (between 0 and 1)[3] are used to derive $F_M(m)$. m values generated are equated to M_w in Equation 6-3[4]. Aftershocks satisfy GR magnitude-frequency scaling (e.g.: Nanjo et al., 2007, Shcherbakov et al., 2005a, Shcherbakov et al., 2006, Shcherbakov et al., 2005b), such that earthquakes in the synthetic time series will be representative of both mainshock and aftershock events. However, time-dependent influences on aftershock magnitudes (e.g.: Bath's law, Båth (1965)) are not included in this modelling for simplicity.

Each model iteration represents the occurrence of an earthquake and it is assumed that no processes affect PLMs during the inter-seismic period. Continuous real time is not included in the model. In reality, how model iterations translate to continuous time will be dependent upon the seismicity of the region being modelled. In regions of high seismicity, units of time will involve larger numbers of iterations than in regions of low seismicity.

[3] Random numbers were generated using the Matlab 'rand' function

[4] $\ln D_N = -2.710 + \log[\left(1 - \frac{a_c}{\mathrm{PGA}}\right)^{2.335} (\frac{a_c}{\mathrm{PGA}})^{-1.478}] + 0.424 M_w$

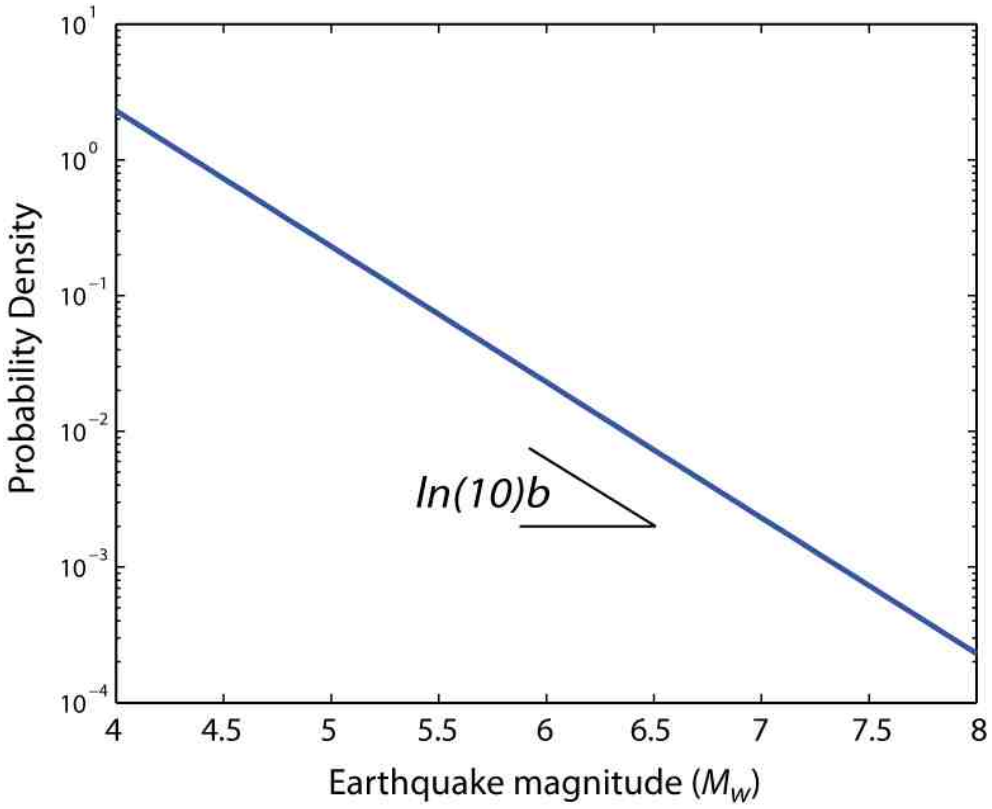

Figure 6-5 Earthquake magnitude probability density function, derived using $m_{min} = 4$, $m_{max} = 8$, $b = 1$

For each earthquake, PGA (g where 1g = 9.81 m s^{-2}) is calculated using an attenuation function. These predictive relationships commonly express PGA as a function of earthquake magnitude and distance from the seismic source, along with additional terms to account for differences in the style of faulting and geological site effects (Abrahamson et al., 2008, Campbell and Bozorgnia, 2008). Common functional forms for predictive relationships are based on the following observations (Kramer, 1996)L

1. $\ln PGA$ is approximately proportional to the earthquake magnitude, as earthquake magnitude is typically defined as the logarithm of peak ground motion parameters (Gutenberg and Richter, 1936, Gutenberg and Richter, 1944, Gutenberg and Richter, 1954).

2. The attenuation of waves causes amplitudes to decrease with distance (R) from the seismic source, according to $\frac{1}{R}$ for body waves (P and S waves) and $\frac{1}{\sqrt{R}}$ for surface waves (Love and Rayleigh waves).

3. Fault rupture areas increase with earthquake magnitude. This results in some waves arriving at a point from greater distances, which increases the effective distance from the seismic source.

4. Seismic source characteristics (e.g.: strike-slip, normal or reverse faulting), and whether the site is located in the hanging wall or footwall for thrust events, influences the strength of ground accelerations.

5. Earth materials influence the strength of ground motions. Damping occurs as the energy of waves is absorbed by the material they travel through, causing PGA to decrease exponentially with R.

6. Local site characteristics including hardness of rock, structural contrasts and facture density and distribution cause variable PGA damping and amplification.

The combination of these observations results in the following typical form for attenuation functions (after Kramer, 1996):

Equation 6-12

$$\ln PGA = c + c_2 m + c_3 M^{c_4} + c_5 \ln[R + c_6 e^{c_7 M}] + c_8 R + f(source) + f(site)$$

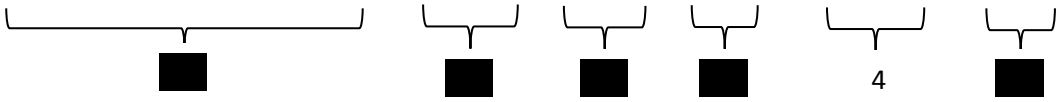

where c_{1-8} are regression coefficients. More recently published attenuation models provide a more accurate representation of ground motions, achieved through extensive terms to account for the seismic source and local site characteristics. For example, Campbell and Bozorgnia (2008) express PGA as a function of 11 independent variables and 16 constants. If this level of complexity were incorporated into this study, the outputs of modelling would be influenced by a large number of factors, making it difficult to analyse the system behaviour. However, simplified attenuation models express PGA as a function of earthquake magnitude and distance from the seismic source (e.g.: Campbell, 1981, Munson and Thurber, 1997). In order to reduce the system complexity the following attenuation model from Campbell (1981) is used:

Equation 6-13

$$\ln PGA = -4.141 + 0.868\, M_w - 1.09 \ln[R + 0.0606\, e^{0.7 M_w}]$$

where PGA is in units of acceleration (ms^{-2}) normalised to the gravitational acceleration, g, and R is the closest distance to the fault rupture in kilometres. Figure 6-6 shows PGA values predicted using Equation 6-13. This model captures the primary relationships defining PGA. Excluded from the model are material damping, variable source characteristics and site effects.

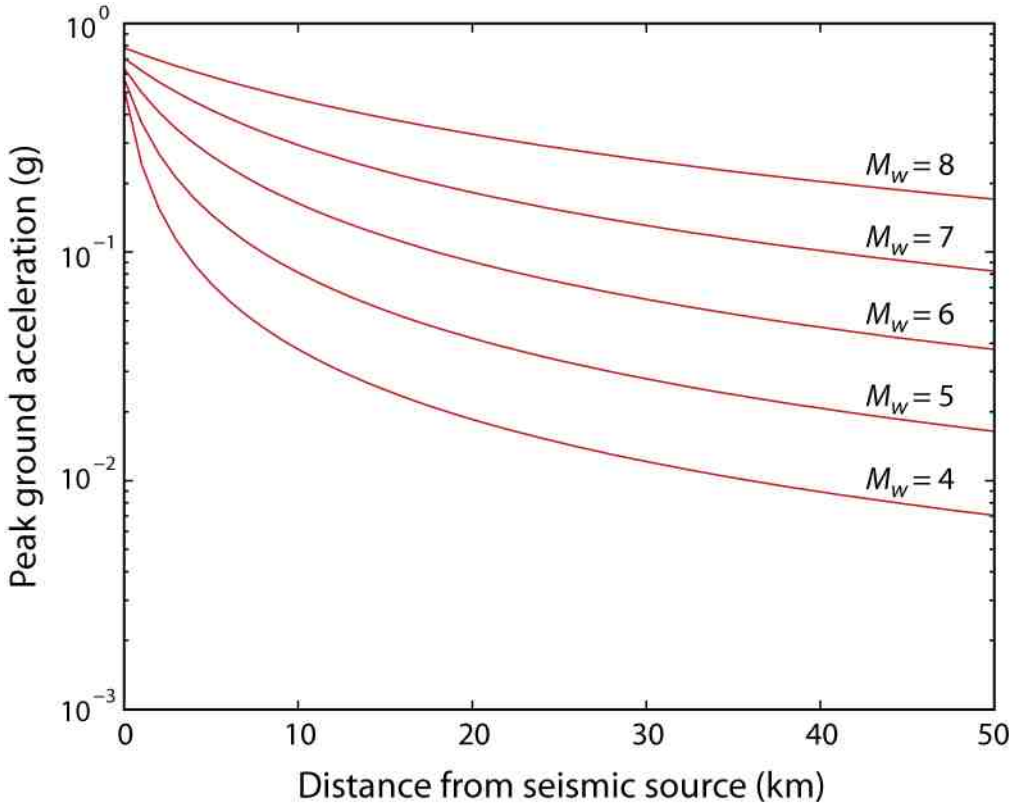

Figure 6-6 PGA-distance curves predicted using Equation 6-13.

6.1.5 Model set-up, parameters and outputs

While β and R can be varied to represent populations of PLMs of different gradients and at different distances from the seismic source, the focus of this chapter is on the temporal behaviour of landslide populations rather than spatial variability. Therefore these variables were held at fixed values. The sections that follow examine the temporal behaviour of hillslopes of 40^o gradient at 1 km distance from an active seismic source. A schematic diagram of the model set-up is shows in Figure 6-7.

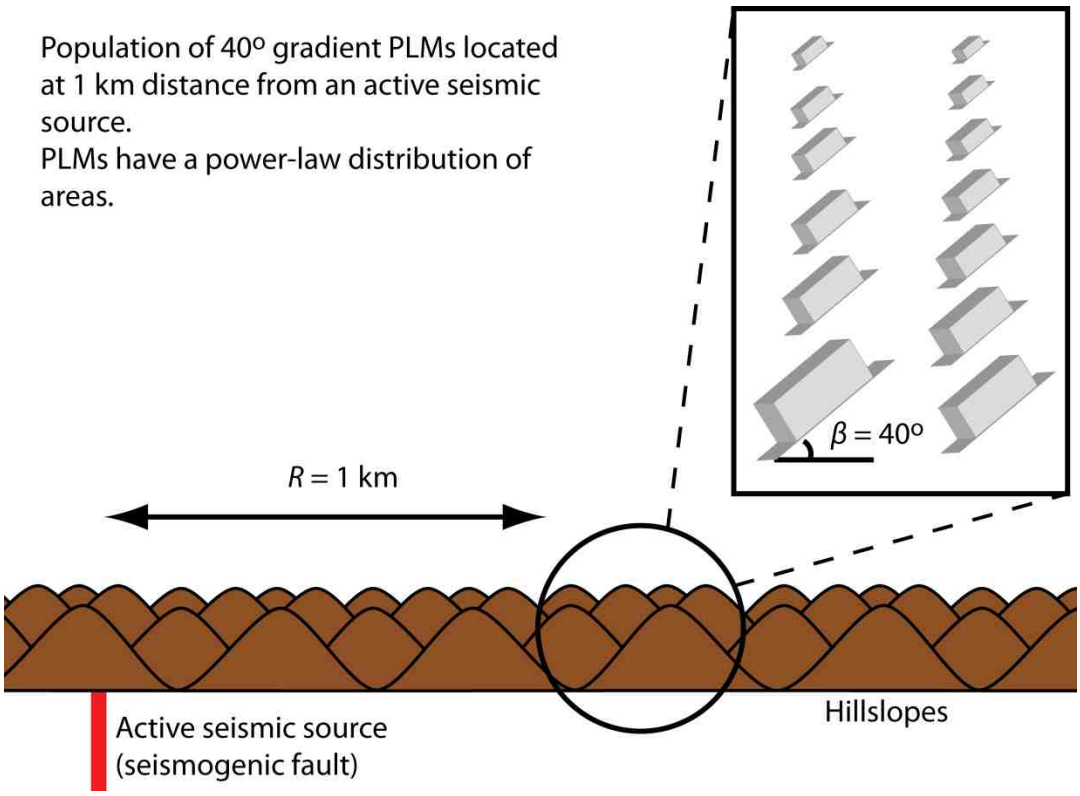

Figure 6-7 Schematic diagram of model experimental set-up. A population of Newmark sliding blocks represents the 40^{o} hillslopes of a mountain range, located 1 km from an active seismic source.

Limiting the model variable space in this way also ensures that the computational demands of the modelling do not become impractical and allows the behaviour of the model to be understood conceptually. In order for PLMs to reach the point of failure, τ_{fr} must be less than τ (or $\tan\beta$). As long as τ_{fr} is less than τ, altering τ_{fr} has no effect on the model behaviour. For this reason, τ_{fr} was set arbitrarily to 0 so that 40^{o} PLMs can reach the point of failure. Four remaining parameters can now be varied and used to calibrate the model. These are given in Table 6-1, along with what is known or can be inferred regarding their potential range of values.

Table 6-1 Numerical model parameters

Parameter	Property	Range
τ_{fp}	PLM peak strength	$\tau<\tau_{fp}<?$
k	Rate of PLM strength decay with strain	$0<k<?$
α_{PLM}	Scaling exponent of the PLM area MF distribution	$0<\alpha_{PLM}<?$
b	Gutenberg-Richter b-value	$0.5 \leq b \leq 1.5$

? indicates that the upper bound of the range is unknown

Two outputs were derived from the model.

- $\boldsymbol{\alpha_{FLM}}$

α_{FLM} is the scaling exponent describing the MF distribution of failed landslide masses, calculated by fitting Equation 6-6 using the method of Clauset et al. (2009).

- $\boldsymbol{PP_{LsA}}$

PP_{LsA} is the potential $P_{Ls}(A)$, indicating the proportion of the total hillslope area that would fail if an earthquake of a given magnitude occurs. PP_{LsA} is therefore analogous to landslide propensity, and is calculated at each iteration of the model, i.e. following each earthquake. At any point in time PP_{LsA} is the answer to the question: *What ratio of the total PLM area would undergo failure if a magnitude m earthquake were to occur now?*

PP_{LsA} can also be understood by considering the factor of safety-area ($FS - A$) space of the model (Figure 6-8). Each time a_c is exceeded, PLMs moves from right to left on the plot, towards the point of failure. When FS<1, failure occurs and FS resets to its maximum. The area to the left of the red line on the plot represents the PP_{LsA} failure zone for a magnitude 7.9 earthquake ($PP_{LsA}(7.9)$). Were a magnitude 7.9 earthquake to occur, all PLMs within this zone would fail. PP_{LsA} is therefore the sum of the areas of PLMs in the failure zone divided by the total area of all PLMs.

Although α_{FLM} and PP_{LSA} are both used to calibrate the model, PP_{LSA} is the main quantitative output. How PP_{LSA} evolves with time is used to investigate temporal changes in landslide propensity.

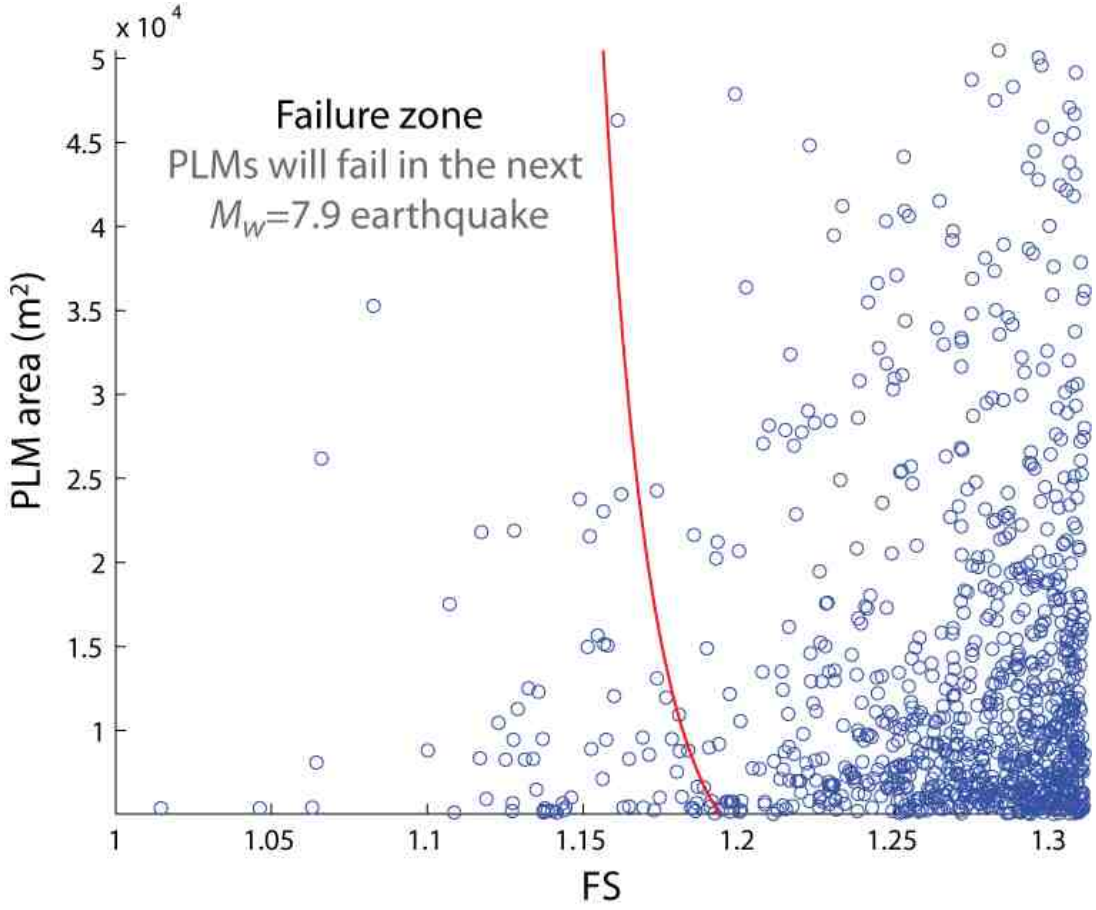

Figure 6-8 Model FS-Area space. Blue circles represent individual PLMs, which move from right to left on the plot as earthquakes exceed a_c and PLMs progress through their failure cycle. The red line is the threshold of the failure zone (region to the left of the red line). When a M_w = 7.9 earthquake occurs, all PLMs within the failure zone undergo failure. PP_{LSA} is the total area of PLMs in the failure zone divided by the total area of PLMs. Note that the failure zone threshold is curved as smaller PLMs require less displacement to achieve the same strength decay as larger PLMs.

6.2 Calibration of model parameters

In order to define a parameter space for τ_{fp}, k and α_{PLM}, PP_{LsA} and α_{FLM} were calibrated to observed hillslope failure probability and magnitude-frequency relationships from landslide inventories. Values of PP_{LsA} and α_{FLM} stabilise as they are calculated over larger numbers of model iterations. A point of stabilisation was defined as the iteration after which PP_{LsA} only varies within a range of ±0.01 and α_{FLM} within ±0.1 for 1000 further iterations, as shown in Figure 6-9 A and B. Stabilised values of PP_{LsA} and α_{FLM} are referred to as $\overline{PP_{LsA}}$ and $\overline{\alpha_{FLM}}$.

$\overline{\alpha_{FLM}}$ was calibrated to a value of 2.5, consistent with typical landslide area scaling exponent values (e.g.: Stark and Guzzetti, 2009, Van Den Eeckhaut et al., 2007). $\overline{PP_{LsA}}$ was calibrated using Equation 4-10[5], which gives a general relationship for landslide density from all five landslide inventories analysed in Chapter 4. As PP_{LsA} is calculated with respect to a given M_w, $PP_{LsA}(M_w = 7.9)$ was used in model calibration and experiments. For larger values of M_w, a stabilised value of $\overline{PP_{LsA}}$ can be achieved with fewer model iterations, and $M_w = 7.9$ is the largest magnitude used in fitting Equation 4-10[5]. Equation 4-10[5] predicts a $P_{ls}(A)$ value of 0.25 when β = 40°, M_W = 7.9 and $ln(PGA)$ is calculated at R = 1 km using Equation 6-13[6]. Therefore $\overline{PP_{LsA}}$ was calibrated to a value of 0.25, such that magnitude 7.9 model earthquakes, on average, trigger failure in 25% of hillslopes. Note that while $\overline{PP_{LsA}}$ stabilises with model iterations, PP_{LsA} shows significant temporal variability. This variability is the focus of analysis in Section 6.3, once the model parameters have been calibrated.

As well as being dependent on τ_{fp}, k and α_{PLM}, $\overline{PP_{LsA}}$ is also dependent on *b*. Therefore, calibration was carried out using a series of earthquake magnitudes generated using Equation 6-11, with *b* set to 1 (Figure 6-9 C). In this way, under 'normal' conditions $\overline{PP_{LsA}}$ corresponds to mean observed levels of landslide propensity, and the effect of changing *b* can be explored through model experiments.

As the total PLM area is constant with time, the model outputs are not affected by changes in the total number of PLMs (n), as long as n is sufficiently large. Experience with the model suggests $n \geq 100$ as a rule of thumb for avoiding a limited number of discrete PP_{LsA} values. As the model was run thousands of times during calibration to iteratively fit the parameters, at this stage a population of 100 PLMs was used order to minimise computational intensity. The upper bound of the PLM magnitude-frequency distribution was left unbounded, in order to calibrate the model for the full range of landslide sizes.

[5] $P_{LS}(A) = \frac{1}{1-e^{\left(-\left(\substack{c_{intercept}+c_{M_W} M_W+c_{FPD} FPD+ \\ c_{SL} SL}\right)\right)}}$

[6] $\ln PGA = -4.141 + 0.868\, m - 1.09 \ln[R + 0.0606\, e^{0.7m}]$

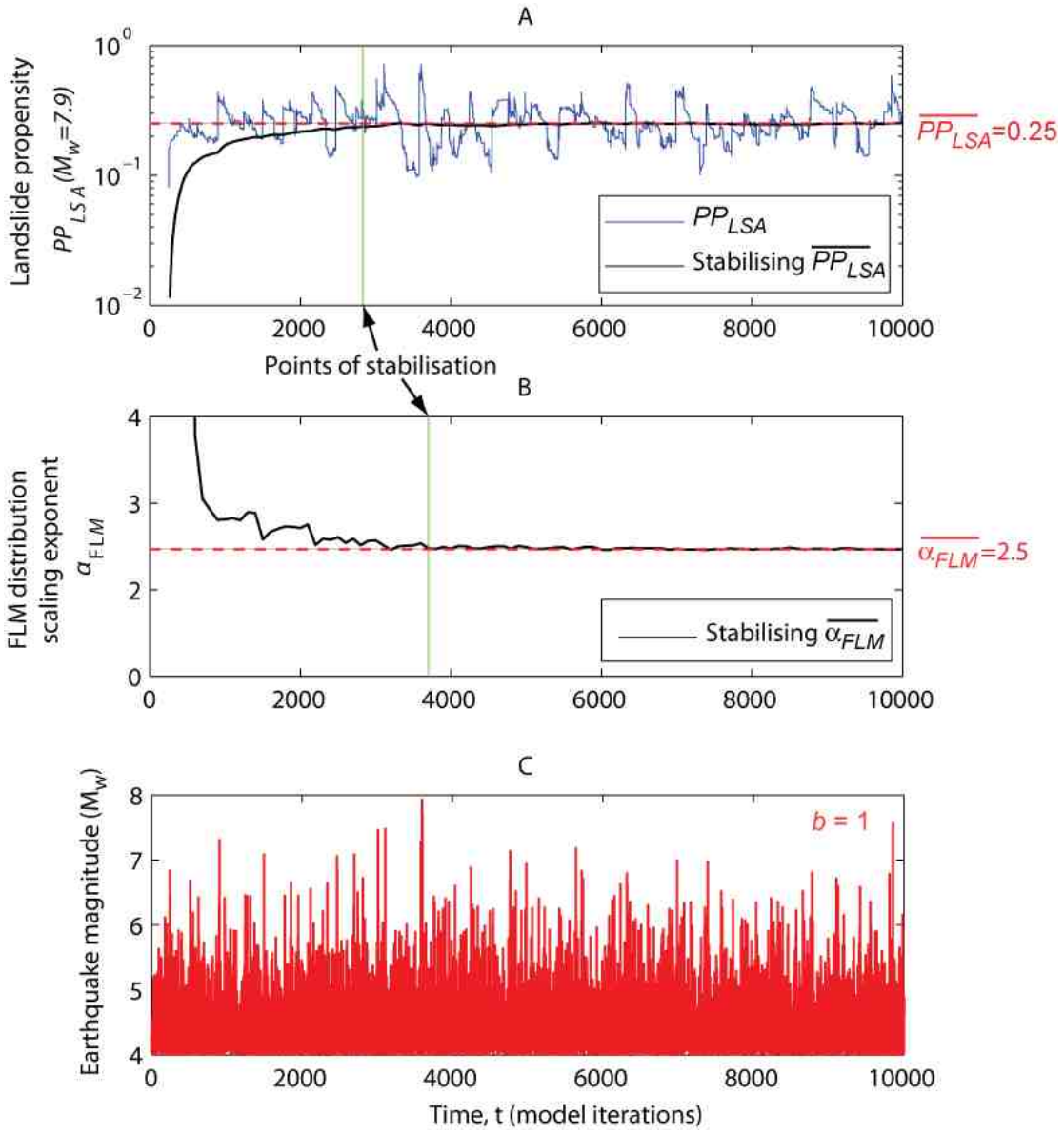

Figure 6-9 Time series showing the stabilisation of variables used in the model calibration process. A: Landslide propensity ($PP_{LSA}(M_w = 7.9)$) calculated at each model iteration is shown by the blue line, while the stabilising mean value is shown by the black line ($\overline{PP_{LSA}}$). The red line represents the final, stabilised value. B: α_{FLM} stabilises as the total population of failed landslide masses increases with model iterations. The red line represents the final, stabilised value. C: Earthquake magntiude time series. t is the model time, which indicates the number of earthquakes that have occurred since the beginning of the current simulation.

6.2.1 Calibration of α_{PLM}

As strain accumulates more rapidly in smaller PLMs, these undergo failure more frequently than larger PLMs. Therefore α_{FLM} values are greater than α_{PLM} values, indicating a steeper tail to the distribution of failed landslide masses than is the case for the distribution of potential landslide masses. α_{FLM} was found to be solely dependent on α_{PLM} and independent of the other model parameters τ_{fp} and k. Figure 6-10 shows the relationship between α_{PLM} and $\overline{\alpha_{FLM}}$. In order to achieve $\alpha_{FLM} = 2.5$, α_{PLM}~2 (2.02). In all simulations that follow, α_{PLM} is therefore fixed at 2.

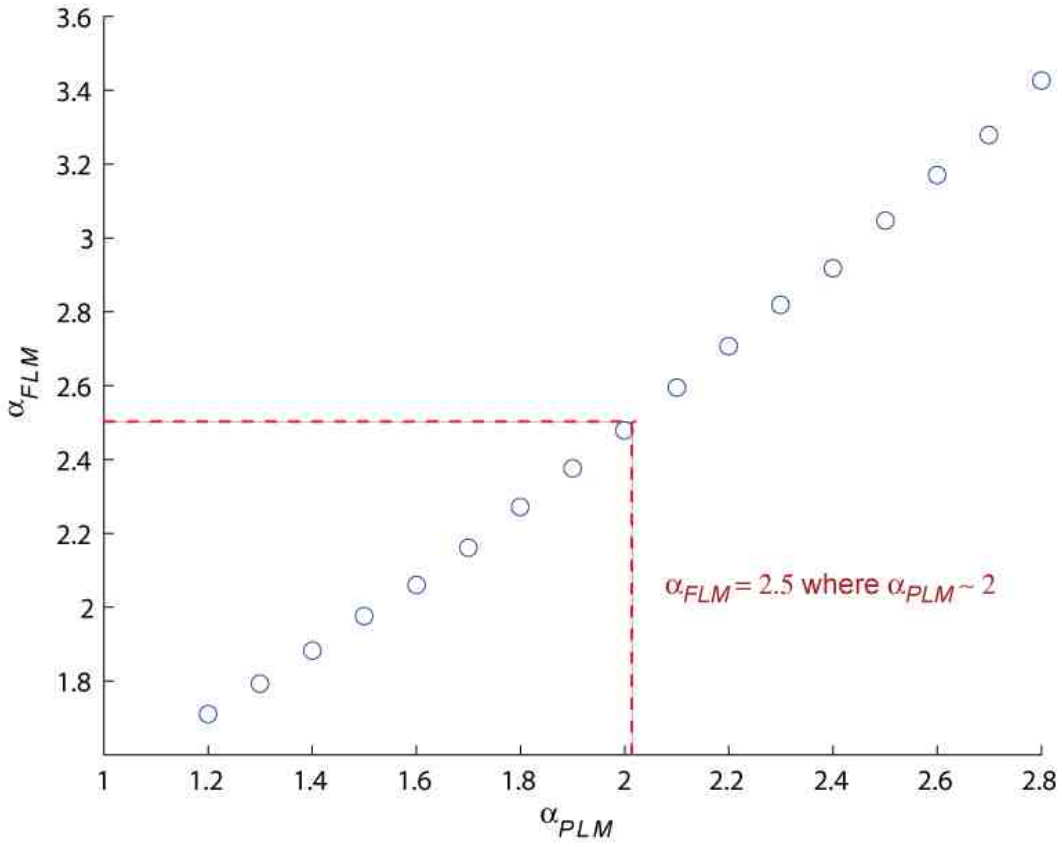

Figure 6-10 Relationship between scaling the exponents α_{FLM} (distribution of failed landslide mass areas) and α_{PLM} (distribution of potential landslide masse areas)

6.2.2 Calibration of τ_{fp} and k

$\overline{PP_{LsA}}$ is simultaneously dependent on both τ_{fp} and k. There are a range of τ_{fp} and k values that produce the same value of $\overline{PP_{LsA}}$. The upper and lower bounds of this range can be estimated based on observations of earthquake-triggered landslides. As τ_{fp} increases, so does the minimum magnitude of earthquake required to exceed a_c (i.e. to initiate strain accumulation and progressive failure, Figure 6-11). As $M_w = 4$ is generally observed to be the lowest magnitude of earthquake that triggers landslides (e.g.: Keefer, 2002), it is assumed that strain accumulation does not initiate during earthquakes much smaller than magnitude 4. Therefore a lower bound on τ_{fp} is ~1.1. Conversely, if τ_{fp} is so large that strain accumulation is never initiated by magnitude 8 earthquakes, then no seismically-driven progressive failure would occur. Therefore an upper bound on τ_{fp} is ~1.8.

-

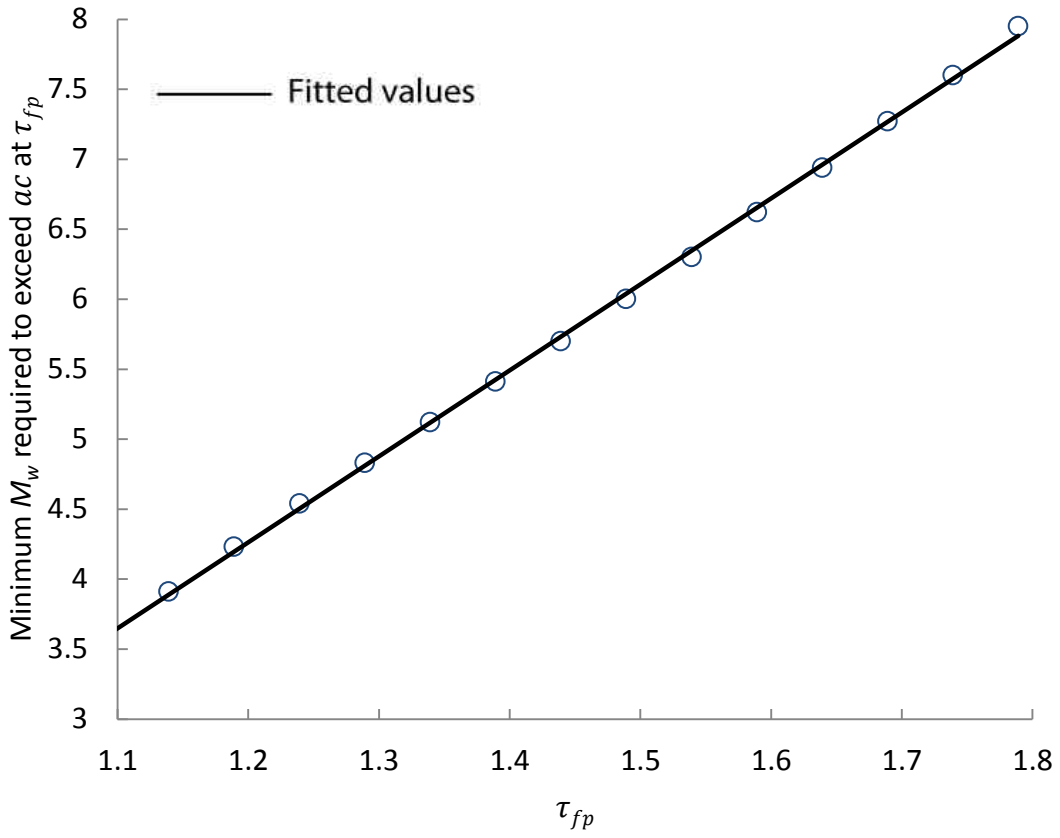

Figure 6-11 Relationship between model parameter τ_{fp} (peak strength) and the minimum magnitude of earthquake required for the PGA to exceed a_c in PLMs at peak strength.

As τ_{fp} increases, the length of earthquake time series required for $\overline{PP_{LsA}}$ to stabilise rapidly increases. For τ_{fp} > 1.45 the number of iterations becomes greater than 10^5 and is very computationally intensive. Therefore calibration has been carried out for $1.1 \leq \tau_{fp} \leq 1.45$. For this range of τ_{fp} values, k was calibrated iteratively until $\overline{PP_{LsA}}$ was 0.25 ± 0.05. This level of tolerance was found necessary to calibrate the model using a population of 100 PLMs. Across this range, calibrated values of τ_{fp} and k display a power-law relationship (Figure 6-12), where:

Equation 6-14

$$k = 10^{9.4786\,\tau_{fp} - 8.8471}$$

Equation 6-14 can therefore be used to define calibrated pairs of values for τ_{fp} and k.

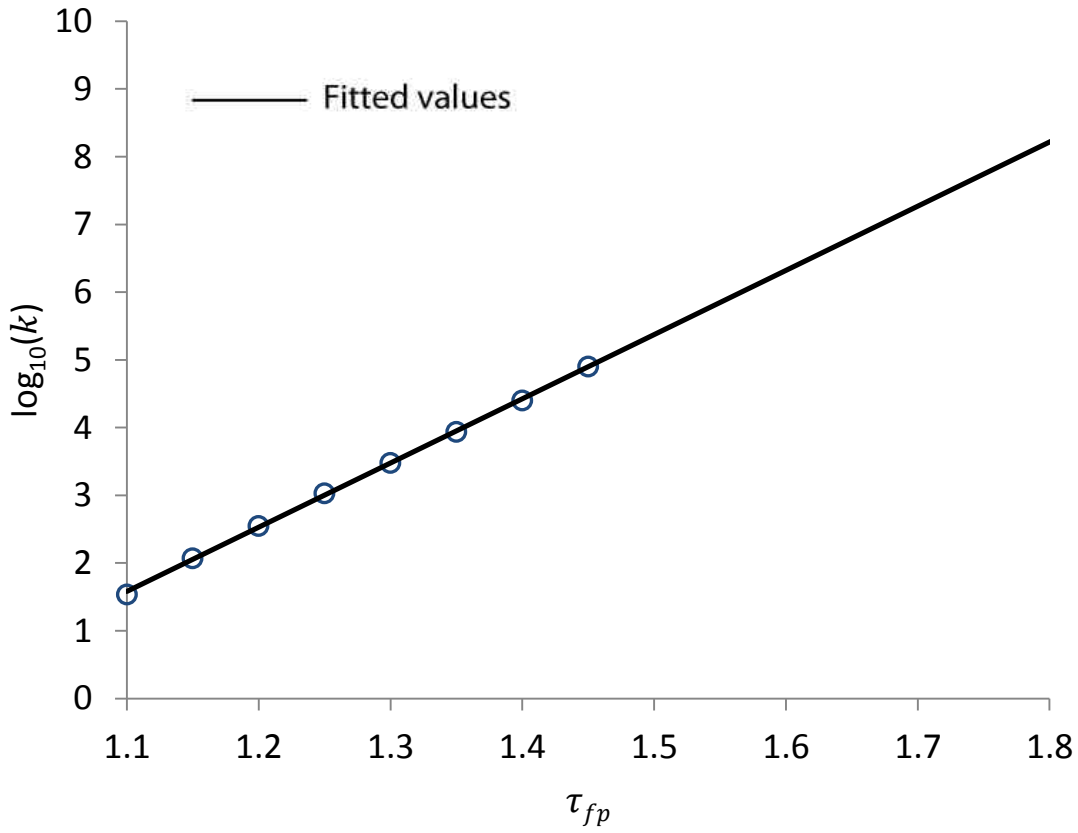

Figure 6-12 Calibrated relationship between model parameters τ_{fp} and k, showing fitted values given by Equation 6-14. The fitted line represents pairs of τ_{fp} and k values for which the model is calibrated, i.e.: on average M_w = 7.9 earthquakes produce failure in 25% of hillslopes

6.2.3 Summary

In order for the MF distribution of failed landslide masses produced by the model to reflect real landslide distributions with a power-law scaling exponent of ~2.5, the MF distribution of the PLM population must have a scaling exponent of ~2. In order for the mean percentage area of landslides triggered by model earthquakes to reflect observed landslide densities, the peak shear strength and rate of strength decay with strain are related via a power-law relationship (Equation 6-14).

6.3 Model behaviour and experiments

When a PLM population is subject to a time series of earthquakes, PP_{LsA} displays significant temporal variability. This suggests that landslide propensity, or the sensitivity of landscapes to landslide triggering, represented by this model varies with time. The purpose of this section is to explore the nature, mechanics and controls on this variability. This is achieved by running the model using synthetic sequences of earthquakes and studying the PP_{LsA} response.

While undertaking this analysis, it was found necessary to alter the size of the PLM population and the range of PLM areas. When using a lower-bounded distribution of PLM areas (> 11,000 m^2), PP_{LsA} was found to exhibit large artificial spikes associated with the passage of infrequent, large PLMs through the failure zone. In order to reduce this artefact the distribution of PLM areas was doubly-bounded across one order of magnitude (A_{min} = 11,000 m^2; A_{max} = 110,000 m^2) and the number of PLMs was increased to 1,000. Preliminary experiments also showed that setting all initial values of τ_f to τ_{fp} produced an artificially noisy PP_{LsA} signal that persisted for large numbers of iterations. Therefore, initial values of τ_f were distributed randomly between τ and τ_{fp}, which greatly reduced this effect[7].

6.3.1 Landslide propensity changes in response to and between large earthquakes

Before examining temporal variability in the response to distributions of different magnitude earthquakes, it is important to understand how the model responds to synthetic or discrete earthquake sequences. This section looks at the response of the system to simplified sequences containing low and high magnitude earthquakes. Low magnitude earthquakes (LM) and high magnitude earthquakes (HM) are used here as relative terms; an earthquake's magnitude is high or low with respect to other earthquakes in the time series. Two stages of the earthquake cycle are of interest: the occurrence of large earthquakes and periods of time between large earthquakes, characterised by the occurrence of subsequent smaller earthquakes. Subjecting the PLM population to a series of constant, low magnitude earthquakes simulates interstitial time between high magnitude earthquakes defined on average over geological time by the return period. PLMs move steadily through their failure cycle and small numbers of landslides occur, but the system does not experience any large perturbations until the next HM earthquake. Under these conditions, the behaviour of the model is strongly dependent on whether or not the magnitude of earthquakes that occur is sufficient to exceed the peak strength of hillslope materials. This can be expressed in terms of the PGA produced by LM earthquakes ($PGA(LM)$, g) relative to critical acceleration when the hillslope material is at peak strength ($a_c(\tau_{fp})$, g).

[7] Random numbers were generated using the Matlab 'rand' function

When low magnitude earthquakes do exceed the critical acceleration at peak strength, $PGA(LM) > a_c(\tau_{fp})$, every PLM accumulates strain and moves towards failure with every earthquake event. An example of the PP_{LsA} response when $PGA(LM) > ac(\tau_{fp})$ is shown in Figure 6-13. Here PP_{LsA} displays a non-static stable state following an initial priming phase (Figure 6-13 A). The continued variability in PP_{LsA} after the priming phase is less for larger PLM populations and narrower ranges of PLM areas, as the influence of having a discrete number of different sized PLMs becomes less. After 200 iterations $\overline{PP_{LsA}}$ has stabilised and no longer varies beyond ±0.01 of its value (Figure 6-13 B). However, after t = 200, variability in PP_{LsA} slowly increases. The long-term standard-deviation ($std(PP_{LsA})$), calculated cumulatively from t = 200 until the end of the simulation at t = 15x10^4, continues to increase over a much longer period (Figure 6-13 C). The reason for this behaviour can be understood through interpretation of FS-A plots (Figure 6-13 D). At t = 1, FS values are distributed randomly between values that correspond with $\tau_f = \tau$ and $\tau_f = \tau_{fp}$. At $t = 1$ the first LM earthquake occurs and all those PLMs sufficiently close to failure fail simultaneously, creating a cluster of PLMs at $\tau_f = \tau_{fp}$. As mean $\overline{PP_{LsA}}$ stabilises, PLMs become more clustered at high FS values (here shown at t = 400). At this point the striped structure of the FS-A distribution is a remnant of the initial cluster of PLMs that failed simultaneously. As this structure disperses, $std(PP_{LsA})$ increases and stabilises.

In order to fully prime the model so that the initial conditions are no longer evident, the simulation must be run until $std(PP_{LsA})$ stabilises. Broadly, once the full distribution of PLMs has completed 100 full failure cycles (i.e. the largest PLM has failed 100 times) the standard deviation of PP_{LsA} has reached its peak and remains approximately constant. The number of earthquakes required to produce 100 full failure cycles increases as τ_{fp} increases and the magnitude of LM earthquakes ($M_w(LM)$) decreases. The analysis that follows is carried out using parameter combinations for which 100 failure cycles is achieved in less than 10^5 iterations.

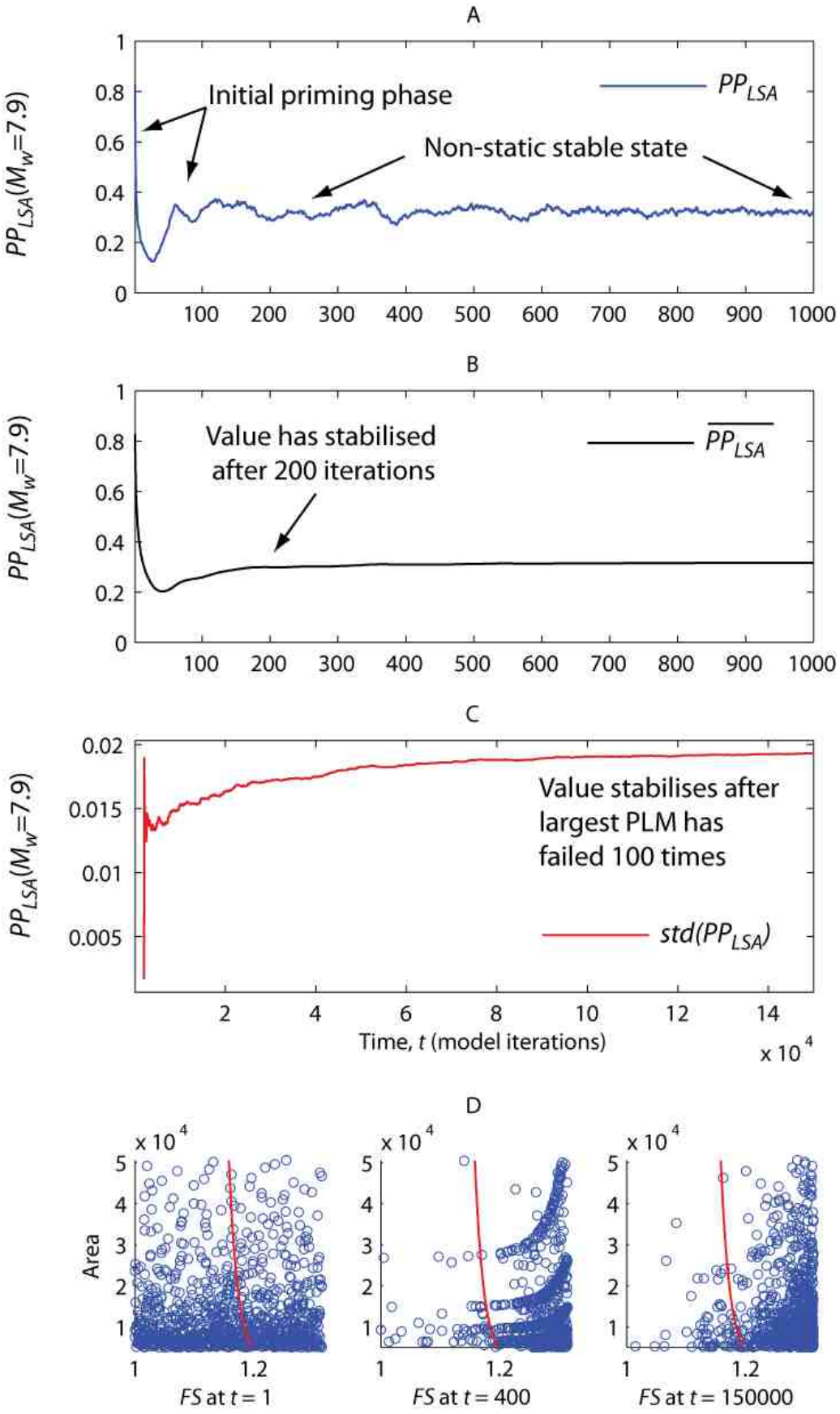

Figure 6-13 Time series showing initial model stabilisation where $PGA(Lm) > a_c(\tau_{fp})$. (A) PP_{LsA}, (B) Cumulative mean of PP_{LsA}, (C) Cumulative standard deviation of PP_{LsA}, in response to sequence of constant, low magnitude earthquakes where $PGA(Lm) > a_c(\tau_{fp})$. (D) FS-A plots for the model iterations indicated.

Once the model is primed and has stabilised under the influence of LM earthquakes, the response of HM earthquakes can be studied (Figure 6-14). When a HM earthquake occurs, PP_{LsA} displays an impulse response then asymptotic decay (Figure 6-14 A). Again this behaviour can be understood by considering the model FS-A space (Figure 6-14 B). Prior to the HM event, at t = 200, the model is in a non-static but stable state with PLMs clustered at high FS values. After a HM earthquake, here at t = 201, a large number of PLMs have reached the point of failure and reset, thus exiting the failure zone. However, Newmark displacements in PLMs that did not fail mean that a larger number of PLMs have accumulated strain and weakened, such that they have entered the failure zone. The result is an immediate increase in landslide propensity when a HM earthquake follows a period of LM earthquakes.

As the system then re-stabilises in response to subsequent LM earthquakes, there is a large dip in PP_{LsA} below the mean, after which two or three additional maxima and minima can be identified. These secondary features occur as PLMs that are close to failure following the HM earthquake fail in clusters due to LM earthquakes, and are then synchronised for two or three further failure cycles. In other words, sections of hillslope that failed around the same time, approach the point of failure together as they again accumulate strain. As these clusters become desynchronised through model time the impulse decays and landslide propensity returns to the same level of variability about the long-term mean.

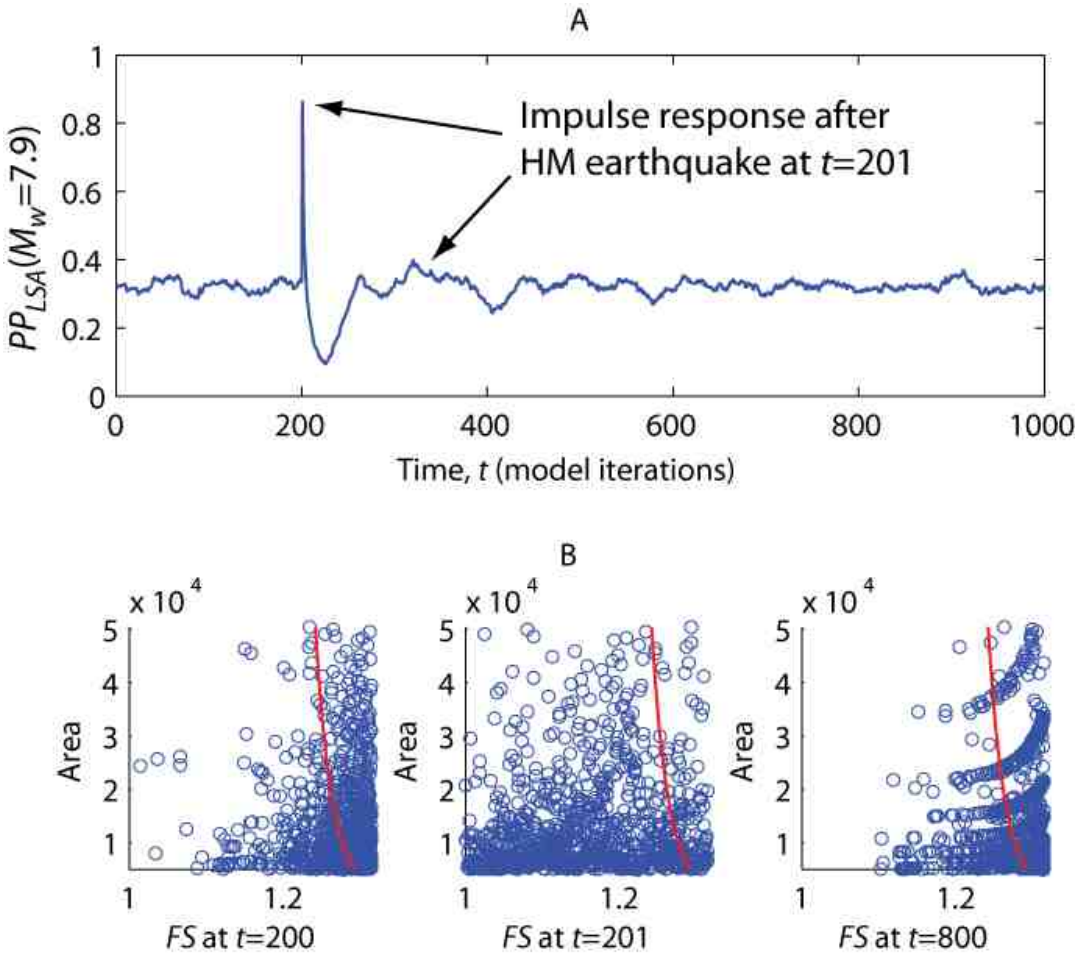

Figure 6-14 Time series showing the model response to a high magnitude earthquake, where $PGA(Lm) > a_c(\tau_{fp})$ (A) Model time series of PP_{LsA} in response to a high magntiude earthquake within a sequence of low magnitude earthquakes; (B) FS-A plots for the model iterations indicated.

As LM magnitude decreases and τ_{fp} increases, there comes a point at which low magnitude earthquakes do not exceed the critical acceleration at peak strength, $PGA(LM) < a_c(\tau_{fp})$. Under these conditions, only PLMs within a limited zone of FS-A space accumulate strain and move towards failure. Here this termed is the 'strain-accumulation zone'. These conditions result in a different type of system behaviour (Figure 6-15). In Figure 6-15 A, the strain-accumulation threshold is at a higher FS than the failure zone threshold and PP_{LsA} decays towards zero, as all PLMs accumulate strain and fail in response to LM earthquakes. Where the strain-accumulation zone threshold is at a lower FS than the failure zone threshold, as in Figure 6-15 B, PP_{LsA} decays towards a non-zero value. All PLMs inside the failure zone and outside of the strain-accumulation zone remain static in FS-A space and therefore remain in the failure zone indefinitely. The failure threshold has a curved form in FS-A space as it is

dependent on landslide size, while the linear strain-accumulation threshold is only dependent on FS.

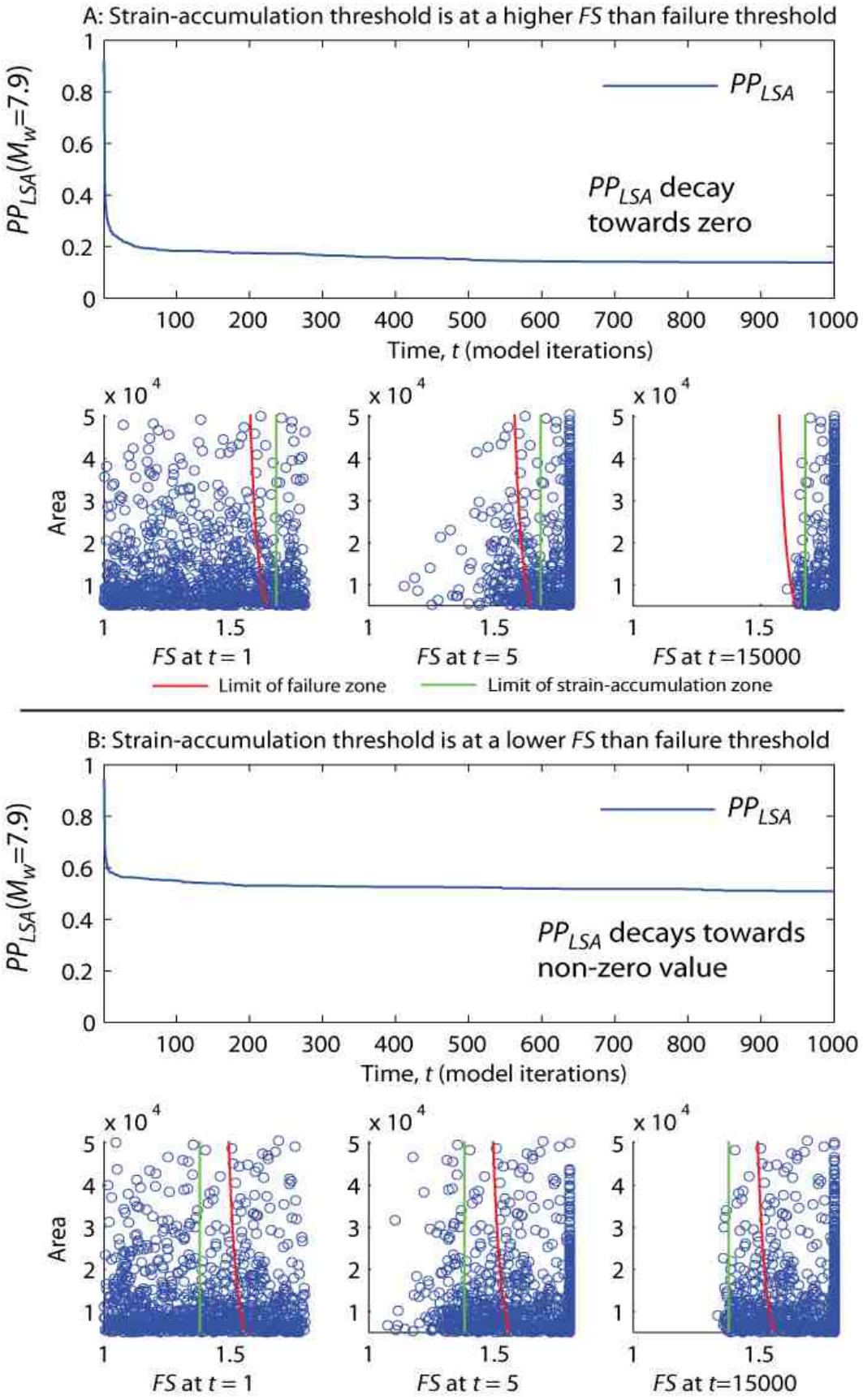

Figure 6-15 Model time series and FS-A plots, when subjected to a sequence of constant magnitude earthquakes, where $PGA(Lm) < a_c(\tau_{fp})$. The FS-A space to the left of the green line is the strain-accumulation zone, while the space to the left of the red line is the failure zone. (A) where the strain-accumulation threshold is at a higher FS than the failure zone threshold, landslide propensity decays towards zero; (B) where the strain-accumulation threshold is at a lower FS than the failure zone threshold, landslide propensity decays towards a non-zero value

If a HM earthquake occurs under these conditions, the PP_{LsA} impulse response displays a simple peak and asymptotic decay. In Figure 6-16, prior to the HM earthquake PP_{LsA} has decayed in response to LM earthquakes. When the HM event occurs, PLMs accumulate strain and move into the failure zone. During subsequent LM earthquakes, the strain-accumulation zone gradually empties. Again PP_{LsA} decays to zero if the strain-accumulation threshold is at a higher FS than the failure zone threshold (Figure 6-16 A), or to a non-zero value if the strain-accumulation threshold is at a lower FS than the failure threshold (Figure 6-16 B).

These results suggest that landslide propensity decays during times between large earthquakes, in response to subsequent lower magnitude events. During these periods landslide propensity may continue to evolve and fluctuate if lower magnitude events continue to drive strain accumulation and trigger landslides. However, if the magnitude of earthquakes is insufficient to exceed the peak strength of hillslope materials, then landslide occurrence will decay with time and eventually cease. At this point landslide propensity becomes static and no long evolves. In sum, large earthquakes produce significant disturbances to the system resulting in impulse responses, characterised by a peak in landslide propensity followed by a return to pre-disturbance conditions as subsequent lower magnitude events occur.

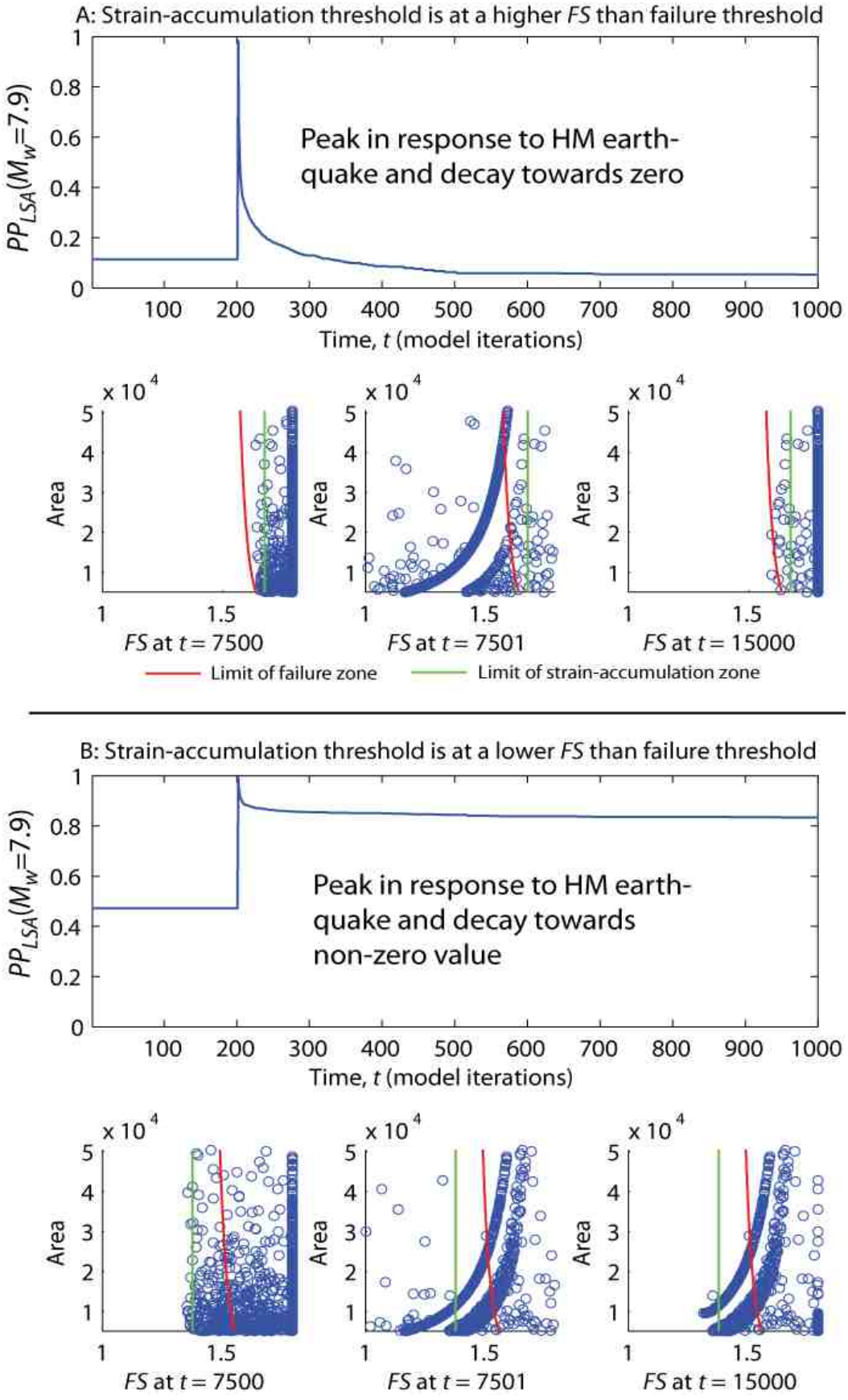

Figure 6-16 Model time series and FS-A plots, when subjected to a high magnitude earthquake, where $PGA(Lm) < a_c(\tau_{fp})$. (A) where the strain-accumulation threshold is at a higher FS than the failure threshold; (B) where the strain-accumulation threshold is at a lower FS than the failure threshold

6.3.2 Controls on the temporal response of landslide propensity to large earthquakes

The characteristics of the impulse response to large earthquakes are dependent on both the sequence of earthquakes that occur and the material properties of the PLM population. This section analyses the effect of altering these factors. Due to the low level of system activity and long simulation timescales required when LM earthquakes do not exceed peak strengths ($PGA(LM) < a_c(\tau_{fp})$), this analysis is carried out under the condition where $PGA(LM) > a_c(\tau_{fp})$.

In order to separate the impulse-response signal from long-term noise associated with the discrete number of PLMs, each impulse-response curve was generated for the same HM earthquake occurring at 30 randomly chosen iterations in the time series (following the first 100 full failure cycles). These 30 time series were combined into a single dataset and the mean PP_{LsA} was calculated for each iteration. This is termed the multiple-series-averaged (MSA) signal. Figure 6-17 shows an example of the MSA response to a series of 10,000 earthquakes, with a HM event occurring at t=5,000. From the MSA signal it is evident that, while the impulse response decays, the effect of the large earthquake persists in the form of a low amplitude resonance. This resonance remains in the system even when the simulation is run for up to the computational limit of 10^5 iterations. Despite the longevity of this effect, the variance it produces is much smaller than the initial phase of the impulse response and is likely to be masked by larger amplitude variability.

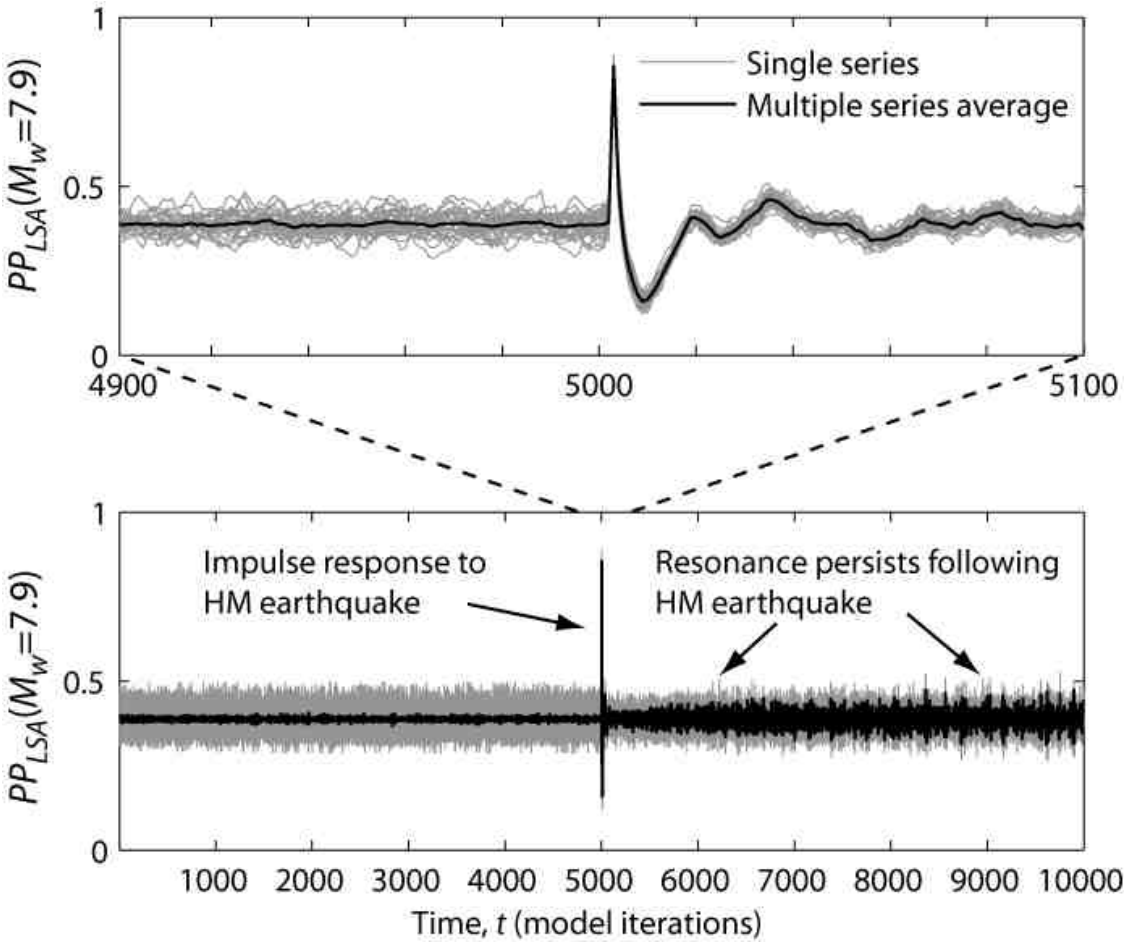

Figure 6-17 Model time series showing the mean response to a HM earthquake averaged from 30 repeated simulations (multiple series average shown in black) where HM earthquakes occur at different points in model time (single series shown in grey). In addition to the short-term impulse response, the effect of the HM earthquake also persists as a long-term, low amplitude resonance.

The response to a large earthquake appears to behave as a damped impulse (Brunsden and Thornes, 1979). The shape of the wave cannot be described without combining several wave and decay signals, and there is currently no physical basis for fitting a particular function to the data. In order to quantitatively analyse the influence of different variables, a number of attributes were extracted from the resulting time series. These characterise the amplitude and period of the impulse response (Figure 6-18):

- $Pmax$ is the PP_{LsA} at $t = t(HM) + 1$ and describes the peak landslide propensity immediately following the HM earthquake
- $Pmin$ is the minimum PP_{LsA} reached in the minima following $Pmax$
- $Pmean$ is the long-term mean PP_{LsA} calculated across 10,000 iterations prior to the large earthquake (following the priming phase)

- $Pminit$ is the iteration at which $Pmin$ is reached

- $Pmeanit1$ is the iteration at which PP_{LsA} reaches $Pmean$ following $Pmax$ and is the initial model-time period taken for PP_{LsA} to decay from its peak back to mean conditions.

- $Pmeanit2$ is the model-time period taken for PP_{LsA} to reach $Pmean$ following $Pmin$. As variability in PP_{LsA} quickly returns to normal conditions following the initial peak and trough, $Pmeanit2$ provides a reasonable metric for assessing the legacy of the earthquake.

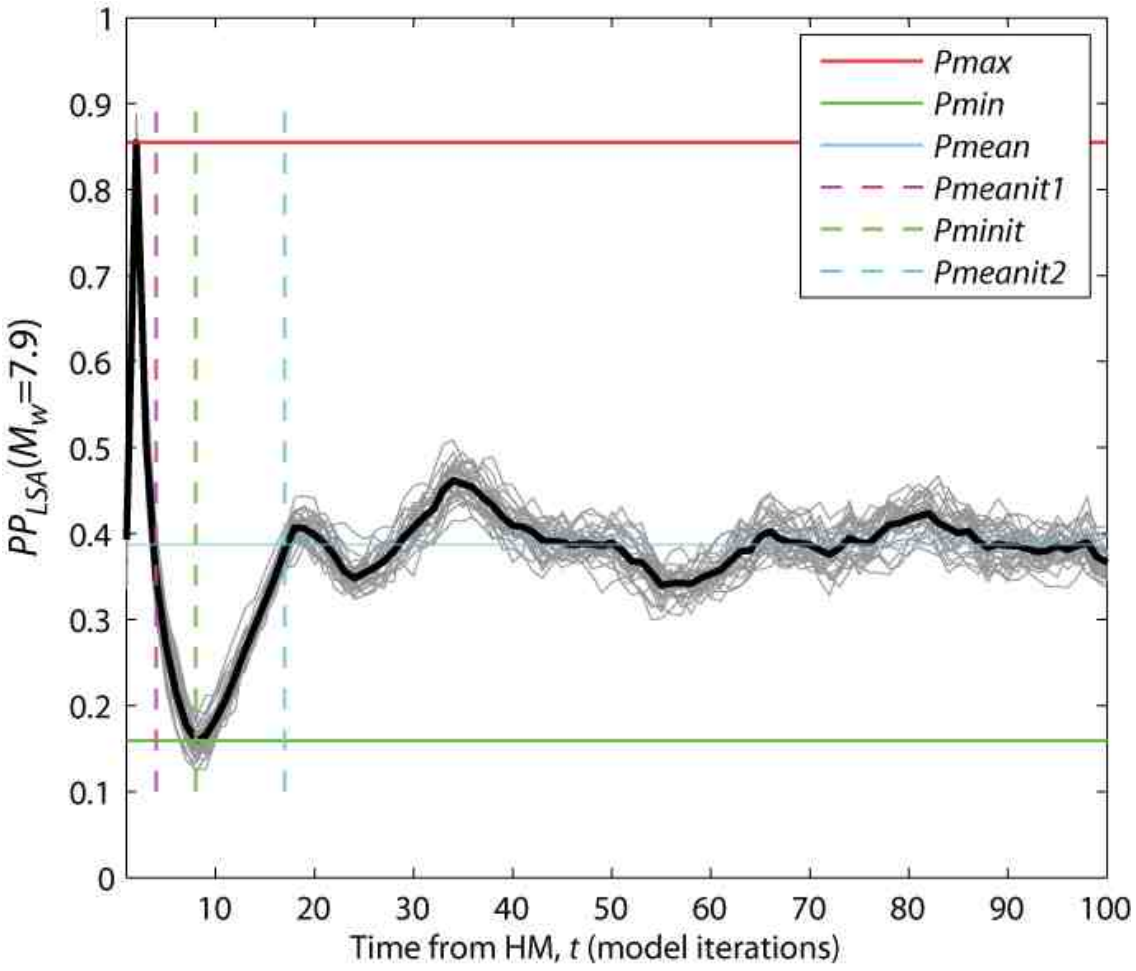

Figure 6-18 Illustration of attributes used to characteristise the amplitude and period of the PP_{LsA} impulse response, for quantitative analysis. The thick black line represents the average of multiple time series (MSA) from which the attributes are derived.

The PP_{LsA} response is dependent upon the HM magnitude $M_w(HM)$, LM magnitude $M_w(LM)$ and τ_{fp} (which is coupled to k via Equation 6-14[8]). The effect of these variables was tested individually by varying one at a time while holding the others constant. Figure 6-19 shows MSA response curves for $M_W(HM)$ varying between 5.6 and 8, where $M_w(LM)$ is fixed at 5.5 and τ_{fp} is fixed at 1.1. The main effect of increasing $M_W(HM)$ is an increase in the amplitude of the impulse, characterised by an increasing range between $Pmax$ and $Pmin$. The saturation of these relationships at high $M_W(HM)$ values occurs where additional PLMs cannot be added to the failure zone without causing others to fail and exit the failure zone. The initial time to decay from $Pmax$ to $Pmean$ $(Pmeanit)$ is shorter following larger HM events, as more

[8] $k = 10^{9.4786\,\tau_{fp}-8.8471}$

PLMs are left with lower FS values and so evacuate the failure zone sooner. Correspondingly, these clusters of PLMs approach failure for second and third times slightly earlier that those produced by smaller HM events, and so $Pminit$ and $Pmeanit2$ also have smaller values. While a larger $M_W(HM)$ effectively gives a cluster of PLMs a *head start*, the period of the impulse is not affected by altering $M_W(HM)$, as the rate at which PLMs accumulate strain following the HM earthquake is unchanged. Note that $Pmeanit$, $Pminit$ and $Pmeanit$ are not calculated at lower $M_W(HM)$ values as the amplitude of the impulse response is too low to resolve these parameters.

Figure 6-20 shows MSA response curves for $M_w(LM)$ varying between 5 and 6, where $M_W(HM)$ is fixed at 8 and τ_{fp} is fixed at 1.1. Increasing $M_w(LM)$ results in an increase in $Pmean$, indicating that on average a larger population of PLMs reside in the failure zone when LM earthquakes are larger. Changing $M_w(LM)$ has little impact on the amplitude of the PP_{LsA} oscillation, with no change in $Pmax$ and only a slight increase in $Pmin$, which appears to be proportional to the change in $Pmean$. However, changing $M_w(LM)$ has a large effect on the duration and period of the impulse. As $M_w(LM)$ increases $Pmeanit1$, $Pminit$ and $Pmeanit2$ decay non-linearly, as the rate at which PLMs accumulate strain increases. Therefore, if small earthquakes occur between large earthquakes, the timescale required for PP_{LsA} to return long-term mean conditions is much longer than if moderate earthquakes occur between large earthquakes.

Figure 6-21 shows MSA response curves for τ_{fp}varying between 1.1 and 1.3, where HM is fixed at 8 and LM is fixed at 5.5. Note that as τ_{fp}increases, k also increases (Equation 6-14). Altering τ_{fp} has little effect on the amplitude of the impulse: $Pmean$ decreases with τ_{fp}, accompanied by a slight increase in $Pmax$ and decrease in $Pmin$. However, there are major changes in the timescale and shape of the function. $Pmeanit$ increases linearly with τ_{fp}, while $Pminit$ and $Pmeanit2$ increase non-linearly. This is due to the non-linear shape of the relationship between Newmark displacement and slope stability (See Figure 2-5). Immediately following the large earthquake PLMs in the failure zone have a limited range of FS values, so accumulate strain and fail at similar rates. The small increase in $Pmeanit$ is due to the fact that

PLMs with a higher strength prior to the HM earthquake are generally further from failure after the HM earthquake. However, following failure PLMs with higher τ_{fp} and FS accumulate strain far more slowly than those with lower τ_{fp} and FS. For example, experiencing a PGA of 0.43 g in a magnitude 5.5 earthquake, a 40^{o} PLM with a τ_f of 1.1 and FS of 1.3 will accumulate 0.002 m of Newmark displacement, while the same PLM with a τ_{fp} of 1.3 and an FS of 1.6 will accumulate 8x10^{-7} m of Newmark displacement. As a result the number of iterations required to fail PLMs a second time, and thus the lag time between maxima increases rapidly with τ_{fp}.

The magnitude of HM earthquakes therefore primarily determines the amplitude of changes in landslide propensity. While $M_W(HM)$ has only has a limited influence on how landslide propensity evolves with time following the HM earthquake, for earthquakes with larger $M_W(HM)$ a more rapid initial decay in landslide propensity can be expected. The post-HM evolution of landslide propensity is strongly dependent on the magnitude of subsequent earthquakes and the peak strength of hillslope materials. Additionally these properties also affect the long-term mean landslide propensity. While these experiments have been limited to the condition $PGA(LM) > ac(\tau_{fp})$, as $M_w(LM)$ further decreases and as τ_{fp} further increases the period of the impulse will continue to increase as rates of strain accumulation become infinitesimally small. Finally, from $PGA(LM) < ac(\tau_{fp})$, post-HM landslide propensity decays over very long periods towards static conditions.

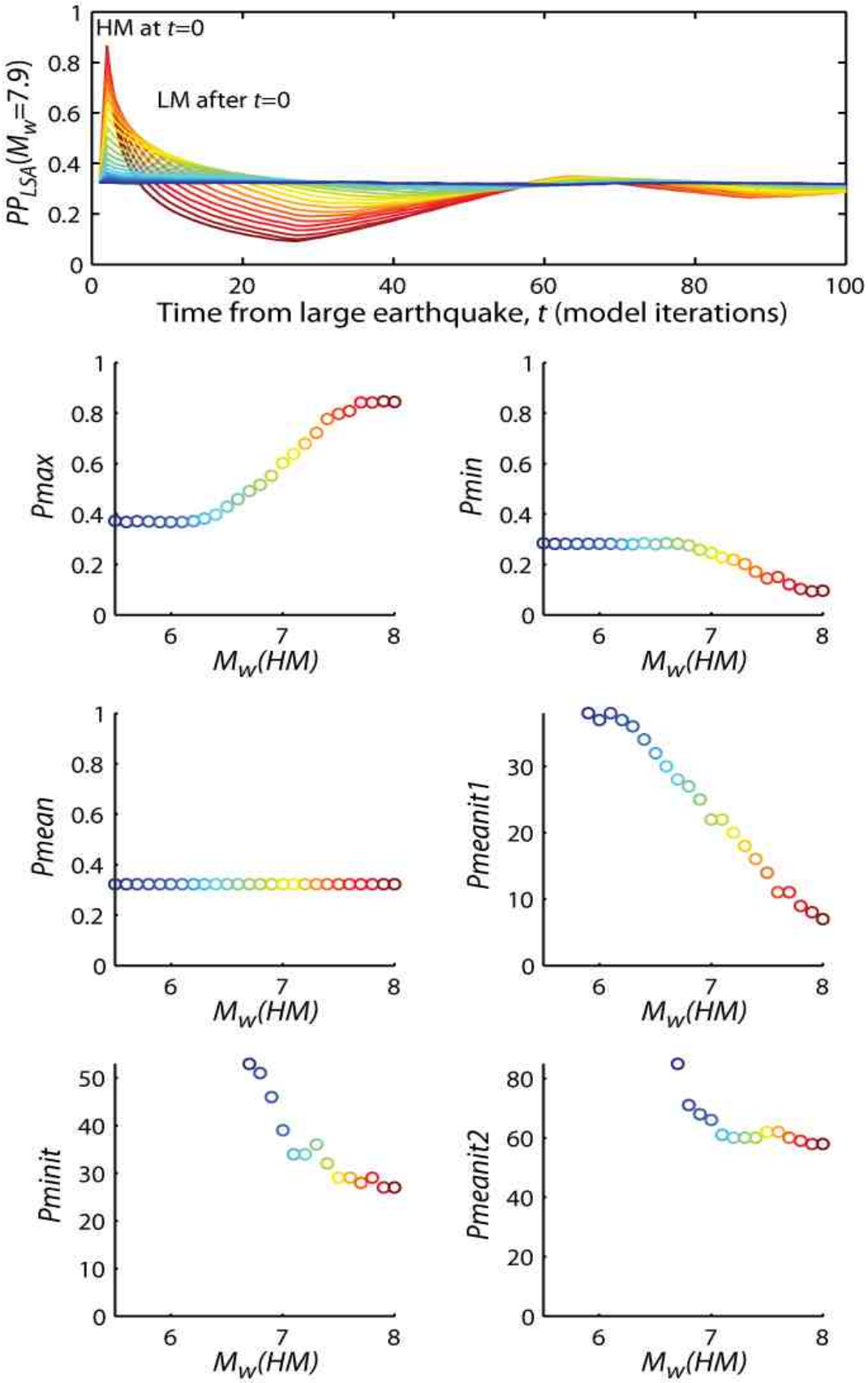

Figure 6-19 Model output showing the landslide propensity (PP_{LSA}) response to a single large earthquake, and the effect of changing the large earthquake's magntiude ($M_W(HM)$), when the magnitude of subsequent smaller earthquakes $M_w(LM)$ and the PLM peak strength (τ_{fp}) are held constant. The time series shows temporal PP_{LSA} response for the different $M_W(HM)$ values and the and scatter plots show the corresponding change in the impulse response attributes (Figure 6-18)

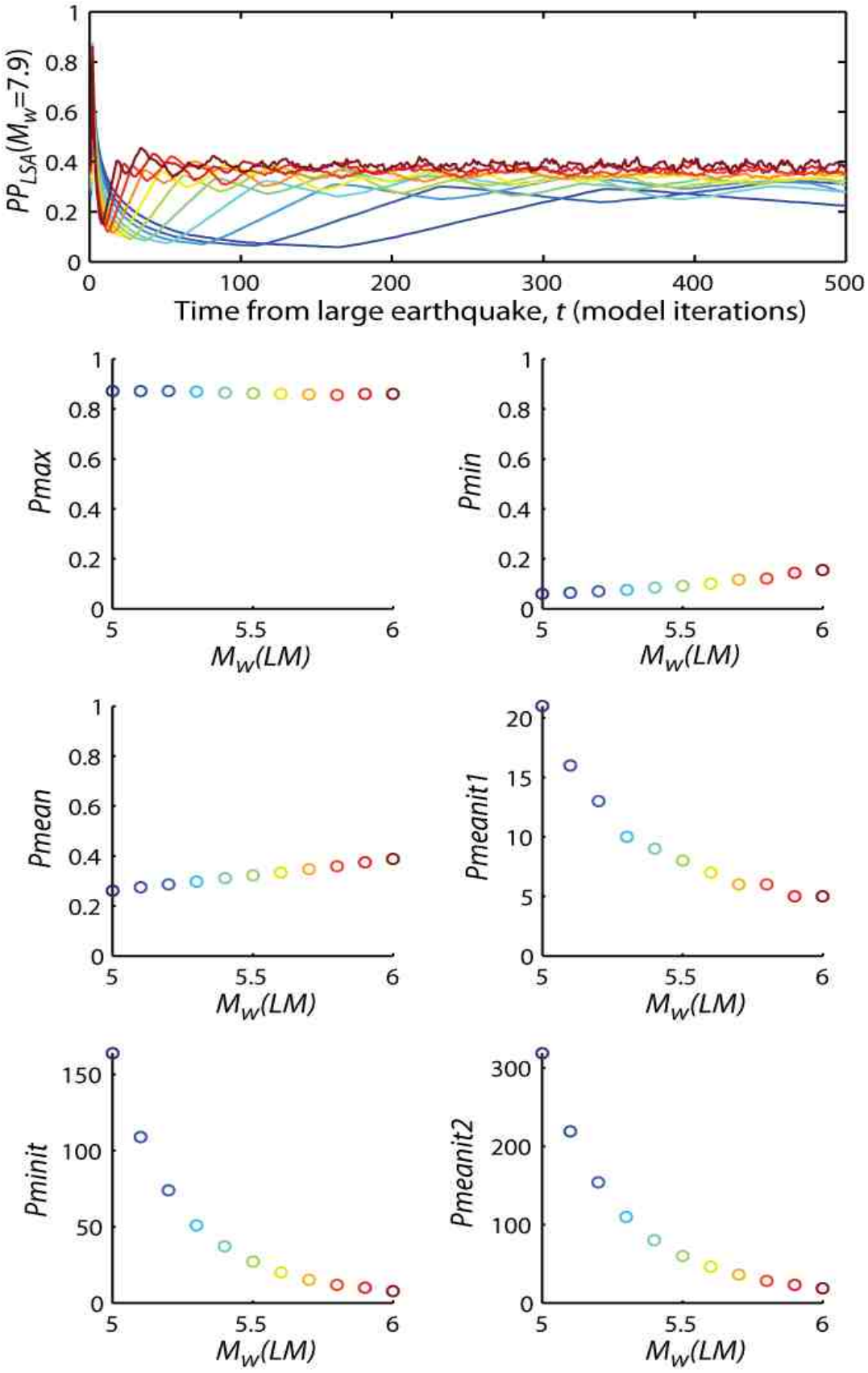

Figure 6-20 Model output showing the landslide propensity (PP_{LsA}) response to a single large earthquake, and the effect of changing the magnitude of subsequent small earthquakes ($M_W(LM)$), when the magnitude of the large earthquake $M_w(HM)$ and the PLM peak strength (τ_{fp}) are held constant. The time series shows temporal PP_{LsA} response for the different $M_W(LM)$ values and the and scatter plots show the corresponding change in the impulse response attributes (Figure 6-18)

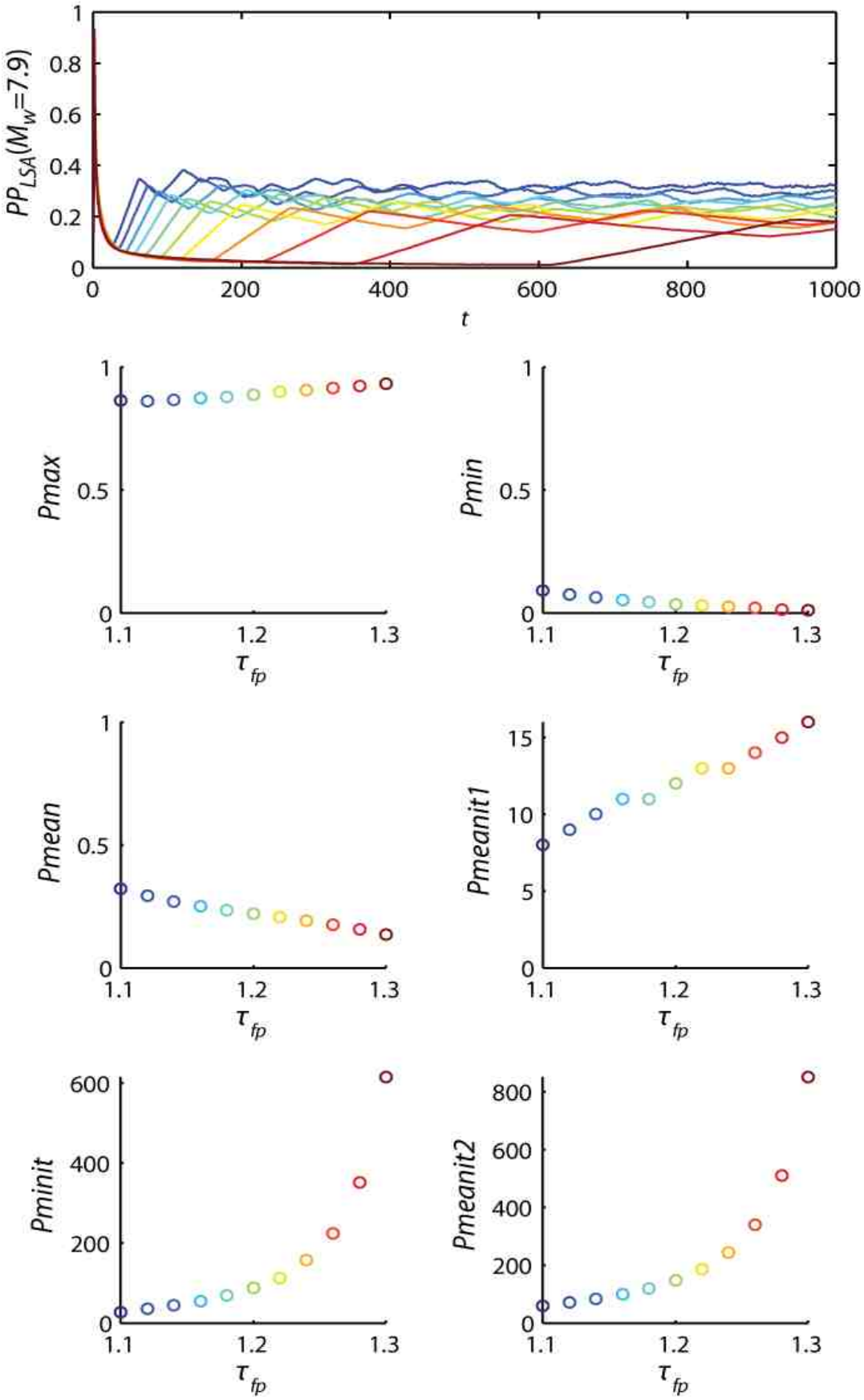

Figure 6-21 Model output showing the landslide propensity (PP_{LsA}) response to a single large earthquake, and the effect of changing the PLM peak strength (τ_{fp}), when the magnitude of the large earthquake $M_w(HM)$ and subsequent lower magnitude earthquakes ($M_W(LM)$), are held constant. The time series shows temporal PP_{LsA} response for the different τ_{fp} values and the and scatter plots show the corresponding change in the impulse response attributes (Figure 6-18)

6.3.3 Long-term behaviour

As levels of accumulated strain evolve in response to individual earthquakes, this produces long-term patterns of variability in landslide propensity. In order to determine the likely time-scale and nature of this variability, the model is run using GR distributed sequences of earthquakes. This results in a PP_{LsA} signal exhibiting a combination of impulse peaks associated with HM earthquakes, decay patterns associated with LM earthquakes, and low levels of variability associated with the clustered legacy of previous large events. The nature of this long-term temporal behaviour is dependent upon the model parameter $\tau_{fp} - k$ combination, and the b-value of the GR distribution. Again the effect of these parameters can be studied by varying each individually.

Figure 6-22 shows a long-term PP_{LsA} signal in response to a GR distribution of earthquakes, where b = 1 and τ_{fp} is 1.1 (Figure 6-22 A) and 1.5 (Figure 6-22 B). The range of temporal variability in landslide propensity is very large for both values of τ_{fp}. While the mean is calibrated to ~0.25, the proportion of area affected by landslides in magnitude 7.9 earthquakes ranges from <0.1 to >0.9. However, as τ_{fp} varies, the pattern of variability changes. When $\tau_{fp} = 1.1$, PP_{LsA} displays a higher frequency but lower range of temporal variability than when $\tau_{fp} = 1.5$. This behaviour can be understood by looking at the change in PP_{LsA} produced by each individual earthquake in the time-series, shown in Figure 6-23 when $\tau_{fp}$is 1.1 (Figure 6-23 A) and 1.5 (Figure 6-23 B). In general low magnitude earthquakes produce a reduction in landslide propensity, while higher magnitude earthquakes produce an increase. However, if landslide propensity prior to the earthquake is high, the change is more likely to be negative, while if landslide propensity is low, the change is more likely to be positive. Despite the increase in landslide propensity produced when a larger earthquake occurs following a series of smaller earthquakes, even large ($M_w > 7$) earthquakes a capable of producing a decrease if landslide propensity is already high (i.e.: immediately following another large earthquake). When τ_{fp} is 1.1, all magnitudes of earthquake are capable of producing an increase. However, when τ_{fp} is 1.5, only magnitudes greater than 6.1 produce an increase in landslide propensity, as lower magnitude earthquakes are insufficient to exceed the critical acceleration threshold in PLMs at peak strength. Thus, for τ_{fp}= 1.1, impulse peaks occur more regularly, with shorter periods of decay.

While for τ_{fp}= 1.5 the long-term signal is punctuated by fewer peaks associated with large earthquakes and longer periods of decay associated with smaller earthquakes.

Figure 6-24 shows long-term PP_{LsA} signal where τ_{fp}= 1.1 and b is 1 (Figure 6-24 A) and 1.5 (Figure 6-24 B). Note that both series of earthquakes are generated from the same sequence of random numbers, so the time series has the same temporal pattern of larger and smaller events, but the relative magnitudes of the earthquakes differ. When b is larger, the number of large earthquakes relative to the number of small earthquakes is less. Thus impulse peaks are smaller and occur less frequently than for smaller values of b.

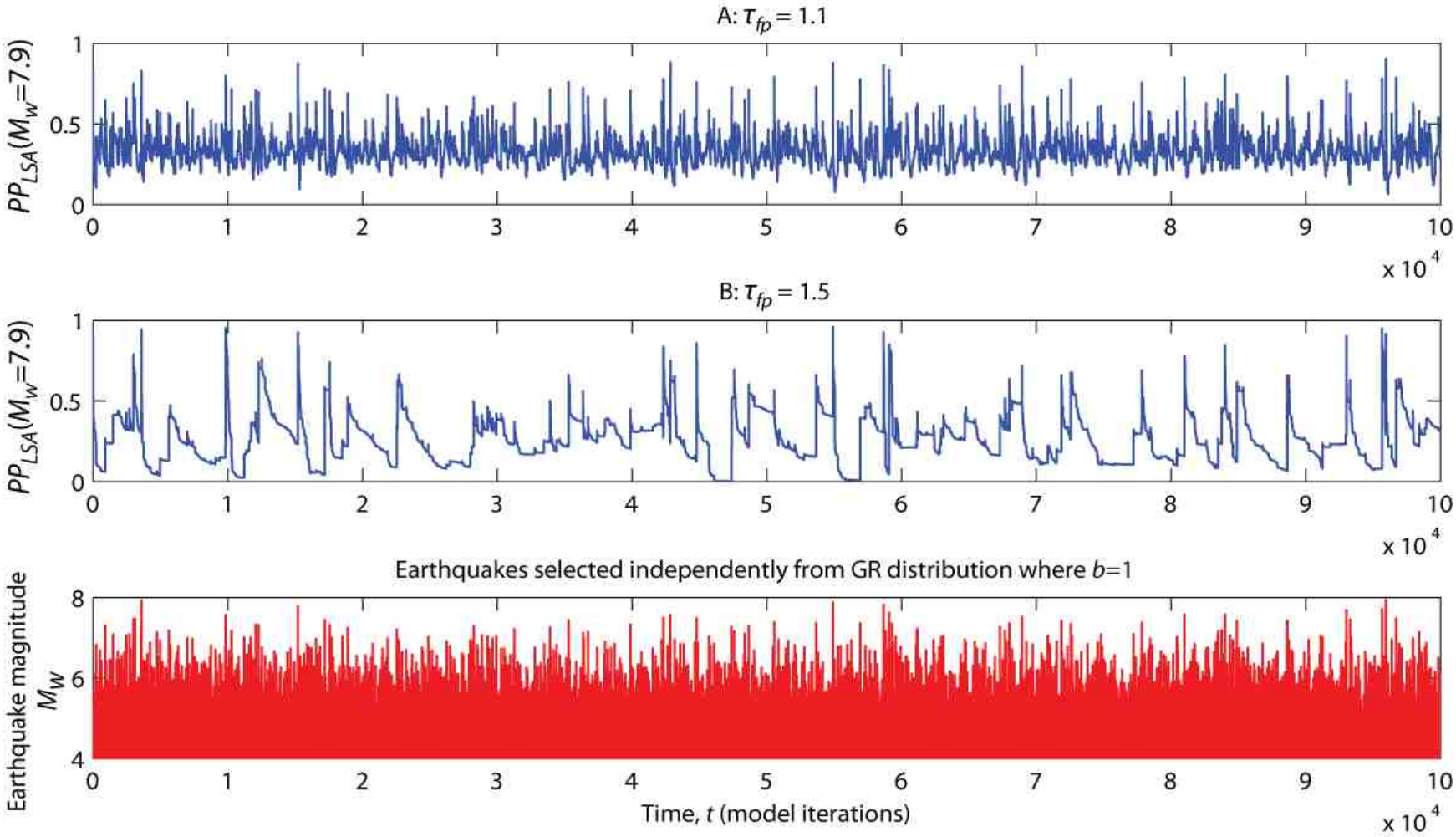

Figure 6-22 Long term landslide propensity ($PP_{LsA}(M_w = 7.9)$) time-series in response to a series of GR distributed earthquakes, when $\tau_{fp} = 1.1$ (A) and $\tau_{fp} = 1.5$ (B), and b = 1

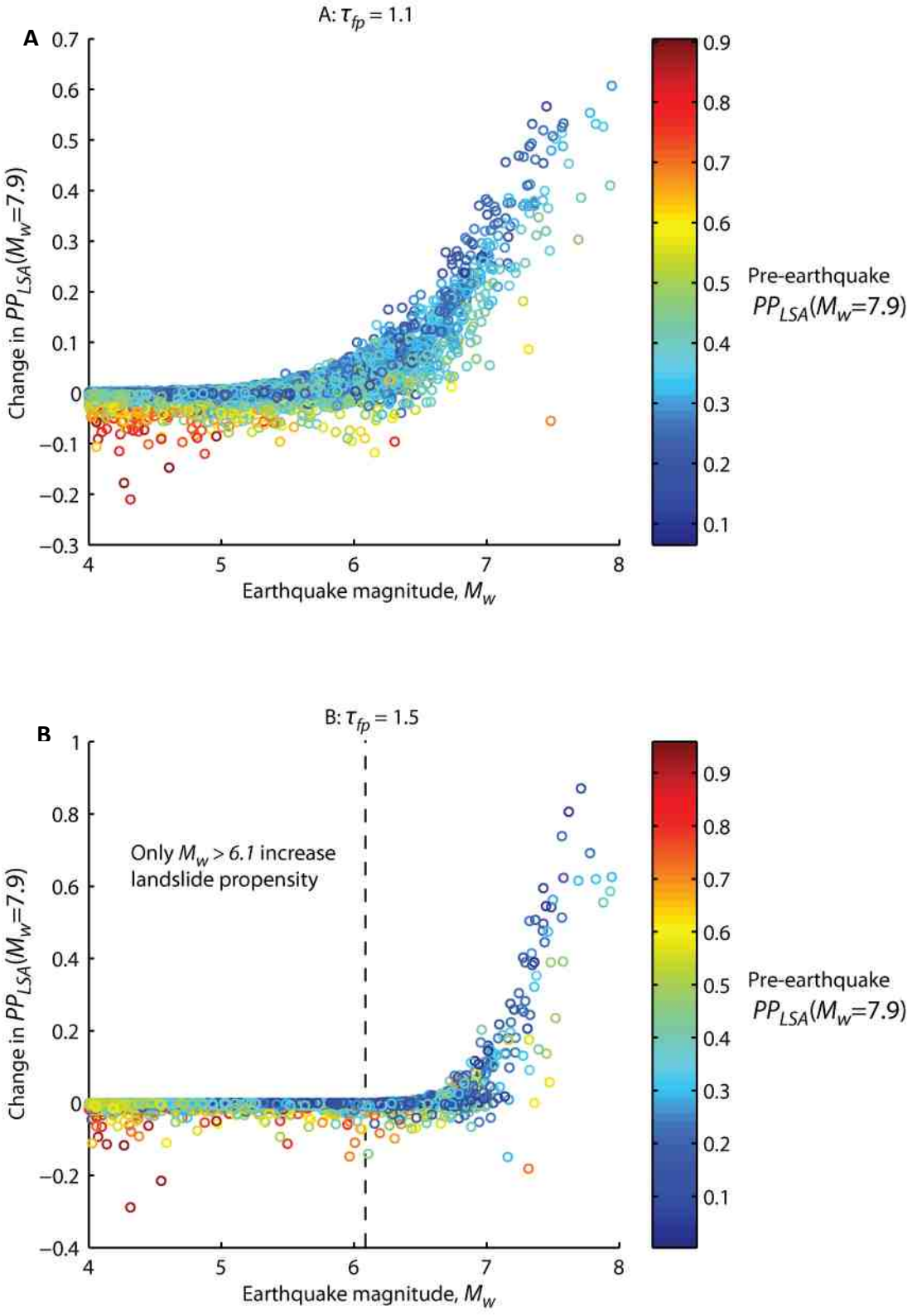

Figure 6-23 Plots showing the change in landslide propensity ($PP_{LsA}(M_w = 7.9)$) produced by inidivudal earthquakes in the time series given in Figure 6-22, when $\tau_{fp} = 1.1$ (A) and $\tau_{fp} = 1.5$ (B). The colour scale indicates $PP_{LsA}(M_w = 7.9)$ prior to each earthquake. In B the dashed line indicates the magnitude threshold below which earthquakes do not increase landslide propensity, because the PGA does not exceed critical acceleration in PLMs at peak strength.

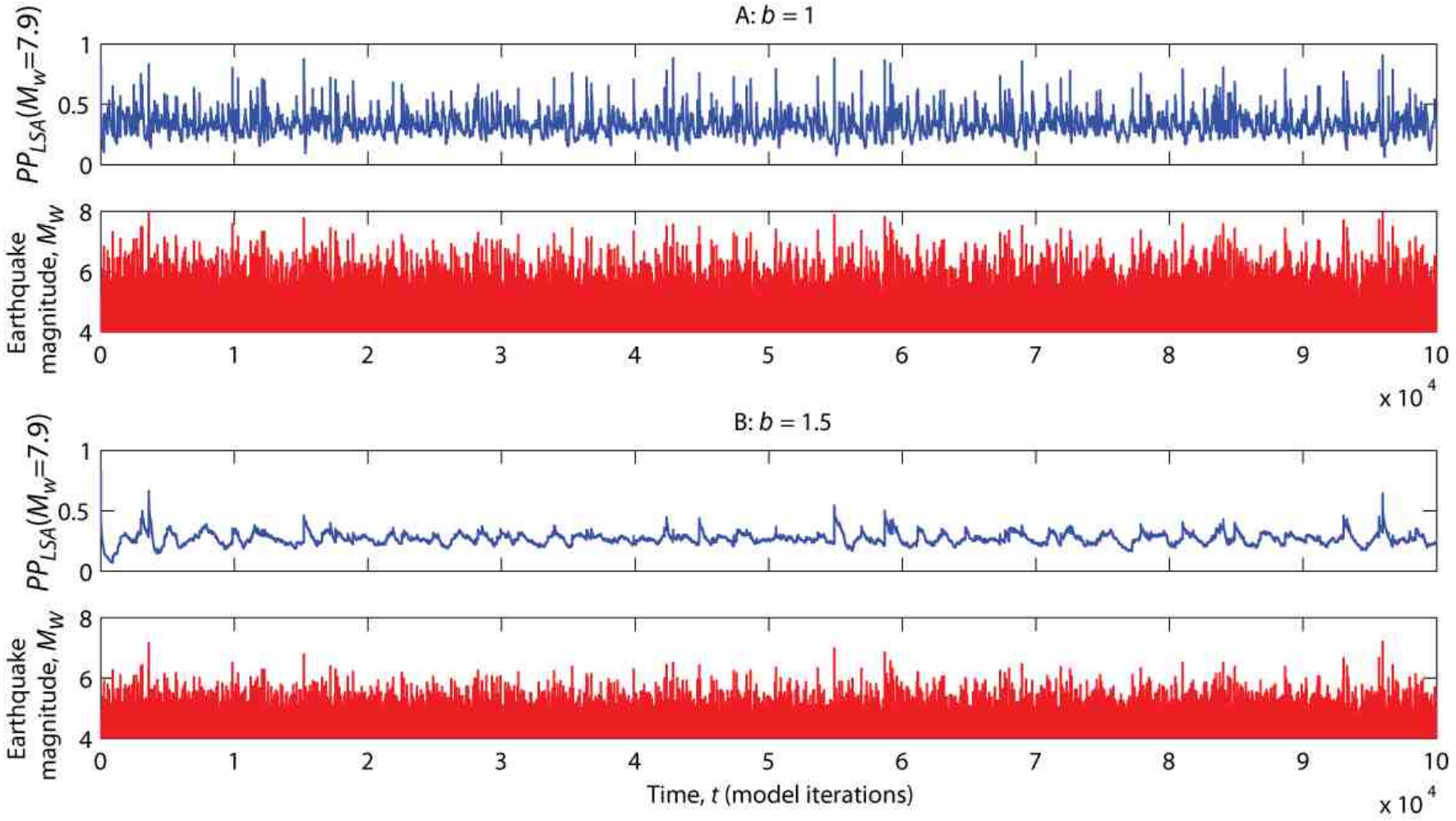

Figure 6-24 Long term $PP_{LSA}(M_w = 7.9)$ time-series in response to GR distributed earthquakes when b = 1 (A) and b = 1.5 (B), and τ_{fp} = 1.1

For understanding the likelihood of a landscape being in different landslide propensity states, it is useful to consider the long-term distribution of PP_{LsA} values. With this information, even if the recent seismic history is unknown the long-term seismicity of a region could potentially be used to predict the PP_{LsA} distribution. Over long time-scales PP_{LsA} is distributed about a central value, however the shape of the distribution changes with τ_{fp} and b. As shown in Figure 6-25, as τ_{fp} increases, values become more dispersed resulting in an increase in the standard deviation of the distribution, and at the same time PP_{LsA} reaches lower minimum values. Note that the mean PP_{LsA} does not change as the effect of change τ_{fp} is balanced by the corresponding change in k. At higher values of τ_{fp} the distribution begins to exhibit additional peaks either side of the central value. These correspond to levels at which peaks and periods of near constant PP_{LsA} (during decay phases) commonly occur. While these features appear to be prominent over these timescales, is it unclear whether they would persist across longer earthquake time series. As b decreases both the mean and standard deviation of PP_{LsA} values increase. This indicates that, while more frequent large earthquakes produce a higher level of variability, the average sensitivity of the landscape to landslide triggering is also higher when more large earthquakes and less small earthquakes occur.

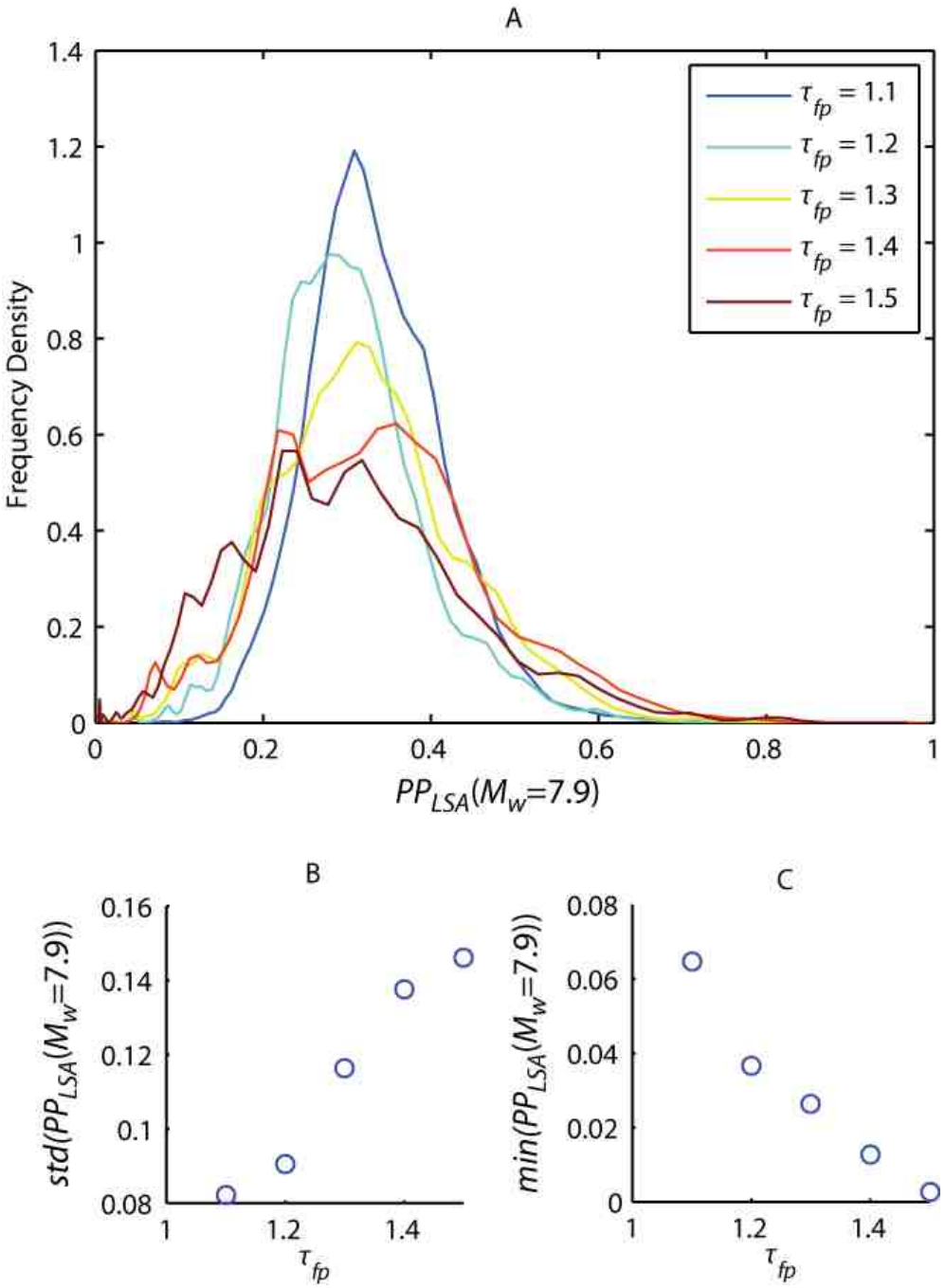

Figure 6-25 Long-term distributions of landslide propensity (A), $PP_{LsA}(M_w = 7.9)$, for different values of τ_{fp}; Relationships between τ_{fp} and distribution standard devaition (B) and minimum (C).

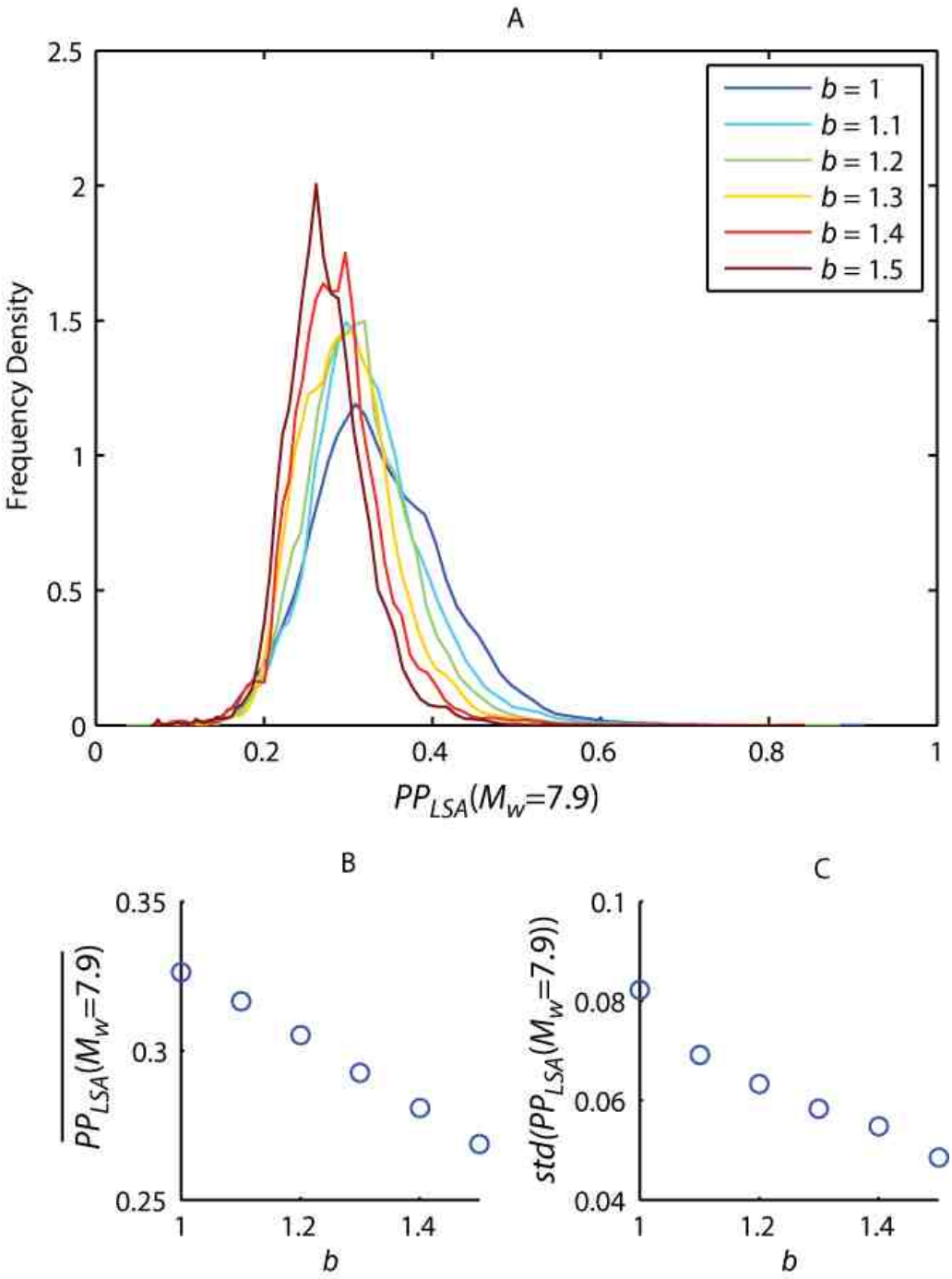

Figure 6-26 Long-term distributions of landslide propensity, $PP_{LSA}(M_w = 7.9)$, for different values of b; Relationships between b and distribution mean (B) and standard deviation (C).

6.4 Summary

Modelling evolving landslide masses in hillslopes as a population of strain-softening Newmark sliding blocks, shows how the temporal evolution of failure in brittle hillslope materials may influence landslide propensity across time. Changes in the FS in PLM populations results in periods when more or fewer landslides are close to the point of failure and would be triggered by the next large earthquake, producing temporal

variability in landslide propensity. The temporal pattern of this variability is linked to the relative magnitudes of earthquakes in the time-series. When large earthquakes follow periods of smaller earthquakes, strength degradation initially accumulates in the system more rapidly than it is removed via the ongoing failure of PLMs, resulting in a net increase in landslide propensity. When smaller earthquakes follow larger earthquakes, damage is removed from the system more rapidly than it accumulates, resulting in a decrease in landslide propensity. The temporal pattern of landslide propensity variability takes the form of an impulse-response function, which peaks immediately following large earthquakes, followed by a decay in response to subsequent smaller earthquakes. However, in response to sequences of GR distributed earthquakes, the system exhibits a transient long-term behaviour, in which landslide propensity is constantly changing.

Having established how the model system behaves, and how different factors influence the temporal evolution of landslide propensity, it is now possible to explore the implications of these findings for understanding the behaviour of real landscapes. This detailed discussion is now provided in Chapter 7, where model outputs are synthesised with an understanding of landslide spatial distributions and related to empirical observations of earthquake-triggered landslides.

Chapter 7 - Discussion

The lack of consideration previously given to integrating progressive hillslope failure driven by seismic loading into models of regional-scale landsliding, has resulted in a limited understanding of how landslide activity varies with time in seismically active landscapes. As a consequence, landslide models at the scale of areas affected by earthquakes have been built on the assumption that landslide propensity is constant with time and that there is no temporal dependence or memory within the system (Guzzetti et al., 2003, Guzzetti et al., 2005, Guzzetti et al., 2006, Meunier et al., 2007). This knowledge gap provides a potential candidate for explaining the substantial uncertainty in current ETL models. In order to investigate the effect of memory on ETL activity, this thesis first applied an empirical approach through analysis of spatial distributions of landslides triggered by earthquakes. A generalised understanding of spatial patterns of hillslope failure was established by investigating the influence of current earthquake characteristics and static landscape conditions on hillslope failure probability. This understanding was used to develop a conceptual model explaining observed patterns of regional-scale ETL activity by considering hillslope failure through brittle material deformation. Spatial distributions of hillslope failure in the 1929 and 1968 New Zealand earthquakes hint at the influence of hillslope memory on regional-scale landslide activity. However, due to the limited temporal coverage of landslide data and difficulties in controlling for the influence of additional forcings affecting hillslope stability, only a limited understanding of the effect of hillslope memory can be gained through such empirical investigation. Therefore, to provide a controlled environment to investigate the temporal response of hillslopes, a numerical model was developed with the aim of answering the following research questions:

- *What is the impact of large earthquakes on subsequent landslide activity?*
- *How can long-term patterns of variability in landslide propensity be linked to seismic history?*
- *How does the way in which landslides evolve affect the importance of earthquake-triggered landslides in long-term erosion rates and levels of landslide hazard?*

This chapter discusses these questions. Throughout this chapter a number of additional model outputs are generated, to provide examples for discussion. The model parameters used are given with each example, and have been chosen to best demonstrate the relevant effects. Comparison of outputs is also made between the statistical landslide probability models developed in Chapter 4, and the numerical model developed in Chapter 6. For clarity of discussion, the statistical model is referred to as time-independent, as landslide events are assumed to be independent of one another in time, while the numerical model is referred to as time-dependent, as the previous events affect future events and the impact of an earthquake is therefore dependent on the precise time of occurrence. Critically, these terms do not refer to the nature of the strain accumulation process, as they are commonly used in geotechnical literature (e.g.: Petley et al., 2005a, Petley et al., 2005b, Petley et al., 2008, Bell, 2000, Singh, 1975).

7.1 What is the impact of large earthquakes on subsequent landslide activity?

The model outputs from Chapter 6 suggest that the change in landslide propensity produced by a single large earthquake, preceded and followed by smaller earthquakes, takes the form of an impulse response. Immediately following the earthquake there is a peak in landslide propensity, followed by either a simple decay to static conditions or an oscillating recovery to a non-static by low variability state. The magnitude of the impulse peak is strongly dependent on the magnitude of the earthquake of interest, while the decay period is dependent on the magnitude of subsequent events and the hillslope material properties. This type of oscillating temporal response has long been hypothesised for geomorphic systems, where the current state or sensitivity of the system is influenced by historical processes (Thornes, 1983, Brunsden and Thornes, 1979, Schumm and Lichty, 1965). This is particularly the case when the external shock to the system takes the form of a pulsed input, such that the imposed disturbance is short in relation to the timescale being considered (Brunsden and Thornes, 1979), as is the case when earthquake-triggered landslides are considered across the return period of multiple earthquakes. The modelling framework developed here provides a tool to quantitatively investigate the nature of this complex, time-dependent landscape response in the case of earthquake-triggered landslides.

In order to validate the model predictions and explore the relevance to real landscape behaviour, model outputs must be compared with observed changes in landslide activity associated with earthquakes. This first requires a spatial and temporal understanding of the landslide propensity response. As the modelling in Chapter 6 was carried out in a 1-dimensional environment, using a single set of hillslope characteristics, spatial variability the landslide propensity response must first be inferred by synthesising the outputs of Chapter 6, with the understanding of landslide spatial distributions developed in Chapters 4 and 5.

7.1.1 Spatial variability in the landslide propensity response to large earthquakes

While all hillslopes experience impulse peaks in landslide propensity simultaneously when large earthquakes occur, both the amplitude and decay period will vary spatially with the strength of forcing, superimposed onto favourable topography and lithology. The effects of these individual variables are summarised in Figure 7-1. The largest impulse peaks can be expected in regions of strong ground accelerations, which decay with distance from seismic sources as the strength of mainshock ground accelerations attenuates (Figure 7-1 A1 & A2). Following large earthquakes, the subsequent pattern of decay and recovery is dependent on the progression rate in PLMs, which is reflected in spatial patterns of hillslope failure probability (see Section 5.2). As the density of aftershocks decays with distance from the mainshock (e.g.: Bach and Hainzl, 2012, Felzer and Brodsky, 2006), hillslopes in closer proximity to the earthquake rupture will experience stronger ground accelerations during aftershocks. In close proximity to seismic sources, PLMs will accumulate strain and progress towards failure more rapidly, resulting in a short duration impulse period and decay. As ground accelerations produced by smaller earthquakes will exceed peak critical accelerations in these areas, the impulse response is likely to have an oscillating recovery as hillslopes repeatedly fail in synchrony (Figure 7-1 A1 & B1). However, at distance from seismic sources, the progression rate is slower, resulting in a longer impulse response period. Here peak critical accelerations are less likely to be exceeded in small earthquakes, so landslide propensity is likely to exhibit a simple decay towards a static condition (Figure 7-1 A2 & B2). This means that while changes in landslide propensity are greatest close to coseismic faults the legacy of large earthquakes endures for longer at greater distances.

If all other factors remain constant as hilllslope gradients increase, critical accelerations decrease. This implies that steeper hillslopes will experience a more rapid, shorter oscillating decay in landslide propensity, while hillslopes with shallower gradients will have a slower, longer decay towards a static state. Differences in the material properties of different lithologies will also contribute to different impulse periods, with longer periods when peak strength is high, and shorter periods where peak strength is low (Figure 7-1 C).

While distance from the seismic source, hillslope gradient and lithology have been treated as independent in terms of their influence on landslide activity, in reality this is unlikely to be realistic. Spatial patterns of landslide propensity will also reflect interactions between these factors. Although the way in which these factors interact will vary regionally, some broad relationships can be theorised. High relief and steep hillslopes often occur along active faults with high slip rates. These same regions often contain major tectonic structures and are associated with high levels of seismicity. Additionally, topographic amplification effects are stronger in high relief areas (Meunier et al., 2008, Murphy, 2006, Sepulveda et al., 2005). The increase in landslide propensity decay period with distance from seismic sources is therefore likely to be amplified by the fact that hillslope gradients may also decrease away from major faults. In turn, the maximum gradient and relief that hillslopes can sustain is dependent upon material strength (e.g.: Hoek, 2000, Schmidt and Montgomery, 1995). Therefore, in simple terms, steeper hillslopes are likely to be composed of materials with higher peak strengths than shallower hillslopes. The increase in rate of landslide propensity decay with increasing hillslope gradient may therefore be damped by the decrease associated with increasing peak strength.

This spatial variability in and interactions between driving factors is likely to create spatial and temporal complexity in patterns of ETL activity. The following section discusses the extent to which observed complexity in ETL activity reflects that predicted in the model outputs.

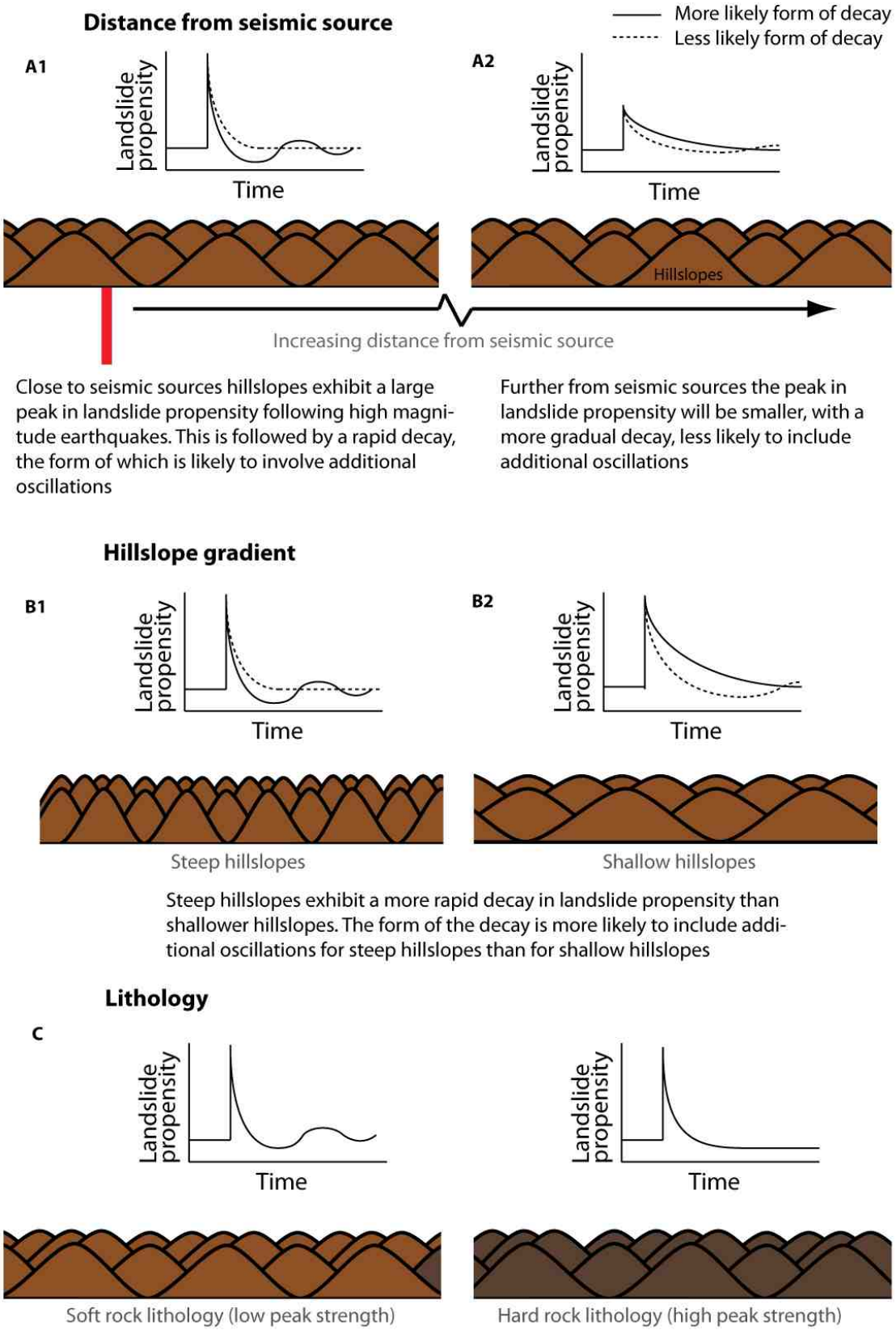

Figure 7-1 Schematic diagram of showing characteristics of spatial variability in temporal changes in landslide propensity following large earthquakes. Impulse responses vary in magnitude and decay period with distance from coseismic sources (A), hillslope gradient (B) and lithology (C)

7.1.2 Observed temporal changes in landslide propensity

While the analysis of model outputs has examined the effect of earthquakes on landslide propensity during subsequent earthquakes, there are currently limited empirical data to validate these results directly, owing to a lack of multi-temporal landslide inventory data during aftershock sequences. Changes in the stability of landslides associated with brittle deformations also affect their propensity to fail in response to elevated pore-pressure (Petley et al., 2005a, Petley et al., 2005b, Iverson, 2000). Therefore, observed changes in rainfall-triggered landslide activity following large earthquakes can also be interpreted in light of the model findings (see Section 5.1.3).

Observations from the Chi-Chi earthquake suggest a post-seismic increase in the occurrence of rainfall-triggered landslides (Lin et al., 2008b, Lin et al., 2008a, Lin et al., 2004), with a return to pre-earthquake levels within ~6 years (Hovius et al., 2011), for the 367 km^2 Chenyoulan catchment, located between 10~20 km from the earthquake fault (See Figure 2-13, pp. 42). When the size of rainfall events is controlled for in analysis, findings suggest that the cause of this behaviour is attributed to changes in the sensitivity of the landscape to landsliding, rather than changes in rainfall magnitude. The amplitude of changes in landslide propensity post-Chi-Chi can be compared to those observed in the numerical model. Hovius et al. (2011) use the area of landslides normalised for the rainfall event magnitude (the total water discharge from the catchment) to represent the sensitivity to landslide triggering by rainfall. This is an equivalent index of landslide propensity to PP_{LsA} used in the numerical model - note that PP_{LsA} considers a fixed strength of earthquake forcing so does not require normalisation. While the data from Hovius et al. (2011) represents the aggregate sensitivity of hillslopes with different gradients that have experienced spatially variable PGAs, relative changes in landslide propensity should be broadly comparable to those modelled in Chapter 6, as the area is limited to a small catchment close to the coseismic fault. Following the M_w = 7.6 Chi-Chi earthquake, observed landslide propensity peaks at around 7 times the pre-earthquake average, indicating a seven fold increase in sensitivity to rainfall-triggered landsliding. Compare this to Figure 7-2, which shows the change in PP_{LsA} for each earthquake in the time series from Figure 6-22, expressed as a ratio of PP_{LsA} prior to each earthquake. A seven-fold increase in

landslide propensity is within the range produced by M_w = 7.6 modelled earthquakes, when hillslope material peak strength is higher and long-term PP_{LsA} variability is therefore greater. This amplitude of change in PP_{LsA} is only observed in the numerical model when the landslide propensity is low prior to the HM earthquake (Figure 6-23). This suggests that, in order to experience a similar increase, hillslopes in the Chenyoulan catchment were in a low state of landslide propensity when the Chi-Chi earthquake occurred. In this case, the area disturbed by landsliding may represent a lower bound of the potential impact of M_w = 7.6 earthquakes in this region. Note that the time between the earthquake and the next large rainfall event, is ~1.5 years, which is probably the reason for the lag time between the Chi-Chi earthquake and the apparent peak in landslide propensity.

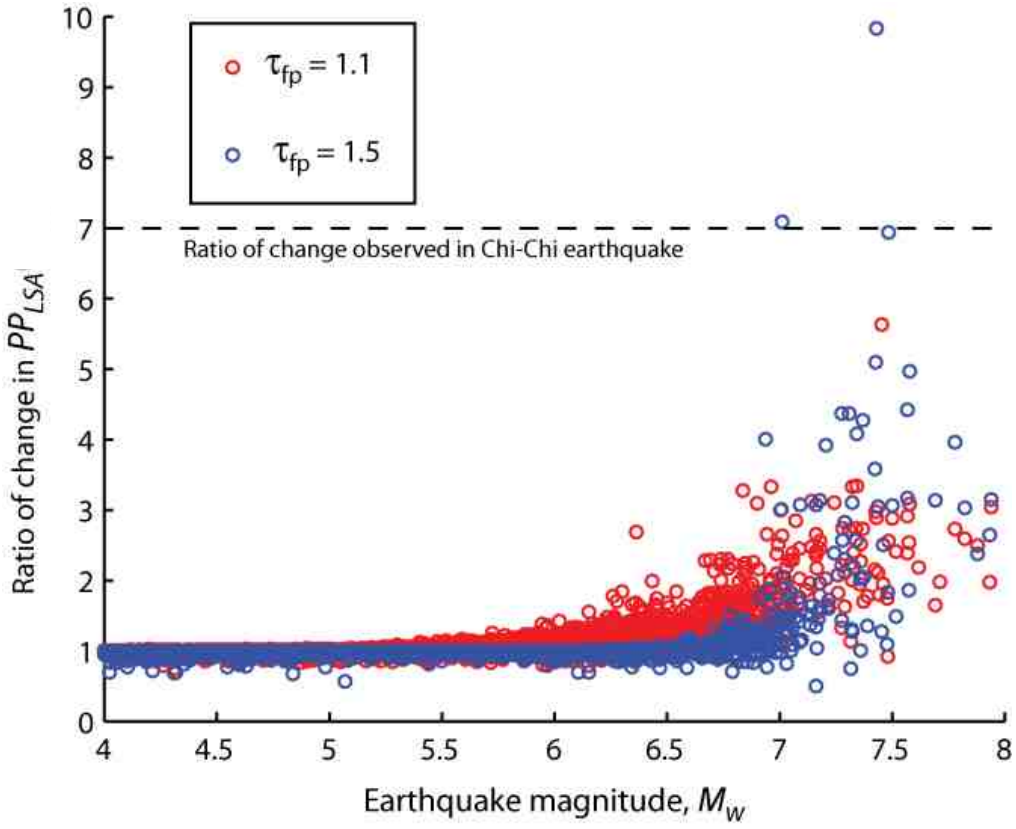

Figure 7-2 Landslide propensity changes produced by different magnitude model earthquakes, expressed as a ratio of landslide propensity prior to each earthquake. Ratios > 1 indicate an increase in landslide propensity, and vice-versa. Results are shown for peak strength values (τ_{fp}) of 1.1 and 1.5, using data from Figure 6-22. The dashed line indicates the change in landslide propensity observed following the Chi-Chi earthquake, which is within the range of model results when τ_{fp} = 1.5.

While limited analysis of spatial variability in the temporal signal has been undertaken for the Chi-Chi earthquake, observations also support the model finding that the peak in landslide occurrence varies spatially with the amplitude of ground accelerations.

Hovius et al. (2011) showed that the density of typhoon-triggered landslides following the Chi-Chi earthquake reflects a combination of spatial patterns of mainshock PGA and rainfall intensity (Figure 7-3). Regions experiencing a higher mainshock PGA experience a larger increase in landslide propensity, and therefore higher rainfall-triggered landslide densities following the earthquake.

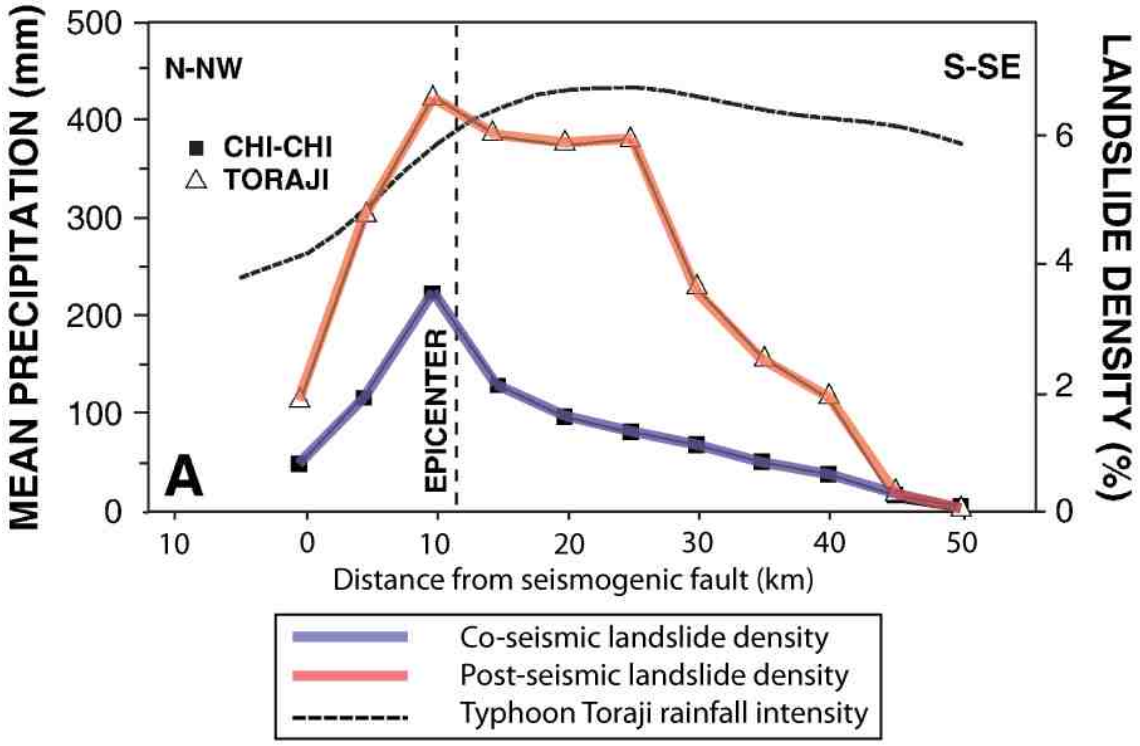

Figure 7-3 Density distributions of landslides triggered by the 1999 Chi-Chi earthquake and subsequent typhoon triggered landslides, with respect to the seismogenic fault (after Hovius et al., 2011: 352). Regions closer to the fault, which experienced higher ground accelerations and co-seismic landslide densities, also experience higher post-seismic landslide densities.

Although the initial increase in landslide propensity can be linked directly with the magnitude of mainshock earthquakes, the rate of decay is dependent on the strength of subsequent forcing events and hillslope material properties, and is only weakly influenced by the mainshock magnitude. For earthquakes of different magnitudes, if the subsequent pattern of aftershocks and rainfall is the same, the rate of landslide propensity decay will be similar. Earthquakes of the same magnitude may be followed by very different decay rates, if the subsequent patterns of aftershocks and rainfall differ. As seismicity and precipitation vary regionally, these differences are likely to be reflected in different landslide responses recorded for different earthquakes. This can be explored through a comparative analysis of the 1999 Chi-Chi and 2005 Kashmir earthquakes. Data from Saba et al. (2010) suggest that the period of post-mainshock

decay in landslide activity following the Kashmir earthquake is around 2 years. This is 3 times shorter than the ~6 year decay observed for the Chi-Chi earthquake, despite the two events having the same mainshock seismic moment and similar depth, with sample areas located at a similar distance from the seismic sources . Accordingly, this difference in decay period should be attributable to some difference in the magnitude of landslide triggering events that followed the mainshock.

Table 7-1 shows two variables with which to gauge the relative strength of subsequent precipitation and seismic forcings following these events. A 50 km radius from the earthquake epicentres was found to enclose the sample areas from both studies. Within this area, the mean annual rainfall was calculated using global gridded mean annual precipitation data from Hijmans et al. (2005). The total seismic moment released within the first two years following the earthquakes is derived from the USGS NEIC PDE catalogue (National Earthquake Information Center, 2012). The catalogue provides a global record of earthquakes with $M_w \geq 4$, and is considered the most complete record of seismicity that includes data for both regions. While magnitude completeness thresholds vary by region, the dataset aims to be complete for $M_w \geq 5.5$ (Engdahl and Villaseñor, 2002). Note that for Pakistan the catalogue is estimated to be complete down to magnitude 4 from 1964 onwards (Sarawar et al. 2011). In order to ensure the relative completeness and comparability of the catalogue for the two regions, a magnitude cut-off of $M_w \geq 5.5$ was also applied to the comparison.

Table 7-1 Comparison of mean annual precipitation and seismic moment release following the Chi-Chi and Kashmir earthquakes

Earthquake	**Landslide propensity decay period (Years)**	**Mean annual precipitation (mm), within 50 km of earthquake epicentre**	**Seismic moment released in first 2 years following the main-shock (Nm), within 50 km of the earthquake epicentre**	
			$\boldsymbol{M_w \geq 4}$	$\boldsymbol{M_w \geq 5.5}$
Chi-Chi	~6	2245	1.9×10^{18}	3.2×10^{17}
Kashmir	~2	1054	7.8×10^{18}	3.8×10^{18}
Difference (Chi-Chi minus Kashmir)	~4	1191	-5.9×10^{18}	-3.4×10^{18}
$\boldsymbol{M_w}$ **equivalent**			1 x M_w 6.4	1 x M_w 6.3

As annual precipitation for the area affected by the Chi-Chi earthquake is more than double that for Kashmir, this analysis suggests that the difference in decay rate is not driven by precipitation. The total seismic moment recorded in the two years following the Kashmir earthquake was 4 to 12 times greater than that following the Chi-Chi earthquake. For the $M_w \geq 5.5$ cut-off, the difference is equivalent to 1 x $M_w = 6.3$ earthquake or 16 x $M_w = 5.5$ earthquakes. The results of Section 6.3.2 suggest that the number of magnitude 5.5 earthquakes required to drive decay from peak to background mean landslide propensity levels increases linearly with material peak strength. These results are shown in Figure 7-4, with a linear extrapolation for peak strength values up to the point where $M_w = 8$ earthquakes would cease to drive strain accumulation. The results suggest that between 7 and 35 x $M_w = 5.5$ earthquakes are required to complete the initial decay from peak to background landslide propensity levels. The difference in seismic moment release following the Chi-Chi and Kashmir earthquakes is therefore sufficient to explain the observed difference in decay period.

This finding suggests that, while high levels of post-mainshock landslide activity have been associated with precipitation events, the role of aftershocks in triggering landslides and determining the prolonged geomorphic response of large earthquakes may be under considered. If this is the case, then a larger percentage of landslides associated with the Kashmir earthquake should have been triggered by aftershocks, than was the case for the Chi-Chi earthquake. Although it has been suggested that landslides following the Chi-Chi earthquake were largely unrelated to aftershocks and mainly triggered by typhoon rainfall, landslide data are not sufficient to test and investigate this quantitatively. As the release of aftershock seismic moment decays rapidly following the mainshock (Figure 7-5), testing this hypothesis further would require repeated landslide mapping at regular intervals in the first days and weeks following the earthquake. Additionally, records of landslides triggered by aftershocks could provide an indication of the extent to which landslide propensity decays in the time shortly after mainshock events, and the sustained potential for rainfall-triggered landsliding. Note that the difference between these events could also be attributed to different lithological material properties. However, the opposing effect of coupled changes in material strength and hillslope gradients (Section 7.1.1) may dampen the overall change in the landslide propensity response associated with lithology.

Quantitative data on material properties and further model experiments are required to test this.

In summary, model outputs suggest that large earthquakes produce an impulse response change in landslide propensity, which varies spatially with patterns of co-seismic and post-seismic landslide activity. The intensity of changes is greatest for hillslopes with the highest densities of co-seismic landslides, while the legacy period is longer in areas that experience fewer post-seismic landslides. Although ETL data are not available to compare with model outputs, temporal patterns of rainfall-triggered landsliding following the Chi-Chi and Kashmir earthquakes reflect this impulse response behaviour. For the Chi-Chi earthquake, both the amplitude and distribution of landslide propensity changes agree with model outputs, while the difference in decay period for the Chi-Chi and Kashmir earthquakes is commensurate with differences in aftershocks.

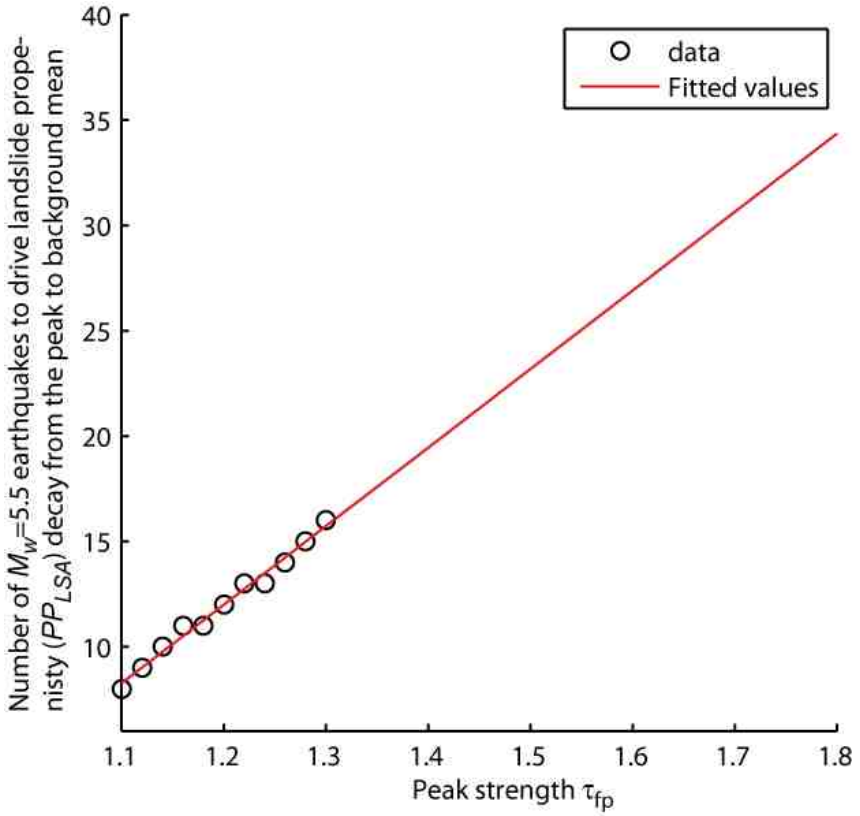

Figure 7-4 Relationship between the number of earthquakes required to reduce landslide propensity to background mean levels and material peak strength. Data are taken from Figure 6-21

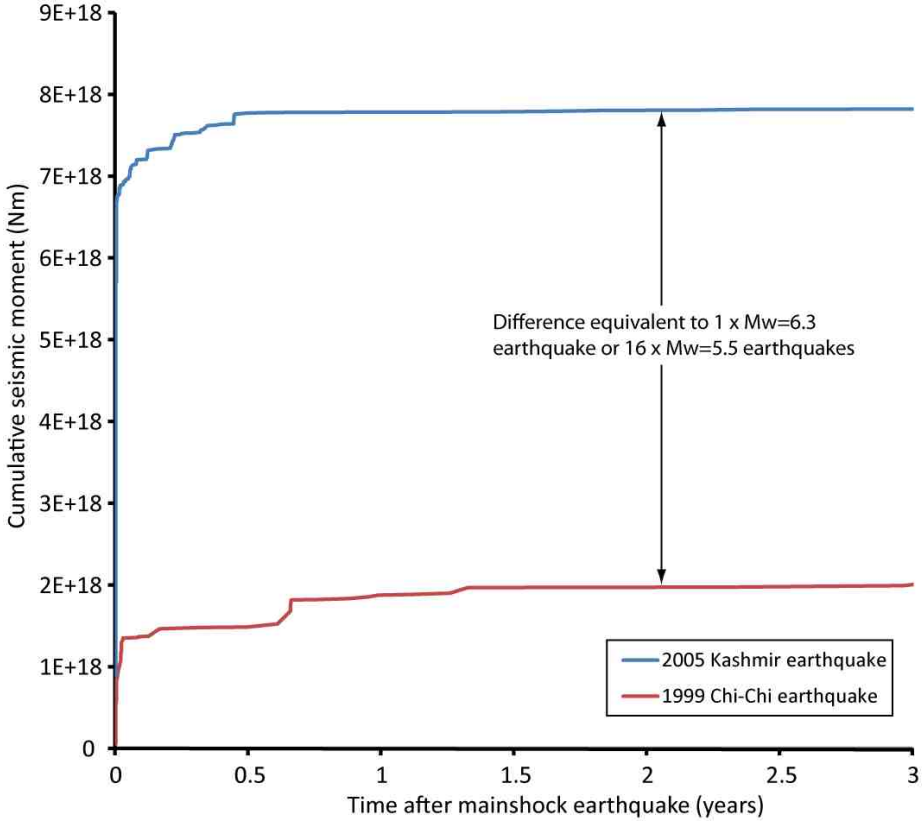

Figure 7-5 Time-series of cumulative seismic moment released following the 1999 Chi-Chi and 2005 Kashmir earthquakes, for areas within 50 km of the earthquake epicentres (data from National Earthquake Information Center, 2012).

7.2 How can long-term patterns of variability in landslide propensity be linked to seismic history?

For every earthquake considered the model suggests that landslide occurrence is influenced by the legacy of previous events. This results in significant uncertainty in predicting the landslide propensity at any point in time and in response to any particular event. In order to address this, the longer-term effect of seismic history on landslide propensity is considered. This section examines how long-term patterns of landslide propensity evolution can be constrained as a function of seismic history and how these principles can be used to explain uncertainty in fitted earthquake-triggered landslide relationships.

7.2.1 Long-term patterns of landslide propensity variability

While Section 7.1 considered the landslide response to individual earthquakes in terms of single damped impulse, the results of Section 6.3.3 suggest that the long-term behaviour is defined by sequences of impulses that overlap one another. The long-term norm for the system is therefore a transient state in which landslide propensity is always changing, rather than a pattern of long-term stability punctuated by infrequent impulses. This behaviour can be understood as a consequence of a high transient-form ratio, TF_r (after Brunsden and Thornes, 1979):

Equation 7-1

$$TF_r = \frac{mean\ recovery\ time}{mean\ recurrence\ time\ of\ events\ (large\ earthquakes)}$$

The model outputs suggest that, in general, large earthquakes occur more regularly than the time taken for landslide propensity to recover following impulse peaks. Therefore, landslide propensity never has chance to stabilise and is in a continual state of change.

In response to sequences of GR-distributed earthquakes, landslide propensity exhibits a large range of temporal variability about a central value. In near-fault regions this variability can result in the percentage of hillslopes that fail in magnitude 7.9 earthquakes ranging from <10% to >90%, for 40^{o} hillslopes. There are two possible

approaches to predicting landslide propensity values, depending on the availability of seismic data. The first approach is simply to constrain the long-term distribution of PP_{LsA} values. The results of Section 6.3.3 show how characteristics of the PP_{LsA} distribution are dependent on the hillslope material properties (coupled peak strength, τ_{fp}, and strength decay, k, parameters) and the earthquake distribution GR b-value. By modelling the long-term distribution of PP_{LsA} values as a function of these variables, uncertainty in landslide models that assume time-independence could be estimated. However, this approach provides no information regarding time-dependent changes in landslide propensity and hazard.

A second approach is to use records of seismic data to predict the temporal evolution of landslide propensity. This can be achieved based on the understanding of how characteristics of the past seismic history influence future landslide propensity. As shown in Figure 6-23, larger earthquakes mostly increase landslide propensity, only producing a decrease on the rare occasion that two large earthquakes occur in close succession. Conversely, smaller earthquakes only act to decrease landslide propensity. Therefore, a sequence of earthquakes dominated by more recent larger events is more likely to result in high landslide propensity, while a sequence dominated by smaller earthquakes, with the last large earthquake occurring prior to these, is more likely to result in low landslide propensity. The threshold magnitude separating these two cases (M_t) increases with the peak strength of the hillslope material (Figure 7-6).

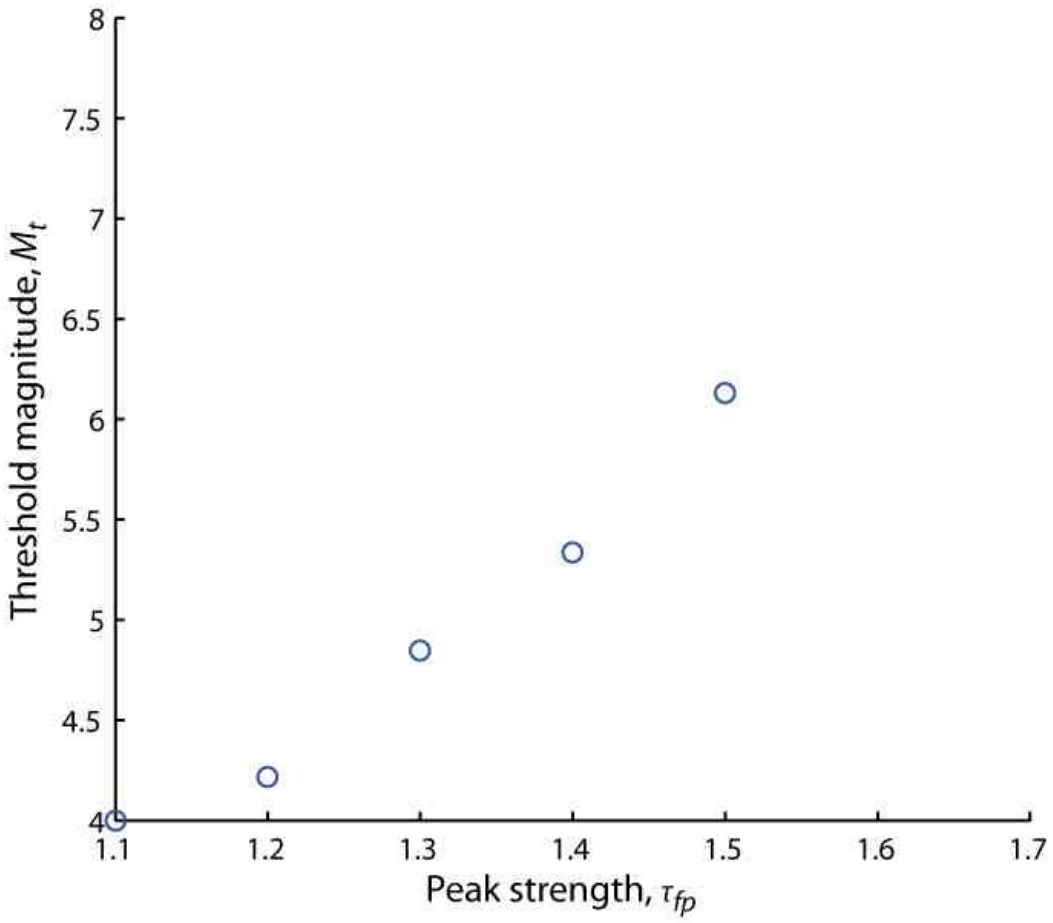

Figure 7-6 Plot of M_t threshold seperating larger earthquakes that mainly increase landslide propensity ($PP_{LsA}(M_w = 7.9)$) and smaller earthquakes that only decrease landslide propensity, against peak strength (τ_{fp})

A generalised index of landslide propensity can therefore be expressed as the ratio of previously released seismic moment generated by earthquakes with $M_w > M_t$ to that generated by earthquakes with $M_w < M_t$, termed the seismic strength ratio, SSR.

Equation 7-2

$$SSR = \frac{log(M_{op})\ M_w > M_t}{log(M_{op})\ M_w < M_t}$$

where M_{op} is the total previously released seismic moment upon which current landslide propensity depends. Note that as seismic moment scales logarithmically with earthquake magnitude, logarithms of seismic moment are used in the calculation. For a test case using $\tau_{fp} = 1.5$, an M_{op} value of 2 x 10^{20} Nm was found to be optimal for predicting PP_{LsA}, which is equivalent to the moment of an $M_w = 7.5$ earthquake. If the last earthquake had a magnitude of 7.5 or greater, current landslide propensity is primarily dependent on this event and likely to be high. If the same seismic moment was released in 1,000 magnitude 5.5 earthquakes, then a longer time-series of

earthquakes is considered in order to gauge how far landslide propensity has decayed since the last large event. The number of previous earthquakes necessary for inclusion in the calculation depends on the magnitude of those events. Where SSR is low, small earthquakes dominate the recent seismic history and landslide propensity is more likely to be low, and vice-versa.

The calculation of SSR is illustrated in Figure 7-7. In order to estimate PP_{LsA} at the end of the time-series, earthquakes prior to this point in time are considered. The cumulative seismic moment is calculated from the present, backwards through the time-series, and earthquakes are included in the calculation of SSR from the point in time where the cumulative seismic moment equals M_{op}.

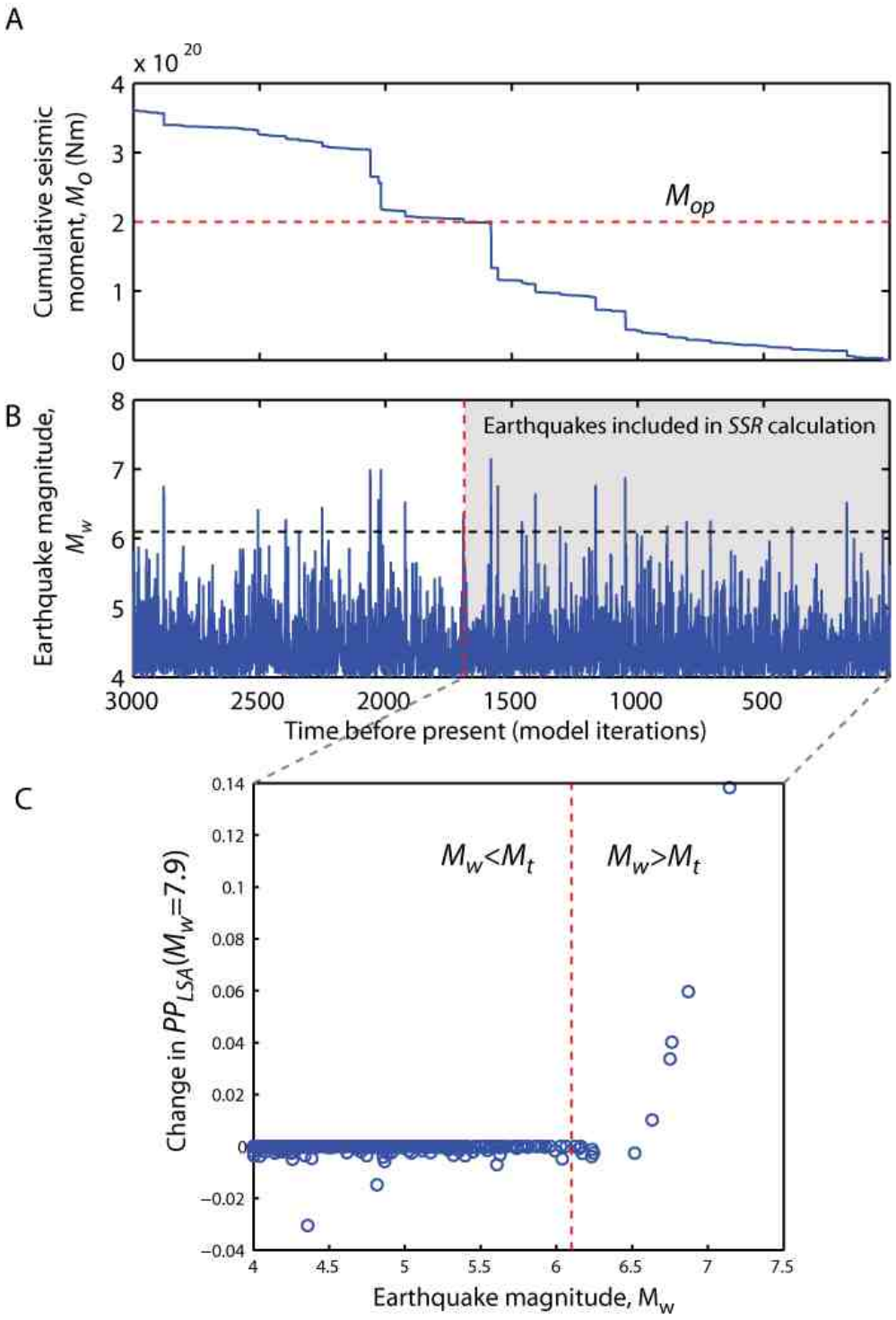

Figure 7-7 Schematic diagram showing how the seismic strength ratio (SSR) is calculated. The timeseries in B represents the history of earthquakes prior to the point in time for which SSR is being calculated. Seismic moment is calculated cumulatively back in time and earthquake magnitudes are used in the calculation up to the point where the total seismic moment equals M_{op} (A). Earthquakes with $M_w > M_t$ generally increase PP_{LsA} and are seperated from earthquakes with $M_w < M_t$, which only decrease PP_{LsA} (C). Equation 7-2 is then used to calculated SSR.

Figure 7-8 shows the relationship between SSR and PP_{LsA}, where $\tau_{fp} = 1.5$. The relationship can be reasonably described via a logistic function, which is appropriate for modelling this relationship, as the response variable is bounded at 0 and 1 (see Section 4.1.1). The clustered structures within the scatter are due to the temporal correlations between sequential observations. The R^2 value indicates that the fitted model explains 46% of the variance in PP_{LsA}. Figure 7-9 shows a comparison between the PP_{LsA} time series generated using the full iterative model and values predicted using the SSR function, with 95% confidence intervals. The SSR model replicates the general saw-tooth pattern of peaks and decay phases, providing a smoothed estimation of the landslide propensity signal. Using the numerical model data, the SSR index provides a reasonable predictor variable of landslide propensity. Major errors in the prediction are associated with periods when the largest PLMs in the distribution move through the failure zone, and would be reduced by aggregating data over a larger PLM population (equivalent to a larger spatial extent). The prediction could be further improved using a more sophisticated index, with detailed modelling of the probable effect of different magnitude earthquakes. However, at this stage SSR is used to provide a first-order theoretical example of predicting the evolution of landslide propensity using records of historical seismicity. If the temporal evolution of landslide propensity in real landscapes obeys the principles captured in the SSR model, then it should be possible to explain some of the observed variability in landslide datasets.

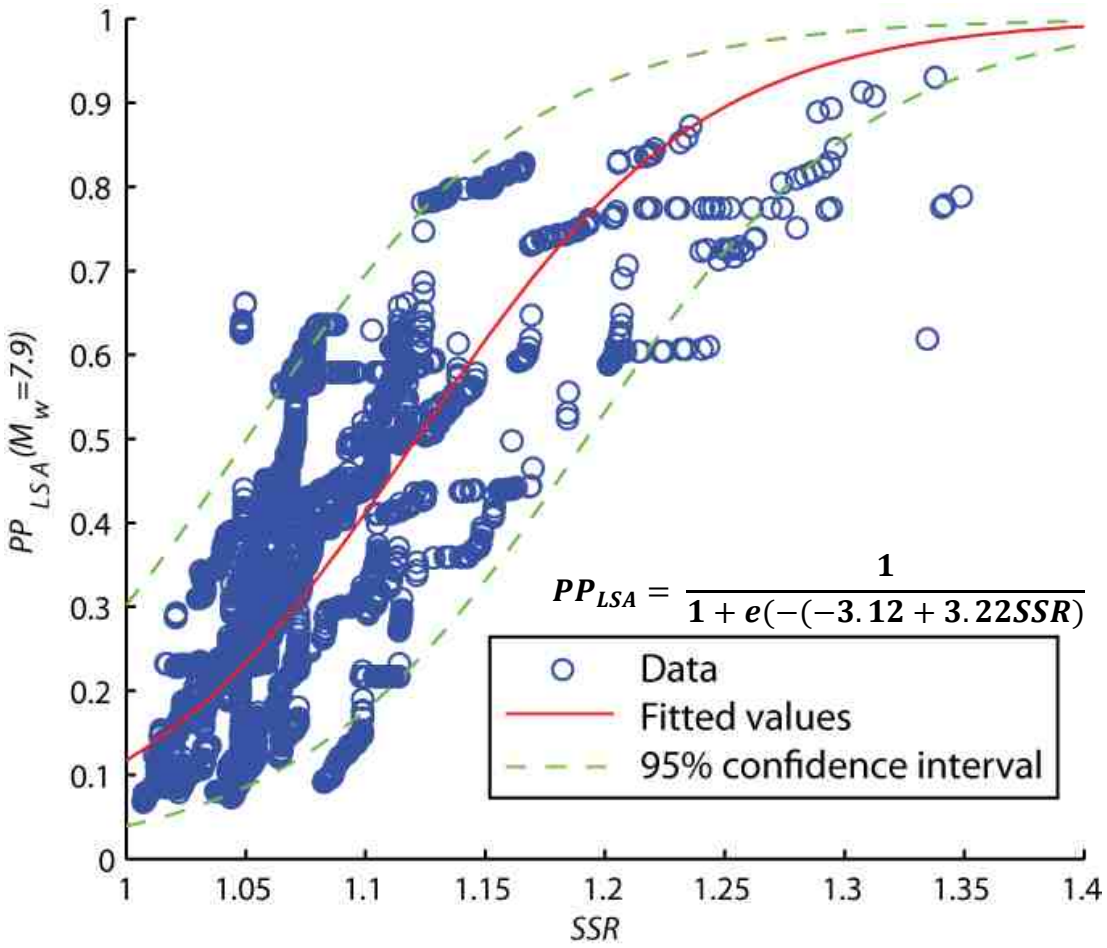

Figure 7-8 Plot showing the relationship between seismic strength ratio (*SSR*) and landslide propensity ($PP_{LSA}(M_w = 7.9)$), described using a logistic function. The model has an R^2 value of 0.46. An SSR of 1 indicates that the seismic moment released by recent earthquakes was distributed equally between larger earthquakes with $M_w > M_t$ and smaller earthquakes with $M_w < M_t$. As SSR increases, larger earthquakes with $M_w > M_t$ account for a greater proportion of recently released seismic moment. Note that SSR can also have values less than 1 if small earthquakes dominate the seismic history, although none appear in this example.

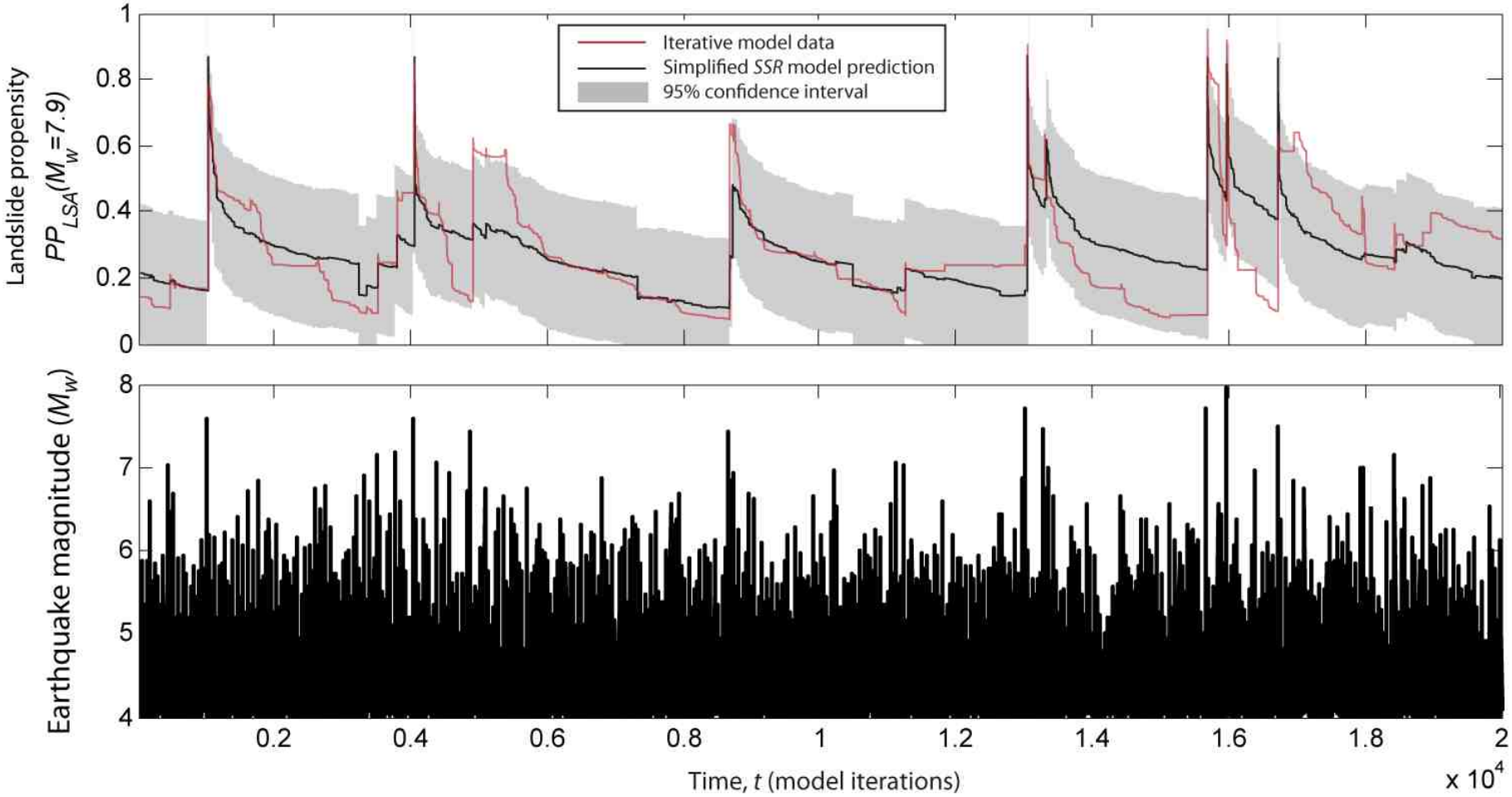

Figure 7-9 Time series comparison of numerical mode landslide propensity (PP_{LsA}) and landslide propensity predicted as a function of seismic strength ratio (SSR)

7.2.2 Seismic history and uncertainty in global earthquake-triggered landslide relationships

As shown in Figure 2-8 (pp. 34), global relationships between numbers and volumes of landslides triggered by earthquakes and earthquake magnitude exhibit large residuals (Malamud et al., 2004b, Keefer, 2002, Keefer, 2009, Keefer, 1994). While there are a number of potential sources of this variability, including differences in topography, lithology and climate (Malamud et al., 2004b), the results of this investigation suggest that seismic history may also have a significant influence. In regions that have more recently experienced a large earthquake, the number of landslides triggered by another earthquake should be greater than in the same region following a long period without a large earthquake (assuming that lower magnitude events have driven a decay in landslide propensity). In order to test this, numbers of landslides recorded for recent earthquakes are analysed relative to recorded earthquake histories.

The USGS centennial catalogue provides a global record of instrumented earthquakes for the period 1900 to 2008 (Engdahl et al., 2002, Engdahl and Villaseñor, 2002). For the period 1964 to 2008 the catalogue is complete down to magnitude 5.5, from 1930 to 1963 it is complete down to magnitude 6.5, and from 1900 to 1930 it is complete down to magnitude 7. This data can be used to provide an indication of the seismic history of different regions where recent earthquake-triggered landslide events have occurred. Table 7-2 gives earthquake parameters and total numbers of recorded landslides (N_L) for 16 earthquakes that occurred between 1989 and 2008. While the use of different mapping methodologies will result in inconsistencies, these data provide a relative indication of the size of triggered landslide distributions. Also included are the magnitudes of the largest recorded earthquake (M_{max}) and most recently recorded earthquake (M_{last}) prior to the landslide-triggering earthquake, along with the intervening time between these events. These data were derived from the centennial catalogue, using events within a 50 km radius of the landslide-triggering earthquakes. Where no previous earthquake has been recorded, these entries are left blank.

Table 7-2 Reported numbers of landslides for recent earthquakes, and characteristics of pre-earthquake seismicity

ID	Earthquake name (Country)	Earthquake parameters (Larson et al., 2012)			Number of mapped landslides (N_L)	Previous earthquake statistics (Engdahl and Villaseñor, 2002)			
		Date	M_w	Focal depth, D (km)		M_{max}	Time since M_{max}(Years)	M_{last}	Time since M_{last}(Years)
1	Loma Prieta (USA)	17/10/1989	6.9	19	1500	6.1	5.5	6.1	5.5
2	Northridge (USA)	17/01/1994	6.7	16.8	11000	6.5	23.0	5.7	6.3
3	Hyogu–ken Nanbu (Japan)	17/01/1995	6.9	20.3	700	-	-	-	-
4	Umbria–Marche (Italy)	26/09/1997	5.7	15	110	5.6	18.0	5.6	18.0
5	Chi-Chi (Taiwan)	21/09/1999	7.6	8	22000	7.2	83.1	7	47.9
6	El Salvador	13/01/2001	7.7	56	500	5.5	4.1	5.5	4.1
7	Avaj (Iran)	22/06/2002	6.5	15	600	-	-	-	-
8	Denali (Alaska)	03/11/2002	7.9	15	8000	-	-	-	-
9	Fiordland (New Zealand)	21/08/2003	7.2	31.8	460	7	10.0	6.1	2.8
10	Tecoman (Mexico)	22/01/2003	7.6	26	4000	8	7.3	6.3	1.7
11	Lake Rotoehu (New Zealand)	18/07/2004	5.4	12	49	6.5	17.4	5.7	17.4
12	Niigata Chuetsu (Japan)	23/10/2004	6.6	13	1212	-	-	-	-
13	Kashmir (Pakistan)	08/10/2005	7.6	12	2424	-	-	-	-
14	Aisen (Chile)	21/04/2007	6.2	12	538	-	-	-	-
15	Iwate-Miyagi Nairiku (Japan)	14/06/2008	6.9	12	4161	7	94.3	6.4	6.5
16	Wenchuan (China)	12/05/2008	7.9	12.8	56000	-	-	-	-

Landslide data sources: 1 Keefer (2000), Malamud et al. (2004b), 2 Harp and Jibson (1995a), Keefer (1994), Keefer (2002) , 3 Malamud et al. (2004b) , 4 Malamud et al. (2004b), 5 Lin et al. (2001), Lin and Tung (2004), Sitar and Bardet (2001), 6 Bommer and Rodriguez (2002), Bommer et al. (2002), 7 Mahdavifar et al. (2006), 8 Jibson et al. (2006), Jibson et al. (2004), 9 Hancox et al. (2003), 10 Keefer et al. (2006), 11 Hancox et al. (2004), 12 Wang et al. (2007), 13 Sato et al. (2007), Kamp et al. (2008), Owen et al. (2008), 14 Sepúlveda et al. (2010), 15 Yagi et al. (2009), 16 Dai et al. (2011)

As the potential for temporal variability in landslide propensity is very large, the effect of seismic history on the number of landslides should be apparent, despite the overprint of other sources of spatial variability. However, as differences in the magnitude and depth of earthquakes provide a first order control on the strength of ground accelerations (Abrahamson et al., 2008, Campbell and Bozorgnia, 2008) these influences must first be accounted for. Table 7-3 gives the results of a multiple regression of $\log_{10} N_L$ as a function of earthquake magnitude (M_w) and focal depth (D).

Table 7-3 Outputs statistics for regression relationship between the number of landslides triggered and earthquake magnitude and depth

	$\log_{10} N_L$
M_w coefficient	1.00
M_w t-value	6.25**
D coefficient	-0.03
D t-value	-3.24**
Constant	-3.07
Constant *t-value*	-2.91**
R^2	0.72
Observations	16

** $p<0.01$

Relationships with both predictor variables are statistically significant at p<0.01 level, where:

Equation 7-3

$$\log_{10} N_L = -3.07 + M_w - 0.03D$$

The number of landslides increases with increasing magnitude and decreases with increasing focal depth, reflecting the greater distance of surface sites from seismic sources of deeper earthquakes. Figure 7-10A shows the relationship between values predicted using Equation 7-3 and observed numbers of landslides, while Figure 7-10B shows the model residuals, indicating variance not explained by the magnitude and focal depth of earthquakes. Residuals >0 indicate earthquakes where the number of landslides is larger than expected, and vice-versa.

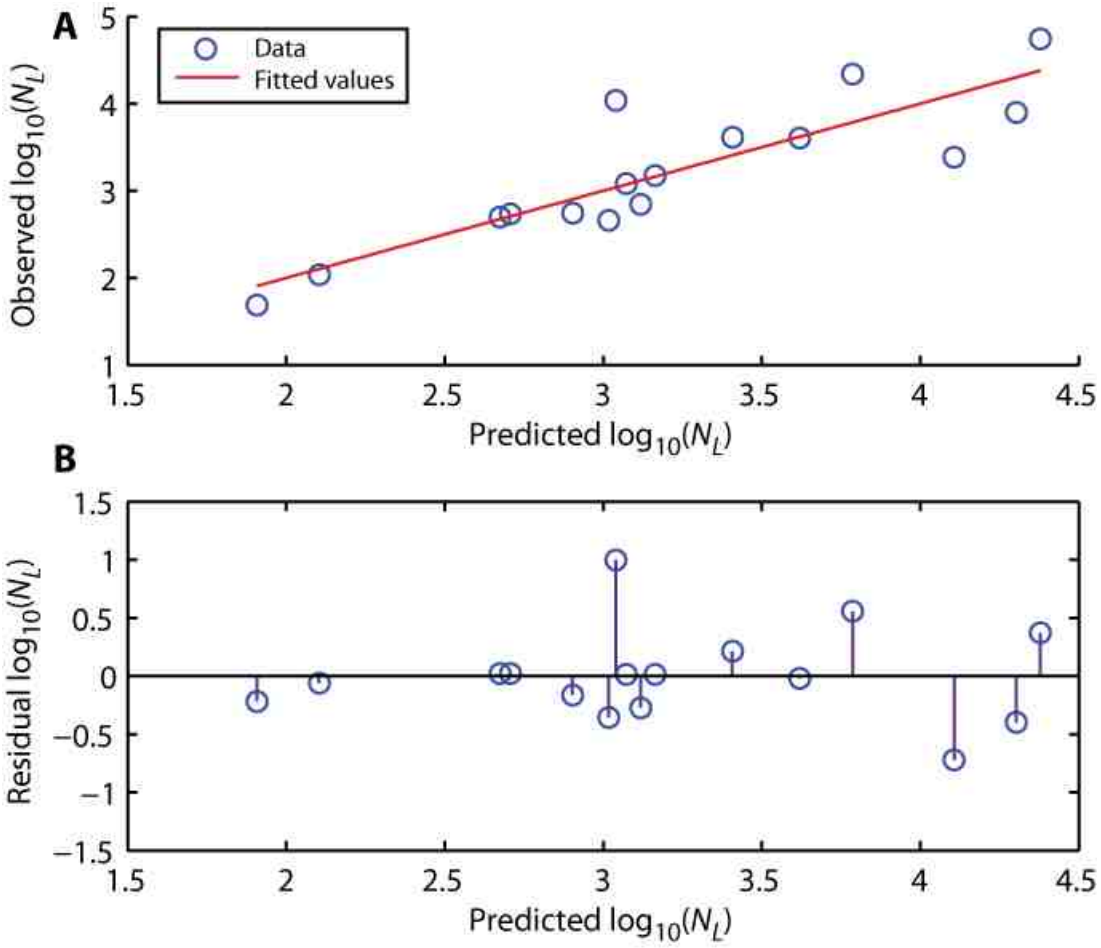

Figure 7-10 Relationships between observed and predicted numbers of landslides, using Equation 7-3 (A). Residuals from fitted relationship in A, where residuals >0 indicate earthquakes where the number of landslides is larger than predicted (B)

These residuals can now be analysed to test for the influence of the recent seismic history. Figure 7-11 shows the residuals plotted against M_{max} and M_{last}. Where no previous earthquake has been recorded, the magnitude is given as <5.5 (as earthquakes below this level are not recorded in the database). The mean residuals for cases with and without a previous recorded earthquake are also indicated. While there is no clear overall relationship, for cases where a previous earthquake >5.5 has been recorded the mean residual is positive, while for cases where no previous earthquake has been recorded, the mean residual is negative. This suggests that, on average, more landslides are triggered by earthquakes preceded by recent large earthquakes, which matches the expected effect of hillslope memory. Although a two-sample t-test returns a p-value of 0.15, indicating that the difference in the means in not statistically significant at the 0.05 level, the uncertainty in this result may be reasonably expected.

The detailed seismic history along with other spatially variable factors influencing landslide propensity have not been taken into account, and the influence of past seismic history on landslide propensity should be clearer when these are considered in analysis. Additionally, inconsistencies in the recording of landslides by different authors have not been controlled for, which may also contribute to errors when comparing total numbers of landslides.

This analysis of landslide data again hints at the influence of hillslope memory of past earthquakes, commensurate with that predicted by model outputs. The major limiting factor at this stage in investigation is now the lack of temporal data for landslide activity across sequences of earthquakes. This would allow the temporal evolution of landslide propensity with respect to seismic history to be observed directly, rather than forcing the use of space-for-time replacement and associated uncertainty. If these results could be properly validated then seismic history indices could be incorporated into probabilistic landslide models like those in Chapter 4. In addition to modelling hillslope failure probability as a function of static conditions, spatial variability in the seismic history and the legacy of previous events could also be taken into account in order to improve predictions.

A logical inversion of this approach is then to use distributions of earthquake-triggered landslides as proxies for the seismic history of regions where the palaeoseismic record is lacking. This would first require statistically significant links to be established between anomalies in ETL activity and past seismicity, through detailed analysis of landslide temporal records. Should these relationships be quantitatively constrained with sufficient confidence, anomalies in ETL distributions may be used to infer the spatial pattern of past seismicity. For instance, higher than expected landslide densities may indicate regions that previously experienced a large earthquake, while lower than expected landslide densities may indicate regions that have not experienced a large earthquake for a long period of time.

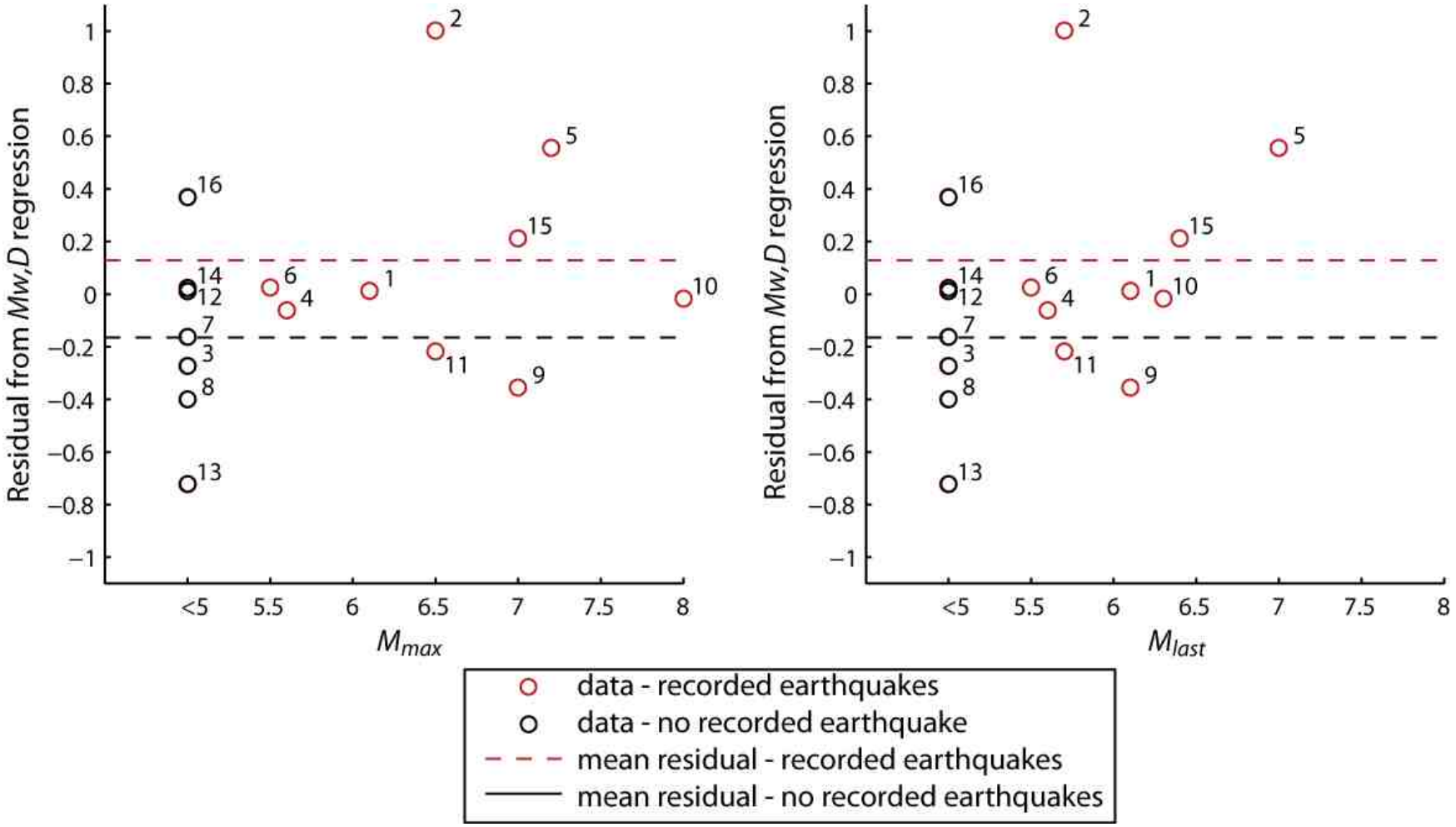

Figure 7-11 Residual in predictions of number of landslides using Equation 7-3, plotted against the magnitude of the largest (A) and most recent (B) earthquakes, recorded in Engdahl and Villaseñor (2002). Where no previous earthquake has been recorded, magnitudes are plotted as <5.

7.3 How does the way in which landslides evolve affect the importance of earthquake-triggered landslides in long-term erosion rates and levels of landslide hazard?

Many models used to undertake quantitative assessment of landslide hazard and erosion rates assume that past and future landslide events are uncorrelated and that the hillslope response to triggering events is therefore independent of time (e.g.: Guzzetti et al., 2006, Guzzetti et al., 2003, Guzzetti et al., 2005, Malamud et al., 2004b, Keefer, 1994). Various authors have raised concerns for the validity and accuracy of time-independent model outputs, in light of evidence of temporal correlations and temporal clustering of landslides (Witt et al., 2010, Korup et al., 2012, Tatard et al., 2010). As a result, predictions inferred from time-independent models may not give a true representation of landscape behaviour and the importance of earthquake-triggered landslides. The outputs of this study suggest that this issue is prevalent when magnitude-frequency distributions of landslide-triggering events vary. This section discusses how differences in the magnitude-frequency distribution of earthquakes affect fundament relationships between seismic forcing and landslides.

7.3.1 The influence of earthquake magnitude-frequency distributions on earthquake-triggered landslide relationships

As the temporal evolution of landslide propensity responds to short-term changes in the balance of small to large earthquakes, landslide propensity over long timescales is dependent on the magnitude-frequency distribution of earthquakes. As the GR b-value is decreases, the long-term mean landslide propensity increases (Section 6.3.3, Figure 6-26). The effect of having more large earthquakes relative to small earthquakes is therefore twofold. Large earthquakes trigger more landslides than small earthquakes, as reflected in the statistical probability models in Chapter 4. However, more large earthquakes also result in a population of landslide masses that is, on average, more sensitive to seismic landslide triggering. The resulting behaviour can be demonstrated by comparing the total area of landslides triggered by GR earthquake distributions with different b-values, using time-dependent and time-independent models, shown in Figure 7-12. As the b-value decreases the total area of landslides increases for both models, as more frequent, large earthquakes trigger more landslides. However, for the time-dependent model the increase is far more pronounced than for the time-

independent model. For example, at b = 0.7 the total area of landslides for the time-dependent model is double that predicted by the time-independent model, while at $b = 1$ these values are equal (note that the time-dependent model was calibrated using $b = 1$). By decreasing critical accelerations, large earthquakes make landslide masses more susceptible to failure in smaller earthquakes. If more large earthquakes occur then more hillslope failures also occur during small earthquakes. If fewer large earthquakes occur, more landslide masses will remain stable during small earthquakes, when their critical accelerations are not exceeded. This mechanism is present in the time-dependent model but does not occur in the time-independent model, resulting in the observed difference in total landslide area.

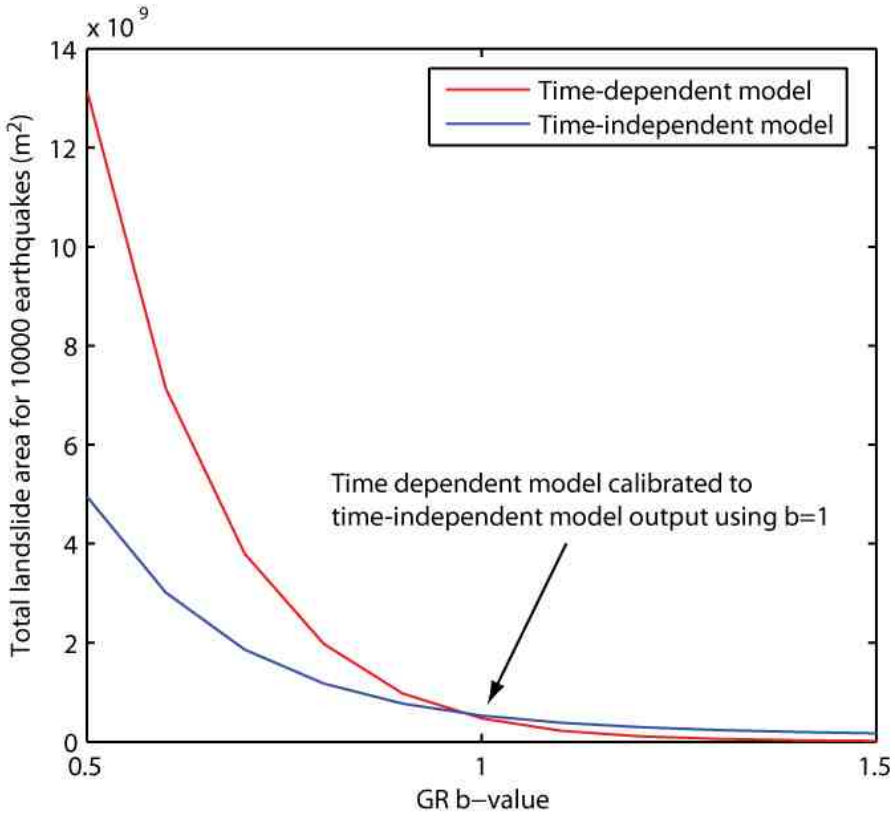

Figure 7-12 Relationship between Gutenberg-Richter b-value and long-term landslide activity (total landslide area for 10,000 earthquakes), using time-dependent (Chapter 6) and time-independent (Chapter 4) models. The red line indicates the total landslide area predicted by the time-dependent numerical model, when 1000 PLMs with 40° gradient area are subjected to 10,000 GR distributed earthquakes, here using a τ_{fp} value of 1.1. The blue line indicates the total landslide area predicted using the time-independent empirical model given in Equation 4-10, with landslide areas generated by multiplying the predicted landslide density for each earthquake with the total PLM area.

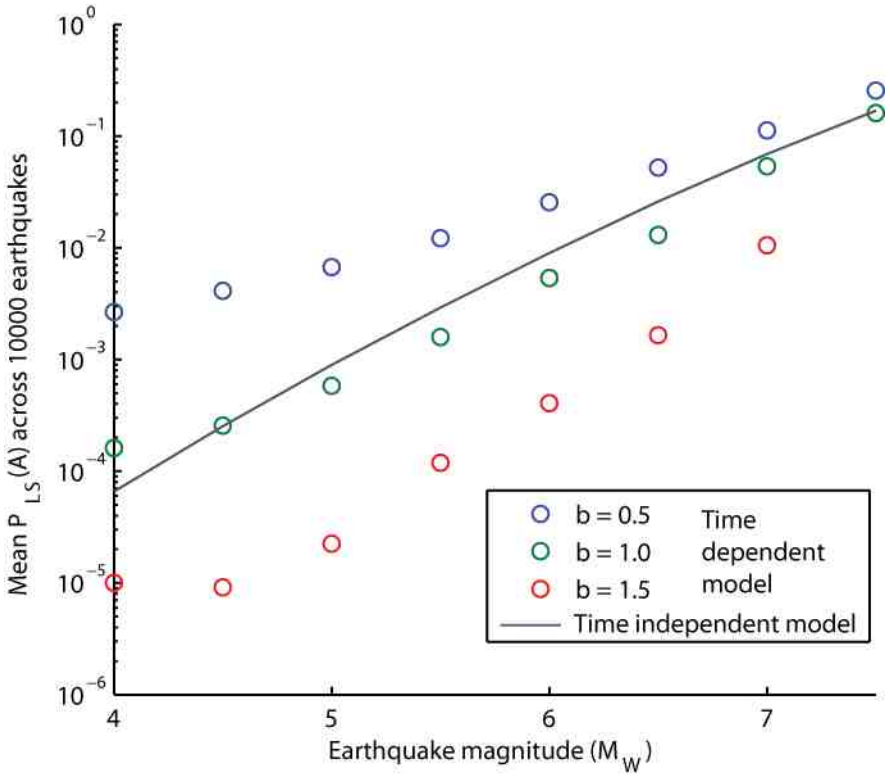

Figure 7-13 Relationships between earthquake magnitude and mean landslide density $P_{LS}(A)$, as defined by the time-independent model from Equation 4-10, and by the time-dependent model for different Gutenberg-Richter b-values

Relationships between earthquake magnitude and total numbers, areas or volumes of landslides are therefore dependent on the magnitude-frequency distribution of earthquakes. This is demonstrated in Figure 7-13, which shows time-dependent model relationships between earthquake magnitude and mean landslide density ($P_{LS}(A)$) when different b-values are used. As b decreases, earthquakes of all magnitudes produce higher average hillslope failure probabilities, while the slope of the relationship also decreases, indicating an increase in the relative importance of lower magnitude events. The relationship from the time-independent model matches that expected when $b = 1$. A change in b of 0.5 results in over an order-of-magnitude difference in mean landslide density for earthquakes with $M_w < 5.5$. As GR b-values vary globally between 0.5 and 1.5 (e.g.: Bayrak et al., 2002, Kulhanek, 2005), this would result in differences of over 2 orders of magnitude in mean landslide densities produced by small to moderate earthquakes.

Variability in relationships between the strength of seismic forcing and landslide density can be seen in different slope coefficients relating PGA and landslide density, found by Meunier et al. (2007). As shown in Figure 7-14, for both vertical and

horizontal PGA, slope coefficients are larger for the Northridge earthquake than for the Chi-Chi earthquake. In other words, landslide density increases more rapidly with PGA in the case of the Northridge earthquake than it does for the Chi-Chi earthquake. Global data from Bayrak et al. (2002), shown in Figure 7-16, suggests slightly lower average b-values in Taiwan (0.6) than California (0.7), which would contribute to the observed difference in slope coefficients. However, as precipitation events also trigger landslides, the difference in climate for these two examples will also influence this relationship through processes not simulated in this study.

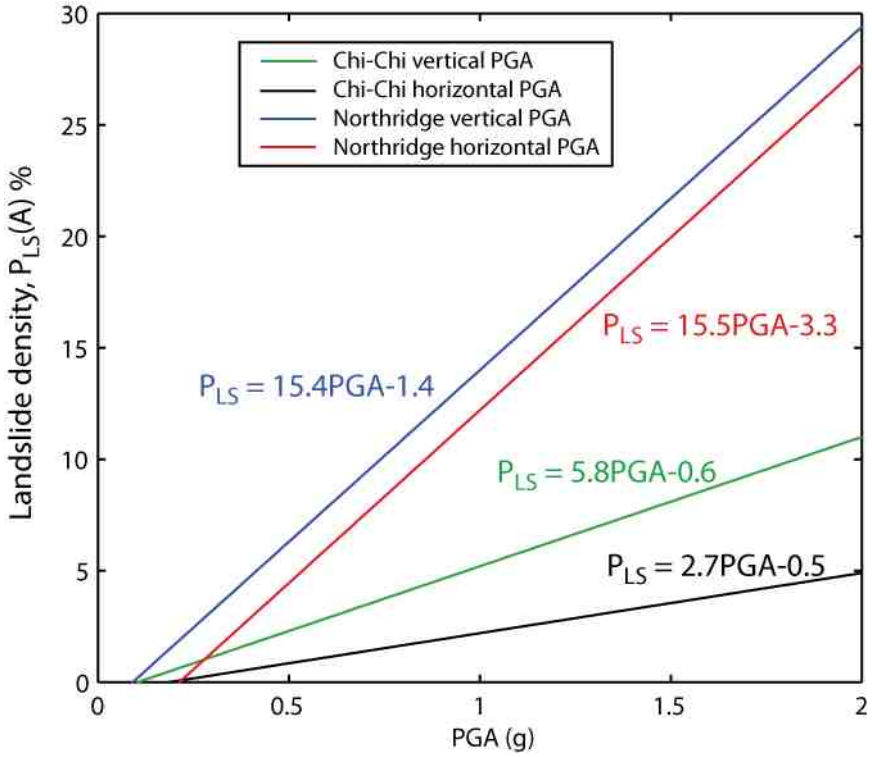

Figure 7-14 Relationships between landslide density and horizontal and vertical components of PGA (after Meunier et al., 2007)

This observation has important implications both for predicting landslide hazard and understanding the long-term contribution of earthquake-induced landslides to erosion rates. Various authors have applied global statistical relationships between earthquake magnitude and the total volume of earthquake-triggered landslide material mobilised, to predict long-term erosion rates using data from seismic catalogues (e.g.: Malamud et al., 2004b, Keefer, 1994). As the majority of landslide material is likely to remain in storage on hillslopes for long periods of time (Malamud et al., 2004b, Pearce and Watson, 1986) these models provide upper-bound estimates of erosion rates. Keefer (1994) predicted erosion rates for 12 regions, based on rates of seismic moment

release recorded in catalogues of historical seismicity. Similarly, Malamud et al. (2004b) predicted erosion rates globally based on gridded seismic intensity (Kossobokov et al., 2000), assuming a fixed b-value of 0.9. If magnitude-volume relationships fitted using data from global earthquakes are assumed to reflect the average condition where b~1, then these models will systematically under-predict erosion rates where b<1 and over-predict erosion rates where b>1. In particular, where b<1, the contribution from aftershocks is likely to be greater than assumed. An example of the implications of this is considered below.

Båth's law states that the largest aftershock will have a magnitude ~1.2 units less than the mainshock (Båth, 1965). Based on a constant magnitude-landslide area relationship, Malamud et al. (2004b) estimated that the largest aftershocks contribute 3.0% of the total landslide area triggered by mainshock events. However, for a time-dependent model, this result is dependent on b. Figure 7-15 shows relationships between mainshock magnitude and the mean landslide area triggered by the largest aftershock (defined as the mainshock $M_w - 1.2$) as a percentage of that triggered by the mainshock. Relationships are shown for different values of b, where τ_{fp} is fixed at 1.5. For the lower value of b, the area of landslides triggered by earthquakes of the largest aftershock magnitude contributes a larger percentage of total landslide areas. As a result, the effect of aftershocks in triggering landslides will be underestimated where $b < 1$. Additionally the relative contribution of aftershocks varies depending on the magnitude of the earthquake in question. When $b = 1$, the largest aftershock of magnitude 8 earthquakes produces a landslide area that is ~3% of the mainshock area, corresponding to Malamud's prediction. However, the largest aftershocks of magnitude 5.2 earthquakes produce a landslide area that is ~24% of the total landslide area triggered by both the mainshock and aftershocks.

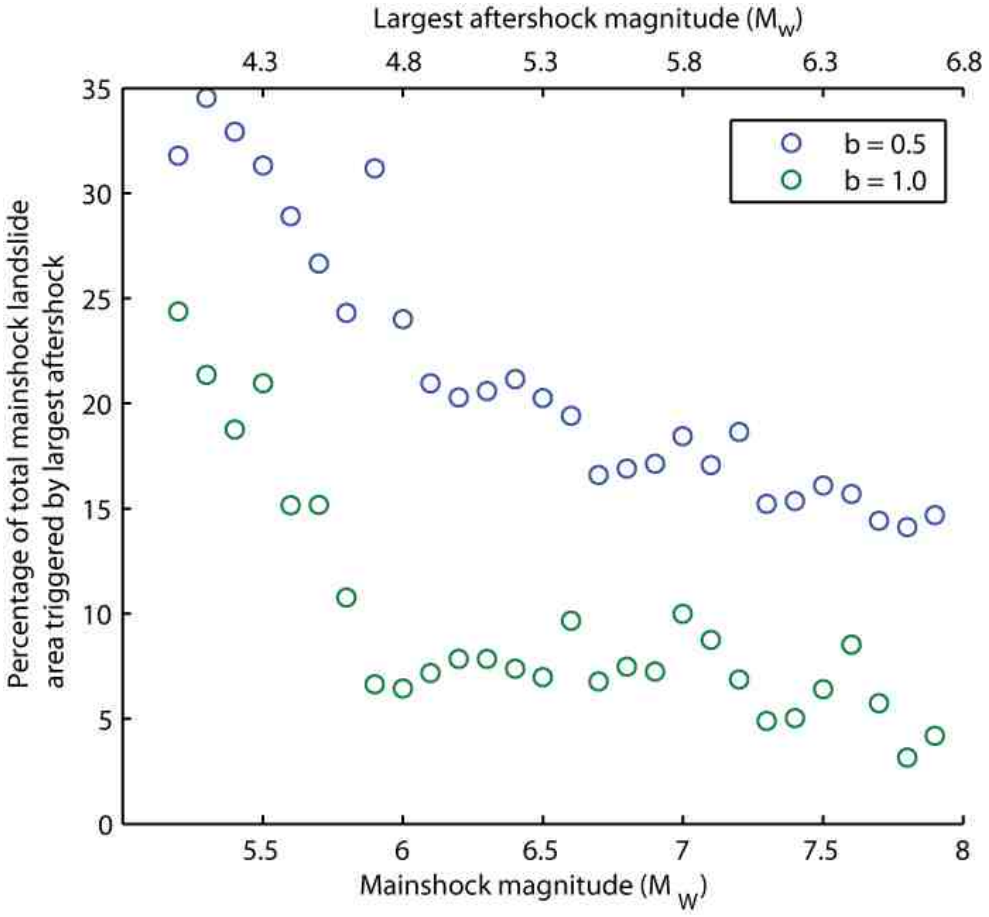

Figure 7-15 Mean area of landslides triggered by the largest aftershock (defined as the mainshock $M_w - 1.2$), according to Båth's law (Båth, 1965), as a percentage of the mean area of landslides triggered by mainshocks, for different b-values. Data were generated by subjecting a population of 1000 PLMs to 10,000 GR-distributed earthquakes, using τ_{fp} = 1.5. Percentages are calculated using 0.2 magnitude units bin spacing.

Spatially, b-values display significant variability across a range of scales. Figure 7-16 shows global variations in the b-value within 27 zones, defined by Bayrak et al. (2002). Lower b-values are observed in oceanic subduction zones around the Pacific Rim, with relatively low values also observed throughout South East Asia, the Himalaya, and along the North Anatolian Fault in Turkey. Statistically significant variations have also been identified at smaller spatial scales. For example, Wiemer and Wyss (2002) Wiemer and Wyss (2002) Figure 7-17 shows mapped variations in b-value between 0.8 and 1.8 across the Himalaya and adjacent regions (Wiemer and Wyss, 2002). Landslide models will suffer from the issues described if the events used to fit earthquake magnitude-landslide relationships are sampled from a different magnitude-frequency distribution to that used in the prediction of erosion rates or probabilistic hazard assessment. This problem will arise when predictions are made using relationships fitted to data collected at a different spatial scale. If data from global events are used to fit a relationship (as in Chapter 4), errors due to regional variability in earthquake

distributions should compensate and the model will be appropriate for predicting either the aggregate global hazard or erosion rate. If this same relationship is used to predict landslide hazard or erosion rate for different regions, the effect of regional differences in earthquake distributions must be taken into account.

The scales of b-value variability of relevance are dependent on the scale at which landslide models are fitted, and then the scale at which they are used to predict. Note that as spatial scales decrease, the accuracy and significance with which GR parameters can be fitted reduces (Wiemer and Wyss, 2002). Due to the relatively short (maximum of ~100 years) dataset of recorded earthquakes, spatial aggregation is required to accurately fit parameters. Additionally, the discrete nature of hillslope failure means that regional-scale landslide models also rely on spatial aggregation. These limits on mapping earthquake distribution variability and landslide probability/density will therefore define the minimum scales at which landslide models can be refined and errors due to earthquake distribution effects analysed.

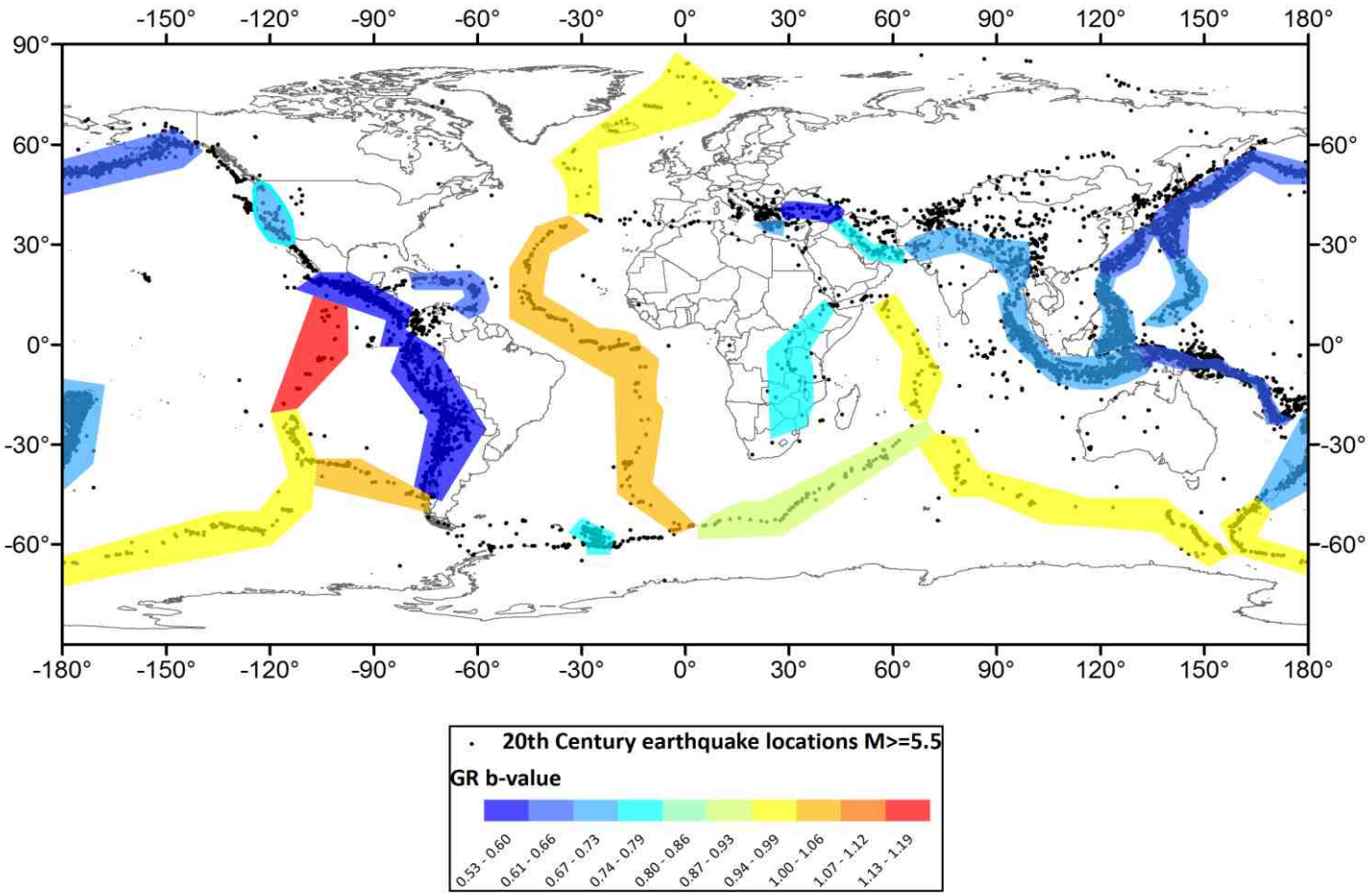

Figure 7-16 Map showing global variability in Gutenberg-Richter b-values, across 27 zones (after Bayrak et al., 2002).

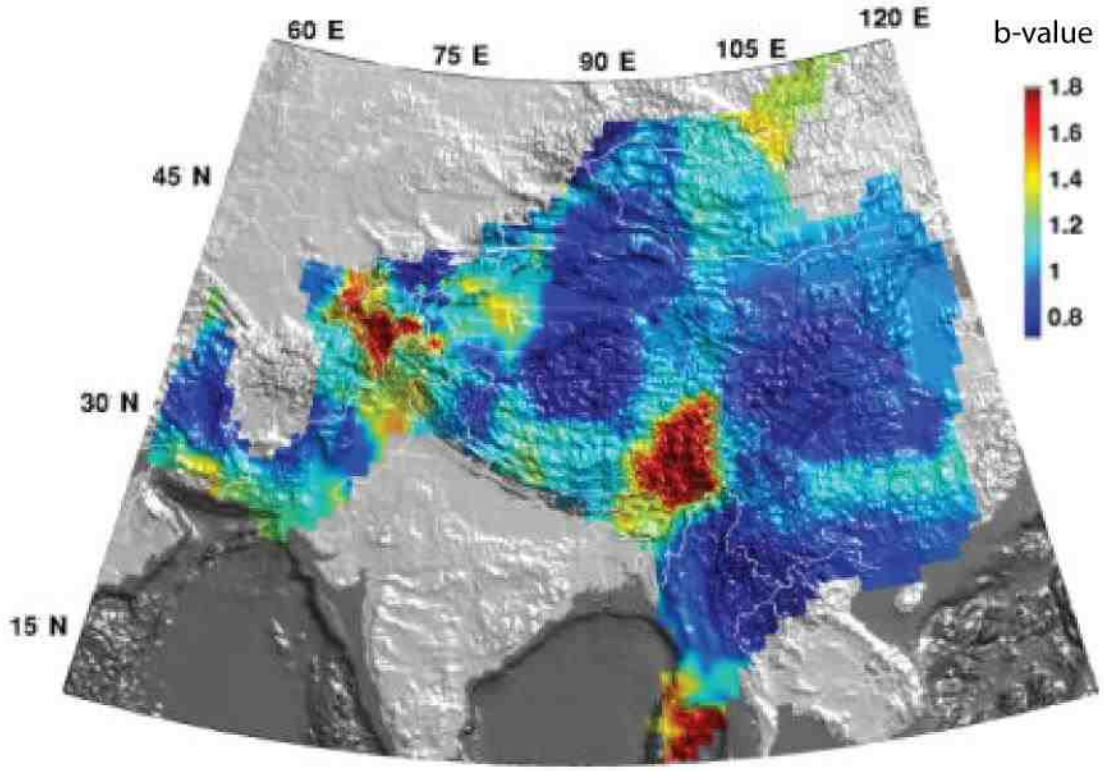

Figure 7-17 Map showing spatial variability in Gutenberg-Richter b-value across the Himalaya and adjacent regions, derived from recorded seismicity (after Wiemer and Wyss, 2002)

7.3.2 Seismicity and the long-term impact of rainfall-triggered landslides

While the current modelling considers only the effect of earthquakes on hillslopes, the evidence presented in Section 7.1.2 suggests that the combined distribution of earthquakes and precipitation events is important in determining the temporal evolution of landslide activity. In light of the longer-term perspectives examined in Sections 7.2 and 7.3, it is worth briefly considering how earthquake and precipitation events may interact over longer timescales.

Results from the Chi-Chi and Kashmir earthquakes suggest that large earthquakes produce an increase in rainfall-triggered landslide propensity, which then decreases as rainfall-triggered landslides occur. Therefore, in the same way that large earthquakes prime the landscape for landsliding in smaller earthquakes, large earthquakes also prepare hillslopes for failure in subsequent rainfall events. Long-term levels of rainfall-landslide propensity will be dependent on the occurrence of high magnitude earthquakes and precipitation events. The effect of rainfall in triggering landslides will therefore be strongly coupled to seismicity in seismically active regions. This is

supported by evidence that long-term erosion rates in Taiwan correlate with both cumulative seismic moment and temporal variability in run-off driven by typhoons (Dadson et al., 2003). Seismicity may also be an important limiting factor to long-term levels of rainfall-triggered landslide activity. This could be the case in regions where the reduction in FS produced by elevated pore pressures is not sufficient to initiate failure in material with high peak strength. Maintaining a population of potential landslide masses available to be triggered by rainfall events would therefore depend on the preparatory effect of large earthquakes, which reduce FS via strain accumulation.

These potential interactions between earthquake and rainfall-triggered landslide processes have implications for understanding the impact of climatic changes on hillslope processes. Where levels of precipitation and storminess increase, elevated pore-pressures are expected to result in higher levels of landslide activity (e.g.: Buma and Dehn, 1998, Beniston and Douglas, 1996). By modelling changes in hillslope FS due to predicted changes in precipitation, various studies have attempted to infer the resulting effect on hillslope stability and landslide activity (Melchiorre and Frattini, 2012, Borga et al., 2002, Carrara et al., 2008, Collison et al., 2000, Dehn and Buma, 1999, Dehn et al., 2000, Dixon and Brook, 2007). Where levels of typhoon activity are predicted to increase in active mountain ranges, a corresponding increase in landslide activity is also predicted (e.g.: Chiang and Chang, 2011). However, current models do not consider the potential influence of seismic events in priming hillslopes for rainfall-triggered failure. This can be explored by applying the failure zone concept introduced in Chapter 5 to rainfall-triggered landslides.

Large earthquakes maintain a flux of PLMs moving from their peak FS to lower FS levels within the failure zone for a given magnitude of rainfall event (Figure 7-18 A). The limit of the failure zone for rainfall-triggered landslides can be defined as the maximum FS that will be reduced to <1 in response to a given increase in pore pressure (for example, using Equation 2-9[9]). Once this rainfall event has occurred, all PLMs in the failure zone have failed and reset to their maximum FS. As observations

[9] $FS = \frac{(\cos^2\beta - u)\tan\phi}{\cos\beta\sin\beta}$ (e.g.: Selby, 2005)

from the Chi-Chi and Kashmir earthquakes suggest that landslide propensity decays in response to rainfall events, this implies that rainfall events are is less effective than large earthquakes in their ability to draw additional PLMs into the failure zone via strain accumulation. This is illustrated in Figure 7-18. An increase in rainfall events will therefore result in an increase in the flux of PLMs leaving the failure zone (i.e. reaching the point of failure), without a corresponding increase in the flux entering the failure zone. As a result the net population of PLMs in the failure zone will decrease. If the frequency of large earthquakes remains unchanged while the frequency of precipitation events increases, the population within the failure zone will become depleted and precipitation events will become less effective in triggering landslides. This negative feedback mechanism would therefore dampen any increase in landslide activity produced by wetter climatic conditions. Conversely, an increase in the seismicity of a region, perhaps associated with major stress re-distribution, could result in a long-term increase in rainfall-triggered landslide activity without any change in climatic conditions.

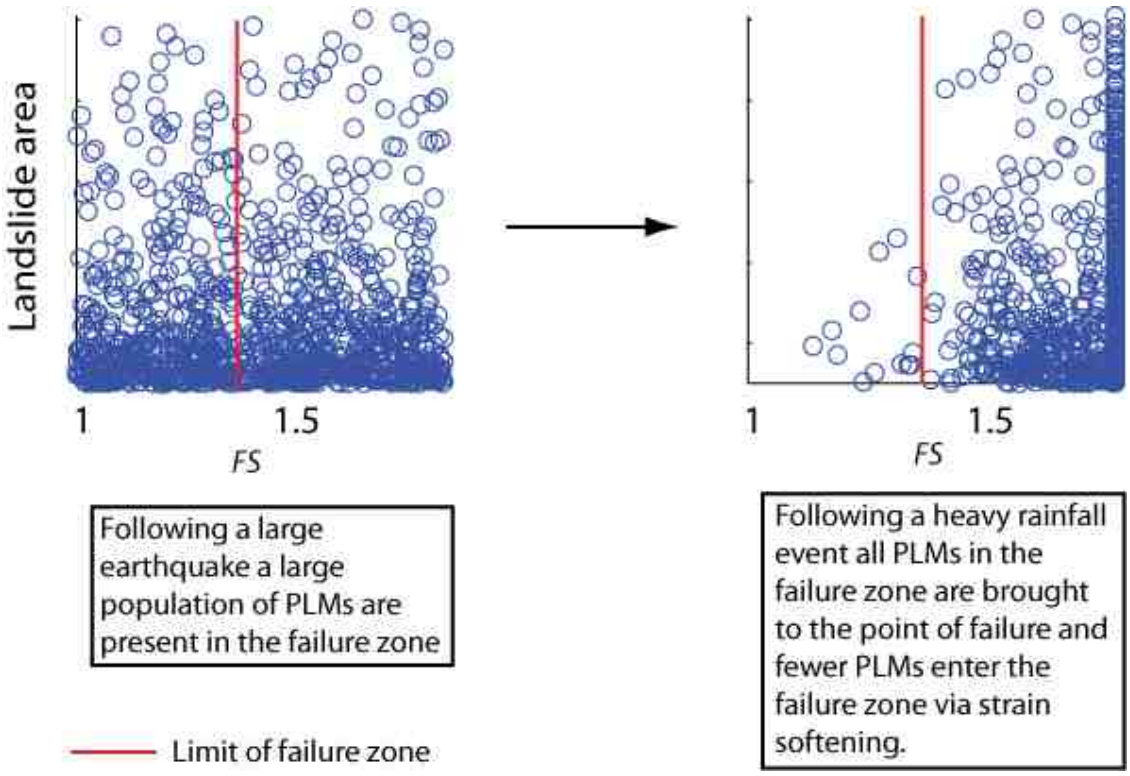

Figure 7-18 Hypothetical FS-Area plots to illustrate interactions between earthquake and rainfall-triggered landslide activity. Large earthquakes increase the population of PLMs in the failure zone, producing an increase in landslide propensity. However, heavy rainfall events reduce the population of PLMs in the failure zone, resulting in a decrease in landslide propensity.

The nature of the interaction between earthquake and rainfall-triggered landsliding inferred here is currently speculative. A major reason for this is the lack of a generalised geotechnical model for estimating strain in landslide masses induced by changes in pore pressure. While a limit-equilibrium analysis can determine the effect of pore pressure changes on the FS as a landslide mass, it does not provide the means to predict displacement and therefore estimate the cumulative and temporal effects of strain-softening. Further investigation in this area therefore requires both empirical observations of interactions between earthquake and rainfall-triggered landsliding, in addition to developments for modelling regional-scale landslide activity, as outlined below.

7.4 Developments required for further quantitative investigation

The results that have been presented throughout this section lend support to the validity of model outputs relative to the behaviour of real landscapes. However, current data provide a far-from-ideal basis for testing and further investigating many of the concepts and predictions developed in this investigation. Additionally, although the current modelling framework represents a step towards better understanding the response of landscapes to earthquakes, developments in a few key areas could also significantly strengthen its predictive capability within and beyond ETLs. It is therefore useful at this stage to outline areas where future research could be most effectively applied, in light of the above discussion.

In terms of empirical studies of ETLs, a key area for development is in the acquisition and analysis of datasets with spatial and temporal coverage appropriate for resolving the complexity of the landscape response to earthquakes, aftershocks and subsequent rainfall events. This requires accurate, multi-temporal mapping of landslide distributions associated with large ($M_w \geq 7$) earthquakes. Ideally datasets should capture the full spatial distribution of landslides associated with the mainshock and aftershocks, as well as landslides triggered by subsequent rainfall events in the region of mainshock landslides. The temporal coverage should span the time prior to and following the mainshock earthquake, with repeated landslide mapping undertaken at a high sample rate, following each event with the potential to trigger landslides. This should include all aftershocks greater than M_w = 4 (Keefer, 2002), and any significant rainfall events. An important addition to current approaches is that an equal importance should be attributed to quantitatively establishing events that triggered no or few landslides, as well as those that triggered many. Correspondingly, the landslide data should be accompanied by distributed ground motion and precipitation data at the same spatial and temporal resolution.

Such data would provide a detailed picture of the spatio-temporal evolution of landsliding, which could be directly compared with model predictions for both synthetic and real event sequences. By providing the means to test various model hypotheses, this data would allow different aspects of the spatio-temporal evolution of landsliding to be explored in much greater detail. These would include spatial

variability in the magnitude and period of landslide propensity changes relative to the strength of seismic forcings, different lithologies and topographic characteristics. Ultimately, distributed models of spatio-temporal landslide evolution could be derived, as an extension to the static spatial models presented in Chapter 4. These would provide useful tools for both geomorphological study of hillslope processes as well as for landslide hazard assessment and planning.

This data could be most ideally attained for a continental earthquake in a thickly vegetated region, allowing newly formed landslides to be clearly distinguished from undisturbed ground (Liu and Woing, 1999, Liu et al., 2002). Additionally, the *ideal* earthquake would need to occur outside of the rainy season, in order for multi-temporal cloud-free satellite or aerial imagery to be attainable (Borghuis et al., 2007). Various sub-tropical to temperate regions around the Pacific Rim provide potential candidate regions, with thickly vegetated landscapes, high levels of relief, seismicity, and established monitoring networks. These include the Southern Alps of New Zealand, the Japanese Alps, the Central Range in Taiwan and the Oregon Coast Range in the USA.

In addition to the use of better empirical data, it is important that observations can be linked back to a conceptual understanding of the landslide process. This means that numerical simulations of regional-scale landslide activity need to be further developed to incorporate different failure types and mechanisms. While this investigation has considered a simple, translational sliding block model of hillslope failure, landslides with different failure geometries and movement types may produce different spatio-temporal landslide activity. The conception of forcing mechanisms acting on landslides is also limited to the effect of horizontal ground accelerations, which are assumed to act as a static body force in the downslope direction, in the current model. However, landslide mass response is also affected by other directional and wave characteristic components of ground accelerations (e.g.: Harp and Jibson, 1995b, Zhang et al., 2013, Moore et al., 2011, Wasowski et al., 2013), as well as changes in pore-pressured induced by both seismic shaking (Asano et al., 2013) and rainfall (Chen et al., 2006, Iverson, 2000). The impact of these factors on landslide activity could be investigated by integrating different geotechnical models into the regional-scale modelling framework. The complexity of current models means that additional challenges need

to be addressed to achieve this, as many of the input parameters will be unknown. While these may be defined through calibration and sensitivity analysis, this is likely to be challenging for models with many more inputs parameters (e.g.: Stead et al., 2012) representing a much larger parameter space. A possible alternative is to carry out bespoke laboratory tests of the response of hillslope materials under dynamic-stress loading, in order to constrained material properties, particularly the strength-decay behaviour, as a model input variable. Regional-scale landslide activity could then be linked with empirical observations of material behaviour, which would in turn allow greater scope for validation of model outputs, through comparison of landslide activity in landscapes formed of different materials. Additionally, different failure geometries would either need to be defined as distributions or modelled as emergent properties, for example using a finite element code to determine critical slip surfaces from a defined topography (e.g.: Murphy et al., 2011a). By conducting this analysis using a three-dimensional, evolving topographic model, the effect of interactions between adjacent hillslopes on long-term landslide activity could also be investigated.

While a number of potential developments in landslide modelling would contribute to the problems addressed in this thesis, a substantial first step could be made if a generalised model was developed, with which to predict strain induced by changes in pore pressure in hillslopes. If this could be incorporated in tandem with the Newmark sliding block model, this would allow investigation into the combined effects of dynamic stresses from seismic waves and changes in pore pressure induced by both rainfall and seismic shaking.

Chapter 8 - Conclusions

This thesis began by highlighting the problem that although hillslope failure is known to develop through time, the cumulative effects of history and the legacy of previous earthquakes on landslide activity are not well understood. As a result, regional ETL models have been built on the assumption that landslide occurrence results from a stochastic, time-independent process. Landslide activity at any point in time has been treated as solely dependent on the current static conditions, and unaffected by hillslope memory of previous events. Empirical evidence and results from numerical modeling presented in this thesis indicate that hillslope memory may have important effects on regional-scale landslide activity for any given earthquake. The results and original contribution to knowledge can be summarized by revisiting the research objectives identified in Chapter 1:

8.1 Objective 1: To produce a generalised earthquake-triggered landslide spatial model that is transferrable between different earthquakes and regions, by using statistical models to investigate the influence of current earthquake and static landscape conditions on the probability of hillslope failure

Statistical models describing the spatial distribution of ETLs have been developed, through logistic regression analysis of inventories of landslides triggered by five large (M_w > 6.7) earthquakes. Through a detailed analysis of landslides triggered by the 1929 Buller and 1968 Inangahua (New Zealand) earthquakes, a subset of variables has been identified that exhibit a consistent, statistically significant influence on hillslope failure probability for both events, with established physical relationships to seismic and hillslope processes. The major influences on failure probability are the distance of sites from the seismic source and the local hillslope gradient, where the underlying influence of hillslope gradient is dependent on the geology. Secondary are the effects of topographic amplification (position on hillslopes), solar radiation, hillslope structural domains and local relief, which modify failure probability to a lesser extent. By extending this analysis to all five earthquakes, generalised models have been developed, which capture the major influences on hillslope failure probability and are transferable between different earthquakes and regions. Earthquake moment magnitude, PGA (or distance from the seismic source) and hillslope gradient have been

found to determine the first-order spatial distribution of landslides with areas greater than 11,000 m^2, which generally represent larger failures that shear bedrock material. These models have substantial potential for use in ETL hazard assessment, as a means for first-order prediction of ETL spatial distributions, using freely available global datasets.

Although the spatial model variables capture the influence of hillslope shear stress and seismic ground accelerations on hillslope stability, neither the spatial distribution nor the temporal evolution of hillslope material strength is included in the models. As a result, these models are fundamentally limited, as they only account for the influence of the current earthquake and static landscape conditions. No indication is provided of how hillslope material damage or memory accrued from previous events, associated with strain-accumulation and progressive failure, may influence landslide activity. As a result, the outputs of these models should be treated with caution, and considered light of the findings from Objectives 2, 3 and 4.

8.2 Objective 2: To test for the influence of hillslope memory and establish the errors involved in a spatial approach to modelling earthquake-triggered landslides, by undertaking a detailed analysis of spatial distributions of landslides triggered by multiple earthquakes in the same region

Hillslope failure probability models for the 1929 Buller and 1968 Inangahua earthquakes have been used to establish where time-independent, spatial ETL models break down, by comparing observed and predicted distributions of landslides. Errors in the landslide distribution predicted for the 1968 earthquake suggest that the legacy of damage to hillslope materials accrued from the 1929 earthquake is an important control on landslide occurrence. Results suggest that hillslopes damaged by the first earthquake were more prone to failure in the second earthquake. These findings highlight potential inadequacies in current spatial models of ETL susceptibility, and the importance of considering the influence of hillslope memory on regional-scale ETL activity. However, current empirical data can only provide a limited insight into this temporal aspect of landslide behaviour, due to the short temporal coverage of landslide inventories and difficulties in controlling for the influence of both earthquake and rainfall events that trigger landslides.

8.3 Objective 3: To develop a new conceptual and numerical model that integrates the site-scale evolution of hillslope progressive failure via brittle deformation processes into modelling regional-scale earthquake-triggered landslide activity

A new model has been developed that integrates the site-scale evolution of hillslope progressive failure into modelling regional-scale earthquake-triggered landslide activity. The model conceptualises the hillslopes of an active mountain landscape as being composed of a population of evolving landslide masses. Seismically-induced brittle-deformation processes are modelled using a modification of the Newmark sliding block approach, which incorporates strain-softening. By capturing the key components of first-time ETL failure via brittle deformation, the model provides a means of reconciling observations of ETL spatial distributions with an understanding of hillslope failure processes. The model has been used to suggest how relationships between predictor variables and landslide probability, identified in Objective 1, are the product of spatial variability in the temporal rate at which hillslopes undergo failure. The apparent stochastic nature of ETL activity has been linked to the inability of current models to determine the stage of different hillslopes in their failure cycle, which is supported by the findings from Objective 2. Model outputs suggest that changes in levels of accumulated strain and damage in hillslopes, that occur response to earthquakes, have the potential to produce regional-scale temporal variability in the sensitivity of landscapes to earthquake-triggered landsliding. These findings concur with oscillating temporal responses long hypothesised for geomorphic systems (Thornes, 1983, Brunsden and Thornes, 1979, Schumm and Lichty, 1965), and the model provides a tool to quantitatively investigate this complex response in the case of earthquake-triggered landslides.

8.4 Objective 4: To investigate the implications of the model results for landslide hazard, predictability and sediment generation through the following research questions:

Model outputs from a series of numerical experiments have been used to explore the following research questions:

i. What is the impact of large earthquakes on subsequent landslide activity?

Model experiments using synthetic earthquake sequences have shown how individual earthquakes alter subsequent landslide propensity. Temporal changes in landslide propensity have been found to take the form of an impulse response, in which landslide propensity is enhanced immediately following large mainshock earthquakes, and then decays with time as subsequent, lower magnitude events occur. The amplitude of changes is primarily dependent on the mainshock magnitude, while the decay period is determined by the hillslope material properties and the magnitude of subsequent aftershocks and other subsequent events that trigger landslides. These findings have important implications for understanding the prolonged geomorphological impact of earthquakes and associated hazards. If a large mainshock earthquake is followed by a strong sequence of aftershocks, then the change in landslide activity immediately following the mainshock will be elevated but decay rapidly with time. Conversely, fewer and weaker aftershocks mean that the disturbance produced by a large earthquake remains within the landscape for longer, resulting in a prolonged period of elevated landslide activity and a slower decay. Observed temporal and spatial patterns of landslide activity following the Chi-Chi and Kashmir earthquakes indicate that post-seismic rainfall-triggered landslide activity evolves in the same manner as earthquake-triggered landslide activity evolution predicted by the model. Differences in the aftershock sequences following these earthquakes provide a possible explanation for observed differences in the time taken for landslide activity to return to background levels following the mainshocks.

ii. How can long-term patterns of variability in landslide propensity be linked to seismic history?

In response to sequences of earthquakes defined by the Gutenberg-Richter law, model outputs suggest that landslide propensity exhibits a continuous transient state, characterised by overlapping impulses from large earthquakes. This temporal variability in the potential for mass wasting and hazard can be accounted for in landslide models in one of two ways. Firstly, variability could be treated as stochastic uncertainty, by constraining the distribution of variability based on hillslope material properties and long-term earthquake magnitude-frequency distributions. However, the range of potential variability is very large, and this approach provides no information regarding temporal changes in landslide propensity. As past seismic

history is a key determinant of landslide propensity, in the absence of landslide data a temporally evolving estimate of landslide propensity can be inferred using historical seismic data. Achieving this by modelling site-scale responses for large numbers of individual landslide masses in response to long sequences of earthquakes is computationally prohibitive. In order to provide a practical approach to achieving this, an index for predicting temporal changes in landslide activity, based on past seismicity, has been developed using numerical model outputs. The index is based on the principle that large earthquakes generally produce a high magnitude net increase in landslide propensity, while each small earthquake generates a lower magnitude net decrease. This principle has been tested by comparing previously unexplainable variability in the numbers of landslides triggered by earthquakes with the seismic history preceding each earthquake. The results tentatively suggest that, for regions that have recently experienced a large earthquake, on average more landslides are triggered in the next earthquake, and vice-versa. Production and analysis of time series data on landslide activity and seismic ground motions is required to further investigate empirical relationships between seismic history and landslide activity, which could be incorporated into probabilistic ETL models. In this way, future models could account for both the current conditions and the legacy of past events, in order to provide time-dependent predictions of landslide hazard.

iii. How does the way in which landslides evolve affect the importance of earthquake-triggered landslides in long-term erosion rates and levels of landslide hazard?

The effects of hillslope memory on landslide activity identified in this study indicate how the behavior of landscapes may differ from that predicted by models that assume ETL events are independent in time. When the effects of earthquake-triggered landslide events accumulate, relationships between the strength of seismic forcing and landslide activity (numbers, areas or volumes of landslides) are dependent on the magnitude-frequency distribution of earthquakes. As numbers of large earthquakes increase relative to the number of smaller earthquakes (GR b-values decrease) higher levels of landslide activity occur in response to smaller earthquakes. Commonly fitted global relationships between earthquake-magnitude and numbers and volumes of triggered landslides will therefore systematically underestimate landslide activity in

regions where b-values are lower than the global average, and overestimate landslide activity where b-values are above the global average. This suggests that corrections must be applied when landslide models calibrated using global data are used to predict regional landslide activity. Similarly, regional variability in relationships between PGA and landslide density can be partially attributed to differences in seismicity, which could be incorporated into these models in the future.

As hillslope memory of earthquakes also affects rainfall-triggered landslide activity, models that treat rainfall-triggered landslides as independent of seismicity are also likely to give an erroneous representation of landscape behavior. A further output of this study is that accurate prediction of climate change impacts on landslide activity requires investigation of the coupled effects of precipitation and seismicity on hillslope stability. The lack of generally applicable geotechnical models for predicting strain induced by changes in pore-pressure is major limiting factor in terms of achieving this.

8.5 Original contribution to knowledge

The influence of site-scale hillslope material strength and stability represents an area of major uncertainty in current understanding of regional-scale landslide activity. This arises due to the lack of regional-scale data constraining variability in hillslope material properties at the site-scale of individual hillslope failures. As brittle-failure in hillslope materials develops through time, material strength and stability reduces. Based on this principle, this thesis has applied a novel approach to investigating the implications of a more physically based approximation of landslide evolution, where the stability of landslides is treated as a function of the legacy of past events. While this approach cannot assign predictions to individual landslide sites, the aggregate behavior of large populations of landslide masses can be investigated, and importantly the widely recognized uncertainty in landslide response to earthquakes can begin to be unpicked.

An important output of this investigation is an understanding of how hillslope material memory at small-scales may influence landslide activity at the regional-scale, resulting in temporal variability in the sensitivity of landscapes to landsliding. Model outputs achieved by approximating this mechanism are in line with observations that large earthquakes are generally followed by periods of elevated landslide activity, despite the fact that the weakest hillslopes in the landscape have already failed co-seismically.

By extrapolating this behavior to longer temporal scales, a predictable long-term signal of changes in landscape sensitivity has been hypothesized and appears to fit with observed global variability in landslide activity. Furthermore, the presence of hillslope material memory invalidates a fundamental assumption of landslide models, that landslide events are time-independent. Relationships between landslide activity and the strength of seismic forcing are dependent on earthquake-magnitude frequency distributions, indicating that current models are susceptible to over- and under-estimate regional-scale landslide activity.

The findings create a new avenue for time-dependent analysis and prediction of the spatio-temporal response of landscapes to earthquakes, which will both improve the accuracy of regional-scale landslide predictions and has potentially important implications for determining the impact of climate change on landslide activity. Although the current temporal coverage of landslide datasets has been highlighted as a fundamental limitation to progress in this field, future data requirements and the means of obtaining them have been outlined. Additionally, the modeling principles developed provide a new approach to understanding the influence of hillslope material properties on regional-scale landslide activity, which needs to be addressed as both temporal as well as a spatial problem.

8.6 Recommendations for future research

A number of areas have been highlighted in which future research could be most effectively applied, in order to develop a better understanding of time-dependent aspects of regional-scale ETL activity. These can be summarised in terms of the following research objectives:

1. To establish empirical relationships between landslide activity and historical events, through analysis of multi-temporal landslide datasets;

The major contribution of this research has been to establish the potential influence of hillslope memory of previous earthquakes on region-scale landslide activity. In order to test these results and integrate the influence of past events into landslide predictions, empirical relationships between landslide activity and historical seismicity must first be established. This requires the generation of detailed multi-temporal landslide datasets

(as outlined in Section 8.6), and analysis, guided by model predictions, in order to test for and constrain the influence of historical processes on landslide activity. A limited number of existing datasets may also form part of this analysis. For example, two years of intensive rockfall monitoring data collected during the 2010/2011 Canterbury earthquakes sequence in New Zealand (Massey et al., 2012) could be used to examine the impact of multiple seismic events on landslide activity and test for temporal correlations in the record. Multi-temporal landslide inventories from the 1999 Chi-Chi earthquake (Hovius et al., 2011) could also be further analysed to test for spatio-temporal aspects of landslide activity hypothesised from model outputs, but not previously examined.

2. To further develop models that integrate a geotechnical understanding of hillslope failure into regional-scale landslide modelling

In parallel with empirical analysis, numerical models of regional-scale landslide activity should be further developed, both to provide hypotheses to test, and to establish a firm understanding of empirical relationships. Efforts should be made to understand how different inputs into geotechnical models vary spatially across large scales, influencing the relative rates at which different hillslopes undergo failure and how the aggregate sensitivity of landscapes evolves. Critically, these models should incorporate the influence of different forcings that drive hillslope failure, specifically the coupled effects of earthquake and precipitation events.

Appendix A - Additional earthquake-triggered landslide event information

i. 1968 Inangahua earthquake

Figure A - 1 shows the regional distribution of uncertainty associated with Shakemap PGA for the 1968 Inangahua earthquake.

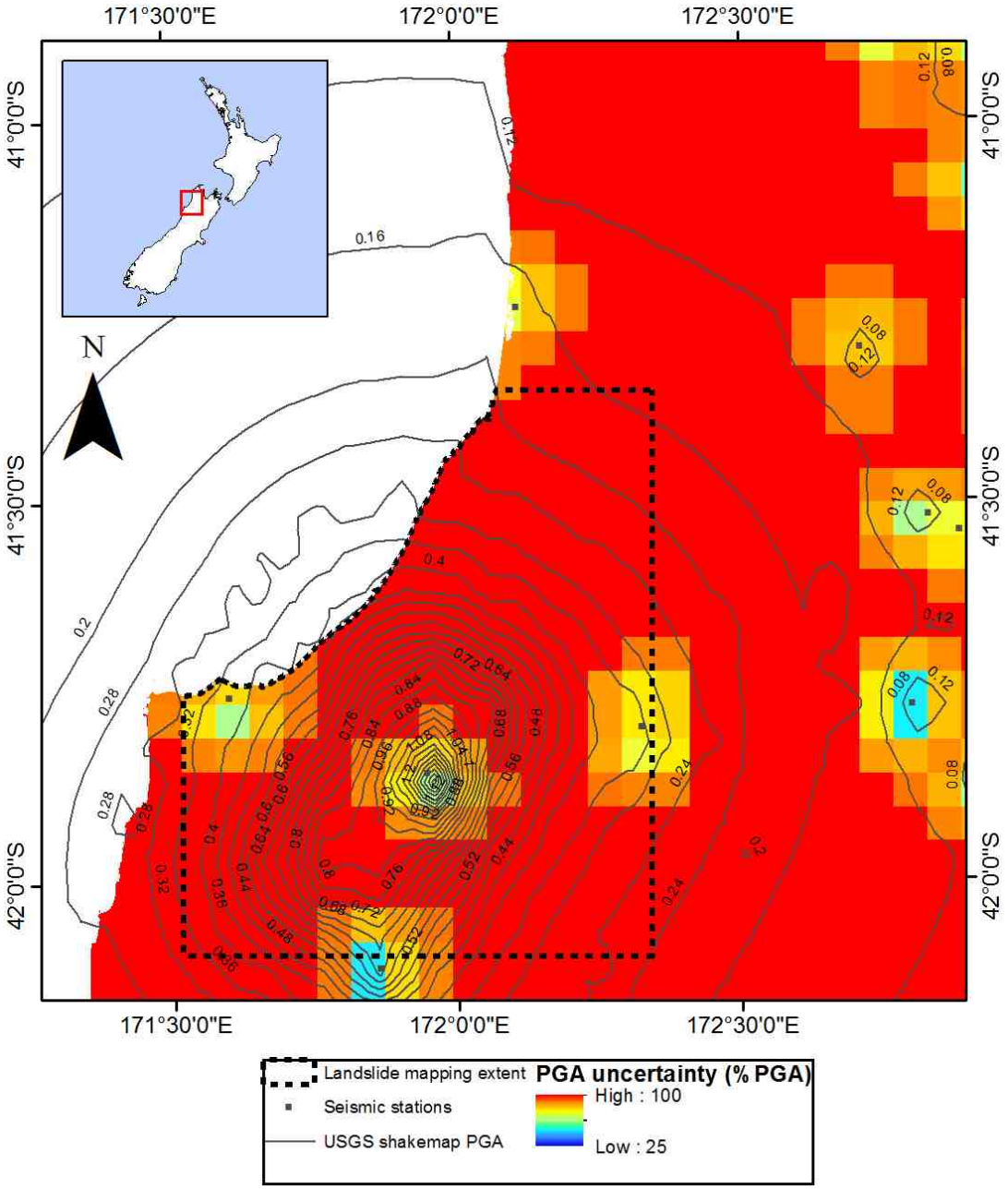

Figure A - 1 Map showing PGA isoseismals and gridded uncertainty (standard deviation in terms of % PGA) for the 1968 Inangahua earthquake (Allen et al., 2008)

ii. 1994 Northridge earthquake

Various fault models for the Northridge earthquake have been generated from a combination of geodetic, strong motion and teleseismic data (Wald et al., 1996, Shen et al., 1996, Hudnut et al., 1996), and can be obtained from the USGS fault model repository (USGS, 2012). The main fault is a blind thrust striking between 113 ° and 136°, dipping between 30 ° and 62° southward, with average slip of 1.3 m and peak slip of ~2.2-3 m (Wald et al., 1996, Shen et al., 1996). Focal depth estimates range from 10 to 19 km (Wald and Heaton, 1994, Jones et al., 1994, Wald et al., 1996, Shen et al., 1996, Hudnut et al., 1996). Shen et al. (1996) suggest that slip may have also occurred on a second minor fault plane, overlying the main rupture to the northwest, with similar strike (119.3^{o}) and dip (52.7^{o}) components. For the fault geometry inferred by Shen et al (1996), based on geodetic data, the main fault has dimensions of 30 x 30 km, extending to a maximum depth of 24 km with a bend in the plane 9.1 km below the surface. The smaller secondary fault is 10 x 12 km, extending to a maximum depth of 12 km. This model corresponds closely with other models of fault geometry and is used in analysis to constrain the location of the seismic source.

Figure A - 2 shows the regional distribution of uncertainty associated with Shakemap PGA for the earthquake.

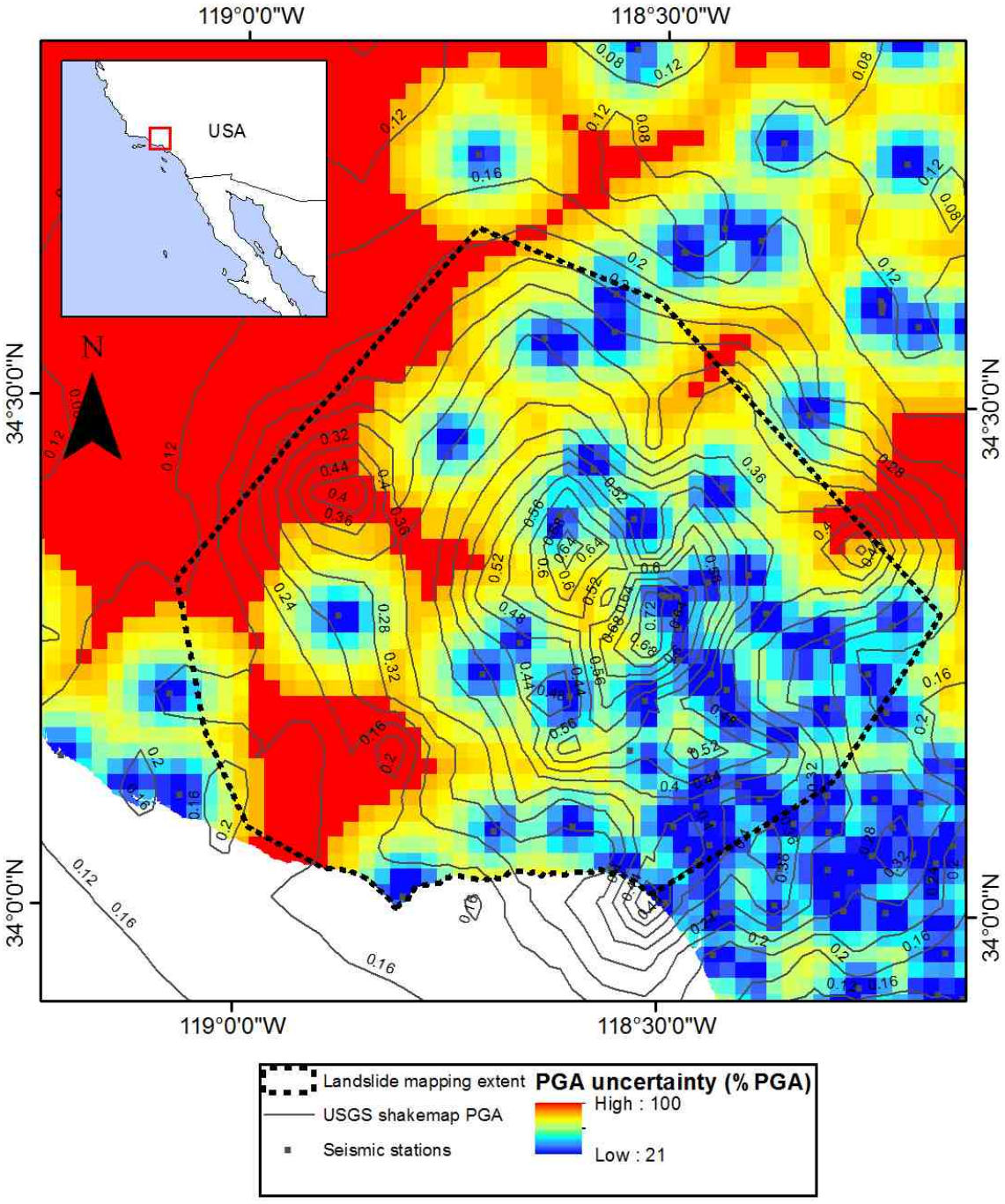

Figure A - 2 Map showing PGA isoseismals and gridded uncertainty (standard deviation in terms of % PGA) for the 1994 Northridge earthquake (Allen et al., 2008)

iii. 1999 Chi-Chi earthquake

The earthquake ruptured a 100 km segment of the Chelungpu fault, with surface ruptures mapped over a length of 90 km (Chen et al., 2001). The fault trends north-south, with a bend to the east at its northern extent, and has a shallow dip of around 30^{o} to the east (Shin and Teng, 2001). The mechanism of coseismic fault movement

was predominantly thrust with a minor component of left-lateral strike-slip (Shin and Teng, 2001). The eastern side of the fault forms the hanging wall and the western side forms the footwall. Fault models best reflecting the surface rupture geometry have 2 or 3 segments, which account for the fault's eastward bend (Ma et al., 2001, Wu et al., 2001). The fault model produced by Wu et al. (2001) is consistent with other models (e.g.: Ma et al., 2001, Zeng and Chen, 2001, Chi et al., 2001) and is used in analysis to constrain the seismic source.

Figure A - 3 shows the regional distribution of uncertainty associated with Shakemap PGA for the earthquake.

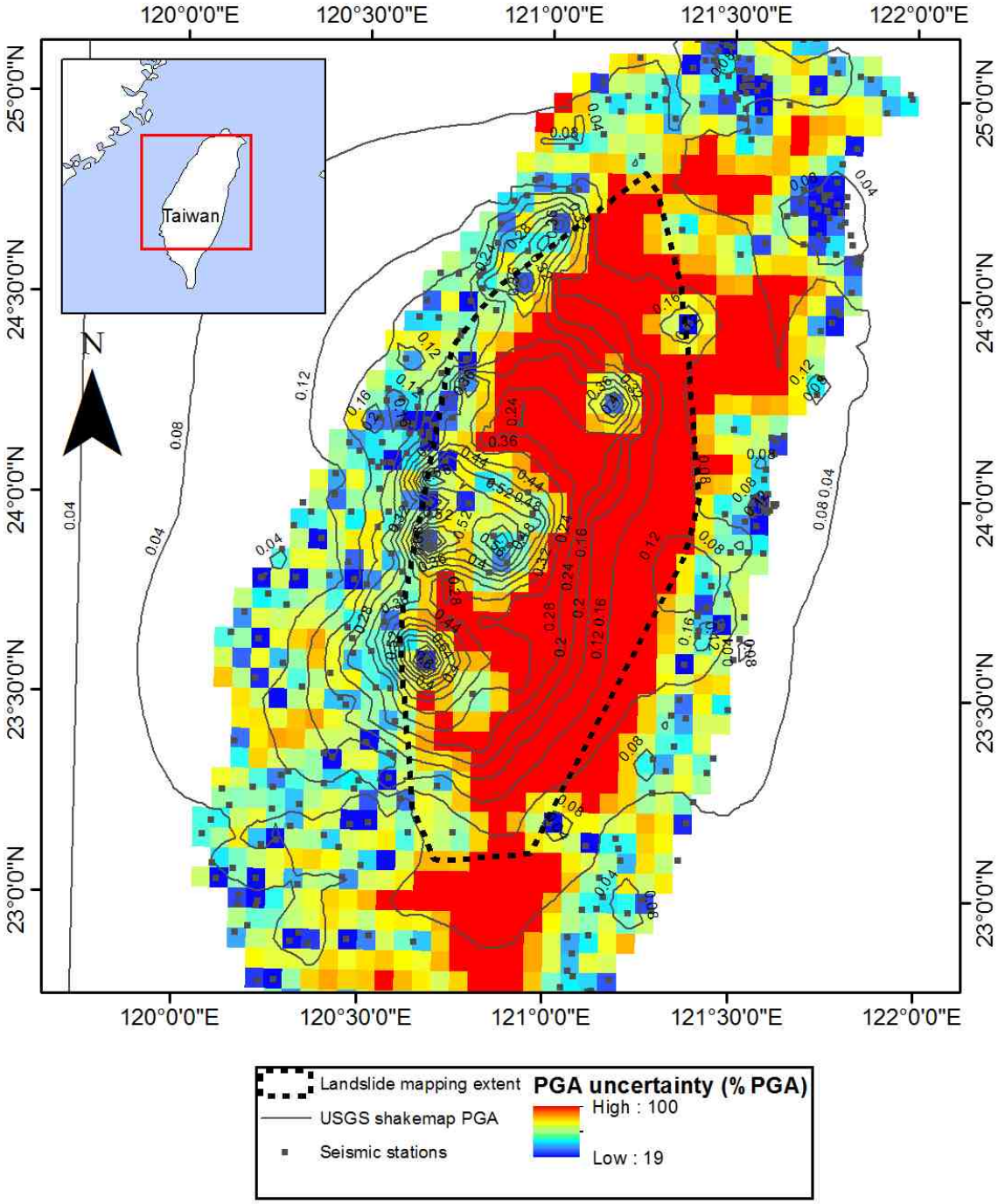

Figure A - 3 Regional uncertainty (standard deviation) in terms of % PGA for the 1999 Chi-Chi earthquake (Allen et al., 2008)

iv. 2008 Wenchuan earthquake

The earthquake produced surface ruptures over an along strike length of 220 km on the Beichuan, Pengguan and Xiaoyudong faults (Densmore et al., 2010). The most comprehensive published fault model for the earthquake, produced through inversion of GPS and InSAR data, suggests a total rupture length of over 280 km (Shen et al., 2009). The overall fault motion is a combination of thrust and dextral strike slip, with the hangingwall in the northwest and the footwall in the southeast. However, a complex fault geometry has been resolved. The main (Beichuan) fault plane dips moderately (~43^{o}) in the southwest, but steepens to almost vertical dip in the northeast. Moving from southwest to northeast the fault motion also changes from predominantly thrust to dextral strike-slip. In the southwest a smaller component of slip also occurred on the secondary Penguan fault (Shen et al., 2009). The fault model produced by Shen et al. (2009) used in analysis to constrain the seismic source.

Figure A - 4 shows the regional distribution of uncertainty associated with Shakemap PGA for the earthquake.

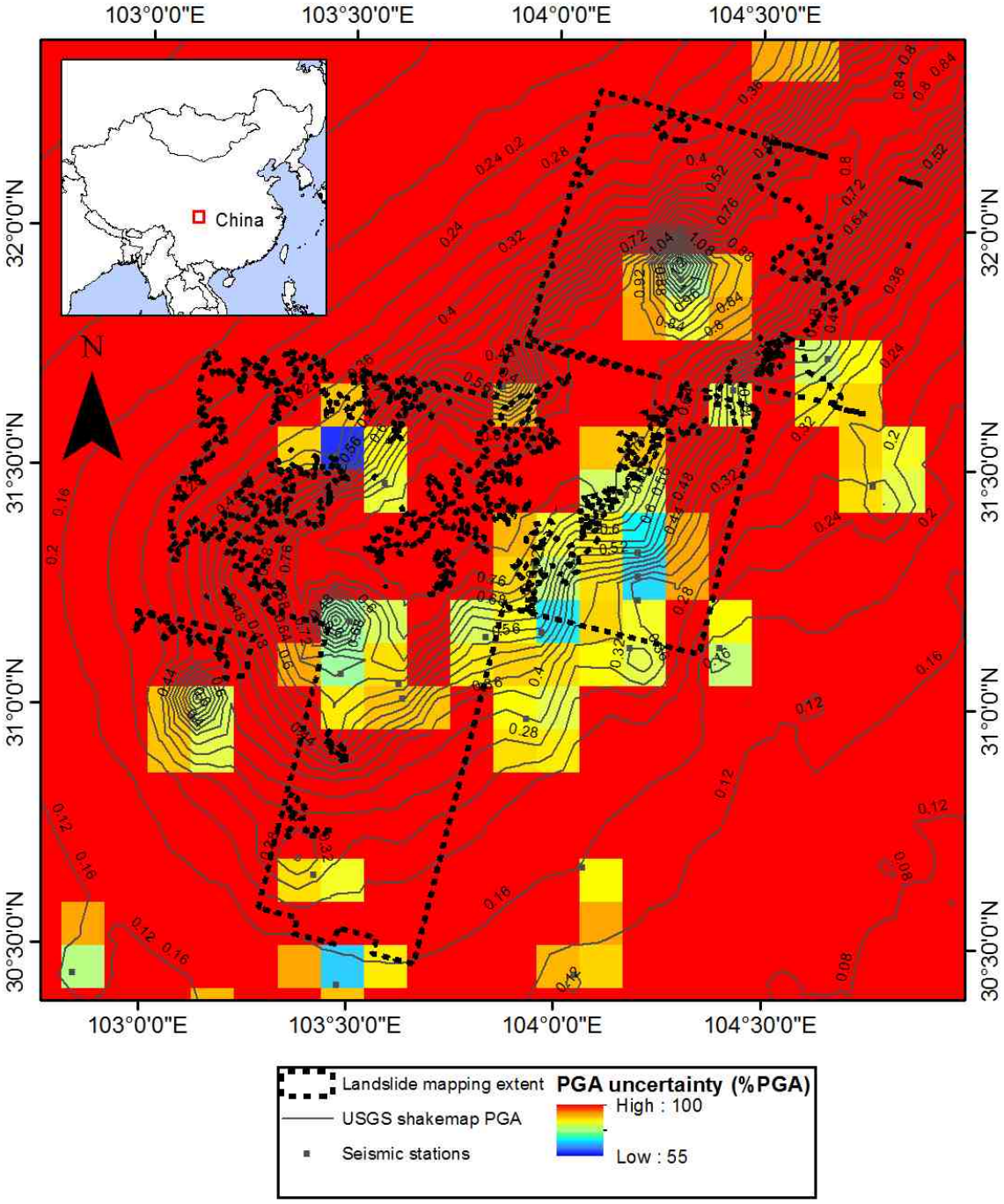

Figure A - 4 Regional uncertainty (standard deviation) in terms of % PGA for the 2008 Wenchuan earthquake (Allen et al., 2008)

Appendix B - Paper presented at the 2012 International Symposium on Earthquake-induced landslides

PARKER, R. N., PETLEY, D., DENSMORE, A., ROSSER, N., DAMBY, D. & BRAIN, M. 2012. Progressive failure cycles and distributions of earthquake triggered landslides. *In:* UGAI, K., YAGI, H. & WAKAI, A. (eds.) *Earthquake induced landslides: Proceedings of the International Symposium on Earthquake induced landslides, Kiryu, Japan, 2012.* New York: Springer.

Progressive failure cycles and distributions of earthquake-triggered landslides

Robert Parker*, David Petley, Alexander Densmore, Nicholas Rosser, David Damby, Matthew Brain

**Corresponding author*

Institute of Hazard, Risk and Resilience, Department of Geography, University of Durham, Durham, DH1 1PY, U.K.

Abstract

Advances in the collection and analysis of landslide inventory data have allowed for greater understanding of spatial distributions of landslides triggered by earthquakes. However, current approaches to analysing and modelling these phenomena do not account for the response of the individual potential landslide masses and their temporally evolving stability. This stems, in part, from the lack of a conceptual model describing the effect of seismic waves on the strength and stability of hillslopes, which can be applied at the regional scale and over long (multiple earthquake) time scales. Here we present such a conceptual model linking weakening via progressive failure, inertial displacements driven by seismic ground accelerations, and the repeating failure of sections of hillslopes through time. We explore the implications of the model for how various characteristics of earthquake-triggered landslide distributions are interpreted and understood. These include the apparently stochastic nature of spatial landslide occurrence, spatial patterns of landsliding, landslide magnitude-frequency distributions, global variability in numbers of landslides triggered by earthquakes, and in particular why in any earthquake smaller areas of hillslope fail than do not, even in regions of apparently high landslide susceptibility. Finally, we also propose means of testing the validity of this model relative to alternative hypotheses.

Keywords

Progressive failure, Newmark, landslide distributions, hysteresis.

Introduction

Newmark analysis forms the basis of most currently available techniques for assessing the effect of seismic accelerations on hillslopes at the regional scale (e.g.: Jibson, 2007). Here a potential landslide is modelled as a rigid perfectly plastic block sat on an inclined surface. Deformation occurs along the shear plane in response to seismic accelerations that exceed the dynamic shearing resistance, which is assumed to be the same as the static shearing resistance. A key assumption of the Newmark approach is that the shearing resistance does not change in response to seismically-induced deformations. However, movement patterns in failing landslide masses and the results of stress-path triaxial tests have shown that cohesive hillslope materials undergo progressive weakening prior to full failure (Petley et al., 2005b, Petley et al., 2005a). Logic also dictates that a stable section of hillslope must undergo weakening and a reduction in stability in order to reach the point of failure, and that once failed, in simplistic terms, a new more stable section of hillslope is produced. This means that the stability of individual locations in the landscape and therefore their sensitivity to earthquake-triggered landsliding is not temporally constant, but can be understood as evolving cyclically with the occurrence of seismic events.

In this paper, we present a conceptual model linking micro-scale deformation-weakening behaviour in hillslope materials and inertial displacements driven by seismic ground accelerations, in order to provide a physical approach to understanding the temporal evolution of hillslope stability in response to seismic events. We explore the implications of the model for understanding various observed characteristics of landslide distributions and propose means of testing the validity of this model relative to alternative hypotheses.

Temporal model of hillslope weakening and failure

Background

Failure in cohesive materials generally requires that the material that forms the eventual shear zone undergoes a transition from peak to residual strength (Bjerrum, 1967). This requires the material to undergo progressive deformation, resulting in the formation and coalescence of cracks that reduce the strength of the material. Based on observations of pre-failure landslide movement patterns (Petley et al., 2002, Kilburn and Petley, 2002) and the results of stress path triaxial tests, Petley et al. (2005b) proposed a conceptual model for the development of progressive first-time failure in hillslopes formed from cohesive materials. The authors proposed that when a temporary reduction in factor of safety (FS) occurs due to elevated pore pressures, local stresses may exceed material strength in parts of the landslide, even though the global FS is still greater than unity. This allows deformation and micro-crack formation to take place in these segments, causing them to transition from peak to residual strength. The stress is then redistributed to other, unsheared, portions of the hillslope. This transfer process eventually reaches the point at which shear stress exceeds shear strength across the whole of the shear zone, such that failure becomes inevitable regardless of pore pressure state. However, it still takes time for the final sections of the shear zone to fail, such that collapse is not instantaneous. Hereafter we refer to this process of deformation, micro-crack formation and weakening by the term "deformation-weakening". Note also that whilst this model was developed for instability associated with hydrologically-triggered landslides, dynamic stresses from the passage of seismic waves may also serve to produce the temporary instabilities required for progressive failure.

Model Description

The Newmark sliding block model (Newmark, 1965) provides a means of analysing the effect of seismic accelerations on hillslope stability in order to predict seismically-induced displacements in landslide masses (for a comprehensive review, see Jibson, 2011). In this research we utilise the Newmark sliding block model as the basis for our conceptual model. We supplement the Newmark approach by changing two assumptions. First, we allow Newmark displacement to result in deformation-weakening, which breaks the assumption of perfectly plastic stress-strain behaviour of Newmark sliding blocks (e.g.: Newmark, 1965, Makdisi and Seed, 1978, Chang et al., 1984, Ambraseys and Menu, 1988). Second, we theorise that the critical acceleration may be exceeded in segments of the landslide block and not the whole mass. This implies that the mass can deform internally, counter to the assumption that the landslide is a rigid block. Note also that we maintain the normal assumption in the Newmark approach of no change in pore pressure both under static and dynamic conditions. In this research we consider the response of multiple individual sections of hillslope at the spatial scale of mountain ranges (regional scale) to multiple earthquakes. While the effect of an earthquake on a section of hillslope is instantaneous, the return period of an earthquake may be hundreds to tens of thousands of years, depending on the large-scale rate of tectonic stress accumulation. This approach presupposes that over these periods of time hillslopes fail in the same location on multiple occasions in response to the multiple earthquakes that occur. Each time a section of hillslope fails, we assume that the material evacuates the shear surface, and the shear surface then forms the new hillslope surface. This new section of hillslope then becomes a new potential landslide. We assume that the geometry of sections of hillslopes does not change as they repeatedly fail – i.e. that the form of failure is that of a pseudo-infinite slope. As the majority of reported earthquake-triggered landslides take the form of shallow rockfalls, disrupted soil slides and rockslides (Keefer, 2002), and occur across all parts of hillslope profiles, from toes to ridge crests (Densmore and Hovius, 2000), this assumption is not unreasonable. Of course, as detachment and failure of material occurs, new hillslope surfaces are also formed from deposition of this material downslope, which in turn forms part of new potential landslide masses. We do not consider this process of mobilisation and deposition at this stage. These assumptions allow us to isolate the effect of material strength evolution without imposing ill constrained assumptions regarding material transport and surface modification from secondary aseismic processes.

The hillslopes of our model landscape are composed of a population of potential landslide masses, each of which is modelled as a Newmark sliding block. Hereafter we refer to these individual sections of hillslope as "blocks". Each block has a peak strength (at which the section of hillslope is at its maximum stability) and a residual strength (at which, if it has not already failed, the section of hillslope is at its minimum stability). Each block also has a surface gradient and a downslope length. A single ridge-to-stream hillslope profile may comprise of a single block or multiple blocks of different sizes, which will determine the size of landslides that occur on that hillslope. In Newmark analysis, sliding block displacement occurs when earthquake shaking exceeds the block's critical acceleration a_c - the horizontal component of acceleration required to overcome the shear strength of the material - thereby temporarily producing FS<1.

$$a_c = (FS - 1)g \sin \alpha$$

$$FS = \frac{\tau_f}{\tau}$$

where a_c is the critical acceleration in terms of g (the acceleration due to Earth's gravity), FS is the static factor of safety (τ is the shear stress acting on the block and τ_f is the shear strength of the material), and α is the angle from the horizontal at which the centre of gravity of the slide mass moves when displacement occurs. The behaviour of a single section of hillslope is illustrated in Figure 1. Initially τ_f at its peak is greater than τ such that the section of hillslope is stable (Figure 1A). In our model, Newmark displacements result in deformation-weakening of the block material, causing a reduction in τ_f and therefore also in FS (Figure 1B). The length of blocks determines the volume of material throughout which deformation-weakening is distributed. To generate the same net reduction in strength, longer blocks must therefore undergo larger displacements than shorter blocks; i.e. maintaining the same displacement-length ratio (strain, ε). If FS is reduced to <1, then failure of the block occurs (Figure 1C), the weakened material evacuates the shear surface and a new hillslope surface layer is formed (Figure 1D). The new block retains the same gradient and length, whilst τ_f resets to its peak level. We term this cycle of weakening, failure and evacuation of material the "failure cycle". For simplicity we assume that blocks are spatially independent of one another.

Any earthquake in which a_c is exceeded will result in a reduction in FS. For a small earthquake generating weak ground accelerations, blocks have to have very low FS at the onset of shaking in order for a_c to be exceeded, and for failure to result from a small reduction in FS. For large earthquakes that generate strong ground accelerations, full transition to instability occurs in blocks that were more stable at the onset of shaking. As earthquakes occur, the weakest blocks reset and others weaken towards failure. An earthquake may reduce the population of potentially unstable blocks through complete failure and reset, but critically this net reduction is counteracted by other blocks that remain intact moving closer to failure, as a result of accumulating coseismic deformation-weakening. Note that, in theory, for blocks in which the residual strength is higher than the shear stress, complete failure may never actually occur; once residual strength is reached these blocks will deform in a plastic manner each time a_c is exceeded.

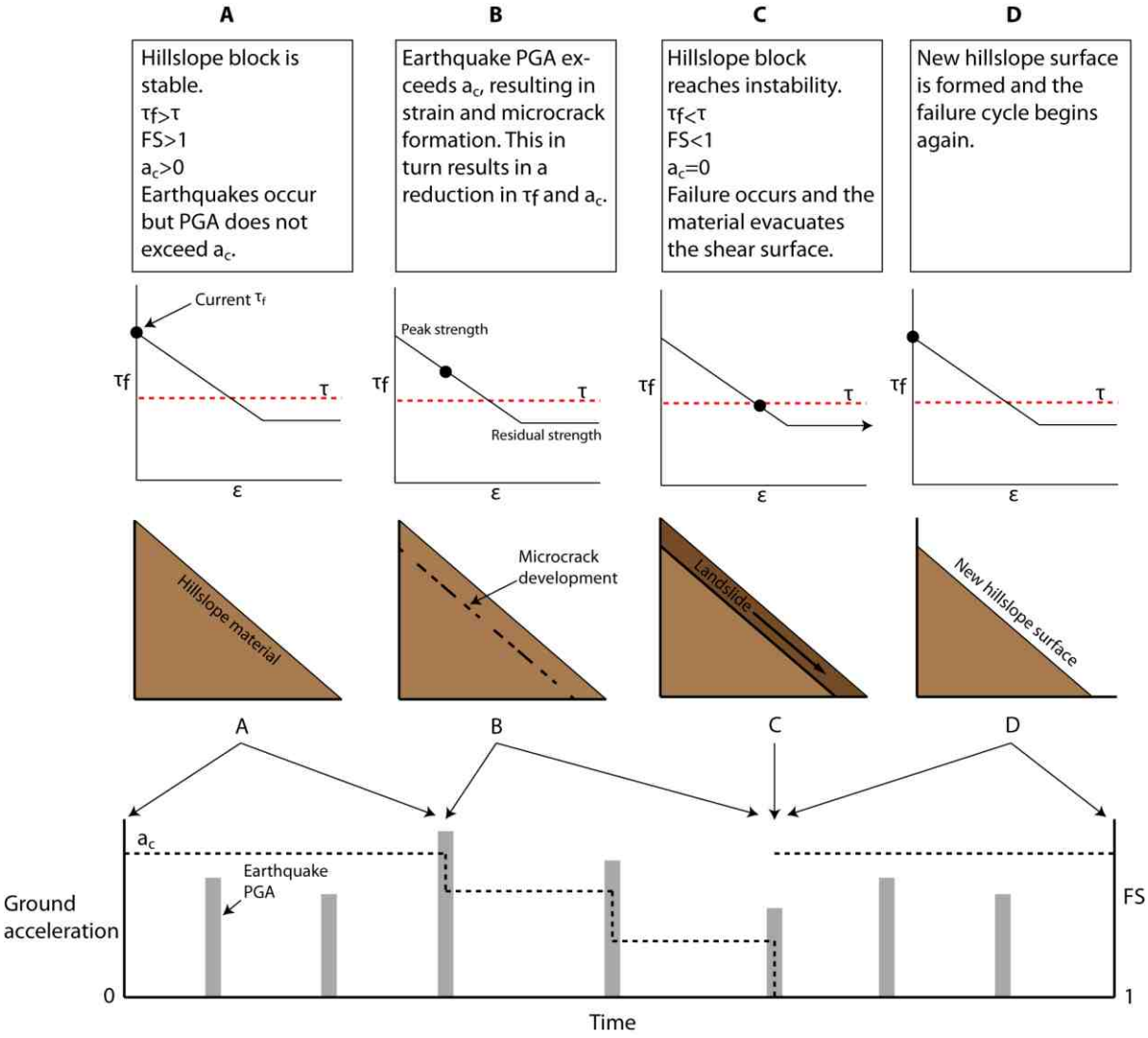

Figure 1: Illustration of the failure cycle occurring in a single hillslope block. The hillslope experiences a time series of earthquakes that drive the failure cycle. Four stages in the cycle are highlighted. For each stage the following are provided: plots of shear strength (τ_f) against strain (ε), on which the static shear stress (τ) is indicated by the red line; illustrations of shear surface development and slope failure; time series of earthquake peak ground accelerations (PGA) on which the evolving value of a_c (proportional to FS) is indicated.

The failure cycle and characteristics of landslide distributions

A number of corollaries follow on from the basic assumptions of our conceptual model, which have implications for how observed characteristics of earthquake-triggered landslide distributions are interpreted. We outline these first, before exploring predictions that may be used to test the model relative to competing hypotheses.

Spatial patterns of landslide probability

Over time, potential landslides progress through the failure cycle at different rates in response to ground accelerations and other factors that induce hillslope stress changes. For simplicity we frame our discussion around the effect of earthquakes, although our arguments are also applicable to hydrologically-induced stress changes. Local factors controlling the rate of progression of blocks through the failure cycle, hereafter termed the "progression rate", can be broken down qualitatively into those pertaining to material rheology, static stresses governed by potential landslide geometry and the strength and duration of seismic accelerations.

In terms of block rheology, the peak strength and rate of strength decay with deformation control the progression rate. Blocks with lower peak strength must undergo less weakening to reach the point of failure than blocks with higher peak strength. Blocks with a higher rate at which strength decays with deformation progress through the failure cycle more rapidly than those with lower rates of strength decay. Different rates of landslide occurrence observed in different lithological units (e.g.:Parise and Jibson, 2000) may be interpreted in terms of lithological variations in material stress-strain behaviour that define strength-decay due to deformation (e.g.: Plumb and Schlumberger Cambridge Research, 1994, Hoek et al., 2005, Liang et al., 2007).

As blocks with steeper gradients have larger shear stresses the static FS is lower than for blocks with shallow gradients. In terms of the Newmark model this corresponds to a lower critical acceleration value, resulting in displacement occurring under weaker ground accelerations in general and larger displacements occurring under strong accelerations. Larger displacements result in a greater amount of deformation-weakening and subsequent decrease in FS. Thus for each earthquake, steeper blocks experience a greater reduction in relative strength (and thus stability) than do shallower blocks. Over time this translates to a higher progression rate for steeper blocks. Consequently a greater proportion of steeper blocks will fail with each event. This is reflected in observed patterns of increasing landslide probability with hillslope gradient (e.g.: Jibson and Keefer, 1989, Keefer, 2000, Lee et al., 2008, Parker et al., 2010, Parker, 2010, Dai et al., 2011). Note that hillslope gradient and peak strength are unlikely to be independent as higher shear strength is required to support steeper slopes. Observed relationships between landslide probability and hillslope gradient will therefore also reflect this interaction.

As the amplitude of seismic accelerations increases, critical acceleration thresholds are exceeded on a larger number of hillslopes. As amplitudes continue to increase above critical acceleration levels, the displacement produced by each seismic wave also increases. Furthermore, as the duration of seismic shaking increases, the cumulative displacement generated also increases. For each earthquake, blocks in regions experiencing seismic accelerations with higher amplitudes and longer durations progress through the failure cycle more rapidly, and thus experience a higher proportion of blocks that fail. This is reflected, for example, in observed patterns of increasing landslide probability with peak ground acceleration (e.g.: Meunier et al., 2007).

Landslide size-frequency distributions

As the length of blocks determines the volume of material throughout which deformation-weakening is distributed, the progression rate decreases with increasing block length. To a reasonable first approximation landslide length, width and depth scale proportionally, and therefore landslide volumes increase with landslide length (e.g.: Larsen et al., 2010). Thus for any earthquake one would expect failure to occur in a greater proportion of small volume blocks than in large volume blocks. Even if the landscape was composed of equal numbers of small and large blocks, the frequency distribution of blocks experiencing failure would be skewed in favour of small sizes. Thus, we must distinguish between the size distribution of potential landslide masses – the distribution of blocks that makes up the landscape – and the size distribution of triggered landslide masses – the distribution of blocks that actually fail. Stark and Guzzetti (2009) have argued that the characteristic landslide size-probability distribution - inverse power law decay for large landslides with rollover at small landslide sizes (e.g.: Hovius et al., 1997, Malamud et al., 2004a, Malamud et al., 2004b) – is rooted in a stochastic survival process of rupture growth. However, this process determines the probability of landslide rupture reaching a given area – the probability distribution of potential landslide masses - not the probability that a landslide with a given rupture area fails in any particular event – the probability distribution of triggered landslides. Our model suggests that the latter is a product of both the rupture-process-driven potential landslide size-probability distribution, and relative differences in rates at which potential landslides of different sizes progress through the failure cycle.

Stochastic spatial occurrence of landslides

Whether or not a block actually fails depends on the state of the block in its failure cycle at the onset of shaking. The stochastic nature of spatial landslide occurrence therefore, in part, results from not knowing the seismic history of each block and therefore the position of each block in its failure cycle at the onset of shaking. This means that even for two identical successive earthquakes (with the same spatial pattern of ground accelerations), failure will occur for different populations of potential landslides. The fact that generally smaller areas of the landscape experience failure than do not, even in regions identified as having high landslide susceptibility, implies that the majority of blocks are not sufficiently close to failure prior to the earthquake to reach the point of failure as a result of the earthquake. These potential landslides may have experienced a large drop in their FS as a result of the earthquake, but still require further weakening to bring them to the point of failure.

Global variability

A key output of this modelling is that the total proportion of blocks that actually fail in a particular earthquake depends on the population of blocks primed for failure – those sufficiently close to failure prior to the earthquake that they reach the point of failure as a result of the earthquake. Critically, this population may not necessarily be of a constant size. As blocks progress through the failure cycle, each at different rates, and as strong seismic events cause the simultaneous failure and reset of multiple blocks, there is potential for variability in block numbers primed for failure. The result of changes in this population is variability in landslide probability through time and therefore in the sensitivity of landscapes to earthquake-triggered landsliding. Global relationships between landslide frequency and earthquake magnitude (e.g.: Malamud et al., 2004b), and area affected by landslides and earthquake magnitude (e.g.: Keefer, 1984, Rodríguez et al., 1999) exhibit unexplained variance of up to an order of magnitude. This has been attributed to variations in physiographic characteristics of different regions that are not taken into account in the analysis. However, this observed global variability may also be rooted in time-dependent variability in landscape sensitivity.

Tests for model validation

We have hypothesised the existence of an ordered system at the root of stochastic spatial patterns of earthquake-triggered landsliding. This hypothesis runs counter to ideas that the occurrence of earthquake-triggered landslides is rooted in a stochastic system resulting from (essentially unknowable) variability in ground accelerations and/or hillslope material properties. Both of these models are capable of generating stochastic spatial patterns of earthquake-triggered landsliding. A fundamental difference is that, according to our model, the system should exhibit memory or hysteresis. In this view, the response of a potential landslide mass to seismic accelerations is not only dependent on the current environment, but also the past environment (the history of seismic accelerations in the time since that section of hillslope last failed). Determining which of these models provides a better representation of the system's behaviour requires tests for the presence or absence of this hysteresis. For instance, the strength of ground accelerations required for a potential landslide mass to progress to the point of failure becomes less as FS decreases. Therefore, sections of hillslopes that experience strong ground accelerations during one earthquake but do not fail, then have the potential to failure under weaker accelerations during a future earthquake. Where landslide inventories exist for multiple earthquakes with overlapping spatial extents, tests for this hysteresis may be formulated.

Conclusions

Current approaches to analysing earthquake-triggered landslide distributions and modelling the effect of earthquakes on hillslopes at the region scale do not consider changes in shearing resistance in response to seismically-induced deformations, and therefore cannot account for the temporally-evolving stability of individual potential landslide masses. The reduction in stability required for stable sections of hillslope to reach the point of failure can be understood by recognising that seismically-driven deformation in hillslopes results in the formation and coalescence of cracks, which reduce the strength of sections of

hillslope until they fail. Over multiple-earthquake timescales, this process must repeat, such that sections of hillslopes experience a continual cycle of weakening and failure. The rate at which these potential landslide masses progress through the failure cycle determines the time-averaged probability of landsliding. The progression rate is dependent on the stress-strain behaviour of hillslope materials, the size and gradient of potential landslide masses and the strength and duration of seismic accelerations. Observed patterns of increasing landslide probability with hillslope gradient and peak ground acceleration, and variations in landslide probability among different lithological units, may therefore be interpreted as reflecting variations in progression rates. Similarly, our model suggests that the size-probability distribution of triggered landslides is not only the product of the size-probability distribution of potential landslides, but also the scaling of progression rate with landslide size. Whether or not a hillslope fails as the result of an earthquake is dependent on both the amount of weakening produced by that earthquake and the history of seismic damage accumulated on the hillslope. The apparent stochastic nature of spatial landslide occurrence and variability in total numbers of landslides triggered by earthquakes of similar magnitudes can therefore be understood as the product of both the current earthquake and the seismic history of individual slopes. Further work to determine the validity of this model relative to competing hypotheses requires tests for evidence of this hysteresis in landslide datasets.

Acknowledgements

Funding for this research is provided by the Willis Research Network, with support from the New Zealand Institute of Geological and Nuclear Sciences. We thank D. Milledge, W. Murphy, C. Massey, G. Hancox, R. Jibson, D. Keefer and P. Stafford for assistance.

References

Ambraseys, N. N. & Menu, J. M. 1988. Earthquake-induced ground displacements. *Earthquake Engineering & Structural Dynamics,* 16**,** 985-1006.

Bjerrum, L. 1967. Progressive failure in slopes of overconsolidated plastic clay and clay shales. *Journal of soil mechancis and foundations, Division of the American Society of Civil Engineers,* 93**,** 1-49.

Chang, J. C., Chen, W. F. & Yao, J. T. P. 1984. Seismic displacments in slopes by limit analysis. *Journal of Geotechnical Engineering,* 110**,** 860-874.

Dai, F. C., Xu, C., Yao, X., Xu, L., Tu, X. B. & Gong, Q. M. 2011. Spatial distribution of landslides triggered by the 2008 Ms 8.0 Wenchuan earthquake, China. *Journal of Asian Earth Sciences,* 40**,** 883-895.

Densmore, A. L. & Hovius, N. 2000. Topographic fingerprints of bedrock landslides. *Geology,* 28**,** 371-374.

Hoek, E., Marinos, P. G. & Marinos, V. P. 2005. Characterisation and engineering properties of tectonically undisturbed but lithologically varied sedimentary rock masses. *International Journal of Rock Mechanics and Mining Sciences,* 42**,** 277-285.

Hovius, N., Stark, C. P. & Allen, P. A. 1997. Sediment flux from a mountain belt derived by landslide mapping. *Geology,* 25**,** 231-234.

Jibson, R. W. 2007. Regression models for estimating coseismic landslide displacement. *Engineering Geology,* 91**,** 209-218.

Jibson, R. W. 2011. Methods for assessing the stability of slopes during earthquakes-A retrospective. *Engineering Geology,* 122**,** 43-50.

Jibson, R. W. & Keefer, D. K. 1989. Statistical-Analysis of Factors Affecting Landslide Distribution in the New Madrid Seismic Zone, Tennessee and Kentucky. *Engineering Geology,* 27**,** 509-542.

Keefer, D. K. 1984. Landslides Caused by Earthquakes. *Geological Society of America Bulletin,* 95**,** 406-421.

Keefer, D. K. 2000. Statistical analysis of an earthquake-induced landslide distribution - the 1989 Loma Prieta, California event. *Engineering Geology,* 58**,** 231-249.

Keefer, D. K. 2002. Investigating landslides caused by earthquakes - A historical review. *Surveys in Geophysics,* 23**,** 473-510.

Kilburn, C. R. J. & Petley, D. N. 2002. Forecasting giant, catastrophic slope collapse: lessons from Vajont, Northern Italy. *Geomorphology,* 54**,** 21-32.

Larsen, I. J., Montgomery, D. R. & Korup, O. 2010. Landslide erosion controlled by hillslope material. *Nature Geosci,* 3**,** 247-251.

Lee, C. T., Huang, C. C., Lee, J. F., Pan, K. L., Lin, M. L. & Dong, J. J. 2008. Statistical approach to earthquake-induced landslide susceptibility. *Engineering Geology,* 100**,** 43-58.

Liang, W., Yang, C., Zhao, Y., Dusseault, M. B. & Liu, J. 2007. Experimental investigation of mechanical properties of bedded salt rock. *International Journal of Rock Mechanics and Mining Sciences,* 44**,** 400-411.

Makdisi, F. I. & Seed, H. B. 1978. Simplified Procedure for Estimating Dam and Embankment Earthquake-Induced Deformations. *Journal of the Geotechnical Engineering Division,* 104**,** 849-867.

Malamud, B. D., Turcotte, D. L., Guzzetti, F. & Reichenbach, P. 2004a. Landslide inventories and their statistical properties. *Earth Surface Processes and Landforms,* 29**,** 687-711.

Malamud, B. D., Turcotte, D. L., Guzzetti, F. & Reichenbach, P. 2004b. Landslides, earthquakes, and erosion. *Earth and Planetary Science Letters,* 229**,** 45-59.

Meunier, P., Hovius, N. & Haines, J. 2007. Regional patterns of earthquake-triggered landslides and their relation to ground motion. *Geophys. Res. Lett.,* 34.

Newmark, N. M. 1965. Effects of earthquakes on dams and embankments. *Geotechnique,* 15**,** 139-159.

Parise, M. & Jibson, R. W. 2000. A seismic landslide susceptibility rating of geologic units based on analysis of characteristics of landslides triggered by the 17 January, 1994 Northridge, California earthquake. *Engineering Geology,* 58**,** 251-270.

Parker, R., Petley, D., Rosser, N., Densmore, A. & Whadcoat, S. 2010. Mapping and monitoring the spatial distribution of landslide hazards induced by the 2008 Wenchuan Earthquake, Sichuan Province, China. *Geologically Active - 11th International Association for Engineering Geology Congress*. Aukland, New Zealand.

Parker, R. N. 2010. *Controls on the distribution of landslides triggered by the 2008 Wenchuan earthquake, Sichuan Province, China*. MSc, University of Durham.

Petley, D. N., Bulmer, M. H. & Murphy, W. 2002. Patterns of movement in rotational and translational landslides. *Geology,* 30**,** 719-722.

Petley, D. N., Higuchi, T., Dunning, S., Rosser, N. J., Petley, D. J., Bulmer, M. H. & Carey, J. 2005a. A new model for the development of movement in progressive landslides. *In:* HUNGR, O., FELL, R., COUTURE, R. & EBERHARDT, E. (eds.) *Landslide risk management*. Amsterdam: A. T. Balkema.

Petley, D. N., Higuchi, T., Petley, D. J., Bulmer, M. H. & Carey, J. 2005b. Development of progressive landslide failure in cohesive materials. *Geology,* 33**,** 201-204.

Plumb, R. A. & Schlumberger Cambridge Research, U. 1994. Influence of composition and texture on the failure properties of clastic rocks. *Rock Mechanics in Petroleum Engineering*. Delft, Netherlands: Society of Petroleum Engineers

Rodríguez, C. E., Bommer, J. J. & Chandler, R. J. 1999. Earthquake-induced landslides: 1980-1997. *Soil Dynamics and Earthquake Engineering,* 18**,** 325-346.

Stark, C. P. & Guzzetti, F. 2009. Landslide rupture and the probability distribution of mobilized debris volumes. *Journal of Geophysical Research-Earth Surface,* 114.

References

ABRAHAMSON, N., ATKINSON, G., BOORE, D., BOZORGNIA, Y., CAMPBELL, K., CHIOU, B., IDRISS, I. M., SILVA, W. & YOUNGS, R. 2008. Comparisons of the NGA ground-motion relations. *Earthquake Spectra,* 24**,** 45-66.

ABRAHAMSON, N. A. & SOMERVILLE, P. G. 1996. Effects of the hanging wall and foot wall on ground motions recorded during the Northridge earthquake. *Bulletin of the Seismological Society of America,* 86**,** S93-S99.

ADAMAKI, A., PAPADIMITRIOU, E. E., TSAKLIDIS, G. M. & KARAKOSTAS, V. 2011. Statistical properties of aftershock rate decay: Implications for the assessment of continuing activity. *Acta Geophysica,* 59**,** 748-769.

ADAMS, R. D. & LOWRY, M. A. 1971. The Inangahua earthquake sequence, 1968. *Royal Society of New Zealand bulletin,* 9**,** 129-135.

ALLEN, T. I., WALD, D. J., HOTOVEC, A. J., LIN, K., EARLE, P. S. & MARANO, K. D. 2008. An Atlas of ShakeMaps for Selected Global Earthquakes. *U.S. Geological Survey Open-File Report.* United States Geological Survey.

AMBRASEYS, N. N. & MENU, J. M. 1988. Earthquake-induced ground displacements. *Earthquake Engineering & Structural Dynamics,* 16**,** 985-1006.

AMBRASEYS, N. N. & SRBULOV, M. 1994. Attenuation of earthquake-induced ground displacements. *Earthquake Engineering & Structural Dynamics,* 23**,** 467-487.

ANDERSON, H., BEANLAND, S., BUCK, G., DARBY, D., DOWNES, G., HAINES, J., JACKSON, J., ROBINSON, R. & WEBB, T. 1994. The 1968 May 23 Inangahua, New Zealand, earthquake: an integrated geological, geodetic, and seismological source model. *New Zealand Journal of Geology and Geophysics,* 37**,** 59-86.

ANDERSON, H., WEBB, T. & JACKSON, J. 1993. Focal mechanisms of large earthquakes in the South Island of New Zealand: implications for the accommodation of Pacific-Australia plate motion. *Geophys. J. Int,* 115**,** 1032-1054.

ARIAS, A. 1970. MEASURE OF EARTHQUAKE INTENSITY. *In:* HANSEN, R. J. (ed.) *Seismic Design for Nuclear Power Plants.* Cambridge, Mass.: Massachusetts Inst. of Tech. Press.

ASANO, S., OCHIAI, H. & OKADA, Y. 2013. Observations on Earthquake Acceleration and Pore Water Pressure in a Hilly Region. *In:* UGAI, K., YAGI, H. & WAKAI, A. (eds.) *Earthquake-Induced Landslides.* Springer Berlin Heidelberg.

ATKINSON, P., JISKOOT, H., MASSARI, R. & MURRAY, T. 1998. Generalized linear modelling in geomorphology. *Earth Surface Processes and Landforms,* 23**,** 1185-1195.

AYALEW, L. & YAMAGISHI, H. 2005. The application of GIS-based logistic regression for landslide susceptibility mapping in the Kakuda-Yahiko Mountains, Central Japan. Elsevier.

BACH, C. & HAINZL, S. 2012. Improving empirical aftershock modeling based on additional source information. *Journal of Geophysical Research-Solid Earth,* 117.

BAK, P., CHRISTENSEN, K., DANON, L. & SCANLON, T. 2002. Unified scaling law for earthquakes. *Physical Review Letters,* 88.

BAKER, M. R. & DOSER, D. 1988. Joint inversion of regional and teleseismic earthquake waveforms. *Journal of Geophysical Research,* 93**,** 2037-2045.

BÅTH, M. 1965. Lateral inhomogeneities of the upper mantle. *Tectonophysics,* 2**,** 483-514.

BAYRAK, Y., YILMAZTÜRK, A. & ÖZTÜRK, S. 2002. Lateral variations of the modal (a/b) values for the different regions of the world. *Journal of Geodynamics,* 34**,** 653-666.

BEAVAN, J. 2011. *RE: Pers coms - correspondance regarding regional patterns of tectonic deformation and strain localisation in New Zealand.*

BEAVAN, J. & HAINES, J. 2001. Contemporary horizontal velocity and strain rate fields of the Pacific-Australian plate boundary zone through New Zealand. *Journal of Geophysical Research,* 106**,** 741-770.

BELL, F. G. 2000. *Engineering properties of soils and rocks,* Oxford, Blackwell Science.

BENISTON, M. & DOUGLAS, G. F. 1996. Impacts of climate change on mountain regions. *In:* WATSON, R. T., ZINYOWERA, M. C., MOSS, R. H. & DOKKEN, D. J. (eds.) *Climate change 1995. impacts, adaptations and mitigation of climate change: scientific-technical analysis.* Cambridge: Cambridge University Press.

BENITES, R. A., HAINES, A. J., NEW ZEALAND. EARTHQUAKE, C., INSTITUTE OF, G. & NUCLEAR SCIENCES, L. 1994. *Quantification of seismic wavefield amplification by topographic features,* Wellington, N.Z., Institute of Geological & Nuclear Science.

BERRYMAN, K. R. 1980. Late Quaternary movement on White Creek Fault, South Island, New Zealand. *New Zealand journal of geology and geophysics,* 23**,** 93-101.

BIENIAWSKI, Z. T. & VANHEERDEN, W. L. 1975. Significance of Insitu Tests on Large Rock Specimens. *International Journal of Rock Mechanics and Mining Sciences,* 12**,** 101-113.

BJERRUM, L. 1967. Progressive failure in slopes of overconsolidated plastic clay and clay shales. *Journal of soil mechancis and foundations, Division of the American Society of Civil Engineers,* 93**,** 1-49.

BLAKE, T. F., HOLLINGSWORTH, R. A. & STEWART, J. P. 2002. Recommended proceedures for implementation of DMG special publication 117 - guidelines for analysing and mitigating landslide hazards in California. Los Angeles, CA: Southern California Earthquake Centre.

BOMMER, J. J., BENITO, M. B., CIUDAD-REAL, M., LEMOINE, A., LOPEZ-MENJIVAR, M. A., MADARIAGA, R., MANKELOW, J., DE HASBUN, P. M., MURPHY, W., NIETO-LOVO, M., RODRIGUEZ-PINEDA, C. E. & ROSA, H. 2002. The El Salvador earthquakes of January and February 2001: context, characteristics and implications for seismic risk. *Soil Dynamics and Earthquake Engineering,* 22**,** 389-418.

BOMMER, J. J. & RODRIGUEZ, C. E. 2002. Earthquake-induced landslides in central America. *Engineering Geology,* 63**,** 189-220.

BORGA, M., FONTANA, G. D. & CAZORZI, F. 2002. Analysis of topographic and climatic control on rainfall-triggered shallow landsliding using a quasi-dynamic wetness index. *Journal of Hydrology,* 268**,** 56-71.

BORGHUIS, A. M., CHANG, K. & LEE, H. Y. 2007. Comparison between automated and manual mapping of typhoon-triggered landslides from SPOT-5 imagery. *International Journal of Remote Sensing,* 28**,** 1843-1856.

BOUCHON, M. 1973. EFFECT OF TOPOGRAPHY ON SURFACE MOTION. *Bulletin of the Seismological Society of America,* 63**,** 615-632.

BOZBEY, I. & GUNDOGDU, O. 2011. A methodology to select seismic coefficients based on upper bound "Newmark" displacements using earthquake records from Turkey. *Soil Dynamics and Earthquake Engineering,* 31**,** 440-451.

BRARDINONI, F. & CHURCH, M. 2004. Representing the landslide magnitude-frequency relation: Capilano River Basin, British Columbia. *Earth Surface Processes and Landforms,* 29**,** 115-124.

BRUNETTI, M. T., GUZZETTI, F. & ROSSI, M. 2009. Probability distributions of landslide volumes. *Nonlinear Processes in Geophysics,* 16**,** 179-188.

BRUNSDEN, D. & THORNES, J. B. 1979. Landscape Sensitivity and Change. *Transactions of the Institute of British Geographers,* 4**,** 463-484.

BUMA, J. & DEHN, M. 1998. A method for predicting the impact of climate change on slope stability. *Environmental Geology,* 35**,** 190-196.

CALIFORNIA GEOLOGICAL SURVEY 2008. Guidelines for Evaluating and Mitigating Seismic Hazards in California. *California Division of Mines and Geology Special Publication,* 117**,** 74.

CAMPBELL, K. W. 1981. Near-source attenuation of peak horizontal acceleration. *Seismological Society of America,* 71**,** 2039-2070.

CAMPBELL, K. W. & BOZORGNIA, Y. 2008. NGA ground motion model for the geometric mean horizontal component of PGA, PGV, PGD and 5% damped linear elastic response spectra for periods ranging from 0.01 to 10 s. *Earthquake Spectra,* 24**,** 139-171.

CAPOLONGO, D., REFICE, A. & MANKELOW, J. Evaluating earthquake-triggered landslide hazard at the basin scale through GIS in the Upper Sele river Valley. Symposim on Assessment and Mitigation of Multiple Hazards, 2002 2002 Nice, France. 595-625.

CARRARA, A., CROSTA, G. & FRATTINI, P. 2008. Comparing models of debris-flow susceptibility in the alpine environment. *Geomorphology,* 94**,** 353-378.

CHANG, J. C., CHEN, W. F. & YAO, J. T. P. 1984. Seismic displacments in slopes by limit analysis. *Journal of Geotechnical Engineering,* 110**,** 860-874.

CHEMENDA, A., BOUISSOU, S. & BACHMANN, D. 2005. Three-dimensional physical modeling of deep-seated landslides: New technique and first results. *J. Geophys. Res.,* 110**,** F04004.

CHEN, H., DADSON, S. & CHI, Y.-G. 2006. Recent rainfall-induced landslides and debris flow in northern Taiwan. *Geomorphology,* 77**,** 112-125.

CHEN, R. H. 1981. Three-dimensional slope stability analysis. *Joint Highway Research Project.* West Lafayette, Indiana: Purdue University, Indiana State Highway Commission.

CHEN, T. C., LIN, M. L. & HUNG, J. 2004. Pseudostatic analysis of Tsao-Ling rockslide caused by Chi-Chi earthquake. *Engineering Geology,* 71**,** 31-47.

CHEN, X., ENDER, P., MITCHELL, M. & WELLS, C. (eds.) 2012a. *Logistic Regression with Stata,* http://www.ats.ucla.edu/stat/stata/webbooks/logistic/.

CHEN, X.-Q., LI, Y., GAO, Q. & JIA, S.-T. 2012b. Distribution characteristics of Geo-hazards in Ganxi Valley after the Wenchuan earthquake. *Environmental Earth Sciences,* 65**,** 965-973.

CHEN, Y.-G., CHEN, W.-S., LEE, J.-C., LEE, Y.-H., LEE, C.-T., CHANG, H.-C. & LO, C.-H. 2001. Surface Rupture of 1999 Chi-Chi Earthquake Yields Insights on Active Tectonics of Central Taiwan. *Bulletin of the Seismological Society of America,* 91**,** 977-985.

CHI, W.-C., DREGER, D. & KAVERINA, A. 2001. Finite-Source Modeling of the 1999 Taiwan (Chi-Chi) Earthquake Derived from a Dense Strong-Motion Network. *Bulletin of the Seismological Society of America,* 91**,** 1144-1157.

CHIANG, S. H. & CHANG, K. T. 2011. The potential impact of climate change on typhoon-triggered landslides in Taiwan, 2010-2099. *Geomorphology,* 133**,** 143-151.

CLARKE, B. A. & BURBANK, D. W. 2011. Quantifying bedrock-fracture patterns within the shallow subsurface: Implications for rock mass strength, bedrock landslides, and erodibility. *Journal of Geophysical Research-Earth Surface,* 116.

CLAUSET, A., SHALIZI, C. R. & NEWMAN, M. E. J. 2009. Power-law distributions in empirical data. *SIAM Review,* 51**,** 661-703.

COLE, W. F., MARCUM, D. R., SHIRES, P. O., COTTON, S. A. A. I., CLARK, B. R. & INC., L. A. A. 1998. Analysis of earthquake-reactivated landslides in the epicentral region, central Sant Cruz Mountains, California. *In:* KEEFER, D. K. (ed.) *The Loma Prieta, California, Earthquake of October 17, 1989 - Landslides: U.S. Geological survey professional paper 1551-C.*

COLLISON, A., WADE, S., GRIFFITHS, J. & DEHN, M. 2000. Modelling the impact of predicted climate change on landslide frequency and magnitude in SE England. *Engineering Geology,* 55**,** 205-218.

CORNELL, C. A. & VAN MARKE, E. H. The major influences on seismic risk. Proc. Third World Conf. on Earthquake Engineering, 1969 Santiago, Chile. 69-93.

COX, D. R. 1958. Regression analysis of binary sequences (with discussion). *Journal of the Royal Statistical Society B,* 20**,** 215-242.

COX, N. J. pers coms. *RE: Correspondance: Analytical weighting for logistic regression.*

CRAWFORD, A. M. & CURRAN, J. H. 1982. The influence of rate- and displacement-dependent shear resistance on the response of rock slopes to seismic loads. *International Journal of Rock Mechanics and Mining Sciences & Geomechanics Abstracts,* 19**,** 1-8.

CROSTA, G. B. & AGLIARDI, F. 2003. Failure forecast for large rock slides by surface displacement measurements. *Canadian Geotechnical Journal,* 40**,** 176-191.

CUI, P., CHEN, X.-Q., ZHU, Y.-Y., SU, F.-H., WEI, F.-Q., HAN, Y.-S., LIU, H.-J. & ZHUANG, J.-Q. 2011. The Wenchuan Earthquake (May 12, 2008), Sichuan Province, China, and resulting geohazards. *Natural Hazards,* 56**,** 19-36.

CULMANN, K. 1866. *Die graphische statik*, Meyer & Zeller.

DADSON, S. J., HOVIUS, N., CHEN, H., DADE, W. B., LIN, J. C., HSU, M. L., LIN, C. W., HORNG, M. J., CHEN, T. C., MILLIMAN, J. & STARK, C. P. 2004. Earthquake-

triggered increase in sediment delivery from an active mountain belt. *Geology,* 32**,** 733-736.

DADSON, S. J., HOVIUS, N., CHEN, H. G., DADE, W. B., HSIEH, M. L., WILLETT, S. D., HU, J. C., HORNG, M. J., CHEN, M. C., STARK, C. P., LAGUE, D. & LIN, J. C. 2003. Links between erosion, runoff variability and seismicity in the Taiwan orogen. *Nature,* 426**,** 648-651.

DAHAL, R. K., BHANDARY, N. P., TIMILSINA, M., YATABE, R. & HASEGAWA, S. Earthquake-Induced Landslides. Earthquake-Induced Landslides: Proceedings of the International Symposium on Earthquake-Induced Landslides, Kiryu, Japan, 2012, 2012. Springer Verlag, 149.

DAI, F. C. & LEE, C. F. 2001. Frequency-volume relation and prediction of rainfall-induced landslides. *Engineering Geology,* 59**,** 253-266.

DAI, F. C. & LEE, C. F. 2003. A spatiotemporal probabilistic modelling of storm-induced shallow landsliding using aerial photographs and logistic regression. *Earth Surface Processes and Landforms,* 28**,** 527-545.

DAI, F. C., XU, C., YAO, X., XU, L., TU, X. B. & GONG, Q. M. 2011. Spatial distribution of landslides triggered by the 2008 Ms 8.0 Wenchuan earthquake, China. *Journal of Asian Earth Sciences,* 40**,** 883-895.

DAVIS, L. L. & WEST, L. R. 1973. OBSERVED EFFECTS OF TOPOGRAPHY ON GROUND MOTION. *Bulletin of the Seismological Society of America,* 63**,** 283-298.

DE MICHELE, M., RAUCOULES, D., DE SIGOYER, J., PUBELLIER, M. & CHAMOT-ROOKE, N. 2010. Three-dimensional surface displacement of the 2008 May 12 Sichuan earthquake (China) derived from Synthetic Aperture Radar: evidence for rupture on a blind thrust. *Geophysical Journal International,* 183**,** 1097-1103.

DEHN, M. & BUMA, J. 1999. Modelling future landslide activity based on general circulation models. *Geomorphology,* 30**,** 175-187.

DEHN, M., BURGER, G., BUMA, J. & GASPARETTO, P. 2000. Impact of climate change on slope stability using expanded downscaling. *Engineering Geology,* 55**,** 193-204.

DELLOW, G. D. & HANCOX, G. T. The influence of rainfall on earthquake-induced landslides in New Zealand. Earthquakes and Urban Development : New Zealand Geotechnical Society 2006 Symposium, 2006 Nelson, New Zealand. Institution of Professional Engineers New Zealand, 355-368.

DENG, J. L., KAMEYA, H., MIYASHITA, Y., KUWANO, J., KUWANO, R. & KOSEKI, J. 2011. STUDY ON DIP SLOPE FAILURE AT HIGASHI TAKEZAWA INDUCED BY 2004 NIIGATA-KEN CHUETSU EARTHQUAKE. *Soils and Foundations,* 51**,** 929-943.

DENSMORE, A. L., ANDERSON, R. S., MCADOO, B. G. & ELLIS, M. A. 1997. Hillslope Evolution by Bedrock Landslides. *Science,* 275**,** 369-372.

DENSMORE, A. L. & HOVIUS, N. 2000. Topographic fingerprints of bedrock landslides. *Geology,* 28**,** 371-374.

DENSMORE, A. L., LI, Y., RICHARDSON, N. J., ZHOU, R., ELLIS, M. & ZHANG, Y. 2010. The Role of Late Quaternary Upper-Crustal Faults in the 12 May 2008 Wenchuan Earthquake. *Bulletin of the Seismological Society of America,* 100**,** 2700-2712.

DIETRICH, W. E., MCKEAN, J., BELLUGI, D. & PERRON, T. 2007. The prediction of shallow landslide location and size using a multidimensional landslide analysis in a digital terrain model. *In:* CHEN, C. L. & MAJOR, J. J. (eds.) *Debris-Flow Hazards Mitigation: Mechanics, Prediction, and Assessment.* Rotterdam: Millpress Science Publishers.

DIXON, N. & BROOK, E. 2007. Impact of predicted climate change on landslide reactivation: case study of Mam Tor, UK. *Landslides,* 4**,** 137-147.

DOSER, D. I., WEBB, T. H. & MAUNDER, D. E. 1999. Source parameters of large historical (1918–1962) earthquakes, South Island, New Zealand. *Geophys. J. Int.,* 139**,** 769-794.

DOWNES, G. L. 1995. *Atlas of isoseismal maps of New Zealand earthquakes,* Lower Hutt, New Zealand, Institute of Geological & Nuclear Sciences Limited.

DOWRICK, D. J. 1991. Magnitude reassessment of New Zealand earthquakes. *Earthquake Engineering & Structural Dynamics,* 20**,** 577-596.

DOWRICK, D. J. 1994. Damage and intensities in the magnitude 7.8 1929 Murchison, New Zealand. *Earthquake. Bulletin of the New Zealand National Society for Earthquake Engineering,* 27**,** 190-204.

DOWRICK, D. J. 1996. The modified Mercalli earthquake intensity scale; revisions arising from recent studies of New Zealand earthquakes. *Bulletin of the New Zealand National Society for Earthquake Engineering,* 29 92-106.

DOWRICK, D. J. & RHOADES, D. A. 1998. Magnitudes of New Zealand earthquakes, 1901-1993. *Bull N.Z. Nat. Soc. Earthq. Eng.,* 31**,** 260-280.

DOWRICK, D. J. & SMITH, E. G. C. 1990. Surface wave magnitudes of some New Zealand earthquake 1901-1988. *Bull. NZ National Society for Earthquake Engineering,* 23**,** 198-210.

EBERHARDT, E., STEAD, D. & COGGAN, J. S. 2004. Numerical analysis of initiation and progressive failure in natural rock slopes - the 1991 Randa rockslide. *International Journal of Rock Mechanics and Mining Sciences,* 41**,** 69-87.

ELGAMAL, A. & HE, L. C. 2004. Vertical earthquake ground motion records: An overview. *Journal of Earthquake Engineering,* 8**,** 663-697.

ENGDAHL, E. R. & VILLASEÑOR, A. 2002. Global Seismicity: 1900-1999. *In:* LEE, W. H. K., KANAMORI, H., JENNINGS, P. C. & KISSLINGER, C. (eds.) *International Handbook of Earthquake and Engineering Seismology, Part A, Chapter 41.* Academic Press.

ENGDAHL, E. R., VILLASEÑOR, A. & WILLIAM H.K. LEE, H. K. P. C. J. A. C. K. 2002. 41 Global seismicity: 1900-1999. *International Geophysics.* Academic Press.

ENGELDER, T. 1993. *Stress Regimes in the Lithosphere,* Princeton, Princeton University Press

.

ESRI 2012. ArcGIS Resource Centre: Desktop 10. http://help.arcgis.com/en/arcgisdesktop/10.0/help/.

FAN, C. H., ALLISON, R. J. & JONES, M. E. 1994. The effects of weathering on the characteristics of argillaceous rocks. *In:* ROBINSON, D. A. & WILLIAMS, R. B. G. (eds.) *Rock Weathering and Landform Evolution.* Chichester: John Wiley & Sons.

FANNIN, R. & JAAKKOLA, J. 1999. Hydrological response of hillslope soils above a debris-slide headscarp. *Canadian Geotechnical Journal,* 36**,** 1111-1122.

FELZER, K. R. & BRODSKY, E. E. 2006. Decay of aftershock density with distance indicates triggering by dynamic stress. *Nature,* 441**,** 735-738.

FRANKLIN, A. G. & CHANG, F. K. 1977. Earthquake resistance of earth and rock-fill dams: Permanent displacements of earth embankments by Newmark sliding block analysis. *Miscellaneous Paper S-71-17, Report 5.* Vicksburg, Mississippi: U.S. Army Engineer Waterways Experiment Station.

FURNIVAL, G. M. & WILSON, R. W. 1974. Regression by leaps and bounds. *Technometrics,* 16**,** 499-511.

FYFE, H. E. 1929. Movement of the White Creek Fault, New Zealand. *N.Z. J. Sci Tech,* 11**,** 192-197.

GALLI, M., ARDIZZONE, F., CARDINALI, M., GUZZETTI, F. & REICHENBACH, P. 2008. Comparing landslide inventory maps. *Geomorphology,* 94**,** 268-289.

GARCIA-RODRIGUEZ, M. J., MALPICA, J. A., BENITO, B. & DIAZ, M. 2008. Susceptibility assessment of earthquake-triggered landslides in El Salvador using logistic regression. *Geomorphology,* 95**,** 172-191.

GEONET 2011. New Zealand earthquake catalogue. http://magma.geonet.org.nz/resources/quakesearch/: New Zealand Earthquake Commission and GNS Science.

GERSTENBERGER, M., WIEMER, S. & GIARDINI, D. 2001. A systematic test of the hypothesis that the b value varies with depth in California. *Geophys. Res. Lett.,* 28**,** 57-60.

GNS SCIENCE 2011a. New Zealand Active Faults Database. http://data.gns.cri.nz/af/.

GNS SCIENCE 2011b. New Zealand Digitial Terrain Model based on LINZ NZMG 20 m contour data and spot heights. GNS Science.

GODT, J., SENER, B., VERDIN, K., WALD, D., EARLE, P., HARP, E. & JIBSON, R. Rapid assessment of earthquake-induced landsliding. Proceedings of the World Landslide Forum, 2009 Tokyo, Japan. 4.

GORSEVSKI, P. V., GESSLER, P. E., FOLTZ, R. B. & ELLIOT, W. J. 2006. Spatial Prediction of Landslide Hazard Using Logistic Regression and ROC Analysis. *Transactions in GIS,* 10**,** 395-415.

GOULD, W. & STATACORP 1994. Clarification on analytic weights with linear regression. *Stata Technical Bulletin,* 20**,** http://www.stata.com/support/faqs/statistics/analytical-weights-with-linear-regression/.

GRANT-TAYLOR, T. L. 1964. Stable angles in Wellington greywacke. *New Zealand Engineering,* 19**,** 129-30.

GREENLAND, S. 1989. Modeling and Variable Selection in Epidemiologic Analysis. *Am J of Public Health,* 79**,** 340-349.

GUTENBERG, B. & RICHTER, C. F. 1936. Magnitude and Energy of Earthquakes. *Science* 83 183-185.

GUTENBERG, B. & RICHTER, C. F. 1944. Frequency of earthquakes in California. *Bulletin of the Seismological Society of America,* 34**,** 185.

GUTENBERG, B. & RICHTER, C. F. 1954. Seismicity of the Earth and Associated Phenomena, 310 pp. Princeton: Princeton Univ. Press.

GUTHRIE, R. H., HOCKIN, A., COLQUHOUN, L., NAGY, T., EVANS, S. G. & AYLES, C. 2010. An examination of controls on debris flow mobility: Evidence from coastal British Columbia. *Geomorphology,* 114**,** 601-613.

GUZZETTI, F., ARDIZZONE, F., CARDINALI, M., GALLI, M., REICHENBACH, P. & ROSSI, M. 2008. Distribution of landslides in the Upper Tiber River basin, central Italy. *Geomorphology,* 96**,** 105-122.

GUZZETTI, F., CARDINALI, M. & REICHENBACH, P. 1996. The influence of structural setting an lithology on landslide type and pattern. *Environmental and Engineering Geology,* 2**,** 531–555.

GUZZETTI, F., GALLI, M., REICHENBACH, P., ARDIZZONE, F. & CARDINALI, M. 2006. Landslide hazard assessment in the Collazzone area, Umbria, Central Italy. *Natural Hazards and Earth System Sciences,* 6**,** 115-131.

GUZZETTI, F., MALAMUD, B. D., TURCOTTE, D. L. & REICHENBACH, P. 2002. Power-law correlations of landslide areas in central Italy. *Earth and Planetary Science Letters,* 195**,** 169-183.

GUZZETTI, F., REICHENBACH, P., CARDINALI, M., ARDIZZONE, F. & GALLI, M. 2003. The impact of landslides in the Umbria region, central Italy. *Natural Hazards and Earth System Science,* 3**,** 469-486.

GUZZETTI, F., REICHENBACH, P., CARDINALI, M., GALLI, M. & ARDIZZONE, F. 2005. Probabilistic landslide hazard assessment at the basin scale. *Geomorphology,* 72**,** 272-299.

HAINES, J. 1991. 1929 Murchison earthquake. *Neotectonics of the Buller Region Workshop.* Department of Scientific and Industrial Research Geology and Geophysics, New Zealand.

HAINZL, S. & FISCHER, T. 2002. Indications for a successively triggered rupture growth underlying the 2000 earthquake swarm in Vogtland/NW Bohemia. *J. Geophys. Res.,* 107**,** 2338.

HANCOX, G. T. 1969. Geological report on the Lyell dam site and reservoir slope stability in relation to landsliding in the upper Buller Gorge during the 1968 Inangahua earthquake. *DSIR New Zealand Geological Survey File Report LD7/911 and 971/2 August 1969.*

HANCOX, G. T. 2011. *RE: Pers coms - email correspondance regarding observations of landslides following the 1929 Buller and 1968 Inangahua earthquakes.* Type to PARKER, R.

HANCOX, G. T., COX, S. C., TURNBULL, I. M. & CROZIER, M. J. 2003. *Reconnaissance studies of landslides and other ground damage caused by the Mw7. 2 Fiordland earthquake of 22 August 2003,* Lower Hutt, New Zealand, Institute of Geological and Nuclear Sciences.

HANCOX, G. T., DELLOW, G., SAVENEY, M. M., SCOTT, B. & VILLAMOR, P. 2004. *Reconnaissance studies of landslides caused by the ML 5.4 Lake Rotoehu earthquake and swarm of July 2004,* Lower Hutt, New Zealand, Institute of Geological and Nuclear Sciences.

HANCOX, G. T., PERRIN, N. D. & DELLOW, G. D. 1998. Earthquake-induced landsliding in New Zealand and implications for MM intensity and seismic hazard assessment: a summary of recent study. *Proc. Tech. Conference and AGM.* Wairakei, NZ Nat. Soc. Earthq. Eng., Lower Hutt, New Zealand.

HANCOX, G. T., PERRIN, N. D. & DELLOW, G. D. 2002. Recent studies of historical earthquake-induced landsliding, ground damage, and MM intensity in New Zealand. *Bulletin NZ National Society for Earthquaker Eng.,* 35**,** 59-95.

HARP, E. L. & JIBSON, R. L. 1995a. Inventory of Landslides Triggered by the 1994 Northridge, California Earthquake. http://pubs.usgs.gov/of/1995/ofr-95-0213: U.S. Geological Survey Open File Report 95-213.

HARP, E. L. & JIBSON, R. W. 1995b. Seismic Instrumentation of Landslides - Building a Better Model of Dynamic Landslide Behavior. *Bulletin of the Seismological Society of America,* 85**,** 93-99.

HARP, E. L. & JIBSON, R. W. 1996. Landslides triggered by the 1994 Northridge, California, earthquake. *Bulletin of the Seismological Society of America,* 86**,** S319-332.

HARRELL, F. E. 2001. *Regression Modelling Strategies: with applications to linear models, logistic regression, and survival analysis,* New York, Springer-Verlag.

HARRELL, F. E. & LEE, K. L. 1985. A comparison of the discrimination of discriminant analysis and logistic regression under multivariate normality. *In:* SEN, P. K. (ed.) *Bio-statistics: Statistics in Biomedical, Public Health, and Environmental Sciences. The Bernard G. Greenberg Volume.* Amsterdam: North-Holland.

HAVAEJ, M., STEAD, D., LORIG, L. & VIVAS, J. Modelling Rock Bridge Failure And Brittle Fracturing In Large Open Pit Rock Slopes. 46th U.S. Rock Mechanics/Geomechanics Symposium, June 24 - 27, 2012, 2012 Chicago, Illinois. 9.

HAVENITH, H.-B., JONGMANS, D., FACCIOLI, E., ABDRAKHMATOV, K. & BARD, P. Y. 2002. Site effect analysis around the seismically induced Ananevo rockslide, Kyrgyzstan. *Bulletin of the Seismological Society of America,* 92**,** 3190-3209.

HAYAKAWA, Y. S., OGUCHI, T. & LIN, Z. 2008. Comparison of new and existing global digital elevation models: ASTER G-DEM and SRTM-3. *Geophysical research letters,* 35**,** 1-5.

HENDERSON, J. 1937. The west Nelson earthquakes of 1929 (with Notes on the Geological Structure of West Nelson). *The New Zealand Journal of Science and Technology,* XIX**,** 66-144.

HERGARTEN, S. & NEUGEBAUER, H. J. 2000. Self-organized criticality in two-variable models. *Physical Review E,* 61**,** 2382-2385.

HIJMANS, R. J., CAMERON, S. E., PARRA, J. L., JONES, P. G. & JARVIS, A. 2005. Very high resolution interpolated climate surfaces for global land areas. *International Journal of Climatology,* 25**,** 1965-1978.

HOEK, E. 1983. Strength of jointed rock masses, 23rd Rankine Lecture. *Geotechnique,* 33**,** 187-223.

HOEK, E. 2000. Practical Rock Engineering. http://www.rocscience.com/hoek/corner/Practical_Rock_Engineering.pdf.

HOEK, E. & BROWN, E. T. 1997. Practical estimates of rock mass strength. *International Journal of Rock Mechanics and Mining Sciences,* 34**,** 1165-1186.

HOEK, E., CARRANZA-TORRES, C. & CORKUM, B. HOEK-BROWN FAILURE CRITERION – 2002 EDITION. NARMS-TAC Conference, 2002 Toronto. 267-273.

HOEK, E., KAISER, P. K. & BAWDEN, W. F. 1995. *Support of underground excavations in hard rock,* Rotterdam, Balkema.

HOEK, E., MARINOS, P. G. & MARINOS, V. P. 2005. Characterisation and engineering properties of tectonically undisturbed but lithologically varied sedimentary rock masses. *International Journal of Rock Mechanics and Mining Sciences,* 42**,** 277-285.

HOSMER, D. W. & LEMESHOW, S. 2000. *Applied logistic regression,* New York, John Wiley & Sons Inc.

HOVIUS, N., MEUNIER, P., LIN, C.-W., CHEN, H., CHEN, Y.-G., DADSON, S., HORNG, M.-J. & LINES, M. 2011. Prolonged seismically induced erosion and the mass balance of a large earthquake. *Earth and Planetary Science Letters,* 304**,** 347-355.

HOVIUS, N., STARK, C. P. & ALLEN, P. A. 1997. Sediment flux from a mountain belt derived by landslide mapping. *Geology,* 25**,** 231-234.

HOVIUS, N., STARK, C. P., CHU, H. T. & LIN, J. C. 2000. Supply and removal of sediment in a landslide-dominated mountain belt: Central Range, Taiwan. *Journal of Geology,* 108**,** 73-89.

HUDNUT, K. W., SHEN, Z., MURRAY, M., MCCLUSKY, S., KING, R., HERRING, T., HAGER, B., FENG, Y., FANG, P., DONNELLAN, A. & BOCK, Y. 1996. Co-Seismic Displacements of the 1994 Northridge, California, Earthquake. *Bulletin of the Seismological Society of America,* 86**,** S19-S36.

HUDSON, J. A. & HARRISON, J. P. 1997. *Engineering rock mechanics: An Introduction to the Principles,* Oxford, Pergamon.

IMAIZUMI, F. & SIDLE, R. 2007. Linkage of sediment supply and transport processes in Miyagawa Dam catchment. *J. Geophys. Res. ,* 112**,** F03012.

IVERSON, R. M. 2000. Landslide Triggering by Rain Infiltration. *Water Resour. Res.,* 36**,** 1897-1910.

IWAHASHI, J., WATANABE, S. & FURUYA, T. 2003. Mean slope-angle frequency distribution and size frequency distribution of landslide masses in Higashikubiki area, Japan. *Geomorphology,* 50**,** 349-364.

JAEGER, J. C., COOK, N. G. W. & ZIMMERMAN, R. W. 2008. *Fundamentals of rock mechanics,* Oxford, Blackwell Publishing.

JARVIS, A., REUTER, H. I., NELSON, A. & GUEVARA, E. 2008. Hole-filled SRTM for the globe Version 4. available from the CGIAR-CSI SRTM 90m Database (http://srtm.csi.cgiar.org).

JIBSON, R., HARP, E. & MICHAEL, J. M. 1998. A method for producing digital probabilistic seismic landslide hazard maps: an example from the New Madrid seismic zone. *Geological Society of America Bulletin,* 105**,** 521-536.

JIBSON, R. W. 1993. Predicting earthquake-induced landslide displacements using Newmark's sliding block analysis. *Transportation Research Record,* 1411**,** 9-17.

JIBSON, R. W. 2007. Regression models for estimating coseismic landslide displacement. *Engineering Geology,* 91**,** 209-218.

JIBSON, R. W. 2011. Methods for assessing the stability of slopes during earthquakes-A retrospective. *Engineering Geology,* 122**,** 43-50.

JIBSON, R. W., HARP, E. L. & MICHAEL, J. A. 2000. A method for producing digital probabilistic seismic landslide hazard maps. *Engineering Geology,* 58**,** 271-289.

JIBSON, R. W., HARP, E. L., SCHULZ, W. & KEEFER, D. K. 2004. Landslides triggered by the 2002 Denali fault, Alaska, earthquake and the inferred nature of the strong shaliing. *Earthquake Spectra,* 20**,** 669-691.

JIBSON, R. W., HARP, E. L., SCHULZ, W. & KEEFER, D. K. 2006. Large rock avalanches triggered by the M 7.9 Denali Fault, Alaska, earthquake of 3 November 2002. *Engineering Geology,* 83**,** 144-160.

JIBSON, R. W. & MICHAEL, J. A. 2009. *Maps showing seismic landslide hazards in Anchorage, Alaska*. U.S. Geological Survey Scientific Investigations Map 3077.

JOHNSON, K. L. 1985. *Contact Mechanics,* Cambridge, Cambridge University Press.

JONES, L. M., AKI, K., BOORE, D., CELEBI, M., DONNELLAN, A., HALL, J., HARRIS, R., HAUKSSON, E., HEATON, T., HOUGH, S., HUDNUT, K., HUTTON, K., JOHNSTON, M., JOYNER, W., KANAMOIL, H., MARSHALL, G., MICHAEL, A., MOIL, J., MURRAY, M., PONTI, D., REASENBERG, P., SCHWARTZ, D., SEEBER, L., SHAKAL, A., SIMPSON, R., THIO, H., TINSLEY, J., TODOROVSKA, M., TRIFUNAC, M., WALD, D. & ZOBACK, M. L. 1994. The magnitude 6.7 Northildge, California, earthquake of 17 January 1994. *Science* 266**,** 389-397.

KAMP, U., GROWLEY, B. J., KHATTAK, G. A. & OWEN, L. A. 2008. GIS-based landslide susceptibility mapping for the 2005 Kashmir earthquake region. *Geomorphology,* 101**,** 631-642.

KEEFER, D. K. 1984. Landslides Caused by Earthquakes. *Geological Society of America Bulletin,* 95**,** 406-421.

KEEFER, D. K. 1994. The Importance of Earthquake-Induced Landslides to Long-Term Slope Erosion and Slope-Failure Hazards in Seismically Active Regions. *Geomorphology,* 10**,** 265-284.

KEEFER, D. K. 2000. Statistical analysis of an earthquake-induced landslide distribution - the 1989 Loma Prieta, California event. *Engineering Geology,* 58**,** 231-249.

KEEFER, D. K. 2002. Investigating landslides caused by earthquakes - A historical review. *Surveys in Geophysics,* 23**,** 473-510.

KEEFER, D. K. 2009. Earthquake triggered landslides, 20 years later. *In:* LEE, C. T. (ed.) *The next generation of research on earthquake-induced landslides: An international conference in commemoration of the 10th Anniversary of the Chi-Chi Earthquake.* Taiwan: National Central University.

KEEFER, D. K., WARTMAN, J., NAVARRO OCHOA, C., RODRIGUEZ-MAREK, A. & WIECZOREK, G. F. 2006. Landslides caused by the M 7.6 Tecomán, Mexico earthquake of January 21, 2003. *Engineering Geology,* 86**,** 183-197.

KEEFER, D. K. & WILSON, R. C. 1989. Predicting earthquake-induced landslides, with emphasis on arid and semi-arid environments. *In:* P.M. SADLER AND D.M. MORTON (EDITORS) (ed.) *Landslides in a Semi-Arid Environment with Emphasis on the Inland Valleys of Southern California.* Riverside, CA: Inland Geological Society of Southern California Publications.

KHAZAI, B. & SITAR, N. 2004. Evaluation of factors controlling earthquake-induced landslides caused by Chi-Chi earthquake and comparison with the Northridge and Loma Prieta events. *Engineering Geology,* 71**,** 79-95.

KIJKO, A. 2004. Estimation of the Maximum Earthquake Magnitude, mmax. *Pure and Applied Geophysics,* 161**,** 1655-1681.

KILBURN, C. R. J. & PETLEY, D. N. 2002. Forecasting giant, catastrophic slope collapse: lessons from Vajont, Northern Italy. *Geomorphology,* 54**,** 21-32.

KOONS, P. O., UPTON, P. & BARKER, A. D. 2012. The influence of mechanical properties on the link between tectonic and topographic evolution. *Geomorphology,* 137**,** 168-180.

KORUP, O. 2006. Effects of large deep-seated landslides on hillslope morphology, western Southern Alps, New Zealand. *J. Geophys. Res.,* 111**,** F01018.

KORUP, O., DENSMORE, A. L. & SCHLUNEGGER, F. 2010. The role of landslides in mountain range evolution. *Geomorphology,* 120**,** 77-90.

KORUP, O., GÖRÜM, T. & HAYAKAWA, Y. 2012. Without power? Landslide inventories in the face of climate change. *Earth Surface Processes and Landforms,* 37**,** 92-99.

KOSSOBOKOV, V. G., KEILIS-BOROK, V. I., TURCOTTE, D. L. & MALAMUD, B. D. 2000. Implications of a Statistical Physics Approach for Earthquake Hazard Assessment and Forecasting. *Pure and Applied Geophysics,* 157**,** 2323-2349.

KOTTEK, M., GRIESER, J., BECK, C., RUDOLF, B. & ., F. R. 2006. World Map of the Köppen-Geiger climate classification updated. *Meteorol. Z.,* 15**,** 259-263.

KRAMER, S. L. 1996. *Geotechnical earthquake engineering,* Upper Saddle River, Prentice-Hall, Inc.

KRAMER, S. L. & SMITH, M. W. 1997. Modified Newmark Model for Seismic Displacements of Compliant Slopes. *Journal of Geotechnical and Geoenvironmental Engineering,* 123**,** 635-644.

KULHANEK, O. 2005. *Seminar on b-value,* December 10-19, 2005, Dept. of Earth Sciences, Seismolgy, Uppsala University, Uppsala, Sweden.

KUTTER, B. L. 1983. Deformation of centrifuge models of clay embankments due to 'bumpy road' earthquakes. *International Journal of Soil Dynamics and Earthquake Engineering,* 2**,** 199-205.

KUTTER, B. L., AND JAMES, R. G. 1989. Dynamic centrifuge model tests on clay embankments. *Geotechnique,* 39**,** 91-106.

LARSON, E., EKSTROM, G. & NETTLES, M. 2012. Global CMT Catalogue. http://www.globalcmt.org/CMTsearch.html.

LAVÉ, J. & BURBANK, D. 2004. Denudation processes and rates in the Transverse Ranges, southern California: Erosional response of a transitional landscape to external and anthropogenic forcing. *J. Geophys. Res.,* 109**,** F01006.1-F01006.31.

LAWLESS, J. F. & SINGHAL, K. 1978. Efficient screening of non-normal regression models. *Biometrics,* 34**,** 318-327.

LAWLESS, J. F. & SINGHAL, K. 1987a. ISMOD: An all subsets regression program for generalized linear models I: Statistical and computational background. *Computer methods and programs in biomedicine,* 24**,** 117-124.

LAWLESS, J. F. & SINGHAL, K. 1987b. ISMOD: An all subsets regression program for generalized linear models II: Program guide and examples. *Computer methods and programs in biomedicine,* 24**,** 117-124

.

LEE, C. T., HUANG, C. C., LEE, J. F., PAN, K. L., LIN, M. L. & DONG, J. J. 2008a. Statistical approach to earthquake-induced landslide susceptibility. *Engineering Geology,* 100**,** 43-58.

LEE, C. T., HUANG, C. C., LEE, J. F., PAN, K. L., LIN, M. L. & DONG, J. J. 2008b. Statistical approach to storm event-induced landslides susceptibility. *Natural Hazards and Earth System Sciences,* 8**,** 941–960.

LEE, S. & EVANGELISTA, D. G. 2006. Earthquake-induced landslide-susceptibility mapping using an artificial neural network. *Natural Hazards and Earth System Sciences,* 6**,** 687-695.

LEE, S. & MIN, K. 2001. Statistical analysis of landslide susceptibility at Yongin, Korea. *Environmental Geology,* 40**,** 1095-1113.

LEE, S. T., YU, T. T. & PENG, W. F. 2012. Effect of Earthquake on Subsequent Typhoon-Induced Landslides Using Remote Sensing Imagery in the 99 Peaks Region, Central Taiwan. *Key Engineering Materials,* 500**,** 773-779.

LEROUEIL, S., LOCAT, A., EBERHARDT, E. & KOVACEVIC, N. 2012. Progressive failure in natural and engineered slopes. *In:* EBERHARDT, E., FROESE, C., TURNER, A. K. & LEROUEIL, S. (eds.) *Landslides and Engineered Slopes.*

LI, Y., CHEN, G., TANG, C., ZHOU, G. & ZHENG, L. 2012. Rainfall and earthquake-induced landslide susceptibility assessment using GIS and Artificial Neural Network. *Nat. Hazards Earth Syst. Sci,* 12**,** 2719-2729.

LIANG, W., YANG, C., ZHAO, Y., DUSSEAULT, M. B. & LIU, J. 2007. Experimental investigation of mechanical properties of bedded salt rock. *International Journal of Rock Mechanics and Mining Sciences,* 44**,** 400-411.

LIAO, H. W. & LEE., C. T. 2000. Landslides triggered by the Chi-Chi earthquake. *Asian Conference on Remote Sensing.* http://www.a-a-r-s.org/acrs/proceeding/ACRS2000/Papers/HM00-7.htm.

LIN, C. W., LIU, S. H., LEE, S. Y. & LIU, C. C. 2006. Impacts of the Chi-Chi earthquake on subsequent rainfall-induced landslides in central Taiwan. *Engineering Geology,* 86**,** 87-101.

LIN, C. W., SHIEH, C. L., YUAN, B. D., SHIEH, Y. C., LIU, S. H. & LEE, S. Y. 2004. Impact of Chi-Chi earthquake on the occurrence of landslides and debris flows: example from the Chenyulan River watershed, Nantou, Taiwan. *Engineering Geology,* 71**,** 49-61.

LIN, G.-W., CHEN, H., CHEN, Y.-H. & HORNG, M.-J. 2008a. Influence of typhoons and earthquakes on rainfall-induced landslides and suspended sediments discharge. *Engineering Geology,* 97**,** 32-41.

LIN, G. W., CHEN, H., HOVIUS, N., HORNG, M. J., DADSON, S., MEUNIER, P. & LINES, M. 2008b. Effects of earthquake and cyclone sequencing on landsliding and fluvial sediment transfer in a mountain catchment. *Earth Surface Processes and Landforms,* 33**,** 1354-1373.

LIN, J. C., JEN, C. H. & JOU, T. C. 2001. Earthquake Landslide Hazard: Case Study of Chi-Chi Earthquake, Taiwan. *International Conference on Geomorphology.* Tokyo.

LIN, J. S. & WHITMAN, R. V. 1986. Earthquake induced displacement of sliding blocks. *Journal of Geotechnical Engineering,* 112**,** 44-59.

LIN, M. L. & TUNG, C. C. 2004. A GIS-based potential analysis of the landslides induced by the Chi-Chi earthquake. *Engineering Geology,* 71**,** 63-77.

LIN, W.-T., CHOU, W.-C., LIN, C.-Y., HUANG, P.-H. & TSAI, J.-S. 2005. Vegetation recovery monitoring and assessment at landslides caused by earthquake in Central Taiwan. *Forest Ecology and Management,* 210**,** 55-66.

LIU, J. & WOING, T. A practical approach to creating a landslide database using Taiwan SPOT mosaic. Proceedings of the 20th Asia Conference on Remote Sensing, 1999 Hong Kong, China. http://www.a-a-r-s.org/acrs/proceeding/ACRS1999/Papers/GEO99-4.htm.

LIU, J. K., WONG, C. C., HUANG, J. J. & YANG, M. J. Landslide enhancement images for the study of torrential rainfall landslides. Proceeding of the 23rd Asian conference on Remote Sensing, 2002 Kathmandu. 193-198.

LIU-ZENG, J., ZHANG, Z., WEN, L., TAPPONNIER, P., SUN, J., XING, X., HU, G., XU, Q., ZENG, L., DING, L., JI, C., HUDNUT, K. W. & VAN DER WOERD, J. 2009. Co-seismic ruptures of the 12 May 2008, Ms 8.0 Wenchuan earthquake, Sichuan: East–west crustal shortening on oblique, parallel thrusts along the eastern edge of Tibet. *Earth and Planetary Science Letters,* 286**,** 355-370.

LOCKNER, D., NAKA, H., TANAKA, H., ITO, H., IKEDA, R. & OMURA, K. 2009. Geometry of the Nojima fault at Nojima-Hirabayashi, Japan-I. A simple damage structure inferred from borehole core permeability. *Pure and Applied Geophysics,* 166**,** 1649-1667.

LOEW, S., GISCHIG, V., MOORE, J. R. & KELLER-SIGNER, A. 2012. Monitoring of potentially catastrophic rockslides. *In:* EBERHARDT, E., FROESE, C., TURNER, A. K. & LEROUEIL, S. (eds.) *Landslides and Engineered Slopes.* London, UK: Taylor & Francis Group.

LONDE, P. 1988. Discussion on the determination of the shear stress failure in rock masses. *J. Geotech. Engng Div. ASEC,* 14**,** 374-6.

MA, K.-F., MORI, J., LEE, S.-J. & YU, S. B. 2001. Spatial and Temporal Distribution of Slip for the 1999 Chi-Chi, Taiwan, Earthquake. *Bulletin of the Seismological Society of America,* 91**,** 1069-1087.

MAHDAVIFAR, M. R., SOLAYMANI, S. & JAFARI, M. K. 2006. Landslides triggered by the Avaj, Iran earthquake of June 22, 2002. *Engineering Geology,* 86**,** 166-182.

MAKDISI, F. I. & SEED, H. B. 1978. Simplified Procedure for Estimating Dam and Embankment Earthquake-Induced Deformations. *Journal of the Geotechnical Engineering Division,* 104**,** 849-867.

MALAMUD, B. D., TURCOTTE, D. L., GUZZETTI, F. & REICHENBACH, P. 2004a. Landslide inventories and their statistical properties. *Earth Surface Processes and Landforms,* 29**,** 687-711.

MALAMUD, B. D., TURCOTTE, D. L., GUZZETTI, F. & REICHENBACH, P. 2004b. Landslides, earthquakes, and erosion. *Earth and Planetary Science Letters,* 229**,** 45-59.

MASSEY, C. I., GERSTENBERGER, M., MCVERRY, G. & LITCHFIELD, N. 2012. Canterbury Earthquakes 2010/2011 Port Hills slope stability: Additional assessment of the life-safety risk from rockfalls (boulder rolls). *GNS Consultancy Report 2012/214.*

MCCAFFREY, R. & ABERS, G. 1988. SYN3: A program for inversion of teleseismic body waveforms on microcomputers. *Air Force Geophysics Laboratory Technical Report.* Air force geophysica laboratory, Hanscom AFB, MA.

MCFADDEN, L. D., EPPES, M. C., GILLESPIE, A. R. & HALLET, B. 2005. Physical weathering in arid landscapes due to diurnal variation in the direction of solar heating. *Bull. Geol. Soc. Am.,* 117**,** 161-173.

MEGAHAN, W. F., DAY, N. F. & BLISS, T. M. 1978. Landslide occurrence in the western and central Northern Rocky Mountain physiographic province in Idaho. *In:* YOUNGBERG, C. T. (ed.) *Forest soils and land use: Proceedings of the Fifth North American Forest Soils Conference.* Fort Collins: Colorado State University.

MELCHIORRE, C. & FRATTINI, P. 2012. Modelling probability of rainfall-induced shallow landslides in a changing climate, Otta, Central Norway. *Climatic Change,* 113**,** 413-436.

MEUNIER, P., HOVIUS, N. & HAINES, J. 2007. Regional patterns of earthquake-triggered landslides and their relation to ground motion. *Geophys. Res. Lett.,* 34**,** 1-5.

MEUNIER, P., HOVIUS, N. & HAINES, J. A. 2008. Topographic site effects and the location of earthquake induced landslides. *Earth and Planetary Science Letters,* 275**,** 221-232.

MEUNIER, P., UCHIDA, T. & HOVIUS, N. 2013. Landslide patterns reveal the sources of large earthquakes. *Earth and Planetary Science Letters,* 363**,** 27-33.

MILES, S. B. & KEEFER, D. K. 2009. Evaluation of CAMEL - comprehensive areal model of earthquake-induced landslides. *Engineering Geology,* 104**,** 1-15.

MILLEDGE, D. 2008. *Modelling Shallow Landslides: The Importance of Hydrological Controls and Lateral Reinforcement.* PhD, Durham University.

MOGI, K. 1962. Magnitude-frequency relationship for elastic shocks accompanying fractures of various materials and some related problems in earthquakes. *Bull. Earthquake Res. Inst. Univ. Tokyo,* 40**,** 831-883.

MONTGOMERY, D. R. 2001. Slope Distributions, Threshold Hillslopes, and Steady-state Topography. *American Journal of Science,* 301**,** 432-454.

MONTGOMERY, D. R. & BRANDON, M. T. 2002. Topographic controls on erosion rates in tectonically active mountain ranges. *Earth and Planetary Science Letters,* 201**,** 481-489.

MONTGOMERY, D. R., DIETRICH, W. E., TORRES, R., PRESTRUD ANDERSON, S., HEFFNER, J. T. & LOAGUE, K. 1997. Hydrologic response of a steep, unchanneled valley to natural and applied rainfall. *Water Resources Research,* 33**,** 91-109.

MOONEY, W. D., BEROZA, G. C. & KIND, R. 2007. Fault zones from top to bottom: a geophysical perspective. *In:* HANDY, M. R., HIRTH, G., HOVIUS, N. (ed.) *Tectonic Faults Agents of Change on a Dynamic Earth.* Cambridge: MIT Press.

MOORE, J. R., GISCHIG, V., AMANN, F., HUNZIKER, M. & BURJANEK, J. 2012. Earthquake-triggered rock slope failures: Damage and site effects. *In:* EBERHARDT, E., FROESE, C., TURNER, K. & LEROUEIL, S. (eds.) *Landslides and Engineered Slopes, 2 Volume Set +CDROM: Protecting Society through Improved Understanding.* Boca Raton: CRC Press.

MOORE, J. R., GISCHIG, V., BURJANEK, J., LOEW, S. & FÄH, D. 2011. Site Effects in Unstable Rock Slopes: Dynamic Behavior of the Randa Instability (Switzerland). *Bulletin of the Seismological Society of America,* 101**,** 3110–3116.

MOORE, J. R., SANDERS, J. W., DIETRICH, W. E. & GLASER, S. D. 2009. Influence of rock mass strength on the erosion rate of alpine cliffs. *EARTH SURFACE PROCESSES AND LANDFORMS,* 34**,** 1339–1352.

MUNSON, C. G. & THURBER, C. H. 1997. Analysis of the attenuation of strong ground motion on the island of Hawaii. *Bulletin of the Seismological Society of America,* 87**,** 945-960.

MURPHY, W. 2006. The role of topographic amplification on the initiation of rock slopes failures during earthquakes. *In:* EVANS, S. G., MUGNOZZA, G. S., STROM, A. & HERMANNS, R. L. (eds.) *Landslides from Massive Rock Slope Failure.*

MURPHY, W., PARKER, R. N. & HANCOX, G. 2011a. Back analysis of landslides triggered by earthquakes – some implications for future practice. *International Symposium on Rock Slope Stability in Open Pit Mining and Civil Engineering*.

MURPHY, W., PARKER, R. N. & HANCOX, G. Back analysis of landslides triggered by earthquakes – some implications for future practice. International Symposium on Rock Slope Stability in Open Pit Mining and Civil Engineering, 2011b Vancouver, Canada.

N.A.S.A. LAND PROCESSES DISTRIBUTED ACTIVE ARCHIVE CENTER 2011. ASTER GDEM V2. *In:* USGS/EARTH RESOURCES OBSERVATION AND SCIENCE (EROS) CENTER (ed.). Sioux Falls, South Dakota.: ASTER GDEM is a product of METI and NASA.

NANJO, K. Z., ENESCU, B., SHCHERBAKOV, R., TURCOTTE, D. L., IWATA, T. & OGATA, Y. 2007. Decay of aftershock activity for Japanese earthquakes. *Journal of Geophysical Research-Solid Earth,* 112**,** B08309.

NATHAN, S., RATTENBURY, M. S. & SUGGATE, R. P. 2002. *Geology of the Greymouth area. Institute of Geological & Nuclear Sciences 1:250000 geological map 12*. Lower Hutt, New Zealand: GNS Science.

NATIONAL EARTHQUAKE INFORMATION CENTER 2012. USGS NEIC Catalogue.

NEW ZEALAND SOCIETY FOR EARTHQUAKE ENGINEERING 1992. A revision of the Modified Mercalli intensity scale. Report of a study group of the New Zealand Society for Earthquake Engineering. *Bulletin NZ National Society for Earthquaker Eng.,* 25**,** 345-357.

NEWMARK, N. M. 1965. Effects of earthquakes on dams and embankments. *Geotechnique,* 15**,** 139-159.

NG, K. Y. 2007. *Mechanisms of shallow rainfall-induced landslides in residual soils in humid tropical environments.* PhD, University of Durham.

NICHOL, J. & WONG, M. S. 2005. Satellite remote sensing for detailed landslide inventories using change detection and image fusion. *International Journal of Remote Sensing,* 26**,** 1913-1926.

NIWA 2011. National Climate Database. *In:* RESEARCH, N. I. O. W. A. A. (ed.). http://cliflo.niwa.co.nz/.

NZ TOPO MAP. 2012. http://www.topomap.co.nz/ [Online].

OHISHI, K., SAITOH, K., KATAGIRI, M., KATAKAMI, N. & TERASHI, M. Comparison of embankment behaviors in static tilting and shaking table tests. Proc., 1st Int. Conf. on Earthquake Geotechnical Engineering, 1995 Tokyo. 1075-1080.

OHLMACHER, G. C. & DAVIS, J. C. 2003. Using multiple logistic regression and GIS technology to predict landslide hazard in northeast Kansas, USA. *Engineering Geology,* 69**,** 331-343.

OLAMI, Z., FEDER, H. J. S. & CHRISTENSEN, K. 1992. SELF-ORGANIZED CRITICALITY IN A CONTINUOUS, NONCONSERVATIVE CELLULAR AUTOMATON MODELING EARTHQUAKES. *Physical Review Letters,* 68**,** 1244-1247.

OWEN, L. A., KAMP, U., KHATTAK, G. A., HARP, E. L., KEEFER, D. K. & BAUER, M. A. 2008. Landslides triggered by the 8 October 2005 Kashmir earthquake. *Geomorphology,* 94**,** 1-9.

OZCEP, F., EROL, E., SARACOGLU, F. & HALILOGLU, M. 2012. Seismic landslide analysis: Gurpinar (Istanbul) as a case history. *Environmental Earth Sciences,* 66**,** 1617-1630.

PAL, I., NATH, S. K., SHUKLA, K., PAL, D. K., RAJ, A., THINGBAIJAM, K. K. S. & BANSAL, B. K. 2008. Earthquake hazard zonation of Sikkim Himalaya using a GIS platform. *Natural Hazards,* 45**,** 333-377.

PARISE, M. & JIBSON, R. W. 2000. A seismic landslide susceptibility rating of geologic units based on analysis of characteristics of landslides triggered by the 17 January, 1994 Northridge, California earthquake. *Engineering Geology,* 58**,** 251-270.

PARKER, R. N. 2010. *Controls on the distribution of landslides triggered by the 2008 Wenchuan earthquake, Sichuan Province, China.* MSc Thesis, University of Durham.

PARKER, R. N., DENSMORE, A. L., ROSSER, N. J., DE MICHELE, M., LI, Y., HUANG, R., WHADCOAT, S. & PETLEY, D. N. 2011. Mass wasting triggered by the 2008 Wenchuan earthquake is greater than orogenic growth. *Nature Geoscience,* 4**,** 449-452.

PARKER, R. N., PETLEY, D., DENSMORE, A., ROSSER, N., DAMBY, D. & BRAIN, M. 2013. Progressive failure cycles and distributions of earthquake-triggered landslides. *In:* UGAI, K., YAGI, H. & WAKAI, A. (eds.) *Earthquake-induced landslides: Proceedings of the International Symposium on Earthquake induced landslides, Kiryu, Japan, 2012.* New York: Springer.

PEARCE, A. J. & O'LOUGHIN, C. L. 1985. Landsliding during a M7.7 earthquake: Influence of geology and topography. *Geology,* 13**,** 855-858.

PEARCE, A. J. & WATSON, A. J. 1986. EFFECTS OF EARTHQUAKE-INDUCED LANDSLIDES ON SEDIMENT BUDGET AND TRANSPORT OVER A 50-YR PERIOD. *Geology,* 14**,** 52-55.

PELLETIER, J. D., MALAMUD, B. D., BLODGETT, T. & TURCOTTE, D. L. 1997. Scale-invariance of soil moisture variability and its implications for the frequency-size distribution of landslides. *Engineering Geology,* 48**,** 255-268.

PERKINS, D. M. 1997. Landslide hazard maps analogues to probabilistic earthquake ground motion hazard maps. *Landslide Risk Assessment***,** 327-332.

PETLEY, D. N. & ALLISON, R. J. 1997. The mechanics of deep-seated landslides. *Earth Surface Processes and Landforms,* 22**,** 747-758.

PETLEY, D. N., BULMER, M. H. & MURPHY, W. 2002. Patterns of movement in rotational and translational landslides. *Geology,* 30**,** 719-722.

PETLEY, D. N., HIGUCHI, T., DUNNING, S., ROSSER, N. J., PETLEY, D. J., BULMER, M. H. & CAREY, J. 2005a. A new model for the development of movement in progressive landslides. *In:* HUNGR, O., FELL, R., COUTURE, R. & EBERHARDT, E. (eds.) *Landslide risk management.* Amsterdam: A. T. Balkema.

PETLEY, D. N., HIGUCHI, T., PETLEY, D. J., BULMER, M. H. & CAREY, J. 2005b. Development of progressive landslide failure in cohesive materials. *Geology,* 33**,** 201-204.

PETLEY, D. N., PETLEY, D. J. & ALLISON, R. J. 2008. Temporal Prediction in Landslides - understanding the Saito effect. *10th International Symposium on Landslides and Engineered Slopes.* Xi'an, China.

PLUMB, R. A. 1994. Influence of composition and texture on the failure properties of clastic rocks. *In:* SCHLUMBERGER CAMBRIDGE RESEARCH, U. (ed.) *Rock Mechanics in Petroleum Engineering.* Delft, Netherlands: Society of Petroleum Engineers

PRADEL, D., SMITH, P. M., STEWART, J. P. & RAAD, G. 2005. Case history of landslide movement during the Northridge earthquake. *Journal of Geotechnical and Geoenvironmental Engineering,* 131**,** 1360-1369.

RATHJE, E. M., ABRAHAMSON, N. A. & BRAY, J. D. 1998. Simplified frequency content estimates of earthquake ground motions. *Journal of Geotechnical and Geoenvironmental Engineering,* 124**,** 150-159.

RATHJE, E. M. & BRAY, J. D. 2000. Nonlinear coupled seismic sliding analysis of earth structures. *Journal of Geotechnical and Geoenvironmental Engineering,* 126**,** 1002-1014.

RATTENBURY, M. S., COOPER, R. & JOHNSTON, M. R. 1998. *Geology of the Nelson area. Institute of Geological & Nuclear Sciences 1:250000 geological map 9*. Lower Hull, New Zealand: GNS Science.

RATTENBURY, M. S., TOWNSEND, D. B. & JOHNSTON, M. R. 2006. *Geology of the Kaikoura area. Institute of Geological & Nuclear Sciences 1:250 000 geological map 13*. Lower Hutt, New Zealand: GNS Science.

ROBINSON, R., ARABASZ, W. J. & EVISON, F. F. 1975. Long-term behaviour of an aftershock sequence: the Inangahua, New Zealand, earthquake of 1968. *Geophysical journal of the Royal Astronomical Society,* 41**,** 31-49.

ROCKFIELD 2011. ELFEN. Swansea, http://www.rockfield.co.uk: Rockfield Software Ltd.

RODGERS, D. W. & LITTLE, T. A. 2006. World's largest coseismic strike-slip offset: The 1855 rupture of the Wairarapa Fault, New Zealand, and implications for displacement/length scaling of continental earthquakes. *J. Geophys. Res.,* 111**,** B12408.

RODRÍGUEZ, C. E., BOMMER, J. J. & CHANDLER, R. J. 1999. Earthquake-induced landslides: 1980-1997. *Soil Dynamics and Earthquake Engineering,* 18**,** 325-346.

SABA, S. B., VAN DER MEIJDE, M. & VAN DER WERFF, H. 2010. Spatiotemporal landslide detection for the 2005 Kashmir earthquake region. *Geomorphology,* 124**,** 17-25.

SATO, H. P., HASEGAWA, H., FUJIWARA, S., TOBITA, M., KOARAI, M., UNE, H. & IWAHASHI, J. 2007. Interpretation of landslide distribution triggered by the 2005 Northern Pakistan earthquake using SPOT 5 imagery. *Landslides,* 4**,** 113-122.

SCHMIDT, K. M. & MONTGOMERY, D. R. 1995. Limits to Relief. *Science,* 270**,** 617-620.

SCHOLZ, C. H. 1968. The frequency-magnitude relation of microfracturing in rock and its relation to earthquakes. *Bull. Seismol. Soc. Am.,* 58**,** 399-415.

SCHUMM, S. A. & LICHTY, R. W. 1965. Time, space, and causality in geomorphology. *American Journal of Science,* 263**,** 110-119.

SELBY, M. J. 2005. *Hillslope materials and processes,* Oxford, UK, Oxford University Press.

SEPÚLVEDA, S., SEREY, A., LARA, M., PAVEZ, A. & REBOLLEDO, S. 2010. Landslides induced by the April 2007 Aysén Fjord earthquake, Chilean Patagonia. *Landslides,* 7**,** 483-492.

SEPULVEDA, S. A., MURPHY, W., JIBSON, R. W. & PETLEY, D. N. 2005. Seismically induced rock slope failures resulting from topographic amplification of strong ground motions: The case of Pacoima Canyon California. *Engineering Geology,* 80**,** 336-348.

SHCHERBAKOV, R., TURCOTTE, D. L. & RUNDLE, J. B. 2004. A generalized Omori's law for earthquake aftershock decay. *Geophysical research letters,* 31**,** L11613.

SHCHERBAKOV, R., TURCOTTE, D. L. & RUNDLE, J. B. 2005a. Aftershock statistics. *Pure and Applied Geophysics,* 162**,** 1051-1076.

SHCHERBAKOV, R., TURCOTTE, D. L. & RUNDLE, J. B. 2006. Scaling properties of the Parkfield aftershock sequence. *Bulletin of the Seismological Society of America,* 96**,** S376-S384.

SHCHERBAKOV, R., YAKOVLEV, G., TURCOTTE, D. L. & RUNDLE, J. B. 2005b. Model for the distribution of aftershock interoccurrence times. *Physical Review Letters,* 95.

SHEN, Z.-K., GE, B. X., JACKSON, D. D., POTTER, D., CLINE, M. & SUNG, L.-Y. 1996. Northridge Earthquake Rupture Models Based on the Global Positioning System Measurements. *Bulletin of the Seismological Society of America,* 86**,** S37-S48.

SHEN, Z. K., SUN, J. B., ZHANG, P. Z., WAN, Y. G., WANG, M., BURGMANN, R., ZENG, Y. H., GAN, W. J., LIAO, H. & WANG, Q. L. 2009. Slip maxima at fault junctions and rupturing of barriers during the 2008 Wenchuan earthquake. *Nature Geoscience,* 2**,** 718-724.

SHIN, T.-C. & TENG, T.-L. 2001. An Overview of the 1999 Chi-Chi, Taiwan, Earthquake. *Bulletin of the Seismological Society of America,* 91**,** 895-913.

SHIN, T. C., KUO, K. W., LEE, W. H. K., TENG, T. L. & TSAI, Y. B. 2000. A preliminary report on the 1999 Chi-Chi (Taiwan) earthquake. *Seism. Res. Lett.,* 71**,** 23-29.

SHOU, K. J., HONG, C. Y., WU, C. C., HSU, H. Y., FEI, L. Y., LEE, J. F. & WEI, C. Y. 2011. Spatial and temporal analysis of landslides in Central Taiwan after 1999 Chi-Chi earthquake. *Engineering Geology,* 123**,** 122-128.

SIMONS, N., MENZIES, B. & MATTHEWS, M. 2001. *A short course in soil and rock slope engineering,* London, Thomas Telford Publishing.

SINGH, D. P. 1975. A study of creep of rocks. *International Journal of Rock Mechanics and Mining Sciences & Geomechanics Abstracts,* 12**,** 271-276.

SITAR, N. & BARDET, J. P. 2001. Landslides. *In:* ARNOLD, J. U. A. C. (ed.) *Chi-Chi, Taiwan, Earthquake of September 21, 1999 Reconnaissance Report.* Earthquake Engineering Research Institute Publication 2001–2002, Earthquake Spectra.

SKEMPTON, A. W. 1960. Terzaghi's discovery of effective stress. *In:* BJERRUM, L., CASAGRANDE, A., PECK, R. B. & SKEMPTON, A. W. (eds.) *From theory to practice in soil mechanics.* New York: Wiley.

SKEMPTON, A. W. & DE LORY, F. A. 1957. Stability of natural slopes in London Clay. *Proceedings of the 9th International Conference on Soil Mechanics and Foundation Engineering (Tokyo),* 3**,** 261-70.

SMITH, R. L. 1992. Suppressor Variables in Multiple Regression/Correlation. *Educational and Psychological Measurement,* 52**,** 17-29.

SOMERVILLE, P. G., SMITH, N. F., GRAVES, R. W. & ABRAHAMSON, N. A. 1997. Modification of empirical strong ground motion attenuation relations to include the amplitude and duration effects of rupture directivity. *Bulletin of the Seismological Society of America,* 68**,** 199-222.

STAFFORD, P. J. 2011. *RE: Pers coms - email correspondence regarding earthquake simulation procedure.* Type to PARKER, R.

STARK, C. P. & GUZZETTI, F. 2009. Landslide rupture and the probability distribution of mobilized debris volumes. *Journal of Geophysical Research-Earth Surface,* 114**,** 1-16.

STARK, C. P. & HOVIUS, N. 2001. The characterization of landslide size distribution. *Geophys. Res. Lett,* 28**,** 1091-1094.

STEAD, D., EBERHARDT, E. & COGGAN, J. S. 2006. Developments in the characterization of complex rock slope deformation and failure using numerical modelling techniques. *Engineering Geology,* 83**,** 217-235.

STEAD, D., JABOYEDOFF, M. & COGGAN, J. S. 2012. Rock slope characterization and geomechanical modelling. *In:* EBERHARDT, E., FROESE, C., TURNER, A. K. & LEROUEIL, S. (eds.) *Landslides and Engineered Slopes: Protecting Societ through Improved Understanding.*

STIRLING, M., LITCHFIELD, N., SMITH, W., BARNES, P., GERSTENBERGER, M., MCVERRY, G. & PETTINGA, J. 2007. Updated probabilistic seismic hazard assessment for the Canterbury region. *GNS Science Consultancy Report 2007/232 - ECan Report Number U06/6.*

STIRLING, M. W., MCVERRY, G., BERRYMAN, K. R., MCGINTY, P., VILLAMOR, P., VAN DISSEN, R., DOWRICK, D. J. & COUSINS, J. 2000. Probabilistic seismic hazard assessment of New Zealand. prepared for Earthquake Commission Research Foundation, Institute of Geological and Nuclear Sciences Ltd, Lower Hutt, New Zealand.

STIRLING, M. W., VERRY, G. H. M. & BERRYMAN, K. R. 2002. A New Seismic Hazard Model for New Zealand. *BULLETIN OF THE SEISMOLOGICAL SOCIETY OF AMERICA,* 92**,** 1878-1903.

STRENK, P. M. 2010. *Evaluation of Analytical Procedures for Estimating Seismically Induced Permanent Deformations in Slopes.* Ph.D. thesis, Drexel University.

STRENK, P. M. & WARTMAN, J. 2011. Uncertainty in seismic slope deformation model predictions. *Engineering Geology,* 122**,** 61-72.

SUYEHIRO, S., ASADA, T. & OHTAKE, M. 1964. Foreshocks and aftershocks accopmpanying a perceptible earthquake in central Japan: On the peculiar nature of foreshocks. *Pap. Meteorol. Geophys.,* 19**,** 427-435.

TACHIKAWA, T., KAKU, M., IWASAKI, A., GESCH, D., OIMOEN, M., ZHANG, Z., DANIELSON, J., KRIEGER, T., CURTIS, B., HAASE, J., ABRAMS, M., CRIPPEN, R. & CARABAJAL, C. 2011. ASTER Global Digital Elevation Model Version 2 – Summary of Validation Results. *In:* MEYER, D. (ed.). NASA Land Processes Distributed Active Archive Center and the Joint Japan-US ASTER Science Team.

TANG, C., ZHU, J., QI, X. & DING, J. 2011. Landslides induced by the Wenchuan earthquake and the subsequent strong rainfall event: A case study in the Beichuan area of China. *Engineering Geology,* 122**,** 22-33.

TANG, C. A. 1997. Numerical simulation of progressive rock failure and associated seismicity. *International Journal of Rock Mechanics and Mining Sciences,* 34**,** 249.

TATARD, L., GRASSO, J. R., HELMSTETTER, A. & GARAMBOIS, S. 2010. Characterization and comparison of landslide triggering in different tectonic and climatic settings. *J. Geophys. Res.,* 115**,** F04040.

TAYLOR, D. W. 1948. *Fundamentals of Soil Mechanics,* New York, John Wiley.

TERZAGHI, K. 1936. The shearing resistance of saturared soils. *Proceedings of the first international conference on soil mechanics,* 1**,** 54-6.

TERZAGHI, K. 1950. Mechanisms of landslides. *In:* PAIGE, S. (ed.) *Application of geology to engineering practice (Berkley volume).* New York: Geological Society of America.

THORNES, J. B. 1983. Evolutionary Geomorphology. *Geography,* 68**,** 225-235.

TURCOTTE, D. L. & MALAMUD, B. D. 2004. Landslides, forest fires, and earthquakes: examples of self-organized critical behavior. *Physica a-Statistical Mechanics and Its Applications,* 340**,** 580-589.

UCAR, R. 1986. Determination of shear failure envelope in rock masses. *J. Geotech. Engng Div. ASEC,* 112**,** 303-315.

USGS 1994. The Magnitude 6.7 Northridge, California, Earthquake of 17 January 1994. *Science,* 266**,** 389-397.

USGS 2012. USGS fault model repository. *In:* SURVEY, U. S. G. (ed.). http://earthquake.usgs.gov/regional/sca/slipmodels.php.

UZUOKA, R., SENTO, N., KAZAMA, M. & UNNO, T. 2005. Landslides during the earthquakes on May 26 and July 26, 2003 in Miyagi, Japan. *Soils and Foundations,* 45**,** 149-163.

VAN DEN EECKHAUT, M., POESEN, J., GOVERS, G., VERSTRAETEN, G. & DEMOULIN, A. 2007. Characteristics of the size distribution of recent and historical landslides in a populated hilly region. *Earth and Planetary Science Letters,* 256**,** 588-603.

VAN WESTEN, C. J., VAN ASCH, T. W. J. & SOETERS, R. 2006. Landslide hazard and risk zonation—why is it still so difficult? *Bulletin of Engineering Geology and the Environment,* 65**,** 167-184.

VON RUETTE, J., PAPRITZ, A., LEHMANN, P., RICKLI, C. & OR, D. 2011. Spatial statistical modeling of shallow landslides-Validating predictions for different landslide inventories and rainfall events. *Geomorphology,* 133**,** 11-22.

WALD, D. J. & HEATON, T. H. 1994. A dislocation model of the 1994 Northridge, California, earthquake determined from strong ground motions. *US Geological Survey Open-File Report 1996-0278.*

WALD, D. J., HEATON, T. H. & HUDNUT, K. W. 1996. The slip history of the 1994 Northridge, California, earthquake determined from strong-motion, teleseismic, GPS, and leveling data. *Bulletin of the Seismological Society of America,* 86**,** S49-S70.

WALD, D. J., LIN, K.-W. & QUITORIANO, V. 2008. Quantifying and Qualifying USGS ShakeMap Uncertainty. *U.S. Geological Survey Open File Report 2008-1238.*

WALD, D. J., QUITORIANO, V., HEATON, T. H., KANAMORI, H., SCRIVNER, C. W. & WORDEN, C. B. 1999. TriNet" ShakeMaps": rapid generation of peak ground motion and intensity maps for earthquakes in southern California. Earthquake Engineering Research Institute.

WALD, D. J., WORDEN, B. C., QUITORIANO, V. & PANKOW, K. L. 2005. ShakeMap manual: technical manual, user's guide, and software guide. U.S. Geological Survey.

WALKER, S. H. & DUNCAN, D. B. 1967. Estimation of the probability of an event as a function of several independent variables. *Biometrika,* 54**,** 167-178.

WANG, H. B., SASSA, K. & XU, W. Y. 2007. Analysis of a spatial distribution of landslides triggered by the 2004 Chuetsu earthquakes of Niigata Prefecture, Japan. *Natural Hazards,* 41**,** 43-60.

WARREN, N. W. & LATHAM, G. V. 1970. An experiment study of thermal induced microfracturing and its relation to volcanic seismicity. *J. Geophys. Res.,* 75**,** 4455-4464.

WARTMAN, J., BRAY, J. D. & SEED, H. B. 2003. Inclined plane studies of the Newmark sliding block procedure. *Journal of Geotechnical and Geoenvironmental Engineering,* 129**,** 673-684.

WARTMAN, J., SEED, H. B. & BRAY, J. D. 2005. Shaking table modelling of seismically induced deformations in slopes. *Journal of Geotechnical and Geoenvironmental Engineering,* 131**,** 610-622.

WASOWSKI, J., DEL GAUDIO, V., CASARANO, D., LOLLINO, P. & MUSCILLO, S. 2013. Local Scale Seismic Landslide Susceptibility Assessment Based on Historic Earthquake Records Combined with Accelerometer Monitoring and Ambient Noise Data. *Earthquake-Induced Landslides.* Springer.

WASOWSKI, J., KEEFER, D. K. & LEE, C.-T. 2011. Toward the next generation of research on earthquake-induced landslides: Current issues and future challenges. *Engineering Geology,* 122**,** 1-8.

WHADCOAT, S. K. 2011. *Landsliding and sediment dynamics following the 2008 Wenchuan Earthquake in the Beichuan area of China.* M.Sc., University of Durham.

WIEMER, S., MCNUTT, S. R. & WYSS, M. 1998. Temporal and three-dimensional spatial analyses of the frequency–magnitude distribution near Long Valley Caldera, California. *Geophysical Journal International,* 134**,** 409-421.

WIEMER, S. & WYSS, M. 2002. Mapping spatial variability of the frequency-magnitude distribution of earthquakes. *In:* RENATA, D. & BARRY, S. (eds.) *Advances in Geophysics.* Elsevier.

WILSON, C. & DIETRICH, W. 1987. The contribution of bedrock groundwater flow to storm runoff and high pore pressure development in hollows. *IN: Erosion and Sedimentation in the Pacific Rim. IAHS Publication*.

WILSON, R. C. & KEEFER, D. K. 1983. Dynamic analysis of a slope failure from the 6 August 1979 Coyote Lake, California, earthquake. *Bulletin of the Seismological Society of America,* 73**,** 863.

WITT, A., MALAMUD, B. D., ROSSI, M., GUZZETTI, F. & PERUCCACCI, S. 2010. Temporal correlations and clustering of landslides. *Earth Surface Processes and Landforms,* 35**,** 1138-1156.

WOOLLEY, K. K. 1997. How Variables Uncorrelated with the Dependent Variable Can Actually Make Excellent Predictors: The Important Suppressor Variable Case. *Paper presented at the annual meeting of the Southwest Educational Research Association, Austin, January, 1997,* http://ericae.net/ft/tamu/supres.htm.

WU, C., TAKEO, M. & IDE, S. 2001. Source Process of the Chi-Chi Earthquake: A Joint Inversion of Strong Motion Data and Global Positioning System Data with a Multifault Model. *Bulletin of the Seismological Society of America,* 91**,** 1128-1143.

WU, F. C., XU, J. Q., ZHAO, X. L. & HU, W. N. 1990. AN OBSERVED EFFECT OF TOPOGRAPHY ON SURFACE MOTION. *Acta Geophysica Sinica,* 33**,** 188-195.

XU, C., XU, X., DAI, F. & SARAF, A. K. 2012. Comparison of different models for susceptibility mapping of earthquake triggered landslides related with the 2008 Wenchuan earthquake in China. *Computers & Geosciences,* 46**,** 317-329.

XU, X., WEN, X., YU, G., CHEN, G., KLINGER, Y., HUBBARD, J. & SHAW, J. 2009. Coseismic reverse- and oblique-slip surface faulting generated by the 2008 Mw 7.9 Wenchuan earthquake, China. *Geology,* 37**,** 515-518.

YAGI, H., SATO, G., HIGAKI, D., YAMAMOTO, M. & YAMASAKI, T. 2009. Distribution and characteristics of landslides induced by the Iwate-Miyagi Nairiku Earthquake in 2008 in Tohoku District, Northeast Japan. *Landslides,* 6**,** 335-344.

YESILNACAR, E. & TOPAL, T. 2005. Landslide susceptibility mapping: A comparison of logistic regression and neural networks methods in a medium scale study, Hendek region (Turkey). *Engineering Geology,* 79**,** 251-266.

YILMAZ, I. & KESKIN, I. 2009. GIS based statistical and physical approaches to landslide susceptibility mapping (Sebinkarahisar, Turkey). *Bulletin of Engineering Geology and the Environment,* 68**,** 459-471.

ZENG, Y. & CHEN, C.-H. 2001. Fault Rupture Process of the 20 September 1999 Chi-Chi, Taiwan, Earthquake. *Bulletin of the Seismological Society of America,* 91**,** 1088-1098.

ZHANG, D. & WANG, G. 2007. Study of the 1920 Haiyuan earthquake-induced landslides in loess (China). *Engineering Geology,* 94**,** 76-88.

ZHANG, Y., CHEN, G., ZHENG, L. & LI, Y. 2013. Numerical Analysis of the Largest Landslide Induced by the Wenchuan Earthquake, May 12, 2008 Using DDA. *In:* UGAI, K., YAGI, H. & WAKAI, A. (eds.) *Earthquake-Induced Landslides: Proceedings of the International Symposium on Earthquake induced landslides, Kiryu, Japan, 2012.* New York: Springer.